Thermal stability and mechanical property of polymer layered graphite oxide composites

by

Frances Therese Cerezo

B App Sci (Applied Chemistry) Honours

A thesis presented in fulfilment for the Degree of

Doctor of Philosophy

Discipline of Applied Chemistry

School of Applied Sciences

Science Engineering and Technology

RMIT University

Melbourne, Australia

2006

Statement of Authenticity

I, hereby declare that the work presented in this thesis, unless otherwise acknowledged, is that of the candidate alone and has not been submitted previously, in whole or in part, for any other academic award.

The work described in this research project was carried out in the Discipline of Applied Chemistry, RMIT University since the official date of commencement of the program.

Frances Therese Cerezo

Acknowledgements

I wish to thank my supervisor Professor Robert A. Shanks for his advice, assistance, time and patient during the course of this project.

I would like to thank my co-supervisor Dr Christopher Preston for his assistance and patient during the duration of this project.

I would like to thank Dr Gandara Amarasinghe for her technical, emotional support and her continuous belief in me but most of all her friendship.

I would like to thank Dr Antonietta Genovese for all her technical advice. I would also like to thank her for her patience and specially her friendship.

Polymer Research Group, the challenges, interaction has been an important part of this experience and therefore my gratitude extends to all members. I would like to thank Nelson Mora, Sirisart Oujai, Mende Joveski and Maggie Lu Guang Chen for there technical assistance, suggestions and for all the fun we shared.

I would like to thank Daniel Kaminski for his patience, advice and friendship. Thank you for the laughs.

To Simon Peake, for the enjoyable time we share and hopefully continue to share in the future. Thank you for being a great distraction.

I am indebted to my parents Rolando and Thelma for all their tremendous support during my studies from the past, and present. To my sister, Anne and my brother Arvin, for making me laugh and sane….thank you.

I gratefully acknowledge the financial support for my postgraduate studies provided by Co-operation Research Centre (CRC) in awarding me a CRC scholarship. In addition to the training and seminar I have attended throughout the duration of my PhD studies.

Journal paper

F.T. Cerezo, C.M.L. Preston and R.A. Shanks Structural, mechanical and dielectric properties of poly(ethylene-co-methyl acrylate-co-acrylic acid) graphite oxide nanocomposites. Composites Science and Technology; online

F.T. Cerezo, C.M.L. Preston and R.A. Shanks. Morphology, thermal stability and mechanical behaviour of poly(propylene-grafted maleic anhydride) layered expanded graphite oxide composites. Macromolecular Materials and Engineering; submitted

F.T. Cerezo, C.M.L. Preston and R.A. Shanks. Effects of layered expanded graphite oxide on the thermal and dynamic mechanical properties of poly(propylene-grafted maleic anhydride). Journal of Applied Polymer Science; submitted

F.T. Cerezo, C.M.L. Preston and R.A. Shanks and A. Genovese. Intercalation of graphite with acids. Carbon; submitted

Refereed conference paper

1st Advanced Materials Modern Science of Advanced Materials, Townsville, Australia; 2004.

F.T. Cerezo, C.M.L. Preston and R.A. Shanks. Structural, mechanical and dielectric properties of poly(ethylene-co-methyl acrylate-co-acrylic acid) graphite oxide nanocomposites

Conference paper

27th Australian Polymer Symposium, Adelaide, Australia; 2004. Frances T. Cerezo, Robert A. Shanks and Christopher M. Preston. Structural, mechanical and thermal properties of poly(propylene-g-maleic anhydride) expanded graphite oxide nanocomposites

27th Australian Polymer Symposium, Adelaide, Australia; 2004. Darren Simon, Frances T. Cerezo and Robert A. Shanks. Surface roughness and morphology of block copolymers thin films with different solvent and substrate

1st International Conference on Materials for Advanced Technologies (ICMAT), Conference Proceedings Symposium I Advanced Polymers, Singapore; 2003. F.T. Cerezo, C.M.L. Preston and R.A. Shanks, S. Houshyar Characterization of graphite oxide and expanded graphite oxide poly(ethylene-co-methyl acrylate-co-acrylic acid) nanocomposites

General abbreviation and nomenclature

SEM	Scanning Eletron Microscope	C-atom	Carbon atom
BET	Brunauer-Emmet-Teller	F-atom	Fluorine atom
FTIR	Fourier Transform Infrared Spectroscopy	O-atom	Oxygen atom
WAXD	Wide Angle X-ray Diffraction	N_2	Nitrogen
DSC	Differential Scanning Calorimetry	C	Carbon
TGA	Thermogravimetry Analysis	CO	Carbon monoxide
DMA	Dynamic Mechanical Analysis	CO_2	Carbon dioxide
DEA	Dielectric Analysis	CF	Carbon fluoride
XRD	X-ray Diffraction	C_4F	Carbon tetrafluoride
TEM	Transmission Electron Microscope	F	Fluorine
NMR	Nuclear Magnetic Resonance	HF	Hydrogen fluoride
DTA	Differential Thermal Analysis	F_2	Fluoride
AFM	Atomic Force Microscopy	Br	Bromine
CRT	cathode ray tube	Cl	Chlorine
EMI	electron magnetic shielding	C_8Br	Graphite bromine
		ICl	Iodine monochloride
EMAA	Poly(ethylene-co-methyl acrylate-co-acrylic acid)	IBr	Iodide bromide
PPMA	Poly(propylene-grafted-maleic anhydride)	C_8Cl	Graphite chloride
PP	Polypropylene	C_5ICl	Graphite iodine monochloride
MA	Maleic anhydride	$FeCl_3$	Ferric chloride
PS	Polystyrene	HCl	Hydrogen chloride
PA-6	Polyamide	Li	Lithium
PI	Polyimide	Na	Sodium
PEO	Poly(ethylene oxide)	K	Potassium
PET	Poly(ethylene terephthalate)	Rb	Rubidium
PU	Polyurethane	Cs	Caesium
PVDF	Poly(vinylidene fluoride)	$HClO_4$	Perchloric acid
PMMA	Poly(methyl methacrylate acid)	H_2SeO_4	Selenic acid
HDPE	High density polyethylene	N_2O_5	Nitrogen pentoxide
PLSN	Polymer layered silicate nanocomposites	P_2O_5	Phosphorous pentoxide
PLGN	Polymer layered graphite nanocomposites	Cr_2O_3	Chromic oxide
PTFE	Poly(tetrafluoroethylene)	$(NH_4)_2S_2O_8$	Ammonium persulfate
OLS	Organically modified layered silicate	MnO_2	Manganese oxide
MMT	Montmorillonite	PbO_2	Lead oxide
GIC	Graphite Intercalated Compound	As_2O_5	Arsenic pentoxide
GO	Graphite Oxide	HIO_3	Iodic acid
EG	Expanded Graphite	H_5IO_6	Periodic acid
EGO	Expanded Graphite Oxide	$FeCl_2$	Ferrous chloride
CEC	cation exchange capacity		
Cl_2	Chlorine	β	beta
HNO_3	Nitric acid	x	weight of adsorbed gas

H_2SO_4	Sulfuric acid
$KClO_3$	Potassium chlorate
CH_3COOH	Acetic acid
$KMnO_4$	Potassium permanganate
$C_{10}H_{21}OH$	Decanol
H_2O	Water
SO_2	Sulfur dioxide
O_2	Oxygen
KCl	Potassium chloride
Mn_2O_7	Manganese heptoxide
K_2SO_4	Potassium sulfate
O_3	Ozone
A_s	surface area
DTG	Derivative weight
TE	Thermal expansion
$T_{c\ onset}$	Onset of crystallisation
$T_{m\ onset}$	Onset of melting
$T_{d\ onset}$	Onset of degradation
T_c	Crystallisation temperature
T_m	Melting temperature
T_d	Degradation temperature
E'	Storage modulus
E"	Loss modulus
Tan(δ)	Loss tangent
T_g	Glass transition temperature
ε'	Permitivity
ε"	Loss factor
σ_c	Conductivity
ΔH_f	Heat of fusion (melting)
ΔG	Gibbs free energy
ΔH	Enthalpy
ΔS	Entropy
T	Temperature
A_E	Activation energy
σ bond	Sigma bonding
π bond	Pi bonding
α	Alpha
δ	Phase angle
ε' or E'	In-phase (storage modulus)
ε" or E'	Out-of-phase (loss modulus)
ε* or E*	Complex modulus

x_m	weight of adsorbed in monolayer
c	BET constant
P	Pressure
P_0	Saturation vapour pressure
s	slope
i	intercept
S	Specific surface area
N	Avogadros's number
A_m	Molecular cross-sectional area
M	Molecular weight
S_t	Surface area
w	weight
n	order of reflection
λ	Wavelength
$d_{(hkl)}$ or d spacing	distance between two adjacent parallel planes; interlayer spacing
θ	angle
$L_{(hkl)}$ or $L_{(c)}$	crystalline thickness perpendicular to reflection plane
K	shape factor
β_0	shape of crystalline factor
FWHM	Full width at half maxima
ΔH_0	Enthapy of melting
σ	stress
F	Force
A	Area
G	Shear modulus
ε	strain
μ	population mean
$\bar{x}$	sample mean
$t_{(n-1)}$	degrees of freedom
s	sample
N	Number of replicate
σ_0	maximum stress
ω	frequency
t	time
ε(t)	strain
E	modulus
ε_0	strain at maximum stress
η	Viscosity
mN	milliNewton
Ω	Ohms
MΩ	megaOhm
rpm	rotation per minute
pH	power of Hydrogen
$\%.min^{-1}$	percentage per minute

A/D	Area/Distance
l	Length
R	Resistance
V	Voltage
I	current
º	degree
ºC	Celsius degree
%	percentage
%wt	weight percent
%vol	volume percent
nm	nanometer
µm	micrometer
cm	centimeter
mm	millimeter
mL	milliliter
L	Liter
s	second
min	minute
h	hour
PA	Pascal
MGPa	Mega Pascal
GPA	Giga Pascal
$kJ.m^2$	kiloJoules per square meter
$\Omega.cm^{-1}$	Ohms per centimeter
$S.cm^{-1}$	Siemens per centimeter
$g.min^{-1}$	grams per minute
$g.mL^{-1}$	grams per milliliter
kV	kiloVolts
$m^2.g^{-1}$	meter square per gram
$Å^2$	Angstrom square
$mL.min^{-1}$	milliliter per minute
mA	milliAmpere
$ºC.min^{-1}$	Celsius degree per minute
$J.g^{-1}$	Joules per gram
m^2	meter square
$N.m^2$	Newton per square meter
$mm.min^{-1}$	millimeter per minute
kPa	kiloPascal
$J.g^{-1}.ºC^{-1}$	Joules per gram per Celsius degree

Table of contents

Table of figures

Table of tables

Abstract

Polymer composites formed from layered fillers with high surface volume ratio show enhanced reinforcement. Graphite oxide is a high modulus material that can be separated into thin layers with high surface area. Polyolefins such as polyethylene and polypropylene require reinforcement for many applications. The aim of this study is to prepare polymer layered graphite oxide composites using functionalised polyolefin to enhance compatibility with various forms of layered graphite oxide in varying concentration. One of the many objectives is to oxidised graphite flakes to form polar functional groups on the graphite surface to enhance compatibility with functionalised polyolefin.

Functionalised polyolefins were reinforced with layered graphite oxide and expanded graphite oxide using solution blending and melt blending methods. Three different mixing methods with varying shear intensity were employed to prepare polymer layered graphite oxide composites.

Graphite oxides were prepared by using oxidation intercalation with Brønsted acids. Four different oxidative treatments were used including the Staudenmaier method. The graphite oxide structure consists of parallel graphite layers stacked in a periodic manner where the surfaces have been oxidised. Heating graphite oxide at high temperature is referred to as an exfoliation process, this process causes expansion of the layered structure with evolution of gases formed from intercalated oxidants and acids in the graphite layers including water, carbon dioxide and sulfur dioxide. The graphite layers separate and expand forming an interconnected network structure. This material is referred to as expanded graphite oxide. The structure of graphite oxide and its expanded form were investigated by scanning electron microscopy.

Graphite oxide and expanded graphite oxide were characterised by various techniques to determine the oxidation treatment and exfoliation process on the graphite properties including surface properties and interlayer spacing (*d* spacing). BET surface area analysis revealed that oxidation of graphite increased the surface area, and exfoliation of this oxidised graphite formed an even larger surface area. The average pore diameter of these graphite oxides were of nanoscale dimensions. FTIR spectroscopy showed the presence of polar functional groups on the surface of graphite oxide and expanded graphite oxide. This result substantiated the statement reported in the literature that oxidative treatment could result in oxidation of carbon bonds on the surface of graphite. The graphite oxide prepared from the Staudenmaier method resulted in a high interlayer spacing.

The crystalline structure, thermal and mechanical properties and electrical conductivity of the prepared polymer layered graphite oxide composites were studied. Oxidised graphite prepared from the Staudenmaier method and its exfoliated form were dispersed in poly(ethylene-co-methyl acrylate-co-acrylic acid) (EMAA) via solution blending to prepare EMAA layered composites. The resulting EMAA layered composites were characterised by wide-angle X-ray diffraction and thermogravimetric analysis. Wide angle X-ray diffraction analysis revealed no change in interlayer spacing of graphite oxide, indicating the absence of EMAA intercalation in the graphite layers. The thermal stability was determined using thermogravimetric analysis. The EMAA layered composites showed higher thermal stability in comparison with pure EMAA. The mechanical properties of these EMAA layered composites were determined through tensile testing and dynamic mechanical analysis. From these analyses, it showed that shear modulus, yield stress and storage modulus of EMAA in the presence of graphite oxide fillers decreased. Analysis of variance was performed to distinguish effects of graphite oxide concentration, oxidative treatment and type of graphite oxide and their complex interactions.

A solution blending method was used to prepare poly(propylene-grafted-maleic anhydride) layered expanded graphite oxide composites (PPMA-EGO). Two types of PPMA-EGO were prepared using different mixing methods - low and high shear were employed. The preparative mixing methods employed affected the dispersion of EGO in the PPMA matrix. The effects of preparative mixing methods on the PPMA-EGO properties were investigated. The interlayer spacing of graphite layers obtained from wide angle X-ray diffraction analysis did not change when it was incorporated into the PPMA matrix. The mechanical properties of PPMA-EGO obtained from dynamic mechanical analysis indicated that EGO had a reinforcing effect on the elastic behaviour of PPMA-EGO. This is due to strong interfacial adhesion between PPMA and EGO as a result of hydrogen bonding. The elastic behaviour of PPMA-EGO was affected by the surface area of graphite flakes. Low sheared PPMA-EGO elastic behaviour was found to be higher compared with that of high sheared PPMA-EGO.

A melt blending method was used to prepare PPMA-EGO with varying EGO concentration. The interconnected network structure of EGO in the PPMA-EGO was not observed as shown by its scanning electron microscopy images. Thermogravimetric analysis of PPMA-EGO indicates increased decomposition temperature of the PPMA matrix. Dynamic mechanical analysis showed enhanced storage modulus of PPMA-EGO. The maximum elastic modulus of PPMA-EGO was observed at 3 %wt of EGO. The electrical conductivity of PPMA-EGO was measured only for EGO concentrations above 2 %wt. The EGO concentration was found to be the most critical factor in the enhancement of the electrical conductivity of PPMA-EGO.

The crystallisation temperature and crystallinity of all polymer layered graphite oxide composites were determined using differential scanning calorimetry. The results indicated that graphite oxide and expanded graphite oxides acted as nucleating agents in inducing the crystallisation of functionalised polyolefin in the layered composites. However, the degree of crystallinity of functionalised polyolefin decreased in the layered composites.

Electrical properties of EMAA layered composites and PPMA-EGO composites prepared via solution blending were determined using dielectric analysis.

Chapter 1 Introduction

The expansion of industrial and economic activities results in a continuous demand for new, low-cost materials able to meet increasingly stringent conditions. Polymers are commonly mixed with a variety of both natural and synthetic compounds to improve their performance. Inorganic components used for this purpose are called fillers and give rise to composites with greater mechanical strength, impact resistance, reduced electrical conductivity, or permeability to gases, such as oxygen, and moisture. In these conventional composites, there is a distinct macroscopic separation between the organic and the inorganic phase without any significant interactions between them. Microscopic dispersion and interfacial adhesion is often achieved by treating the surface of the inorganic material[1].

Nanocomposite constitute a new class of materials with ultra-fine phase dispersion of the order of a few nanometers that endows them with unique properties not shared by conventional materials and offers new technological and economic opportunities[1]. The field of polymer nanocomposites has attracted considerable attention as a method of enhancing polymer properties and also promises new applications, by using nanoscale fillers rather than conventional particulate filled micro or macrocomposites. Polymer nanocomposites are a combination of two or more phases containing different compositions or structures, where the dispersed phase has at least one dimension less than nanometer dimension. They are formed from polymers and a low level of nanofiller such as layered silicate. Nanofillers can be in the form of fine particles, needle-like structures or platelets. Polymer nanocomposites have superior physical and mechanical properties such as mechanical, thermo-mechanical, barrier and flame retardancy, combined with low density. This is because the nanofillers have a large surface area to volume ratio, and in addition they have a reinforcing effect that increases the composite strength, as a result of the strong interaction between the nanofiller and the host polymer. The properties of polymer nanocomposites depend not only on the polymer characteristics, for instance chemical and morphological and dispersion in the host polymer. Polymer nanocomposites can be divided into two idealised types: intercalated and exfoliated nanocomposites depending on the polymer nanocomposites miscibility. Immiscible nanocomposites occur when the nanofillers are not dispersed and agglomerated in microcomposites stacks, which behave as inorganic fillers such as present in microcomposites or conventional composites. If the nanofiller is dispersed then either an intercalated or an exfoliated nanocomposite will form. An intercalated nanocomposite forms when polymer chains are inserted between the nanolayers, forming a highly ordered arrangement of

alternating nanolayer and polymer. An exfoliated nanocomposite looses the ordered structure when the nanofiller particles are uniformly and randomly dispersed within the host polymer. Exfoliated nanocomposites are especially desirable for improved properties because of the thorough dispersion of nanofiller and large surface area to volume ratio between polymer and nanofiller[2,3]. Exfoliated nanocomposites are difficult to obtain and they have only been reported for polymer layered silicate nanocomposites. Nevertheless both nanocomposites have unique properties, for instance intercalated structures have interesting electronic and charge transport properties.

Graphite is naturally abundant and it has been widely used as a conducting filler in preparing conducting polymers. In order to obtain a satisfactory conductivity in conventional graphite fillers, a large amount of graphite is required, as high as 15 to 20 %wt[4]. This often results in a material with poor mechanical properties, high density and processing difficulty. Nanographite is expected to be more effective than traditional graphite because it requires a small amount to modify the macroscopic properties of the polymer matrix. Electrical conductivity with a low concentration of nanographite dispersed in thermoplastics has lead to applications including co-axial cable and electrostatic resistant films and mouldings.

The key to superior polymer nanocomposite properties greatly depends on how the nanofiller particles are dispersed in the host polymer. Polymer layered graphite nanocomposites can be prepared by in-situ polymerisation and solution intercalation, which is a difficult task that involves two approaches. Firstly, graphite flakes are oxidised using acidic oxidising agents to form functional groups on their surface that will facilitate chemical and physical interactions between the graphite oxide and polymer and/or monomer. The second approach is to separate the layers by heating before dispersion in the polymer. However, these approaches are expensive since neither a suitable monomer nor a compatible solvent system is necessarily available. In addition, with increasing environmental concerns alternative processing is of great importance. Another alternative method is polymer melt intercalation, also known as melt blending.

Polymer melt blending using extrusion has been successful in preparing polymer layered silicate nanocomposites. The formation of polymer layered silicate nanocomposites via this process depends upon the thermodynamic interaction between the polymer chains, and the host layered silicates, and the transport of the polymer chains from the bulk melt into the silicate layers. Melt blending offers many advantages over the other methods. Firstly, the

absence of solvent makes this method environmentally benign. Secondly, it is economically advantageous since it is compatible with current industrial mixing and processing techniques such as extrusion and injection molding. In addition, the melt blending method will probably allow the use of polymers that were previously not suitable for in-situ polymerisation and/or solution intercalation. Since graphite, like silicates, is a layered material the same nanoreinforcement concept could be applied with graphite. Polymer melt blending is a promising new approach to fabricate polymer layered graphite nanocomposites using conventional polymer processing.

1.1 Aim

Preparation of polymer layered graphite oxide composites using polyolefins with functionality to promote interfacial adhesion with various forms of layered graphite oxide that have a large surface area to volume ratio and to enhance polymer matrix properties at low concentration. The two types of polyolefin matrix are poly(ethylene-co-methyl-acrylate-co-acrylic acid) (EMAA) and poly(propylene-graft-maleic anhydride) (PPMA). Polymer layered graphite oxide composites posses potential applications in anti-static (fibre or film sheets), semiconducting polymers and other mechanical and functional attributes such as increased modulus, improved creep resistance, higher heat distortion and temperature resistance.

1.1.1 Objectives

- To prepare a series of graphite oxides using Brønsted acids in combination with oxidising agents and other reagents on graphite flakes.
- Characterisation of the crystal structure, surface area properties and thermal behaviour of oxidised graphite and its expanded form.
- To prepare EMAA layered composites with various types of graphite oxides via solution blending.
- Interpretation of the effect on crystal structure, thermal stability, tensile properties, thermo-mechanical and dielectric properties of EMAA matrix due to the presence of graphite oxide.
- Investigation of the effect of type of graphite oxide on the properties of EMAA matrix.
- To prepare PPMA layered expanded graphite oxide in varying concentrations via

solution blending, using two different mixing methods: distributive and dispersive.

- Comparison of the effect of using two mixing methods: distributive and dispersive of layered expanded graphite oxide on the crystal structure, thermal stability and thermo-mechanical and dielectric properties of PPMA matrix.
- To prepare PPMA layered expanded graphite oxide in varying concentration via melt blending.
- Investigation of the effect of dispersion method on the crystal, thermal stability, thermo-mechanical and electric property of PPMA matrix.

The literature review in Chapter 2 describes graphite oxide as graphite that has been treated by nitric acid (HNO_3) and potassium chlorate ($KClO_3$). It is important to note that in this thesis oxidised graphite flakes are referred to as layered graphite oxide and its expanded counterparts are referred to as layered expanded graphite oxide.

1.1.2 Research questions

This proposed research raises some questions that are important for meeting the objectives.

The questions that need to be addressed are:

- What are the effects of oxidation of graphite flakes on its structure and properties?
- Would layered expanded graphite oxide prepared by exfoliating oxidised graphite result in enhanced properties?
- What are the effects of extensive mixing of layered graphite oxide on the thermal stability and mechanical properties, dielectric and/or electrical properties of polymer layered composites?
- What are the effects of extensive mixing of layered expanded graphite oxide on the thermal stability and mechanical, dielectric and/or electrical properties of polymer layered composites?
- Can layered expanded graphite oxide be dispersed in an exfoliated form in a polymer matrix melt by blending via a kneading process?
- What are the effects of increasing layered graphite oxide concentration on the properties of the polymer matrix?

1.2 Structure of thesis

The aim of this project is introduced in this thesis and presented in seven chapters: this chapter covers the introduction, aim and objectives of the project. Chapter 2 presents a literature review of relevant published literature of interest for this project. It covers general aspects of nanocomposites, layered silicates with emphasis placed on layered graphite. The crystalline structure, chemical and physical properties of these layered materials is discussed. In addition, the various methods of preparation and effect of layered materials in a polymer matrix are included in Chapter 2.

Chapter 3 contains the general materials used in this investigation. This chapter contains a brief, general introduction to the analytical techniques utilised to characterise the various types of graphite oxide (GO) and polymer layered graphite oxide composites. A comprehensive outline of the parameters and conditions of the experimental techniques performed to obtain the results presented in this thesis. It is intended as a quick reference guide for other workers who are interested in the preparation and characterisation of layered composites.

Oxidised graphite flake has been shown by several researchers to have polar functional groups present on its surface that can play an important role in facilitating interactions between layered graphite oxide and polymer or monomer. Chapter 4 elucidates a study made of a series of graphite oxides (GO) prepared by utilising Brønsted acids in combination with various oxidising agents and reagents. The influence of the oxidative treatment on the structure, surface area and thermal properties are reported.

In Chapter 5 poly(ethylene-co-methyl acrylate-co-acrylic acid) (EMAA) layered graphite oxide composites with varying concentration of graphite flake, oxidise graphite and its expanded counterparts are prepared via solution blending. The effects of the various types of graphite oxide fillers on the crystal structure, thermal, mechanical and/or electrical properties of EMAA matrix was measured and the results obtained appear in Chapter 5. In addition, a statistical technique was utilised to show the complex interactions and effects of variables such as structure, treatment and concentration on the mechanical properties of the EMAA matrix. Several studies have shown that dielectric or electrical properties of composites of expanded graphite are greatly affected by the dispersion method. In Chapter 6 expanded graphite oxide (EGO) was added into polypropylene (PP) grafted with maleic anhydride

(MA) via solution blending using two different mixing methods: distributive and dispersive. The latter method involves high shear dispersion. The effects of the mixing methods on the thermal and mechanical properties of PPMA-layered expanded graphite oxide composites are reported in Chapter 6.

Melt blending has great advantages over other methods used to prepare polymer layered composites in that it is an environmentally and economically advantageous method due to the absence of solvent. In addition, it is compatible with current polymer processing technology therefore it can be manufactured using industrial processes such as extrusion and injection moulding. In Chapter 7 various EGO concentrations were added into PPMA via melt blending to form PPMA-layered EGO composites. The extent of dispersion of EGO into PPMA was reported using various techniques to determine the effects on PPMA matrix properties. In Chapter 8 is the conclusion of the thesis and suggestions arising for future investigation.

Chapter 2 Literature review

2.1 Introduction

Composite materials are used widely in a diverse range of applications such as in transportation vehicles, construction materials, electronics, sporting goods and consumer products. The properties of polymer composites are affected by the dimensions and microstructure of the dispersed phase. These conventional polymer composites require a high concentration of filler to obtain enhanced properties. However, this often results in a high density material. New materials are sought where properties are enhanced at low filler concentrations. Nanocomposites are a new special class of materials originating from suitable combinations of two or more types of nanoparticles produced by an appropriate technique, resulting in the material having unique physical properties potentially applicable to a wide and diverse range of application areas. Novel properties of nanocomposites can be derived from the successful combination of the characteristics of parent constituents into a single material[5].

Based on the filler geometries, nanocomposites can be classified into three primary categories. Fumed silica dioxide and nanometallic powder are particles, which are characterised by three dimensions in the nanometer range[6,7]. Carbon nanotubes and whisker possess two dimensions in the nanometer range[8]. Silicates such as clay, mica and graphite intercalated compound (GIC) and expanded graphite (EG) fillers possess only one dimension in the nanometer range and have a layered crystal structure[9,10]. The latter form has been widely studied since they are easily available and the intercalation chemistry is reasonably well understood in the literature[11].

Materials with layered structure can have a large surface area to volume ratio through the process of intercalation and exfoliation. Dispersion of nanoparticles into a polymer matrix is used to form polymer nanocomposites. Polymers filled with nanoparticles exhibit unique properties that are not shared by conventional polymer composites, primarily due to the large surface area to volume ratio of the filler. Nanoparticles act as reinforcer for a polymer matrix and enhance mechanical, thermal, electrical and barrier properties depending upon the type of nanoparticle. In addition, some polymer nanocomposites exhibit electrical conductivity. Polymer nanocomposites with enhanced properties, are realised at low nanoparticle concentration as a result are of lower density compared with conventional polymer composites[12].

Polymer layered silicate nanocomposites were reported in the patent literature as early as 1950. Polyamide layered silicate nanocomposites were reported as early as 1976. However, it was not until Toyota researchers successfully synthesised polyamide (PA-6) layered silicate nanocomposites via in situ polymerisation that polymer nanocomposites became more widely studied in academic, government and industrial laboratories[13-15]. PA-6 layered nanocomposites showed enhanced mechanical properties, barrier properties and heat distortion temperature at low layered silicate concentration, as low as 4 %vol[12].

2.2 Layered silicate structure

The layered silicates used in polymer layered silicate nanocomposites (PLSN) belong to the general family of 2:1 layered silicates or also known phyllosilicates, such as mica, talc, montmorillonite, vermiculite, hectorite, saponite, and so on. The silicate crystalline structure consists of two-dimensional, nanometer thick layers, which are made up of two tetrahedral layers of silica fused to an edge-shaped octahedral sheet of either alumina or magnesia. The dimensions of these silicate layers vary from 3 nanometers to several micrometers depending on the type of layered silicate. These silicate layers organize themselves in a parallel conformation called the gallery or the interlayer, forming stacks with relatively weak dipolar and van der Waals forces. These interlayers are usually occupied by hydrated alkali or alkaline earth cations such as K^{+}, Na^{+}, Ca^{++} and Mg^{++}. These cations counterbalance the negative charge generated by the isomorphous substitution of the atoms forming the crystal. For instance the Mg^{++} easily exchanged in the place of Al^{+++} in montmorillonite or Li^{+} instead of Mg^{++} in hectorite. The weak forces allow for various molecules and even polymer to intercalate between the silicate layers[16]. The structure and chemistry of montmorillonite (MMT), hectorite and saponite are provided in Figure 2.1 and Table 2.1[16]. These layered silicates have a large active surface area, a moderate negative surface charge (cation exchange capacity) (CEC), which is the degree of isomorphous substitution. In addition, these layered silicates have layer structure, and they are considered hydrophobic colloids of the constant-charge type. The layer charge indicated by the chemical formula (Table 2.1) is considered as an average over the whole crystal due to the varying charge from layer to layer. However, a small proportion of the charge balancing cations are positioned at the external crystal surface with the majority being found in the interlayer space. The cations are exchangeable for others in solution.

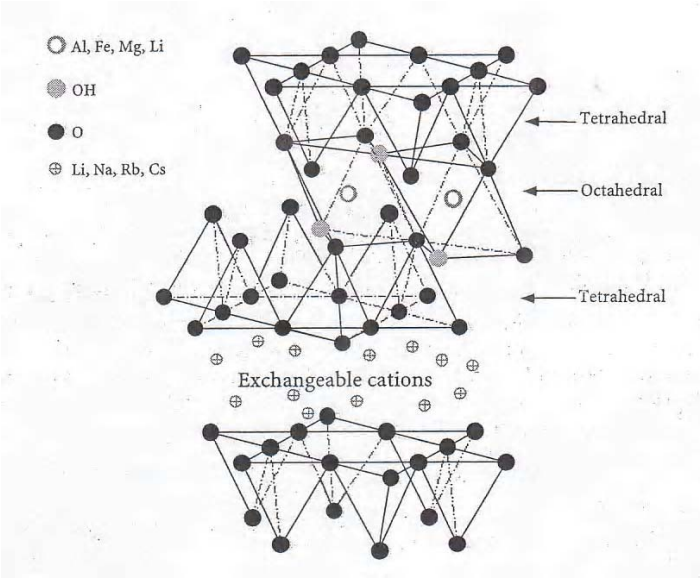

Figure 2.1 The structure of 2:1 layered silicates. M is a monovalent charge compensating cation in the interlayer and x is the degree of isomorphous substitution (CEC)[16]

Table 2.1 Structure and chemistry of various layered silicates[16]

Silicate	Location of isomorphous substitution	Formula
Montmorillonite	Octahedral	$Mx[Al_{4-x}Mg_x](Si_8)O_{20}(OH)_4$
Hectorite	Octahedral	$Mx[Mg_{6-x}Li_x](Si_8)O_{20}(OH)_4$
Saponite	Tetrahedral	$Mx[Mg_6](Si_{8-x}Al_x)O_{20}(OH)_4$

The use of pristine layered silicates, limits the class of polymer that can be intercalated. This limitation is overcome by modifying silicate layers to form organically modified layered silicates (OLS), achieved by ion exchange reactions. This reaction involves the replacement of exchange cationic surfactant by primary, tertiary and quaternary ammonium or phosphonium cation such as alkylammonium or alkylphosphonium cation, which renders the hydrophilic layered silicate surface hydrophobic or organophillic as illustrated in Figure 2.2[1]. The modification of pristine layered silicate, via ion exchange allows intercalation of many engineering polymers in the silicate layers.

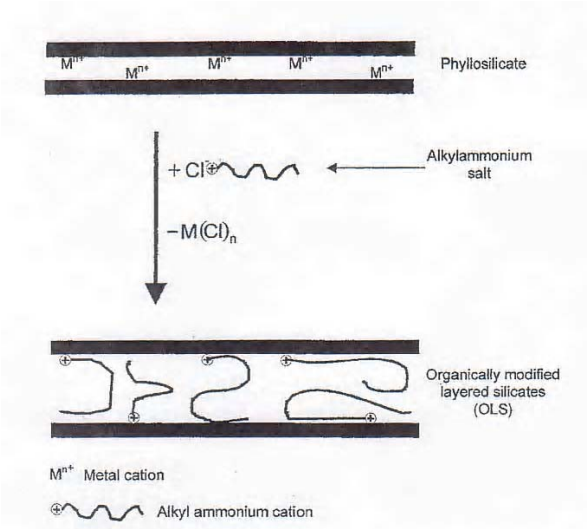

Figure 2.2 Cation exchange reaction between the silicate and an alkylammonium salt[1]

The cationic surfactant has three functions in the silicate layers. Firstly, it lowers the surface energy of the layered silicate and improves the wetting characteristics with the polymer. The cationic surfactant provides functional groups that can interact with the polymer or initiate polymerisation of monomers to improve the compatibility of the interface between the layered silicate and the polymer matrix and lastly, increase interlayer distance. The latter depends on the charge density or CEC of the layered silicate and chain length of cationic surfactant. The three functions described above facilitate the polymer intercalation. The arrangement of the cationic surfactant in the interlayer depends on the charge density of the layered silicate and cationic surfactant. The charge density of the layered silicate and the cationic surfactant can lay either parallel to the silicate layers forming mono or bilayers or radiate away from the surface thereby forming extended mono or bimolecular tilted arrangement "pseudo-trimolecular" or paraffin-type arrangement. In some cases, individual cation chains adopt arrangement with both mono and bilayers and pseudo-trimolecular as illustrated in Figure 2.3[17].

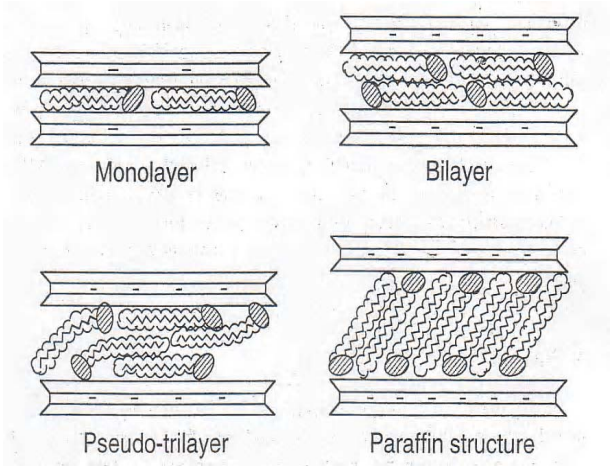

Figure 2.3 Orientations of alkylmmonium ions in the interlayers of layered silicates with various layer densities[17]

2.2.1 Structure of polymer layered silicate nanocomposite

The dispersion of the nanoparticles, such as layered silicates, within a polymer matrix has a significant influence on the properties of a material. In general, nanocomposites can exhibit two extreme types of structure. The first type is an intercalated nanocomposite that is formed by the insertion of a single, extended monomer or polymer chain between the well-ordered host silicate layers. The monomer or polymer chain is intercalated between the silicate layers in an alternating fixed ratio of polymer and silicate layers where a well ordered structure is maintained. Additionally, the distance between the silicate layers and hence the space occupied by the monomer or polymer chain is in the order of a few nanometers[18-21]. The last type is delaminated, which are known as exfoliated nanocomposites. Exfoliated nanocomposites differ from that of intercalated nanocomposites, in that the well ordered structure of the silicate layer is lost and they are dispersed randomly and continuously within the polymer matrix[18,22]. Unlike the intercalated nanocomposites, the interlayer expansion is comparable with the radius of gyration of the polymer[1,19] rather than that of an extended chain as in the case of intercalated nanocomposites. As described above, the simple description of PLSN as intercalated or exfoliated is far from adequate. Additional descriptors such as ordered, disordered or partial are helpful for description of nanoscale morphologies. Figure 2.4 illustrates an expanded classification scheme[23]. Disordered intercalated nanocomposites are due to weak interlayer disruption; as a result a minor fraction of smaller layers near the surfaces of the crystallites may be dispersed. PLSN containing swollen interlayers

still exhibiting registry are partially exfoliated. Exfoliated PLSN can be further described as ordered or disordered depending on the silicate layer separation.

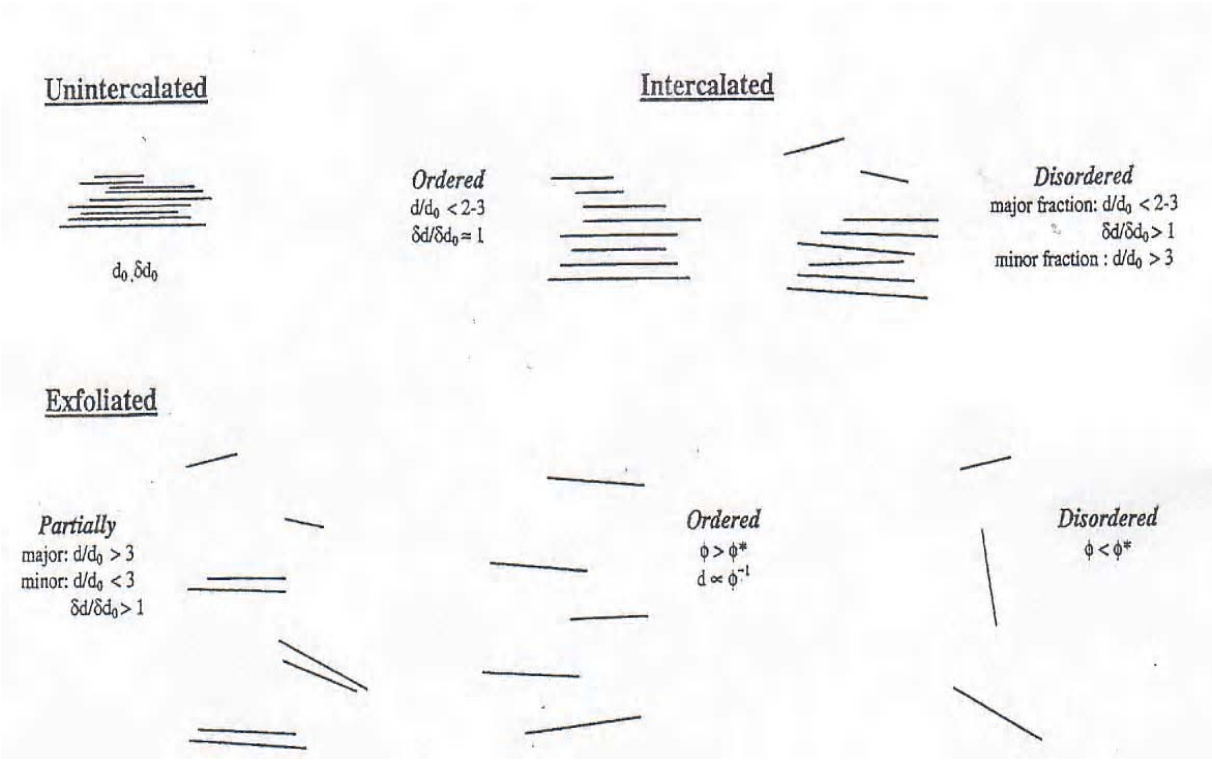

Figure 2.4 Schematic illustration of terminology used to describe PLSN[23]

2.2.2 Miscibility and thermodynamic of nanocomposite formation

Giannelis and other researchers[1,16,19,24] have compared the two types of structure of nanocomposites with an immiscible system, for instance a conventional filled polymer or micromposite corresponds to an immiscible system. In their report, they refer that an intercalated nanocomposite shows limited miscibility whereas an exfoliated nanocomposite shows a totally miscible system. The schematic diagram shows four miscibility systems. As shown in Figure 2.5[25] intercalation and delaminated nanocomposites can coexist in the polymer matrix.

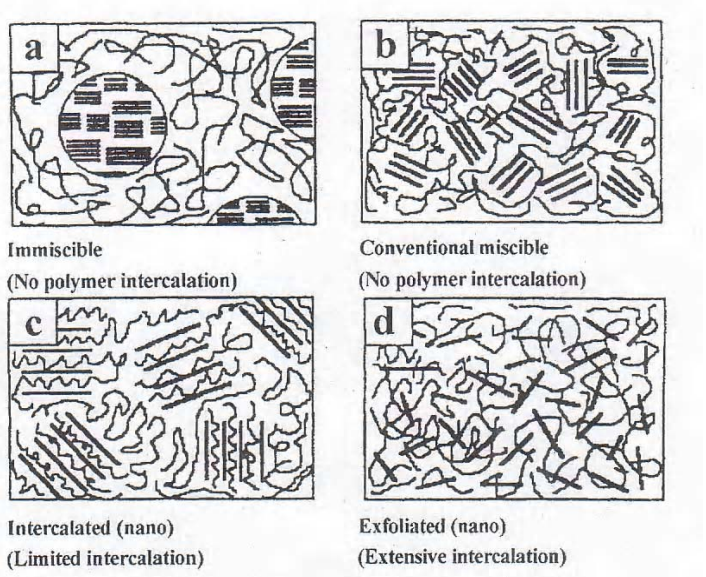

Figure 2.5 Four possible types of PLSN[25]

In general, the interplay of entropic and enthalpic factors determines the outcome of whether dispersion of the nanoparticle in a polymer will form either an intercalated or exfoliated nanocomposite. In order for nanocomposites to form, a spontaneous exchange requires a negative variation in the Gibbs free energy, ΔG. The change in, ΔG, is composed of an enthalpic factor, ΔH, due to the intermolecular interactions and an entropic factor, ΔS, associated with the configurational changes of the constituents, where T is the temperature.

$$\Delta G=\Delta H-T\Delta S \qquad \text{Equation 2.1}$$

Giannelis[16,19,24,26] have developed a mean-field, lattice based model of the formation of polymer layered silicate nanocomposites for OLS. They reported that the decrease in entropy due to the confinement of the polymer chains between the interlayers of the silicate layers is compensated by an increase in entropy associated with the increased in the configuration freedom of the aliphatic chains of the alkylammonium cations as the interlayer distance increase due to polymer intercalation. If the decrease in entropy is higher or equal to the increase in entropy, enthalpy will determine whether or not polymer intercalation will occur. The enthalpy of apolar polymer and layered silicate is unfavourable therefore no intercalation will occur and this leads to an immiscible system. A polar polymer and layered silicate is favourable as a result intercalation will occur. In order for exfoliated nanocomposites to form a highly favourable enthalpy between the polymer and layered silicate is required[19,24].

2.2.3 Preparation method of polymer layered silicate nanocomposite

Polymer nanocomposites can be typically prepared by three different methods:

- in-situ polymerisation
- intercalation of the polymer from solution (solution intercalation or solution blending)
- direct intercalation of the molten polymer (melt intercalation)

Polymer-clay nanocomposites have been successfully prepared using the aforementioned methods. The success has led researchers to adapt the methods to prepare polymer-graphite nanocomposites such as polystyrene (PS)[9,27,28], polyamide (PA-6)[10], poly(methyl methacrylate) (PMMA)[11,29] and high density polyethylene (HDPE)[30].

The in-situ polymerisation approach was the first strategy used to synthesize polymer layered silicate nanocomposites. The method involves the monomer intercalating into the interlayer between the host layers and then being polymerized. The in-situ polymerisation process is illustrated schematically in Figure 2.6.

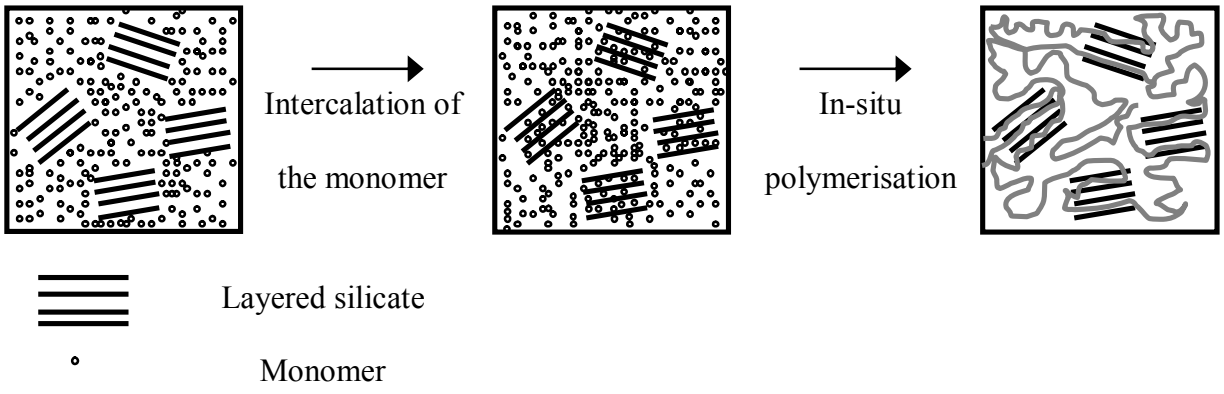

Figure 2.6 Schematic representation of PLSN via in situ polymerisation

The polymer solution intercalation method is based on a solvent system in which the polymer is soluble and the silicate layers are swellable[31]. Preparing nanocomposites via solution intercalation is a two-stage process in which the polymer is exchanged with a previously intercalated a solvent as illustrated schematically in Figure 2.7[1]. This method is similar to that of in-situ polymerisation except that the solvent replaces the function of the polar monomer solution. The polymer solution and host layer dispersion are mixed and the polymer chains intercalate and displace the solvent within the interlayer of the layered silicate. Upon solvent

removal, either an intercalated or exfoliated nanocomposite forms[1,31].

The thermodynamics involved in solution intercalation have been reported for the overall process by Shen et al[31]. They reported that a spontaneous exchange of polymer with the intercalated solvent in the interlayer requires a negative variation in the Gibbs free energy.

The driving force for polymer layered silicate intercalation via solution intercalation is the increase in entropy by desorption of intercalated solvent, which compensates for the decrease in entropy by confinement of the polymer chains in the interlayer.

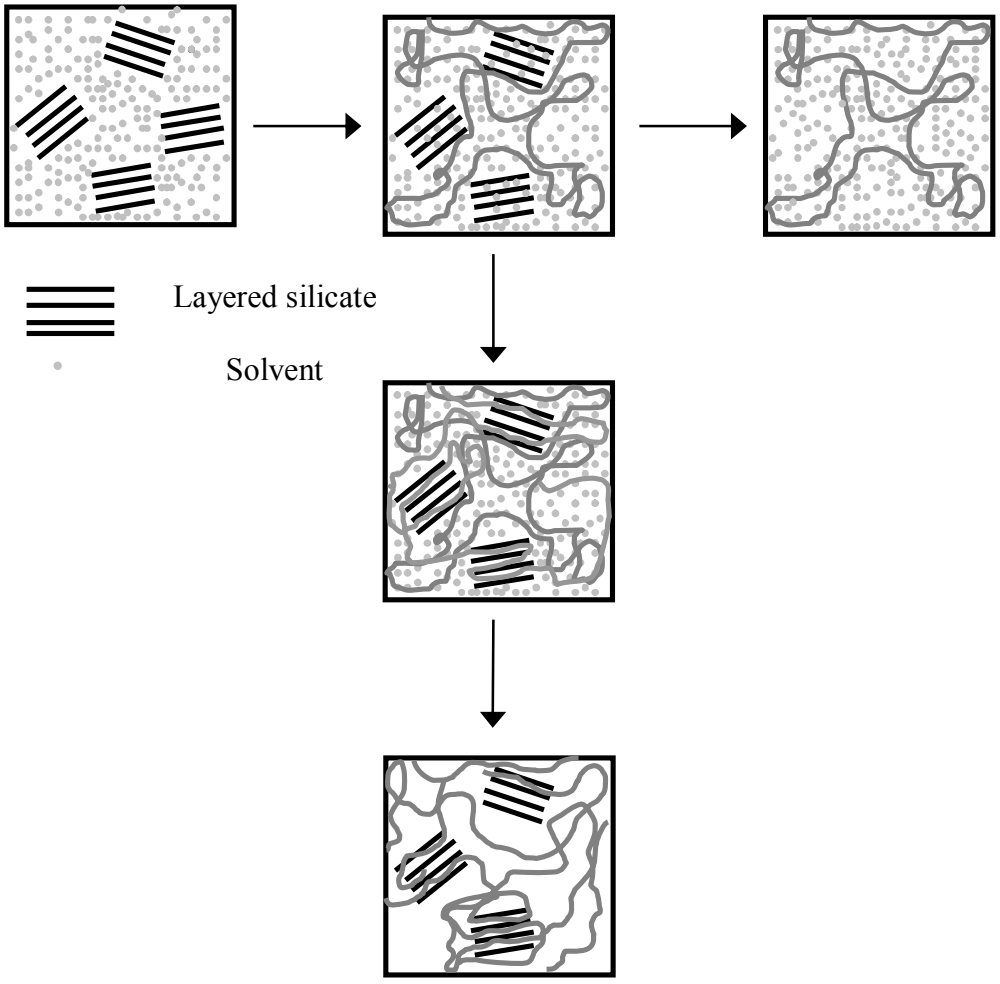

Figure 2.7 Schematic representation of PLSN via solution intercalation

The drawback of in-situ polymerisation and solution intercalation methods is the availability of a suitable solvent and the large amount of solvent that may be required. It has been shown that intercalation only occurs for certain polymer-solvent or monomer-solvent pairs. As a result, application of these methods commercially is impractical. Disposal of a large amount of solvent is usually environmentally unfriendly[1,32].

Melt intercalation has been developed and has eliminated the limitations encountered in in-situ polymerisation and solution intercalation. Polymer melt intercalation became appealing since it came to prominence in the 1990's[31]. A number of polymers filled with either layered silicate or layered graphite have been melt intercalated such as PA-66-clay[33], PP-MMT[25], PA-6 graphite[2], PP-graphite[34] nanocomposites. The melt intercalation method has great advantages over either in-situ polymerisation or solution intercalation. Firstly, the absence of a solvent makes melt intercalation environmentally friendly. Melt intercalation method is compatible with current industrial mixing and processing technology polymer processing techniques and therefore, can be manufactured using industrial process such as extrusion and injection moulding[31,35]. Therefore, melt intercalation allows the use of polymer, which was previously not suitable for in-situ polymerisation or solution intercalation[31,35,36].

The process of melt intercalation can be achieved either by:

- annealing the polymer and the host layer above the glass transition temperature (T_g) or melting temperature (T_m) of the polymer[25,37].
- direct melt intercalation with the aid by shearing forces during processing[25].

During the melt intercalation, the polymer chains diffuse from the bulk polymer into the interlayer of the host layer to form either an intercalated or an exfoliated nanocomposite depending on the degree of intercalation[37]. A schematic diagram in Figure 2.8[1] shows the melt intercalation method. Several reports have been devoted to the driving force and kinetics of solution intercalation, though it is only recently that the thermodynamics and kinetics of melt intercalation have been addressed. The formation of polymer nanocomposites via melt intercalation depends on the thermodynamic interactions between the polymer chains the layered silicate and the transport of the polymer chains from the bulk melt into the layered silicate[25]. According to Giannelis et al[16] report, the spontaneous process that occurs due to the increase in entropy as a result of the greater conformational energy of the aliphatic chains of the alkylammonium cations that is attributed to the increase in the distance of the interlayer caused by insertion of the polymer and concentration gradient give rise to enthalpic force, which then drives the polymer chains into the interlayer[16].

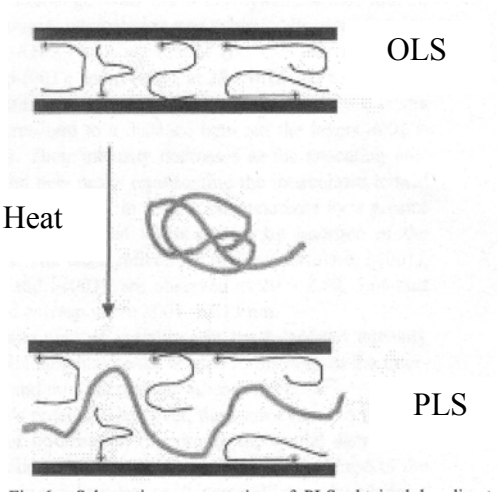

Figure 2.8 Schematic representation of PLSN via melt intercalation[1]

Vaia et al[37] reported the kinetics of polystyrene (PS) melt intercalation in layered silicates. Using XRD and TEM they determined that formation of PS melt intercalation was limited by mass transport into the layered silicate and not specifically by diffusion of the polymer chains within the interlayers. The activation energy (A_E) of nanocomposite formation is similar to that of PS self –diffusion in the bulk melt[19,37].

2.3 Property of polymer layered silicate nanocomposite

The properties of PLSN depend on the type of structure: intercalated and exfoliated. In general exfoliated PLSN are desired for enhanced properties due to the homogenous dispersion of layered silicate and huge interfacial area between polymer and layered silicate.

PLSN exhibit many advantages compared with conventional filled composites. The advantages in the properties of PLSN were first demonstrated by researchers for PA-6 layered silicate nanocomposites. Table 2.2 compares the properties of PA-6 and those of the PA-6 layered silicate nanocomposites containing 4 %wt of silicate layers[17,38].

Table 2.2 Properties of PA-6 and layered silicate PA-6 nanocomposites[38]

Property	PA-6	Layered silicate PA-6 nanocomposite
Tensile modulus (GPa) (ASTM D638 M)	1.11	1.87
Tensile strength (MPa) (ASTM D638)	68.6	97.2
Heat distortion temperature (°C) (ASTM D648)	65	152
Impact strength ($kJ.m^2$) (JIS K7111)	6.21	6.06
Water adsorption (%)	0.87	0.51
Coefficient thermal expansion (CTE) (10^{-5})	13.0	6.30

From the results reported in Table 2.2, the properties of PA-6 in the presence of layered silicate were higher compared with pure PA-6. Interestingly, the increase in tensile strength and tensile modulus are not accompanied by a decrease in impact strength usually displayed by conventionally filled polymer composites. It can be seen that heat distortion temperature of the PLSN is more than twice that of pure PA-6. It is thus suitable for use in automotive components subjected to temperatures in which pure PA-6 would soften and lose mechanical properties [1]. Messersmith and Giannelis[39] prepared epoxy layered silicate nanocomposites and reported similar improvement in the mechanical properties. Epoxy containing 4 %wt layered silicate showed a 60% increase in storage modulus, which is a measure of stiffness in the glassy region compared with the pure epoxy. The equivalent increase in the rubbery region is 450%. The increase in mechanical properties is higher in comparison with conventional filled epoxies, which do not display an improvement even at higher concentration levels (<10 %vol) used in the nanocomposites[19]. Lan and Pinnavaia[19,40] reported a 10-fold increase in modulus and strength for epoxy layered silicate nanocomposites with sub-ambient glass transition temperatures, T_g. This increase was due to the strain induced alignment of the silicate layers in the rubbery state.

A large number of polymers with varying degree of polarity and chain rigidity have been studied as base polymers for PLSN, including poly(ε-caprolactone)[41-44], polystyrene (PS)[3,45,46], polyamide (PA)[33,47,48], polyimide (PI)[49-52], epoxy resin[40,53], poly(ethylene oxide) (PEO)[54], poly(propylene) (PP)[55-57], poly(ethylene terephthalate) (PET)[35], polyurethane (PU)[58], silicone rubber[59]. These polymers in the presence of layered silicate are lighter in weight than conventionally filled polymers since high degrees of stiffness and strength are realised at low concentration levels of layered silicate. They have enhanced barrier properties without requiring multi-polymer layered design that allows for recycling. Their mechanical properties are potentially superior to unidirectional fibre reinforced polymers due to reinforcement from the layered silicate occurs in two dimensions rather than in one[24]. Other advantages of PLSN to other conventionally filled polymers are lower thermal expansion coefficient, reduced gas permeability, greater resistance to solvents, and elevated ion conductivity and fire retardance[1,3,35,60-63]. The success in PLSN properties has led researchers to investigate other possible layered nanoparticles to enhance polymer properties. For instance flake graphite may behave in a similar manner since it has a layered crystal structure and may lead to enhanced polymer properties similar to those of layered silicate.

2.4 Graphite

The formation of PLSN leads to new properties that cannot be derived from conventionally filled composites due to the high aspect ratio of layered silicate and uniform dispersion in polymer matrix. However, PLSN do not possess electrical conductivity, photonic and dielectric properties as some functional composites such as carbon black, metallic powder, polyaniline, and graphite containing polymers[29].

Graphite is naturally abundant and it has been widely used as conducting filler in conducting polymer composites. Conventional graphite fillers are usually micro-diameter powders. Therefore a polymer filled with conventional graphite fillers requires high concentration to obtain conductivity usually as high as 15 to 20%[4]. This results in a material with poor mechanical properties with high density.

Flake graphite is a very good electrical conductor with an electrical conductivity of 10^4 $S.cm^{-1}$ at ambient temperature and it is the stiffest material found in nature, with Young's modulus 1.06 GPa[64]. Like layered silicate, flake graphite exhibits a layered crystal structure. The use of pristine layered graphite, limits the class of intercalable polymers due to their incompatibility, similar to that pristine layered silicate. An improvement of the compatibility between layered graphite and a polymer matrix is made by modifying layered graphite to form a graphite intercalated compound (GIC). This is achieved by chemical oxidation or electrolysis.

2.4.1 Structure of the graphite crystal

The fine structure of graphite was explained by Debye and Scherrer in 1917 and of Hassel and Mark in 1924. Graphite has a layer structure in which the carbon atoms (C-atoms) within each graphite layer are arranged in a series of hexagonal structures. Figure 2.9 represents the crystal structure of graphite and its hexagonal unit cell. The diagram illustrates the hexagonal alpha (α) stacking sequence of the graphite crystal with an ABABAB stacking order, where the C-atoms in every other layer are superimposed over each other. Within each graphite layer, the C-atom in the in-plane (basal plane) is bonded to three other C-atoms at a bond length distance of 0.142 nm[65]. The hexagonal unit cell has dimensions of a=0.246 nm. Six other C-atoms within the same graphite layer are situated at a distance of c=0.671 nm (A plane to A plane). The C-atoms in A and B planes are displaced by half the crystallographic c-axis spacing (c/2) of 0.335 nm, as labelled in Figure 2.9.

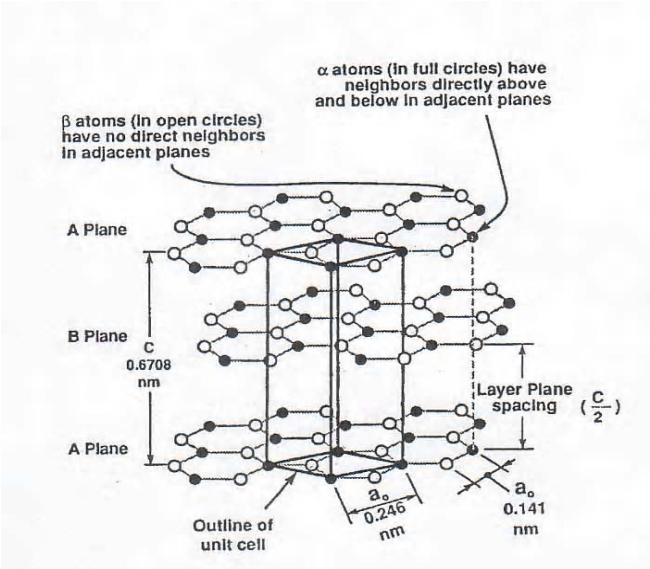

Figure 2.9 Crystal structure of graphite. A series of stacked parallel graphite layer planes. The hexagonal unit cell with dimensions a=0.246 nm and c=0.671 nm. The basal plane bond length is 0.142 nm[66]

Figure 2.10a shows that atoms of the α type differ from the atoms of the beta (β) type in which atoms of the former have neighbours directly above and below in adjacent graphite layer whereas the atoms of the β type have no corresponding atoms in these layers. This figure (Figure 2.10a) shows the view of the stacking sequence perpendicular to the basal plane.

The crystallographic description corresponds to the space group $P6_3/mmc$, in which the 6_3 screw axis is a consequence of the AB stacking order. In addition to the hexagonal graphite structure, the graphite crystal can exist in a rhombohedral structure, however it occurs less frequently due to its thermodynamic instability compared with a hexagonal structure. The rhomobohedral structure (Figure 2.10b), has a stacking sequence of ABCABC where the C-atoms in every third layer are superimposed. The crystallographic description corresponds to the space group R_3m. The crystal lattice dimensions are a=0.225 and c=1.006 nm. Hence, hexagonal graphite crystal structure described above is an ideal structure, which is never found either in natural or synthetic graphite.

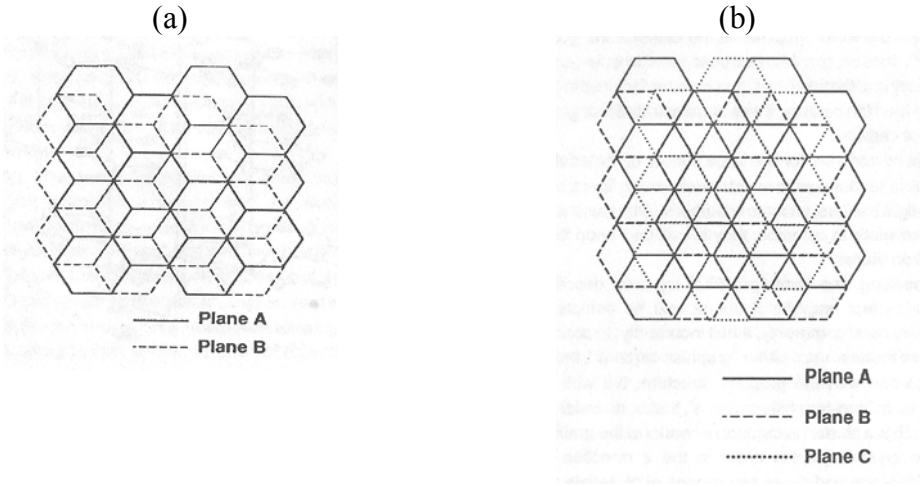

Figure 2.10 (a) Hexagonal graphite crystal showing ABABAB stacking sequence order. View is perpendicular to basal plane (b) Rhomobohedral graphite crystal showing ABCABC stacking order sequence. View is perpendicular to basal plane[66]

2.4.2 Bonding

The C-atoms within the graphite layer is in sp^2 (trigonal) hybridisation. Each C-atom has an electronic configuration of $1s^2$ $2s^2$ $2p^2$. The mechanism of the sp^2 hybridisation is shown in Figure 2.11a. The $1s^2$ electron belongs to the ion core (K shell). The 2s $2p_x$ $2p_y$ electrons of the L shell form three sp^2 orbitals and an un-hybridised (delocalised) electron (Figure 2.11a). These three identical sp^2 orbitals in the same plane and are 120° apart on a layer, as shown in Figure 2.11b.

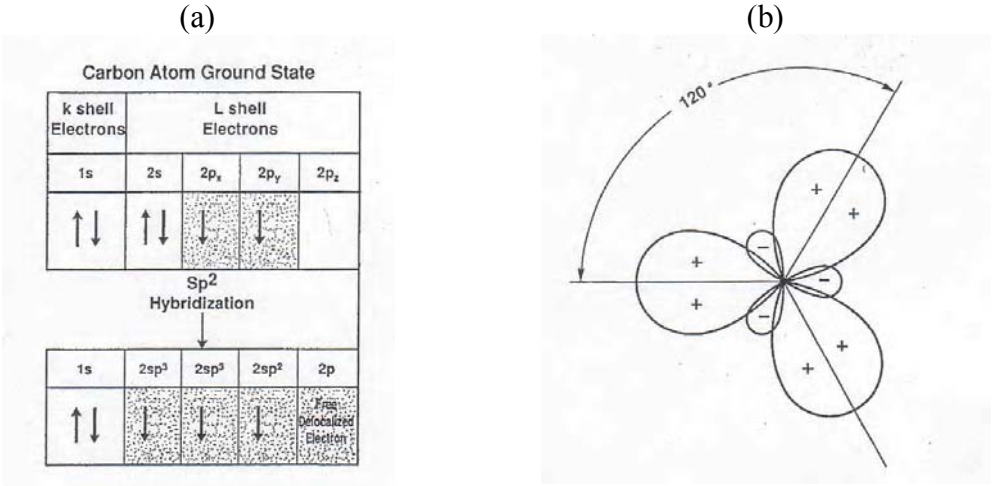

Figure 2.11 (a) sp^2 hybridisation of carbon orbitals. Shaded electrons represent valence electrons (b) Each sp^2 orbitals of C-atom in the same plane are 120° apart[66]

The overlapping of sp^2 orbitals leads to the formation of sigma (σ) bonding between C-atoms in a graphite layer. The σ bonding between C-atoms within each graphite layer forms a series of hexagonal structures in parallel planes. While the delocalised electron that form the pi (π) bonds binds the graphite layer perpendicularly to the graphite layer of the σ bonds, as shown in Figure 2.12. The delocalisation results in highly mobile π electrons. The two types of bonding of the graphite structure; the σ bonding in the graphite layers and the π bonding perpendicular to the graphite layers result in graphite being anisotropic.

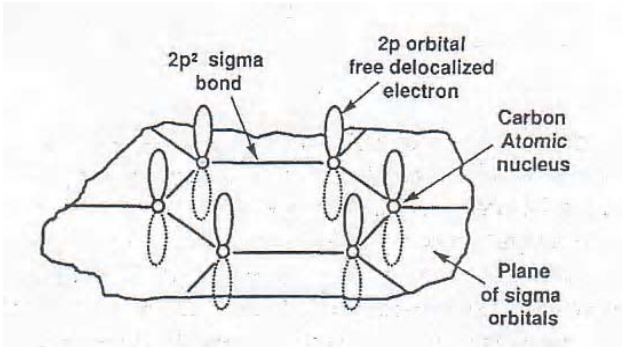

Figure 2.12 The sp^2 hybridised structure showing the σ bonding on the same layer and delocalised electrons is perpendicular to the layer (in-plane)[66]

2.4.3 Crystalline imperfection

As mentioned earlier, the hexagonal graphite structure described above is an ideal structure in which theoretically the stacking sequence ABABAB of the graphite layer is perfect with no crystalline imperfection. However, a varying number of crystalline imperfections may be found in graphite crystalline structures, which include:

- vacant lattice sites due to missing atom within the layer.
- ABABAB stacking order of the graphite layers being no longer maintained
- the graphite layers being no longer perfectly parallel.

Some of the listed imperfections are illustrated in Figure 2.13. Growth defects such as screw and edge dislocations shown in Figure 2.13b are another type of crystalline imperfection which can occur in the graphite crystalline structures. In addition, to the crystalline imperfections, the bulk characteristics of graphite such as porosity and amount of impurities can influence the properties of the bulk material[66].

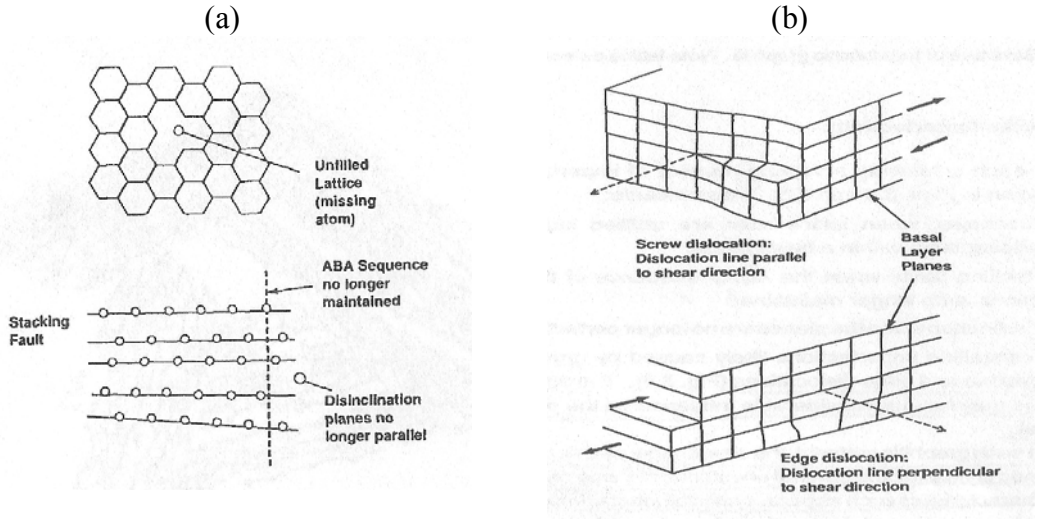

Figure 2.13 (a) Crystalline imperfections in graphite showing unfilled crystal structure, stacking fault and discinclination (b) Shear dislocations in graphite crystal structure[66]

2.4.4 Chemical property

Graphite reacts with many chemical substances to form graphite compounds. The reaction with gases or vapours or other chemical substances occurs at "active sites" such as at the edge of the layers of the graphite crystal, which are the zig-zag face (101) and the arm-chair (112) as shown in Figure 2.14.

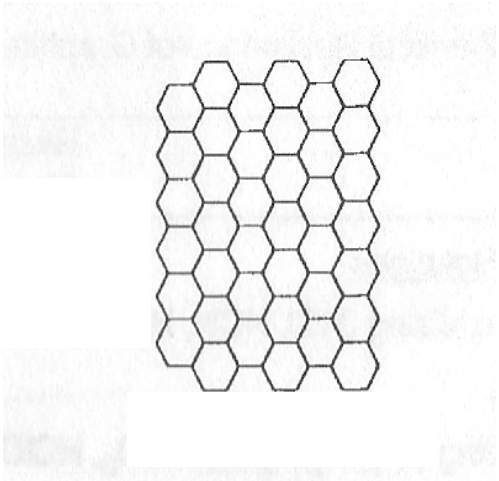

Figure 2.14 The faces of a graphite crystal[66]

In addition, adsorption occurs at crystalline imperfections within the basal plane of the graphite crystal. However, reactions with the graphite surface atoms are slow due to the

graphite crystal structure has large differences in surface energy in different crystallographic directions, and as a result, there are different reaction rates at different sites. The reaction rate that occurs at a layer is slow, whilst fast at the edge of the layer or at crystalline imperfections of graphite crystals. The chemical reactivity is affected by the degree of porosity such that a high porosity leads to large increase in surface area and thereby reactivity. In addition, reactivity increases with increasing temperature and at high temperatures, graphite becomes more reactive. Interestingly, graphite with large crystals and few crystalline imperfections have the best chemical resistance[66]. Graphite has poor resistance to the periodic elements of Column VI particularly oxygen and oxygen compounds. Oxidation begins in air at 350 and 400 °C and forms carbon monoxide (CO) and carbon dioxide (CO_2). The formation of these oxides offers no protection to the graphite surface. In addition, the degree of oxidation depends on the "active site", for such that oxidation is higher along the zig-zag face of the graphite crystal compared with an arm-chair face. However, oxidation can be slowed by reducing the number of "active sites" by increasing the degree of graphitization through the process of pyrolisation at very high temperatures and the crystallite size of graphite[66].

2.5 Graphite compound

Graphite reacts with many chemical substances to form various graphite compounds with different properties such as electrical properties. Graphite compounds can be classified into three groups, surface, substitutional and intercalation compounds[65].

- surface compounds of graphite are formed by reacting with graphite surface atoms.
- substitution compounds of graphite contain foreign species.
- intercalation compounds of graphite are interstitial compounds in which the foreign species is included in the interlayer of the graphite crystals whilst retaining their crystal structure as was shown in Figure 2.9.

The intercalation compounds of graphite are the most studied of all the compounds of graphite. In this section, the intercalation compounds of graphite will be discussed.

The graphite crystal structure, which consists of C-atoms within a graphite layer are bound by strong σ bond and the C-atoms in adjacent graphite layers are weakly bound by π bonds. For this reason, atoms, ions or molecules can be intercalated in the graphite crystal structure whereby atom, ion or molecule intercalates occupy and expand the interlayer spacing of the

graphite crystal structure without disrupting the graphite layers. The guests accommodated within the interlayer spacing of graphite crystal structure are called intercalates, and products composed of intercalates and host graphite are called graphite intercalation compounds (GIC). The intercalation process in graphite is chemical and physical in nature. The type of interaction or bonding between the C-atoms and intercalate depends on the particular intercalate, synthetic conditions and ambient conditions[67]. According to the character of the bonding, the intercalation compounds of graphite are classified into two groups, covalent and ionic bonding.

2.5.1 Covalent bonding

Graphite-fluoride and graphitic acid are types of covalent intercalation compounds of graphite. Covalent bonding favours the presence of conjugated double bonds within the graphite layer planes. Trigonal sp^2 bonding in the graphite layers changes and forms tetrahedral sp^3 bonding. As a result, these compounds are non-conductive.

Fluorination of graphite has been widely studied since first synthesised by Ruff and Rudorff[68]. There are two types of graphite-fluoride and they are carbon monofluoride and tetracarbon monofluoride with an approximate composition of CF and C_4F, respectively. CF is formed by direct reaction of graphite with fluorine above 350 °C, at high pressures or via a fluorine glow discharge (plasma)[65,69]. The presence of covalent C-F bonds in carbon monofluoride was confirmed by infrared transmission spectroscopy measurements, they are probably due to excess fluorine, as suggested by the stoichiometry of $CF_{1.12\pm0.03}$[65]. In addition, fluorine nuclear magnetic resonance (NMR) shows no evidence of mobile fluorine species. The CF is derived from graphite by insertion of covalently bonded fluorine atoms (F-atoms) alternately above and below each graphite layer. Each C-atom bonds to three other C-atoms and one F-atom and disrupts each sp^2 bond in every graphite layer and forms sp^3 bonds. The structure of CF consists of puckered graphite layers of tetrahedral sp^3 bonds rather than planar bonding[65,68,70]. CF has two possible conformations, one consists of layers of trans-linked cyclohexane rings in the chair conformation and the other consists of layers of cis-trans-linked cyclohexane boats. Based on NMR second moment measurement studies, Ebert[71] and Panich[72] showed that the structure of CF consists of graphite layers of cis-trans-linked cyclohexane rings in the boat confirmation. CF is a grey hydrophobic solid not wetted by organic liquids such as benzene, acetone, alcohol, or acetic acid, thus is an electrical insulator.

C_4F is formed by the reaction of graphite with hydrogen fluoride (HF) and fluoride (F_2) at less than 80 °C[73,74]. Rudorff and Rudorff[73] suggested that the hexagonal structure of graphite layers is maintained similar to that of graphite. However, CF assumes an AAAAAA stacking sequence order, where the F-atoms are arranged in two layers, one above and one below each graphite layer. Hence, both CF and C_4F form residual compounds of F_2. McDonnell et al[75], reported that electrical conductivity of C_4F is about 100 times smaller in comparison with pure graphite, however this value is higher than that of CF.

Another type of covalent GIC is graphite oxide, often referred to as graphitic acid, which is poorly understood. The formation of graphitic acid involves chemical oxidation using nitric acid (HNO_3) and potassium chlorate ($KClO_3$). The crystal structure of graphitic acid have been elucidated through the XRD studies of Hoffman in 1930, from then on several crystal structure models have been proposed between 1947 and 1969. According to Hoffman's XRD studies, it is derived from graphite, in that oxygen atoms (O-atoms) are inserted between the graphite layers in such away that an O-atom is bonded to a pair of adjacent C-atoms, alternately, above and below the graphite layers. As a result every layer of O-atoms is followed by layers of C-atoms at a distance of 0.140 nm. Another layer of O-atoms in the next graphite layer of C-atoms at a considerably greater distance exist. Within each graphite layer, the arrangement of C-atoms is the same as in graphite, however the distance between the graphite layers is larger, in fact practically double that found in graphite, which is due to the insertion of the layers of O-atoms in the graphite layers. The distance between the graphite layers can readily undergo expansion. If water molecules diffuse in, this can cause the swelling of graphitic acid. It is not possible to obtain anhydrous graphitic acid due to the O-H groups, as well as the O-atoms in between the graphite layers. This assumption is substantiated both by the acid reaction of moist graphitic acid towards litmus and its ability to exchange protons for other cations[76]. These acidic properties are attributed to the presence of carbonyl groups at the edges of the graphite layers such as at the crystal boundaries. From this, Hoffman considered graphitic acid as graphite oxide contaminated by acidic edge compounds. However, the presence of –OH groups between graphite layers is supported by the observation that methylation of the –OH groups leads to a considerable enlargement of the distance of graphite layers[76]. The FTIR observations of both CO stretching mode indicate the presence of a keto form and the –OH stretching mode, confirming the presence of an enol form showing that graphite oxide consists of enol, keto and epoxy groups dispersed in the

graphite crystal structure[65,67,77]. This structure has an idealised empirical formula of $C_8O_2(OH)_2$[65].

2.5.2 Ionic intercalation compound

Ionic bonding is partially ionic or polar, however the degree of ionicity in GIC is low. In addition, several intercalates retain their molecular identity in the graphite crystal structure. As a result, the nature of bonding is far more complicated than that in many ionic solids, where simple ions are involved. Since many GIC have such a small degree of ionization they should not really be called ionic although they are referred to as ionic intercalation compounds for classification purposes.

The process of ionic intercalation is accompanied by a charge (electron)-transfer between intercalate and the graphite layer. GIC are often classified depending on the direction of electron transfer. In general, GIC are classified into donor GIC and acceptor GIC, depending on the direction of electron transfer. The term donor GIC relates to compounds in which intercalates donate electrons to the graphite layer during the intercalation process. The term acceptor GIC relates to compounds in which intercalates accept electrons from the graphite layer. In general, alkali metals represent intercalates of donor type GIC and halides are acceptor type GIC[78,79]. GIC exist in concentration stages marked by differences in the periodic stacking sequence of the graphite layers and the intercalate layers called the staging phenomenon. The stacking can be of the form of stage 1, 2 and 3 GIC. Each intercalate layer is separated by a definite number of graphite layers, and the stage number n, specify the number of graphite layers between each pair of intercalated layers. As the concentration of the intercalate increases the stage decreases. Figure 2.15 shows a schematic cross-section of stage 1, 2 and 3 GIC[79]. The stages can be identified by XRD and by the intercalation isotherms[80]. Consequently, the stages can be more clearly identified in some GIC than others. GIC can be classified into two compounds and they are lamellar compounds or residue compounds. In the presence of excess external intercalate, GIC have a well ordered interlayer structure and are known as lamellar compounds. When the equilibrium with excess external intercalates is removed, the GIC desorbs intercalate and most intercalate is lost under such a condition. However, a fraction is retained even under vacuum or after heating.

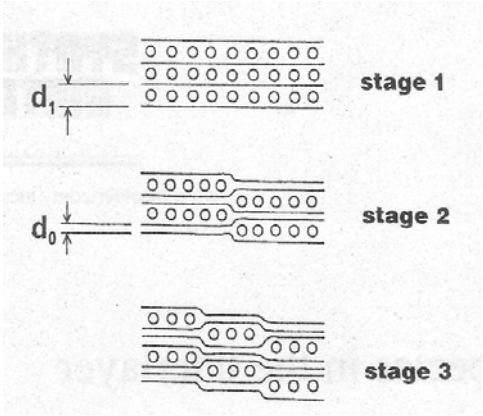

Figure 2.15 Schematic representation of stage 1, 2 and 3 GIC[81]

As a result, when the GIC is in equilibrium with zero partial pressure of external intercalates it is known as a residue compound. A residue compound is compound, which is retained in the graphite crystalline structure. The amount of residue compounds depends on the original crystalline structure of the graphite[73]. GIC can be formed by the spontaneous interaction of intercalate with graphite or by electrolysis.

2.5.3 Graphite halogen

Fluorine (F) and bromine (Br) react readily with graphite compared with iodine (I) and chlorine (Cl). These halogens behave as electron acceptors from graphite, due to their electronegative characteristic, which increases down the periodic table. Hennig's[65] experimental results suggest that there is a certain degree of electron transfer from graphite to the halogen intercalate. In addition, an interaction between intercalate and graphite is favoured, if the halogen has a high electron affinity and a high polarizability.

Fluorine is different from that of the intercalation crystal compound compared with other halogens. As mentioned earlier, fluorine readily reacts with graphite to form covalent CF bonding.

Bromine readily forms graphite-bromine (C_8Br) lamellar compounds by direct addition from the vapour[73] due to its high electron affinity and polarizability. For this reason, C_8Br has been studied widely compared with other graphite halogens[65,82]. Chung[65] reported that C_8Br has at least four stages based on XRD studies shown in Figure 2.16 and intercalation isotherm measurements.

The latter measurements were determined by exposing a known weight of graphite to a series of bromine vapour pressures from zero to the saturation vapour pressure and then back to zero at a constant temperature. Intercalation of bromine in graphite occurs when the bromine pressure surpasses the threshold value for intercalation. Figure 2.16 show that an increase in bromine vapour pressure increases the concentration of absorbed bromine in the interlayer. However, in this range, intercalation of bromine is not homogenous throughout the graphite crystal structure.

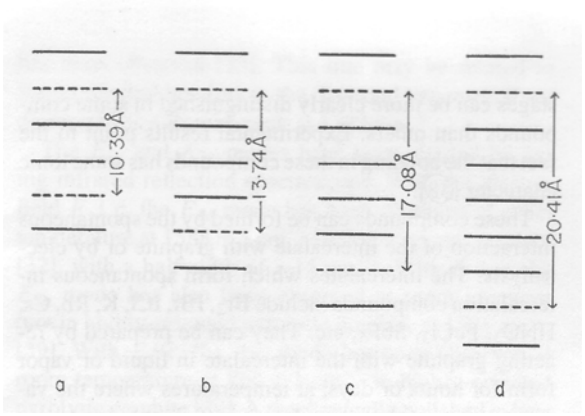

Figure 2.16 Interlayer ordering in C_8Br lamellar compounds of stage 2-5. The dashed lines indicate Bromine intercalated layers in graphite (a) 2nd stage structure ($C_{16}Br$) 6.25 %mol Br (b) 3rd stage structure ($C_{24}Br$) 4.17 %mol Br (c) 4th stage structure ($C_{32}Br$) 3.13 %mol Br (d) 5th stage structure ($C_{40}Br$) 2.50 %mol Br[65]

With further increase of bromine vapour pressure, the structure follows the stages of higher bromine concentrations until it reaches the 2nd stage saturation structure. At intermediate bromine concentrations, XRD patterns (diffractogram) show a mixture of extra lines of both the higher and lower stage structures. Chung[65] reported that debromination occurs in the reverse order, however at lower bromine vapour pressure. This is due to bromine having a tendency to be retained in the compound. Therefore, at zero vapour pressure of bromine, residual compound remains after exposure to bromine. Sharma et al[82] reported bromine residue compounds in the graphite using mass spectroscopy. They reported that C_8Br, which had undergone desorption to 350 °C, showed no further bromine desorption from the graphite during heating under high vacuum to 450 °C, which is indicative of residual bromine in the graphite. The intercalates can be retained in the residue compound by being trapped between the graphite layers as lamellar compounds or trapped at crystal imperfections of the graphite crystal structure.

Iodine and chlorine do not readily intercalate in graphite. However, interhalogens such as iodine monochloride (ICl) and iodide bromide (IBr) can be intercalated into graphite. Graphite-chloride (C_8Cl) has been intercalated under special conditions at room temperature by Hennig and in addition, Juza et al prepared a fully intercalated compound at -78 °C[73]. The C_8Cl appears to be similar to C_8Br. Graphite-iodine monochloride (C_5ICI) readily forms intercalated compound. The bromine residue compounds allow intercalation of iodine in graphite. Colin and Herold[73] reported that removing bromine results in a residue enriched with iodine. The amount of residual compounds retained depends on the original structure of the graphite.

2.5.4 Graphite halide compound

Thiele discovered that besides forming acid-ion compounds, alkali metal compounds and graphite halogen, graphite can be intercalated with a large number of halides[73]. Most of the halides studied are chlorides and fluorides. Like halogens, halides are electron acceptors in graphite. Earlier attempts to form graphite halide compounds such as isomorphous with ferric chloride ($FeCl_3$) failed due to the necessity to break non-graphitic bonds to allow separation of the C-atoms with intercalation of other molecular species. Alternatively, excess halogen may be necessary in order for halides to intercalate into graphite. Graphite halide compounds are prepared generally by heating the graphite with the halide. $FeCl_3$ is the best studied of the graphite halide compounds since it is the oldest and has interesting magnetic properties. The $FeCl_3$ has been prepared according to Thiele[65], where graphite was heated with anhydrous $FeCl_3$. After cooling the mixture, excess $FeCl_3$ was removed by either washing with hydrochloric acid or sublimation. In varying the reaction temperature, which is above 180 °C, different stages were obtained. $FeCl_3$ lamellar compounds of 1 to 6 stages can be formed; stage 1 (69%), stage 2 (53%), stage 3 (42%), stage 4 (35%), stage 5 (30%) and stage 6 (28%). The graphite mixture was maintained at higher temperature than $FeCl_3$ to minimise its condensation. A less common method for preparing $FeCl_3$ is electrochemical intercalation.

Intercalation by other halides has been realised and studied in a semi-quantitative method such as copper chloride and copper bromide[73].

2.5.5 Graphite alkali metal

The alkali metal intercalates include lithium (Li), sodium (Na), potassium (K), rubidium (Rb) and caesium (Cs). The elements K, Rb, and Cs behave similarly, however they are different to Li and Na. Guerard et al[65] reported some of the various stoichiometries of graphite alkali metals. These alkali metals, which form binary graphite alkali metals, have stoichiometries of C_8X, $C_{24}X$, $C_{36}X$, $C_{48}X$ and $C_{60}X$ where X is K, Rb or Cs, which correspond to stages 1, 2, 3, 4, and 5, respectively[65]. Udod[83] reported that stage 1 with intercalate concentration beyond C_8X is possible. Lithium intercalation in graphite occurs differently in that instead of C_8Li it exists as C_6Li. Funabiki et al [84] reported that graphite lithium has three stages, C_6Li, $C_{12}Li$ and $C_{18}Li$, corresponding to stages 1, 2 and 3 respectively[84]. In contrast, Na does not readily intercalate in graphite. However, Herold[73] prepared graphite-sodium (graphite-Na) using small amounts of Na atoms under suitable conditions. According to Asher and Wilson[73], observations of X-ray diffractogram and magnetic properties have shown the formation of graphite sodium compound with an approximate composition of $C_{64}Na$, when Na was heated with graphite powder at temperature 400 °C[73]. In addition to this, ternary graphite alkali metals, which involve two different types of alkali metals, can be formed[85-87]. Despite the relative simplicity of the electronic structure of the alkali metals, their interaction with graphite is still the subject of current debate[88]. The different behaviour between the reactivity of alkali metals with graphite can be explained in many ways, however none can explain all the differences. One explanation is in terms of the size effect of alkali metals. The nearest neighbour distances in the alkali metals increases from Li to Cs (0.300, 0.368, 0.462, 0.486 and 0.525 nm, respectively). The distances obtained in the pure metals can be compared with those in graphite alkali metals. For instance, the nearest neighbour distance is more or less fixed by the graphite crystal at 0.491 nm in stage 1 compound C_8X (X=K, Rb, Cs). It is evident that K and Rb can fit into graphite, however more so for the latter, whilst Cs is compressed. These alkali metals can be intercalated in graphite with differing ease. In the case of Na and Li, the nearest neighbour distances are smaller than that of graphite. For this reason, Na does not readily intercalate in graphite. Herold[73] prepared small amounts of Na atoms intercalated under suitable conditions, whereas Li intercalates in graphite differently, as mentioned above. Hence, the denser packing of C_6Li structure is consistent with the small size of the Li atom[65].

Graphite alkali metal lamellar compounds can be formed by several methods. The first method requires the heating of graphite with known quantities of alkali metal in an evacuated vessel. Graphite alkali metals which have been prepared by this method include those of K, Rb and Cs[73]. The second method is a modified two-bulb method[89] where the alkali metal and the graphite are in two bulbs at different temperatures, 250 and 250 to 600 °C, respectively. The compounds were kept under a stabilization agent (liquid paraffin). The 1st stage structure of saturation was formed by holding both bulbs at the same temperature. Stages 4 to 1 can be formed in order. Consequently, if the temperature difference between the two bulbs was great, the intercalate concentration in the resulting compound was lower. The third method involves electrolytic preparation. The latter method has been successful in preparing C_6Li[84,90-92].

The effect of K, Rb and Cs intercalation on the electrical properties of graphite has been summarised by Chung[65]. For instance decrease in both a and c axes and anisotropy ratio of electrical resistivity hence decrease in the electrical resistivity in the c-axis was more pronounced and decreased continuously with increasing content of alkali metal. According to Blackman et al[65] a limiting decrease in the a-axis was reached at approximately stage 4. Chung[65] summarised the effect of alkali metal intercalations on the magnetic properties of graphite such as change of the magnetic susceptibility from negative to positive and changes in the g-shift and the line-width of the electron spin resonance.

2.5.6 Graphite acid compound

Graphite reacts with a large number of acids to form intercalation compounds that have been referred to as acid salts of graphite or graphite acid salts. They have received much attention due to their high electrical conductivities. The acid intercalates include nitric acid (HNO_3), sulfuric acid (H_2SO_4), perchloric acid ($HClO_4$) and selenic acid (H_2SeO_4). They act as electron acceptors in the graphite crystal structure in which the positive charge of the intercalated or oxidized graphite is balanced by negatively charged ions (NO_3^-, HSO_4^-)[93]. However, only a fraction of these acid molecules intercalate by the ionization process and the rest remain in the graphite crystal structure. Graphite acid salts can be prepared either by a chemical method (oxidation of graphite by a chemical reagent) and/or electrolysis. Graphite-nitrate (graphite-HNO_3) and graphite-bisulfate or graphite-sulfuric acid (graphite-H_2SO_4) are the most extensively studied graphite acid salts.

Graphite-HNO_3 via a chemical method involves nitration in the liquid or vapour phase. In liquid phase nitration, graphite is mixed with HNO_3 of various concentrations. A stage 1 graphite-HNO_3 can be formed by using a mixture of 50 %wt fuming HNO_3 with 50% nitrogen pentoxide (N_2O_5) by distillation from HNO_3 and phosphorous pentoxide (P_2O_5). The graphite-HNO_3 in stage 1 results in a blue compound. However, higher stages of graphite-HNO_3 can be formed in the absence of N_2O_5[65]. For instance, stage 2 graphite-HNO_3 can be formed by the use of fuming HNO_3.

In vapour phase nitration, graphite is exposed to HNO_3 vapour at various partial pressures. Graphite-HNO_3 via vapour phase nitration form compounds compared with graphite-HNO_3 formed via liquid phase intercalation. This is due to liquid phase nitration occurs rapidly at the edges of the graphite crystal structure that the edges expand as a result of intercalation before the acid molecules have time to intercalate into the interior of the graphite layers[65].

In electrolysis, graphite acts as a reference electrode and fuming HNO_3 acts as the electrolyte. According to Sharff et al[94,95], galvanostic and potentiodynamic studies, stage 2 graphite-HNO_3 is obtained by the electrochemical oxidation of graphite in 65% HNO_3. In addition, they obtained stage 1 graphite-HNO_3 using fuming HNO_3, however they found it to be relatively unstable. Avdeev et al[96] reported the anodic oxidation of graphite over a wide range of HNO_3 concentrations (50 to 98%). The potential against charge curves at various concentrations showed step-like behaviour, and the number of steps increased with decreasing HNO_3 concentration, corresponding the successive formation of stage III, II and I graphite-HNO_3.

Graphite-H_2SO_4 lamellar compounds can be prepared by chemical interaction of graphite with a mixture of concentrated H_2SO_4 and sufficient HNO_3 as an oxidizing agent. Other oxidising agents, which have been used successfully to prepare graphite-H_2SO_4, include chromic oxide (Cr_2O_3), potassium permanganate ($KMnO_4$), ammonium persulfate ($(NH_4)_2S_2O_8$), manganese oxide (MnO_2), lead dioxide (PbO_2), arsenic pentoxide (As_2O_5), iodic acid (HIO_3) and periodic acid (H_5IO_6), and tri-and quadrivalent manganese salts have been used[65,73]. The presence of oxidising agent allows for the C-atoms in the graphite layers to lose electrons and obtain a positive charge and combine with HSO_4^- ions. Equation 2.2 shows the reaction, which occurs when graphite is treated with H_2SO_4 in the presence of HNO_3 and other oxidising agent[76].

$$nH_2SO_4 + \text{graphite} + n/2 = O\ n/2\ H_2O + [\text{graphite}.HSO_4]_n \qquad \text{Equation 2.2}$$

Graphite-H_2SO_4 can be prepared by electrolysis in which graphite is made anodic in concentrated H_2SO_4[97,98]. Anodic oxidation process can control the amount of graphite intercalated and allows simultaneous measurement of the physical properties[73]. This means that the number of ions intercalated can be evaluated by applying Faraday's law. This allows the determination of n in the chemical formula $C_nH_2SO_4.xH_2SO_4$. Using weight uptake measurement, the value of x can be obtained if n is known. The stages give rise to steps in the curve of the electrode potential against current or time. Using XRD, n and x was determined. The combination of both techniques indicate that these steps have n=24 in stage 1 and n=48 in stage 2[99]. The value of x is 2.5 in both stages 1 and 2.

Graphite-H_2SO_4 crystal structure consists of graphite layers with HSO_4^- ions and H_2SO_4 molecules between the graphite layers. The HSO_4^- ions between the graphite layers cause an expansion of the graphite crystal structure in the c-axis. In addition to this, oxidation of layered graphite causes a large number of polar functional groups such as hydroxyl, carboxyl, ether groups and possibly carboxylate groups to form on the surface of graphite[100,101].

Graphite-H_2SO_4 can be degraded into graphite again either in the presence of water or exposure to air. In the former, when water is added into H_2SO_4, the blue compound decomposes in a step-wise manner into mixture of higher stage graphite-H_2SO_4 compounds that are not blue[65,76]. The latter causes the graphite-H_2SO_4 to loose its blue colour, which can be attributed to the absorption of water. However, XRD studies indicate the presence of some amount of the stage 1 graphite-H_2SO_4[65]. Graphite-H_2SO_4 were the first to find extensive industrial application compared with graphite-HNO_3 due to their stability[98]. In particular, it has been widely used to produce flexible graphite due to low cost and high efficiency of production. However, many efforts have concentrated on the reduction of sulfur content in graphite-H_2SO_4 and expanded graphite since residual H_2SO_4 makes flexible graphite corrosive. When HSO_4^- ions have intercalated in the graphite layers, graphite-H_2SO_4 has the composition of $C_{24}^+H_2SO_4^-.2\ H_2SO_4$. Therefore, it is possible to exchange the molecules and ions of H_2SO_4 reversibly, by treating graphite-H_2SO_4 with other strong acids to form graphite-H_2SO_4-HNO_3[102,103], graphite-H_2SO_4-H_2SeO_4, graphite-H_2SO_4-CH_3COOH[97,104,105], graphite[97] either by chemical or electrolysis[98,106]. The synthesis of ternary GIC allows one to control precisely the content, structure and properties of both GIC and their processing products such as oxidised, expanded and flexible graphite[97].

2.6 Expanded graphite

Exfoliation process involves thermal treatment of GIC at high temperatures. It is a process in which GIC expands in the dimension perpendicular to the graphite layers of GIC, c-axis, forming an interconnected network with vermicular shape, which is often described as a worm like shape, accordion or honey comb shape; the product is known as expanded graphite (EG). The EG maintains a layered crystal structure similar to flake graphite. During heating evaporation and decomposition of intercalate, the graphite layers collapse and deform randomly and produce different pore sizes and nanolayers adhering to each other forming a network (Figure 2.17). EG is a loose and porous worm-like shaped material with low density. In addition, EG contains polar functional groups on its surface.

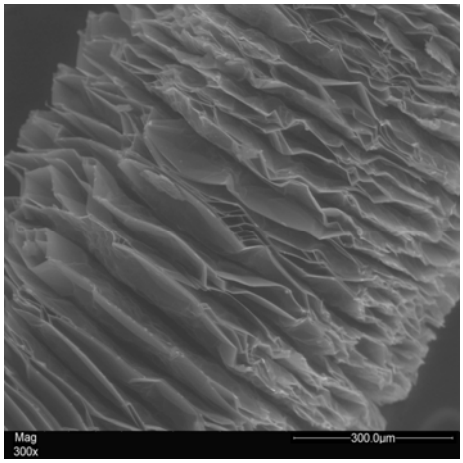

Figure 2.17 SEM micrograph of GIC after exfoliation

In order to obtain EG, flake graphite must be intercalated before it can be exfoliated. In principle, any intercalate can be used. The most common choice of GIC is graphite-H_2SO_4 obtained by reaction with a mixture of H_2SO_4 and HNO_3, as described in Section 2.5.5 of this chapter.

2.6.1 Type of exfoliation

Exfoliation of GIC can be either reversible or irreversible. Reversible exfoliation of GIC was first reported by Martin and Brocklehurst on C_8Br[107].

They reported the following:

1. first exfoliation occurred at 170 °C upon first heating
2. subsequent exfoliation occurred at approximately 120 °C in heating cycles
3. collapse of graphite layers occurred at 110 °C upon cooling
4. second and subsequent exfoliation cycles were reversible
5. GIC crystal structure expansion was 380% at 500 °C

The reversibility of GIC is a consequence of the fact that exfoliation of this nature is a phase transition[108].

Irreversible exfoliation of GIC was first reported by Aylsworth in 1916[108]. Unlike reversible exfoliation, it requires higher temperature for expansion, thus, the transition from reversible to irreversible exfoliation is gradual. With exfoliation cycles to higher temperatures, the amount of residual expansion after the collapse on cooling increases until no second exfoliation occurs on reheating. Generally the latter is more expanded than the former, due to the higher temperature required for it to occur[108].

2.6.2 Method of exfoliation

Since exfoliation is a phase transition which occurs at high temperatures, heating is required. EG is formed by heating GIC internally or externally. Exfoliation via internal heating involves an electric current passing through the GIC[109]. Whilst exfoliation via external heating requires a heating source, the most conventional heating source is a flame. The flame provides rapid heating to high temperatures. The flame temperature can be ≥200 °C. However, GIC can be exfoliated at lower temperatures such as 700 to 800 °C.

2.6.3 Mechanism of exfoliation

Several studies using differential thermal analysis (DTA) and differential scanning calorimetry (DSC) have shown that the exfoliation of GIC is due to the evaporation of intercalate[108]. Furdin[110] reported that regardless of heating method used, there is a competitive mechanism between desorption of the GIC and particle exfoliation. It can be said that desorption is associated with slow evaporation of intercalate at the particle edges, which does not lead to a collapse of graphite layers, whereas exfoliation corresponds to the boiling of intercalate in graphite pockets, leading to the collapse of the graphite layers. The overall process corresponds to two distinct regimes, the latter being more rapid than the former.

Desorption of intercalates depends on rheological phenomena, meaning the ease of flow of intercalate between the graphite layers. Therefore, for irreversible exfoliation, the essential parameter is the thermal transfer existing between the heat source and the GIC[110]. In addition, Furdin[110] reported that the exfoliation temperature does not depend on the heating rate and the stage of the precursor of GIC. Chung[108] conducted a review concerning exfoliation phenomenon of GIC. He reported several mechanisms of exfoliation of GIC. According to the investigation performed by Hooley[108], certain crystalline structure defects seal the edges of the graphite layers together, forming gas-tight pockets in which intercalate is trapped. If the intercalate mobility and solubility are high, intercalate may diffuse out of the gas-tight pockets and into the graphite layers in a short time compared with the amount of time required for the exfoliation cycle. Diffusion of intercalate is one mechanism, which excess intercalate can be loss. However, gas-tight pockets provide as sinks for excess intercalate, as a result graphite layers would lose intercalate while GIC crystal structure as a whole would not. Therefore, gas-tight pockets should expand to a greater degree. This mechanism is consistent with the observations obtained by Anderson and Chung[111]. They observed that a larger expansion occurs during the second exfoliation than the first exfoliation for GIC which are initially desorbed. Another mechanism in which intercalate can be lost either by rupturing of gas-tight pocket or gas-tight pockets form an interconnected network which, in turn opens to the outside of the GIC.

The origin of exfoliation for certain intercalates is the thermal decomposition of intercalate into the gas phase and another solid phase. However, it is not the evaporation of a single phase but instead a phase transition that yields a gaseous product, so that the basic mechanism is similar to that mentioned above. For instance graphite-$FeCl_3$, where the overall reaction is in the form:

$$FeCl_2(s) \rightarrow Cl_2(g) + Fe(s) \qquad \text{Equation 2.3}$$

This reaction (Equation 2.3) shows that chlorine (Cl_2) evaporation shifted the reaction to the right[108]. Chung[108] has reported that intercalate has a tendency to aggregate to form intercalate islands. The size of intercalate island depends on the intercalating conditions. The higher the size of intercalate island, the more easily and the greater degree to which exfoliation may occur. In addition, the degree of the expansion increased with decreasing intercalates activity during intercalation. According to nucleation theory, as the reactant activity increases, competition between nucleation sites increases and the microstructure becomes finer.

The intercalate activity can be decreased either by diluting or heating, and the intercalate island size is expected to increase.

2.6.4 Property and application of expanded graphite

EG is obtained by subjecting GIC to high temperatures causing intercalate to vaporize. Heating GIC causes a sudden increase in the dimension perpendicular to the graphite layers of GIC. EG like flake graphite has a layered structure, however it has larger graphite layer spacing and higher volume expansion ratio and in addition larger specific surface area compared with its precursor. The volume expansion ratio and specific surface area of EG varies with the type of intercalate used. For instance graphite intercalated with HNO_3 leads to rupturing of the gas-tight pockets whilst graphite intercalated with Br does not. Graphite-HNO_3 yields EG with a higher surface area than graphite-Br. Furthermore, exfoliation of GIC intercalated with acids exposes more functional groups such as carbonyl, carboxyl and hydroxyl groups on the surface of EG.

Olsen et al[112] reported transport properties such as electrical resistivity, thermal conductivity and thermoelectric power for graphite-H_2SO_4 after irreversible exfoliation. The a-axis electrical resistivity of irreversibly exfoliated graphite-H_2SO_4 at 27 °C was found higher, $2x10^{-4}$ $\Omega.cm^{-1}$ compared with $5x10^{-5}$ $\Omega.cm^{-1}$ prior to exfoliation. A similar increase in a-axis electrical resistivity was reported by Chung and Wong[113] for graphite-Br at room temperature. Chung and Wong[113] reported that the increase in a-axis electrical resistivity is due to the bending of the graphite layers. However, the opposite was observed for c-axis electrical resistivity of exfoliated graphite-H_2SO_4 and graphite-Br. The c-axis electrical resistivity decreased after exfoliation due to the bending of the graphite layer conducting network[108]. Olsen et al[108] reported the decrease in both a and c-axes thermal conductivity after exfoliation of graphite-H_2SO_4 at 52 °C. The decrease in a-axis thermal conductivity is due to the bending of the graphite layers. The thermal conductivity in the c-axis decreases and is attributed to a decrease in density. The decrease in thermal conductivity for both a and c-axis, makes EG a valuable thermal insulator material. The a-axis thermal conductivity for graphite-H_2SO_4 decreases linearly with increasing temperature, however this behaviour was observed before and after exfoliation. The c-axis thermal conductivity prior to exfoliation of graphite-H_2SO_4 increases with increasing temperature.

The c-axis electrical resistivity is the only transport property that has been measured during reversible exfoliation. Graphite-Br c-axis electrical resistivity decreases at the exfoliation temperature during reversible exfoliation due to elongation of graphite-Br along the c-axis[108].

EG can be mass-produced and used in many applications such as gaskets, seals and fire extinguisher agents[108]. Compression of expanded graphite particles without a binder results in mechanical interlocking among the expanded graphite particles which form a flexible graphite material. This material is useful for high-temperature gaskets since it is inert chemically and has a high temperature resistance. In addition it can be use as a gasket material for electromagnetic interference (EMI) shielding, since its electrical conductivity and high specific surface enhanced the reflection of high frequency electromagnetic radiation[65]. EG can be used as a refractory sealing material that involves the addition of a binder and EG to a refractory aggregate and heating it to obtain a non-porous sealing layer. This prevents gas leakage from blast furnaces and other refractory pressure vessels. Since EG has a large surface area it can be used as a substrate for the study of adsorbed films. EG is available as a fire extinguisher agent, which is valuable for extinguishing metal fires. This is possible since GIC expands upon contact with fire. Other applications are batteries, potential uses in depollution[114-116], medical science[117] and support for active carbons[29].

2.6.5 Polymer layered graphite nanocomposite

The success in PLSN has led researchers to investigate other layered nanoparticles such as flake graphite. Researchers have adapted methods such as in-situ polymerisation, solution intercalation and melt intercalation, which are described in Section 2.2.3 of this chapter to prepare polymer layered graphite nanocomposites.

Generally, it is difficult to obtain composites with graphite dispersed homogenously in a polymer matrix due to their incompatibility. Therefore, like pristine layered silicate, the surface of the layered graphite was modified using a chemical method (oxidation). Layered graphite is commonly oxidised using acids such as H_2SO_4 and HNO_3 to form GIC or graphite acid salt. GIC and EG has higher volume ratio, multi-pores compared with untreated graphite, In addition, oxidation results in the formation of polar functional groups on its graphite surface that can facilitate physical and chemical interactions with polar monomer or polymer[118]. As previously mentioned in this chapter, EG has a higher volume ratio and multi-pores in comparison with GIC. Therefore formation of polymer layered graphite

nanocomposites is possible. A number of polymers are utilised as base polymers for polymer layered graphite nanocomposites (PLGN) including polyamide (PA-6)[2,119], poly(propylene maleic anhydride) (PPMA)[120,121], poly(methyl methacrylate) (PMMA)[11,29], high density polyethylene (HDPE)[30,122], poly(vinylidene fluoride) (PVDF)[123] and polyurethane (PU)[93,124].

Pan et al examined PA-6 layered graphite nanocomposites[10]. The expanded graphite was prepared by heating oxidised graphite above 900 °C. The PA-6 layered graphite nanocomposites were prepared by in situ polymerisation of ε-caprolactam with EG. The expanded graphite layers were dispersed within the PA-6 matrix. They reported the effect of the aspect ratio of the EG on electrical conductivity. From their findings, they showed that the addition of EG improved the electrical conductivity of PA-6 with a sharp transition from an electrical insulator to an electrical semiconductor. The electrical conductivity of PA-6 improved by several orders from 10^{-14} to 10^{-4} S.cm^{-1} when the EG concentration was 0.75 %vol. The formation of a conducting network can be explained by percolation theory [125], the effective medium theory[126,127], the microstructure theory[127] and the thermodynamic theory[128] all of which relate to the dispersed structure and internal microstructure of conducting fillers in polymer matrices. This depends on geometrical arrangement, thermodynamic and dynamic factors including nature of the filler, polymer matrix, preparation methods and processing conditions. In addition, the formation mechanism of the conducting path is related to the differing morphologies and internal microstructures of the conducting filler particles that may lead to the formation of paths in distinct patterns.

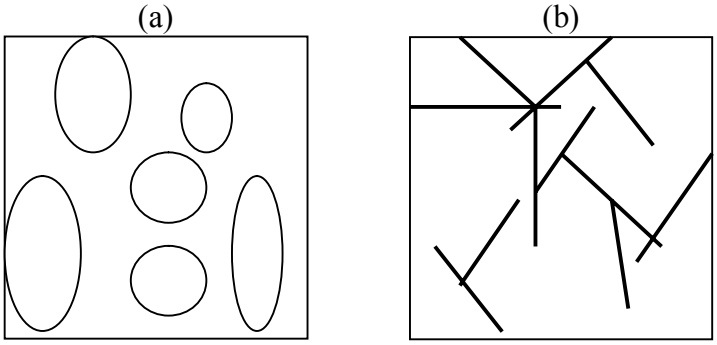

Figure 2.18 Schematic diagram of various geometries of conducting fillers (a) Spherical or elliptical shapes and (b) Sheet-like or fibre-like[10]

For instance, for a given filler concentration, the percolation threshold is lower for a filler with high aspect ratio such as sheet-like or fibre-like compared with fillers with low aspect ratio such as spherical or elliptical filler in the nanocomposites. Therefore the higher the filler

aspect ratio, the lower the percolation threshold necessary in forming a conducting network. Figure 2.18 demonstrates schematically the effect that the geometry of a conducting filler has on the formation of the conducting network[10]. Therefore, the percolation threshold of layered composites is expected to be lower in comparison with conventional composites such as carbon black[18,129]. Furthermore, the fillers used in polymer composites of this type have smaller dimensions than those of conventional composites. For these reasons, the degree of expansion of graphite layers is critical in the formation of a conducting path network in a polymer matrix. This idea is shown schematically in Figure 2.19. The ordered and disordered solid lines represent the graphite layers from a direction parallel to the graphite layers. When the graphite concentration is low, the probability for unexfoliated graphite particles to be in contact is small. However, when the graphite is extensively exfoliated into nanoscale layers, the number and the aspect ratio of the graphite layers are increased[10].

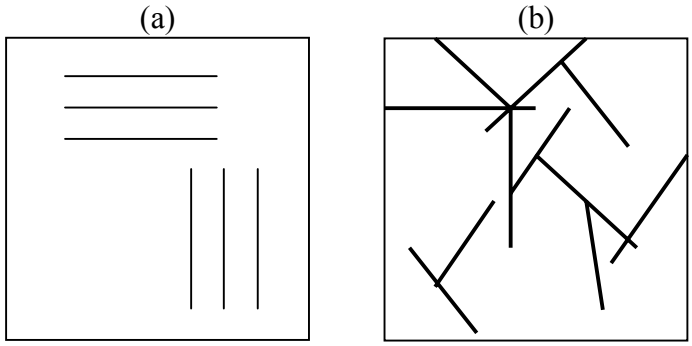

Figure 2.19 Schematic diagram showing the effect of degree of exfoliation of graphite on the formation of a conducting network (a) unexfoliated and (b) exfoliated graphite layers in a polymer matrix. The black lines represent the graphite[10]

In addition, their studies show that flexural modulus of filled the PA-6 was higher than that of pure PA-6. The presence of rigid graphite layers increases the modulus of the PA-6 matrix. Chen et al[9,130] prepared PS-layered graphite nanocomposites by in situ polymerisation. Graphite was oxidised using a mixture of H_2SO_4 and HNO_3 and expanded by heating to 1000 °C, from this they were able to prepare PS layered graphite nanocomposites. They reported similar results to that of Pan et al[10]. However, decreased electrical conductivity was obtained when extensive processing such as rolling from a twin roller was used to prepare as rectangular plates.

Other researchers have reported improved thermal stability of polymer matrix in the presence of layered graphite[131-133]. The improvement in the thermal stability of the nanocomposite was ascribed to the heat shielding effectiveness of the graphite layers[100,134].

PLGN possess potential applications in radiation and electromagnetic shielding, antistatic, shrinkage and corrosion resistant coatings, among other important properties including mechanical and functional attributes such as stiffness, barrier and conducting capabilities[30].

Chapter 3 Materials and experimental techniques

3.1 Introduction

In this chapter, the various materials and preparation of expanded graphite oxide are described, thus treatment and preparation of polymer layered graphite composites are described in their individual chapters. The instruments and experimental techniques utilized to characterize the different types of graphite oxide and polymer layered graphite oxide and expanded graphite oxide composites in this study were briefly discussed and experimental parameters for each technique utilized were described.

3.1.1 Materials

The graphite flakes were supplied by Graftech Inc OH, USA. The size distribution of graphite flakes was measured by sieving. The graphite flake used was 80 mesh, where the size of the mesh opening was 180 μm ($180x10^{-3}$ mm) and its density is 2.0 $g.cm^{-3}$. A poly(ethylene-co-methyl acrylate-co-acrylic acid terpolymer) (EMAA) with 18% methyl acrylate and 6% acrylic acid (Exxon-Mobil Escor AT320) (Melt index=115 $g.min^{-1}$; density=0.95 $g.mL^{-1}$) was used as the host matrix. Polypropylene (PP) pellets were obtained from Orica Aust. Maleic anhydride (MA) was obtained in flake form from Sigma-Aldrich Pty Ltd Benzoyl peroxide used for the preparation of grafted PP was obtained in a powdered form from Sigma-Aldrich Pty Ltd Aust. Poly(propylene-g-maleic anhydride) (PPMA) from Aldrich Chemical Company (0.6 %wt of MA; T_m=152 °C; Melt index=115 $g.min^{-1}$; density=0.90 $g.mL^{-1}$ at 25 °C) was used as the host matrix.

3.1.2 Exfoliation of graphite oxide

Expanded graphite oxide (EGO) was formed by exfoliation process. A ceramic crucible that contains approximately 1 g of oxidized graphite was inserted in a pre-heated muffle furnace, held at a constant temperature of 800 °C for 30 s.

3.1.3 Scanning electron microscopy

3.1.3.1 General introduction to scanning electron microscopy

Scanning electron microscopy (SEM) is a technique designed for direct study of the surface or near surface structure of bulk material under vacuum. The electron gun consists of a filament (cathode), which generates a beam of electrons by applying voltage. The beam of electrons accelerates towards the anode and is demagnified by condenser lenses and focused into a fine spot between 2 to 10 nm in diameter on the material by the objective lenses. The fine beam of electrons is scanned in a rectangular raster over the material. The interactions of these electrons at the material generate secondary electrons and are collected by a detector. Simultaneously, the spot of a cathode ray tube (CRT) is scanned across the screen while the brightness of the spot is modulated by the amplified current from the detector. The beam of electrons in the microscope and the CRT are scanned at the same rate and has a one to one relationship between each point on the CRT screen and a corresponding point on the material. This forms an image which consist pixels that correspond to the topography of the material[135,136]. The image can be recorded by photographing through video prints or storing a digital image.

3.1.3.2 Surface structure property

ESEM scans were performed on a FEI Quanta 200 environmental scanning electron microscope (ESEM) to investigate the structure of materials. The materials were mounted on the stage using a conductive carbon tape and analysed under low vacuum at 0.5 torr with an electron beam power set at 20 kV.

3.1.4 Transmission electron microscopy

3.1.4.1 General introduction to transmission electron microscopy

Transmission electron microscopy (TEM) is a technique used to study the internal structure of a material. The electron gun consists of a filament (cathode), Wehnelt cylinder and an anode. TEM like the SEM constantly generates electrons from the electron gun by applying voltage to the filament under vacuum. The generated electrons are accelerated towards the anode and emerge at the other side. The Wehnelt cylinder concentrates the electrons into a fine focused point. The fine beam of electrons are travel through the condenser lenses whose main

functions are to demagnify the beam of electrons and to control its diameter and convergence angle as it travels through the material. The objective lens forms the first intermediate image and diffraction pattern. The first image usually has a magnification of 50 to 100 times. This is further magnified by a series of intermediate and projector lens and is projected onto the fluorescent screen at the bottom of the column. The images can be studied directly by the operator or film based cameras[136].

In order to visualise the material it must be thin (<200 nm) to allow the electron to pass through it. This often involves sectioning ultra-thin materials using a diamond knife this technique is referred to as ultra-microtomy. Hard (or stiff) polymers such as PS can be sectioned at ambient temperature, however some polymers are too soft (or flexible) for sectioning at ambient temperature and are better sectioned at lower temperature. The latter known as cryo-ultramicrotomy involves sectioning materials at lower temperature under liquid nitrogen (N_2). After sectioning the resultant sections are collected in a liquid filled trough and are mounted on grids prior TEM analysis[137].

3.1.4.2 Internal structure property

Ultra-thin films were obtained by cryo-ultra microtoming using a Diatome STATIC LINE II, at low temperature under N_2 and sectioned using diamond knife. Transmission electron microscopy was performed on TEM Jeol 1010 (2001) to study the internal structure of a material. The ultra-thin films were analysed with an electron acceleration voltage of 200 kV.

3.1.5 Surface area and pore size property

3.1.5.1 General introduction to Brunauer-Emmet-Teller analysis

Brunauer-Emmet-Teller (BET) analysis is a technique in which the surface area of a powdered or porous material is measured from the volume of gas adsorbed onto its surface. The BET analyser measures the entire surface area, both external and internal accessible to the gas. Before any measurements can be performed the material for analysis must be degassed to remove of any gases currently adsorbed onto the surface. The material degassing (or desorption) process is accomplished under vacuum whilst heating the material. After degassing, the material is cooled, in order to allow sufficient gas to be adsorbed for surface area measurement. Commonly, liquid N_2 is used as an adsorbate. The material is cooled to the boiling point of N_2 and adsorption continues until the amount of N_2 adsorbed onto the

materials surface is in equilibrium with the concentration in the gas phase. A series of measurements of the volume of gas adsorbed as a function of pressure are made from which, the volume can be calculated using the relationship adopted by Brunauer, Emmett and Teller (BET) Equation 3.1[138].

$$\frac{x}{x_m} = \frac{c\left(\frac{P}{P_0}\right)}{\left(1-\frac{P}{P_0}\right)\left(1+c-1\frac{P}{P_0}\right)} \qquad \text{Equation 3.1}$$

Where x is the weight of adsorbed gas at a relative pressure, $\frac{P}{P_0}$, x_m is the weight of adsorbed gas in the monolayer and c is the BET constant

For convenience of plotting, Equation 3.1 can be written as (Equation 3.2)[138]

$$\frac{P}{x(P_0-P)} = \frac{1}{x_m c} + \frac{c-1}{x_m c}.\frac{P}{P_0} \qquad \text{Equation 3.2}$$

Based on the BET equation (Equation 3.2), the surface area can be determined when $\frac{P}{x(P_0-P)}$ is plotted against $\frac{P}{P_0}$. This results in a linear relationship, with slope, s, and intercept, *i* in Equation 3.3 and 3.4, can be used to determine x_m (Equation 3.5) and c (Equation 3.6) by solving these two simultaneous equations (Equations 3.3 to 3.4)[138].

$$s = \frac{(c-1)}{x_m c} \qquad \text{Equation 3.3}$$

$$i = \frac{1}{x_m c} \qquad \text{Equation 3.4}$$

$$x_m = \frac{1}{s+i} \qquad \text{Equation 3.5}$$

$$c = \frac{s}{i} + 1 \qquad \text{Equation 3.6}$$

The surface area, S_t ($m^2.g^{-1}$), can be calculated via Equation 3.7[138].

$$S_t = \frac{x_m}{M}.N.A \qquad \text{Equation 3.7}$$

Where M is the molecular weight of the adsorbate, N is Avogadro's constant; 6.02×10^{23} molecules per mole and A_m is the molecular cross-sectional area of the adsorbate. Subsequently, specific surface area, S, can then be calculated as shown in Equation 3.8, by dividing the material weight, w. The molecular cross-sectional area, A_m, of a N_2, is 16.20 $Å_2$ at its boiling temperature of -195.16 °C[138].

$$S = \frac{S_t}{w} \qquad \text{Equation 3.8}$$

The BET analyser determines the difference in the volumes of gas delivered to the tubes containing a powdered material for analysis.

3.1.5.2 BET surface area property

Surface area properties were measured using a BET surface analyser, Micrometrics ASAP 2000, was utilized to measure the surface area of materials. Prior to degassing, materials were placed in a vacuum oven and heated at 100 °C for 24 h to remove solvent and/or moisture. One gram of each dried material was accurately weighed and placed into a tube and vacuum degassed at 100 °C for 24 h in N_2 atmosphere with a flow rate of 20 $mL.min^{-1}$. Filled tubes were then immersed in liquid N_2, and identical pressures were applied during the surface area measurements. The surface area measurements of a differential volume compensated for changing temperature gradients in the material tube.

3.1.6 Fourier transform infrared spectroscopy

3.1.6.1 General introduction to Fourier transform infrared spectroscopy

Fourier transform infrared (FTIR) spectroscopy is an analytical technique used to qualitatively determine the molecular components of a material. A beam (infrared energy) is emitted from a source and enters an interferometer, which encodes all the infrared frequencies. Depending on the type of analysis, the beam can either be transmitted through or reflected from the surface of the material. This is where specific frequencies that are uniquely characteristic of the material are absorbed. IR energy passes to the detector, which measures the interferogram signal. The measured signal is digitised and sent to a computer where Fourier transformation occurs and provides a spectrum. The absorption peaks in the spectra correspond to the frequencies of vibrations and deformations between certain bonds and atoms in the material[139].

3.1.6.2 FTIR spectroscopy

FTIR spectroscopy of materials were analysed to study their components using a Perkin-Elmer FTIR spectrometer Spectrum 2000. Materials were finely ground with solid KBr and pressed into 13 mm-diameter disks. Analysis was preformed in a range of 4000-400 cm^{-1} using 32 scans.

3.1.7 Wide angle X-ray diffraction

3.1.7.1 General introduction to wide angle X-ray diffraction

Wide angle X-ray diffraction (WAXD) is an analytical technique used to determine the identity of crystalline phases in a multiphase powdered material and the atomic and molecular structures of single crystals. This technique has been used to study stress, texture and crystallite size in various materials such as polymers, fibres, thin films, and amorphous solids.

WAXD employs a monochromatic (single-frequency) beam of x-rays. The x-ray beam strikes the crystal surface of the material at an angle, θ. Part of the x-ray beam is scattered by the layer of atoms at the material surface. The unscattered x-ray beam penetrates to the second layer of atoms where further scattering occurs. The remainder of the x-ray beam passes through to the next layer. Diffraction occurs when the wavelength of radiation is comparable with the characteristic spacing between layers of the atoms and the scattering centres are distributed in a highly regular configuration[140]. If the above requirements are satisfied, then the cumulative effect of the scattering results in diffraction of the beam and produces a diffraction pattern (diffractogram). The diffractogram provides a unique "fingerprint" of a material. Analysis of the angle positions, peak intensities, and shapes in WAXD diffractograms is used to give information on crystal structure and physical state[140].

3.1.7.2 Bragg and Scherrer equations

The Bragg law as shown in Equation 3.9 relates to the spacing between crystal planes, $d_{(hkl)}$, in a material in relation to the particular Bragg angle, θ, at which reflections from these planes are observed[140]

$$n\lambda = 2d_{(hkl)} = \sin\theta \qquad \text{Equation 3.9}$$

Where n is the order of reflection and is any integer such that $\sin\theta \leq 1$, λ is the wavelength of incident radiation in nanometer, $d_{(hkl)}$ is the distance between two adjacent parallel planes (interplanar, interlayer or basal or *d* spacing), θ is the incident angle of the X-ray beam to the planes of atoms.

The crystalline thickness or crystallite size perpendicular to the reflection of plane, $L_{(hkl)}$ or $L_{(c)}$, can be determined from the Scherrer equation (Equation 3.10)[141].

$$L_{(hkl)} = \frac{K\lambda}{\beta_0 \cos\theta} \qquad \text{Equation 3.10}$$

β_0 is the half-height width of the diffraction peak (full width at half maxima FWHM) in radian, K is the shape factor of the average crystalline thickness, related to the shape of crystalline thickness and definition of β_0 $L_{(hkl)}$; 0.9. Figure 3.1 shows an individual diffraction peak at FWHM.

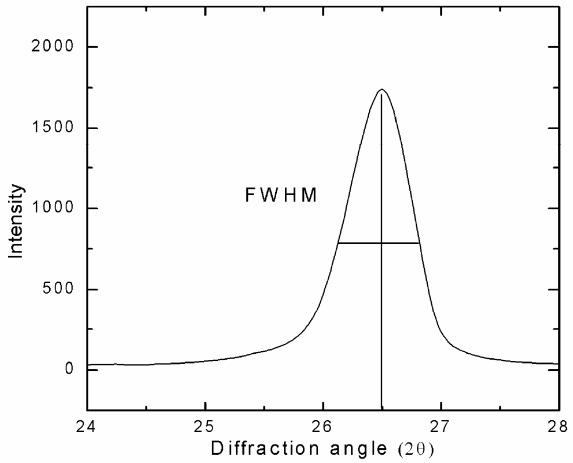

Figure 3.1 Broadening of a diffraction peak (FWHM) is related to the crystallite size according to the Scherrer equation

The crystalline thickness can be estimated from the shape of the peak, peak broadening. The broadening of a particular peak in a diffractogram is related to a particular reflection plane from within the crystal unit cell. It is inversely proportional to the β_0 of an individual peak, hence the narrower the peak the larger the crystallite size.

3.1.7.3 Interlayer spacing and crystalline thickness property

Crystalline information of materials were determined using a wide angle X-ray diffraction on a Bruker D8 Advance diffractometer using Cu-Kα radiation (λ=0.154 nm) with graphite monochromator to determine the structural information of materials. Diffractograms were typically acquired in 2θ ranges from 2 to 50° using a scanning rate of $2°.min^{-1}$ at an acceleration voltage of 40 kV and current of 20 mA. Powdered and film materials were prepared on glass slides.

Some diffractograms were subjected to Lorentz curve fitting to separate specific diffraction planes and provide better estimation of crystalline thickness. Lorentz curve fitting was performed using Origin 6, Microcal Software Inc, Version 6, data analysis, and technical graphics software. The Lorentz curve fitting was chosen as it resembles that of the diffractograms in this investigation. The parameters of the Lorentz curve are shown in Appendix 1.

3.1.8 Differential scanning calorimetry

3.1.8.1 General introduction to differential scanning calorimetry

Differential scanning calorimetry (DSC) is a thermal analysis technique used to study the physical and chemical changes associated with endothermic (heat absorption) or exothermic (heat evolution) processes. The physical and chemical changes are detected by differences in heat flow between a material and an inert reference whilst linearly changing the temperature. DSC is used to determine a material thermal property such as phase transition such as crystallisation, T_c, melting, T_m and glass transition, T_g temperatures, heat of fusion (enthalpy), ΔH_f, and degree of crystallinity, χ_c and heat capacity.

There are different types of DSC, one of which is the power compensated null balance DSC. In this type of DSC, a sample material and reference material are placed in independent, insulated chambers, as represented in the schematic diagram in Figure 3.2. Each individual chamber accommodates a platinum resistance sensor (thermometer) that measures temperature and a resistance heater. When absorption or evolution of heat occurs in the material, electrical power (energy) is applied to or removed from the calorimeter to compensate for the change in materials energy. This allows the system to be maintained at a

"thermal null" state at all times. The amount of energy needed to maintain the system at equilibrium is directly proportional to the energy changes occurring in the material. Hence, the system directly measures energy flow in or out of a material.

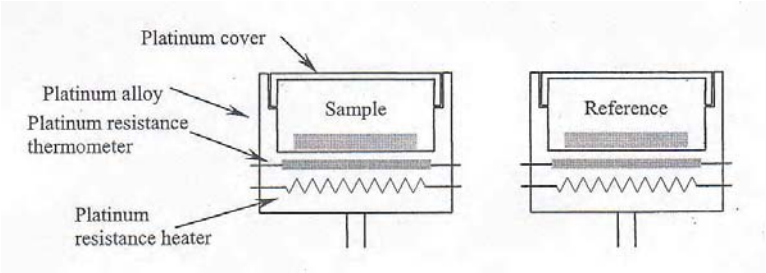

Figure 3.2 Schematic diagram of a power compensation DSC

3.1.8.2 Crystallisation, melting temperature and crystallinity property

The T_c, T_m, χ_c and other thermal properties of materials were measured using a Perkin-Elmer Pyris 1 DSC (Pyris TM software for Windows, Version 3.81, 2000). The instrument was calibrated with indium and zinc. In addition, indium was used to calibrate the heat-flow rate. Materials were weighed using a Perkin-Elmer AD-2Z Autobalance microbalance to an accurate weight between 2 to 5 mg. They were then sealed in crimpled aluminium pans.

Scans were performed in the temperature range of 20 to 200 °C at a heating rate of 10 °C.min^{-1}. An isothermal step was then performed for 5 min at 200 °C to remove any thermal history. The material was then subsequently cooled from 200 to 20 °C at a rate of 10 °C.min^{-1} and then re-heated over the same temperature range. All experiments were performed under N_2 gas with a flow rate of 20 mL.min^{-1}. Baselines were obtained with a matched empty (blank) pan under the same experimental conditions and were used to calculate specific heat capacity.

Measurements from these experiments were recorded and analysed to determine the thermal properties of each material. Typically peak temperatures T_c, T_m and onset temperatures,

$T_{c\ onset}$ and $T_{m\ onset}$ of each material were obtained from crystallisation and melting experiments, respectively. The onset temperature, T_{onset} of each material was calculated. The heat of fusion, ΔH_f, is proportional to the area under the peak. The χ_c was calculated using Equation 3.11 on the basis that polymer matrix has a crystallinity of 100%.

$$\chi_c \frac{\Delta H_f}{\Delta H_0} \qquad \text{Equation 3.11}$$

Where ΔH_0 is the melting enthalpy of polyethylene and polypropylene, 293[142] and 209 $J.g^{-1}$, respectively[143,144].

3.1.9 Thermogravimetric analysis

3.1.9.1 General introduction to thermogravimetric analysis

Thermogravimetric analysis (TGA) is used to measure change in the weight of a material as a function of temperature, or time whilst being subjected to a constant temperature. These measurements provide basic information about the thermal stability of a material and its composition. TGA has been used to characterise both inorganic and organic materials including polymers. The TGA operates on a thermal null balance principle, similar to that of a DSC. A pair of photodiodes is used to register the displacement of a balance beam. A low thermal resistance platinum-wound micro-furnace heats the material while a sensitive balance monitors loss or gain in weight. The micro-furnace functions both as a heater and resistance thermometer. The temperature of the material is monitored by a thermocouple placed near the material chamber. The gases used to purge a material before or after analysis are usually N_2 or air atmospheres.

3.1.9.2 Thermal stability property

Thermal stability behaviour was measured using a Perkin-Elmer TGA Series 7. Materials weighing 1 to 7 mg were placed in an open platinum pan. Analysis was performed from 30 to 700 or 800 °C at a heating rate of 20 $°C.min^{-1}$. A N_2 purge through the material chamber was implemented to obtain a stable thermal environment at 800 °C, followed by a gas change to dry air for the remainder of the heating scan. The same heating parameters were repeated under air. The onset of degradation temperature, $T_{d\ onset}$, maximum degradation rate temperatures, T_d and maximum rate of weight loss under N_2 (thermal degradation) and/or air (thermal oxidation) atmospheres were determined. The T_d was found from the peak maxima in the derivative weight loss curve (DTG curve).

3.1.10 Mechanical testing

3.1.10.1 General introduction to tensile testing

Tensile testing is a technique used to measure material deformation in response to a controlled strain or stress. A typical stress-strain curve shown in Figure 3.3 is obtained by continuously measuring the force developed as the material elongates at a constant rate of extension until it breaks. Tensile stress, σ is defined as (Equation 3.12)

$$\sigma = \frac{F}{A} \qquad \text{Equation 3.12}$$

Where F is the applied force (N) and A is the cross-section area of the material (m^2). The initial slope is the modulus of elasticity or shear modulus, G, which is a measure of stiffness of material. G is the ratio within the elastic region of the stress-strain curve as represented in Equation 3.13.

$$G = \frac{\sigma}{\varepsilon} \qquad \text{Equation 3.13}$$

Where G is the shear modulus in (Pa), σ is the stress ($N.m^2$) and ε is the strain (dimensionless)

The yield stress is when the materials cross-sectional area begins to decrease (neck-down) and is a measure of the strength of the material and its resistance to permanent deformation. The total area under the stress-strain curve is a measure of the energy and/or toughness required to cause failure in a material. The ultimate strength, which is the strain or stress at the breaking point, measures the force needed to fracture the material completely.

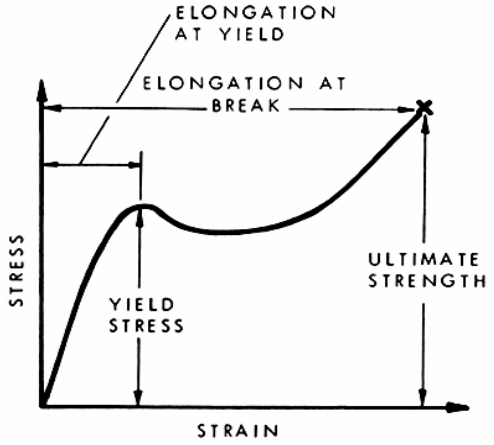

Figure 3.3 General tensile stress-strain curve for polymeric materials[145]

3.1.10.2 Tensile property

Tensile properties of materials were measured using an Instron Universal testing Instrument, model 4465 (Instron Corporation, Series IX Automated Materials Testing System, Australia) with a 5 kN load attached. Instron software (Instron software Version 1.0, 1999) was used to control and record measurements. Test materials were cut from hot pressed films into rectangular test bars according to ASTM D412-98a. Each material was placed under a strain rate of 18 $mm.min^{-1}$ at ambient temperature. Five measurements were recorded for each sample with rejection of measurements from samples that unexpectedly slipped or fractured outside the gauge length region. Average values for the shear modulus, G and yield strength were determined and 95% confidence interval was calculated according to Equation 3.14.

$$\mu = \bar{x} \pm \frac{t_{(n-1)}S}{\sqrt{N}} \qquad \text{Equation 3.14}$$

Where μ is the population mean, $\bar{x}$ is the material mean, N is the number of replicate measurements, $t_{(n-1)}$ represents the statistical parameter determined by the degrees of freedom and s is the material (replicate measurement) standard deviation.

Mechanical measurements were additionally subjected to analysis of variance (ANOVA) performed using statistical software, MINITAB, release 14 Statistical Software 1972-2003 MINITAB Inc.

3.1.11 Dynamic mechanical analysis

3.1.11.1 General introduction to dynamic mechanical analysis

Dynamic mechanical analysis (DMA) is a thermal and mechanical analysis technique in which the viscoelastic properties of a material are measured as a function of temperature, time or frequency. A sinusoidal oscillating stress is applied to a material by a precision motor. A force transducer measures the response stress in the material (flexural, tensile or rotational), which is in the form of a sinusoidal strain response. The response measured is reproducible if the material is within its linear viscoelastic region, meaning the deformation can be fully recovered on removal of the applied force (stress). The applied stress, σ, is described by Equation 3.15[145] as:

$$\sigma = \sigma_0 \sin wt \qquad \text{Equation 3.15}$$

Where t is time, σ_0 is the maximum stress at the peak of sine curve and ω is frequency of oscillation. The viscoelastic properties of a material determine the shape of the strain wave. If a material behaves elastically with the applied stress, it will respond like a Hookean ideal spring. The elastic component of the strain curve can be described as

$$\varepsilon(t) = E\sigma_0 \sin(wt) \qquad \text{Equation 3.16}$$

Where ε(t) is strain, E is modulus. Since σ and ε are linearly related to E in the linear region, Equation 3.16[145] can be rewritten as

$$\varepsilon(t) = \varepsilon\sigma_0 \sin(wt) \qquad \text{Equation 3.17}$$

Where ε_0 is the strain at maximum stress. Equation 3.17[145] illustrated in Figure 3.4a shows an in-phase part of the curve. This curve has no lag between the stress and strain curves along the time axis. If a material behaves viscoelastically with the applied stress, the strain response can be described as

$$\varepsilon(t) = \eta\omega\sigma_0 \cos(\omega t) \text{ or } \varepsilon(t) = \eta\omega\sigma_0 \sin(\omega t + \frac{\pi}{2}) \qquad \text{Equation 3.18}$$

Where η is viscosity. Equation 3.18 [145] can be rewritten as

$$\varepsilon(t) = \omega\varepsilon_0 \cos(\omega t) \text{ or } \varepsilon(t) = \varepsilon_0 \sin(\omega t + \frac{\pi}{2}) \qquad \text{Equation 3.19}$$

Since a viscoelastic material dissipates part of the deformation through damping usually as heat, the strain response (Equation 3.19), is delayed or lags behind the applied stress. Therefore a viscoelastic material is out-of-phase with the applied stress as shown in Figure 3.4b. The distance between the peaks of the stress and strain curves along the time axis is known as phase lag. The phase lag is given as an angle, δ due to the trigonometric nature of the curves. Most materials have a strain response that lies between the elastic and viscoelastic extremes. This model can be described as

$$\varepsilon(t) = \varepsilon_0 \sin(\omega t + \delta) \qquad \text{Equation 3.20}$$

Where ω is frequency of oscillation, t is the time and δ is the phase angle. Using trigonometry the model described by Equation 3.19[145] can be re-written as

$$\varepsilon(t) = \varepsilon_0 [\sin(\omega t)\cos\delta + \cos(\omega t \sin\delta)] \qquad \text{Equation 3 21}$$

The strain response described by Equation 3.16[145] is illustrated in Figure 3.4c.

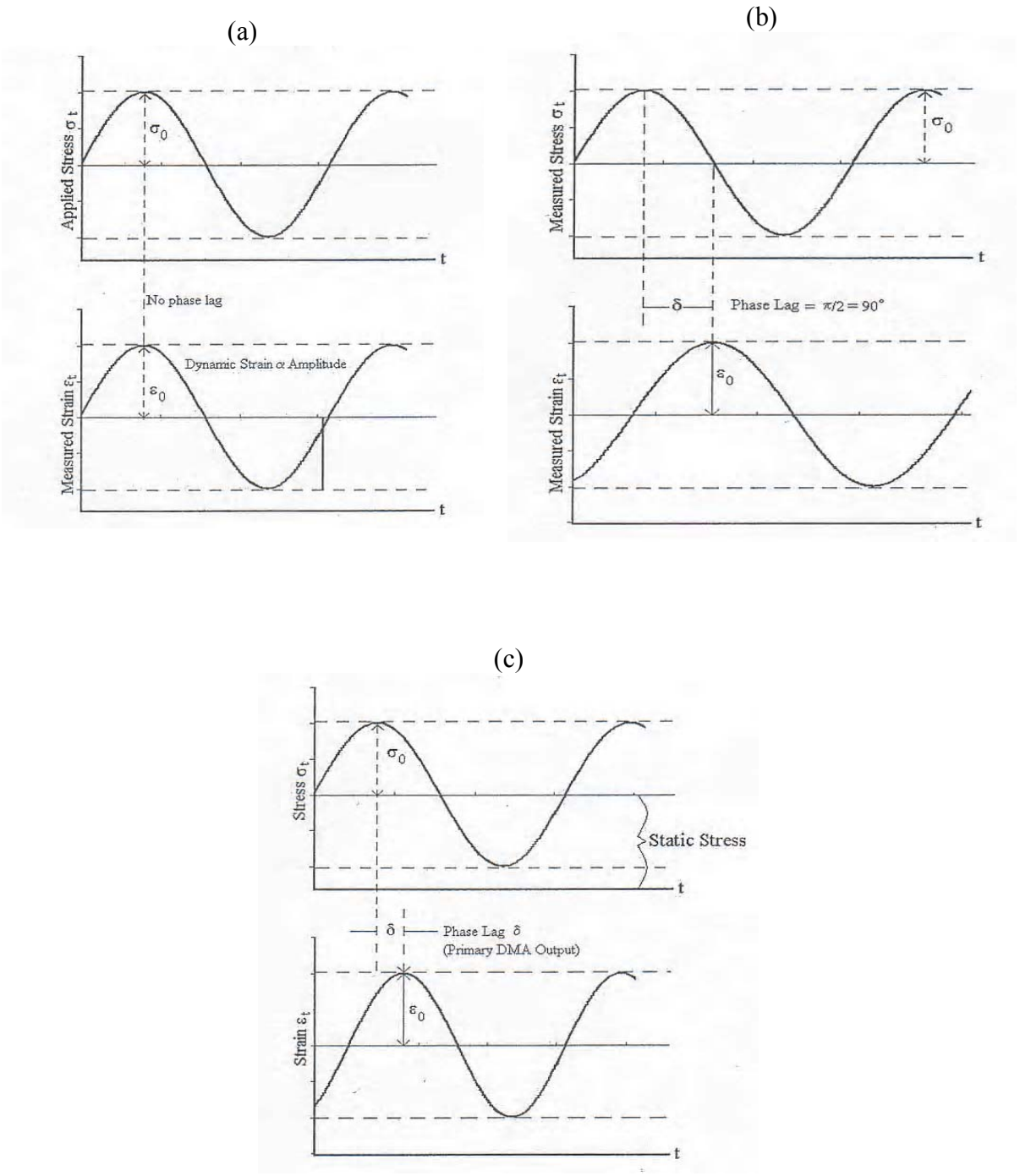

Figure 3.4 (a) In-phase (elastic) δ=0 (b) Out-of-phase (viscous) δ=90° materials strain response to applied stress (c) material between the viscous and elastic extremes[145]

The viscous and elastic component of the material can be described as the in-phase, ε' and out-of-phase, ε″, components respectively and is denoted by

$$\varepsilon' = \varepsilon_0 \sin(\delta) \qquad \text{Equation 3.22}$$

$$\varepsilon'' = \varepsilon_0 \cos(\delta) \qquad \text{Equation 3.23}$$

The vector sum of ε′ and ε″ component results in a complex modulus, ε*, and can be written as[145]

$$\varepsilon^* = \varepsilon' + i\varepsilon'' \qquad \text{Equation 3.24}$$

Where i is the complex number. E* is resolved into two components that describe material behaviour, a real component, whereby the energy is stored and is totally recoverable is denoted as E′ and an imaginary component, whereby the energy is non-recoverable and lost as heat. The relationship between these components is shown in Figure 3.5.

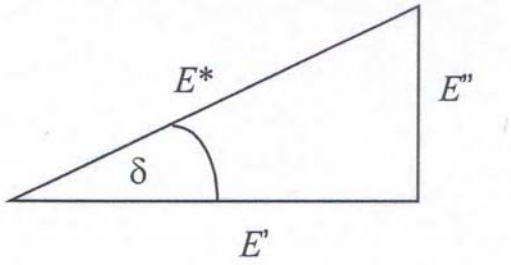

Figure 3.5 The relationship between the phase angle, E*, E′ and E″[145]

E′ elastic (in-phase) modulus is used to measure the elasticity and E″ viscous (out-of-phase) modulus is used to measure the viscoelasticity of a material. As mentioned previously, when the stress and strain curves are compared there is a phase lag δ. The loss tangent, Tan(δ), is the damping factor and is the ratio of E′ and E″ and can be written as[146,147].

$$Tan(\delta) = \frac{E''}{E'} \qquad \text{Equation 3.25}$$

3.1.11.2 Thermo-mechanical property

Thermo-mechanical properties of prepared materials were measured using a Perkin-Elmer DMA7e using Pyris software version 3.81. The instrument was calibrated using indium and zinc standards. The film specimens (3x1.5x1.0 mm) were tested in either extension (tensile) or three-point bending (flexural) mode. Measurements obtained from extension and three-point bending modes were recorded and analysed to determine the thermo-mechanical properties of a material.

E' was used to asses the elastic behaviour of a material. Either the E″ or Tan(δ) peak maxima of their curves can be used to determine the T_g of a material.

Extension mode was performed in the temperature range of –50 to 50 °C at a heating rate of 5 °C.min^{-1} under N_2 gas with a flow rate of 50 mL.min^{-1}. The dynamic and static forces used were 500 and 550 mN, respectively.

Three-point bending mode was performed in the temperature range of –40 to 140 °C at a heating rate of 3 °C.min^{-1} under N_2 gas with a flow rate of 40 mL.min^{-1}. Dynamic and static forces used were 1000 and 2000 mN, respectively.

In addition, parallel plate (compression) mode was used to estimate the thermal expansion, TE of graphite. Temperature range scans performed was 25 to 300 °C at a heating rate of 3 °C.min^{-1} under N_2 gas with a flow rate of 40 mL.min^{-1}.

3.1.12 Dielectric analysis

3.1.12.1 General introduction to dielectric analysis

Dielectric analysis (DEA) or dielectrometry is a characterization technique that provides quantitative thermal and dielectrical information on a wide range of materials such as thermoplastics, elastomers, composites, adhesives and coatings, in various physical states including solids, liquids, pastes and films.

DEA examines the mobility of charged sites in materials. These charge sites are typically ions and dipoles such that the relaxation processes in materials that result from the dipole moments. The mobility of ions and dipoles are measured by applying a sinusoidal voltage (electric field) to the material and measuring the current. The electric field is applied to one electrode, which produces a polarization within the material. This causes a change in amplitude of oscillation, measured in dB and phase lag, δ, measured in degrees (Figure 3.6). amplitude and phase lag are measured by comparing the applied voltage to the measured current at the response electrode[148]. The ions and dipoles in the material will attempt to orient with the applied electric field, while charged ions, usually present as impurities, will move toward the electrode of opposite polarity.

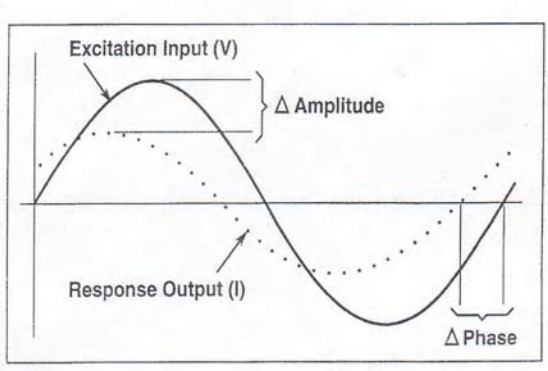

Figure 3.6 Dielectric Excitation and Response[148]

Changes in the degree of alignment of dipoles and ion mobility provide information on the process behaviour, physical and chemical structure of the material being analysed. The measured current can be resolved into two fundamental dielectric characteristics: capacitance and conductance. From these characteristics, dielectric properties can be determined as a function of time, temperature, and frequency.

Capacitance is the ability of a material to store an electrical charge. It is proportional to permittivity (dielectric constant), ε', which is a measure of the energy stored in a material during electric excitation. The energy stored is usually in the form of a non-uniform dipole distribution or ionic charge layers.

Conductance is the ability of a material to transfer electric charge. Conductance is proportional to loss factor, ε" and is the energy absorbed and lost in moving trace ions and depends upon ion mobility that is known as the bulk ionic conductivity, σ[148,149].

The lost energy is due to the viscous drag or moving dipoles and ions within the material. Therefore it is used to characterize molecular relaxations and identify rheological transformations.

Two variables that are critical in the measurement of dielectric properties are A/D ratio and capacitance. The A/D ratio is the ratio of the electrode area, A to the distance, D between electrodes. The A/D ratio and geometry of plate (Figure 3.7) are determining factors in the sensitivity of a measurement. The A/D ratio is used directly to determine ε'.

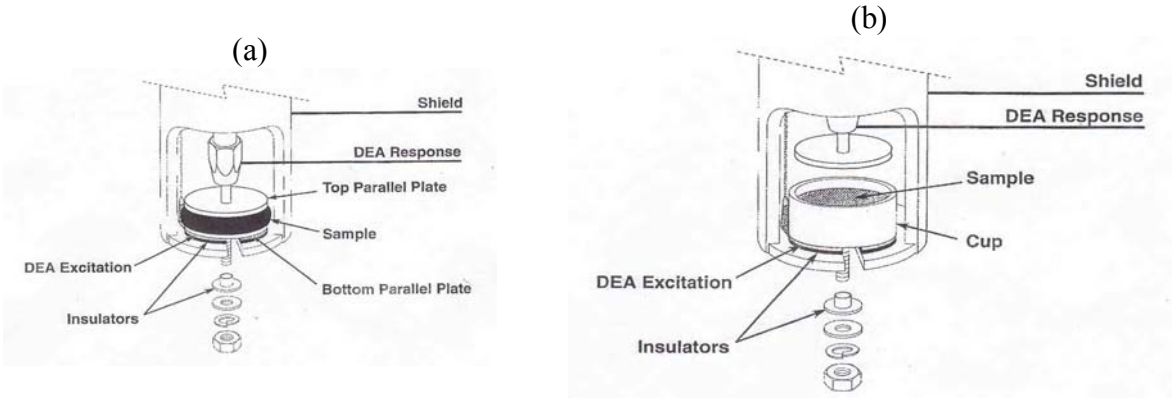

Figure 3.7 Two type of DEA plate geometry for material measurement (a) parallel plate measuring system for elastomers and thermoplastics and (b) cup and plate measuring system for flowing materials such as neat resins and curing liquids[148]

Another factor is base capacitance, which is the stray capacitance in the electrode configuration. This is used to accurately measure ε' and is determined experimentally. For any given experimental apparatus, the software used can automatically subtract the base capacitance in picoFaraday from the measured capacitance in order to obtain the capacitance of the analysed material and this calculation is used to determine ε'[149].

3.1.12.2 Dielectric property

Dielectric properties such as ε' and ε" of materials were measured using a Eumetric system III Microdielectrometer Dielectric Analyser with a mid-conductivity interface in conjunction with a Perkin-Elmer DMA 7e Dynamic Mechanical Analyser. Materials were heated from 25 to 200 °C at a heating rate of 5 °C.min^{-1} using parallel plate test mode (Figure 3.8a). All tests were performed under N_2 gas with a flow rate of 50 mL.min^{-1}.

3.1.13 Electrical conductivity test

Conductivity tests were performed on materials by applying metallic contacts to their surfaces. This was achieved by applying, conductive silver paint to increase and determine the area of electrical conductivity. Figure 3.8 shows a schematic representation of the metallic contacts applied to materials.

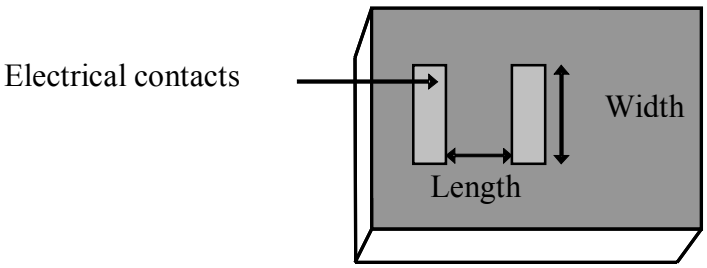

Figure 3.8 Film material with conductive silver paint as electrical contacts

Electrical conductivity, σ_c, and electrical resistance, R, of films was measured at room temperature using a digital multimeter (Keithley 2700 Multimeter Data Acquisition S) with a resistance measuring capability of up to 107 Ω̃ The σ_c of materials was determined using Equation 3.26

$$\sigma_c = \frac{l}{A.R} \qquad \text{Equation 3.26}$$

Where l is the distance between the metallic contacts (cm), A is area of the conductive path defined as the width of the metallic contacts multiplied by the thickness of the film and R is the resistance value measured. When the resistance of a material was higher than the measuring capabilities of the digital multi-meter the following circuit was used to determine its value (Figure 3.9).

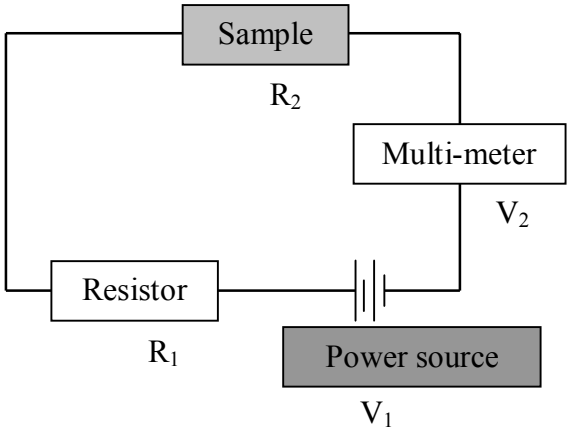

Figure 3.9 Schematic diagram of the electrical conductivity measurement

In this circuit, the power source applies a voltage, V_2 that initially passes through a resistor, R_s with a resistance value of 10 MΩ. It is assumed that the current drop at this resistor is

negligible compared with the drop at the material due to $R_s >> R_l$. The current after R_s, or, I_2, is determined by Equation 3.26. When the current passes through the material, the following approximation $I_2 \sim I_S$ can be measured. Measuring the voltage after it has passed through the material denoted as V_s, and using the value of the current obtained from Equation 3.27, the resistance of the material is calculated using Equation 3.28.

$$I_2 = \frac{V_2}{R_1} \qquad \text{Equation 3.27}$$

$$R_s = \frac{V_s}{I_s} \qquad \text{Equation 3.28}$$

3.1.14 Mixing tool for preparation of polymer layered graphite oxide composite

Graphite oxide was dispersed in the desired polymer matrix on a laboratory scale using two mixing tools: an Ultra-Turrax disperser and Haake Rheochord. Polymer layered graphite oxide composites were prepared using an Ultra-Turrax (IKA Works Asia Sdn Bhd) disperser, as shown in Figure 3.10a. The Ultra-Turrax is a simple device that consists of a speed controller and in-line generator. The in-line generator has a set of rotor blades and stator teeth rows. The maximum shear rate capability of the disperser is 12000 rpm. The generator was immersed in the dissolved matrix polymer to prepare layered graphite oxide composites. Graphite oxide filler was then added in different weight fractions to the polymer solution and dispersion conducted for 10 to 15 min. The gaps between the rotor and stator allowed for uniform dispersion and maximum shearing. When mixing was completed, the polymer layered graphite oxide mixtures were precipitated with an appropriate solvent, filtered, and dried in a vacuum oven. The dried polymer graphite oxide mixture was then melt pressed into films.

(a) (b)

Figure 3.10 (a) Ultra-Turrax disperser and (b) Haake Rheochord

Polymer graphite oxide mixture was prepared via melt blending using a Haake Rheochord. The polymer matrix was introduced into the kneader and kneaded at a screw speed of 60 rpm. Barrel temperatures for Zones 1 to 3 were held constant at 200 °C until the premix was completely fed into the kneader. Graphite oxide filler was then added in different weight fractions to the melted polymer matrix. The mixture was further mixed for 20 min to obtain a homogeneous melt of the matrix filler formulation. When processing was complete, the mixture was removed from the kneader and cooled to room temperature. The cooled mixtures were then melt pressed into films.

Chapter 4 Intercalation of Brønsted acids in layered graphite

4.1 Introduction

In this chapter, Brønsted acids such as nitric-sulfuric acids and sulfuric acid in combination with oxidising agents and/or reagents such as such as potassium chlorate and acetic acid were used to oxidise graphite flakes. The influence of the various oxidising agents and reagent on the crystalline structure, and thermal properties of graphite oxide and its expanded form has been determined. Graphite under certain conditions can react with strong oxidising agents in aqueous solution, thereby generating oxidised functional groups such as hydroxyl, carbonyl, and carboxylic acid on its surface. The presence of these groups on the graphite surface enhances its physical and thermal properties. For instance, intercalating oxidising agents in graphite may increase the interlayer spacing, resulting in facile intercalations between the graphite and the monomers or polymers. Preparations of graphite oxides were described in this chapter. However, the parameters used to characterise the graphite oxides and its expanded form were described in Chapter 3.

4.2 Experimental

4.2.1 Oxidation of graphite

4.2.1.1 Method 1 Staudenmaier method

Graphite flakes were oxidised by fuming concentrated nitric acid (HNO_3) (69%), sulfuric acid (H_2SO_4) (98%) and powdered potassium chlorate ($KClO_3$). A mixture of HNO_3 (25 mL) and H_2SO_4 (50 mL) in a 300 mL flask was cooled to 5 °C in an ice bath. Graphite flakes and $KClO_3$ (1:2 $g.g^{-1}$) was added into the ice water cooled mixture in small portions while stirring continuously. The $KClO_3$ addition was performed slowly 8 times every hour. The reaction continued was for 42 h. The acid-treated graphite oxide was transferred into 1 L of water and filtered. The neutralized and filtered graphite oxide was further washed with water until the pH of the filtrate was greater than 5. The resulting graphite oxide was dried in a vacuum oven at 100 °C to remove remaining any water[4,67,130,150].

4.2.1.2 Method 2 modified Staudenmaier method

Method 1 was modified whereby the amount of $KClO_3$ used in the reaction was halved. The graphite flakes and $KClO_3$ (2:1 $g.g^{-1}$) were added into the ice water cooled mixture of HNO_3 (69%) (25 mL) and H_2SO_4 (98%) (50 mL). The mixture was stirred continuously to ensure uniform wetting of the graphite layers. The acid-treated graphite oxide was washed, filtered, and dried in the same manner as Method 1.

4.2.1.3 Method 3 sulfuric acid, acetic acid, with potassium permanganate

The graphite flakes (5 g), glacial acetic acid (CH_3COOH) (100 g), H_2SO_4 (98%) (25 g) and potassium permanganate ($KMnO_4$) (3.5 g) was placed in a dry three-necked flask equipped with a thermometer and condenser. The mixture was continuously stirred and reacted for 2 h at 25 °C. It was then washed and filtered with water until the oxidised mixture pH was 7. The oxidised mixture was filtered and dried in a vacuum oven at 100 °C to remove any remaining water[105].

4.2.1.4 Method 4 nitric and sulfuric acid with decanol

The graphite flakes (25 g) were placed in a 100 mL round bottom flask containing a stirred mixture of cooled HNO_3 (69%) (10 mL) and H_2SO_4 (98%). After mixing, decanol ($C_{10}H_{21}OH$) (1 g) was added while continuously stirring. The reaction continued for 2 h. The oxidised graphite was washed with 1 L of water, filtered, and dried in a vacuum oven at 100 °C[151].

4.2.1.5 Exfoliation of graphite oxide

Expanded graphite oxide (EGO) was formed by an exfoliation process. A ceramic crucible that contained approximately 2 g of oxidised graphite was inserted in a pre-heated muffle furnace, held at a constant temperature of 800 °C for 30 s. Some graphite oxide was exfoliated at various temperatures; 200, 250, 270, 380 and 400 °C in the same manner as above.

The abbreviations of the various types of graphite oxides and expanded graphite oxides are listed in Table 4.1. The graphite obtained from Graftech, is abbreviated as GO1, and oxidised graphite using Method 1 is abbreviated as GO2. The exfoliated GO2 is abbreviated as EGO2.

Table 4.1 Abbreviations of various types of graphite oxides and expanded graphite oxides

Method	Graphite Oxide	Expanded Graphite Oxide
Graphite Oxide*	GO1	EGO1
Method 1 (Staudenmaier)	GO2	EGO2
Method 2 (modified Staudenmaier)	GO3	EGO3
Method 3 (H_2SO_4-CH_3COOH-$KMnO_4$)	GO4	EGO4
Method 4 (HNO_3-H_2SO_4-$C_{10}H_{21}OH$)	GO5	EGO5

supplied by Graftech

4.3 Results and Discussion

4.3.1 Structural characteristic of graphite oxide and expanded graphite oxide

Graphite is an allotrope of carbon, the structure of which consists of C-atoms bonded in layers; graphite layers are bound by weak van der Waals forces. These weak interlayer forces allow for certain atoms, molecules and ions such as alkali metals, halogens, metal oxides and acids, to be intercalated into the interlayer spaces of the graphite layers. A structured consequence of intercalation is an increase of the interlayer distance of the graphite layers, as a result of the intercalation of the guest, referred to as intercalates[9,27,130,150,152,153]. Intercalation can be achieved by oxidising graphite with acids. The result is a graphite acid salt due to an intercalation process and it is accompanied by a charge transfer between intercalate and the graphite layer. Oxidation of graphite with acids is commonly referred to as graphite-intercalated compound (GIC) or graphite oxide. The structure of graphite oxide is comprised of graphite layers and intercalated layers stacked along the c-axis in a staggered array. According to Shioyama[79], only a fraction of the interlayer spacing is filled with intercalate, which is called the staging phenomena. The staging phenomenon is the way that intercalates is arranged between the graphite layers, it is this that determines the intercalation stages of the resultant graphite oxide. The stacking can be in the formed of stage 1, 2 or stage n, depending on the intercalation condition.

Each intercalate layer is separated by a definite number of graphite layers, and the stage number n indicates the number of graphite layers between adjacent intercalate layers are sandwiched. In stage graphite oxide, an occupied space that is a graphite layer and intercalate is separated from the next occupied space by n-1 unoccupied spaces as shown in the schematic diagram in Figure 4.1[79,154].

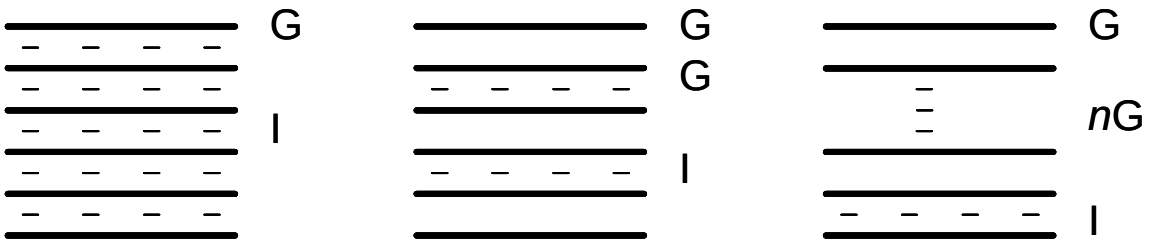

Figure 4.1 Schematic diagram of the stage of GO: solid line, graphite layer: dotted line, intercalated compound

The intercalated acids employed in this study were Brønsted acids: HNO_3 and H_2SO_4, where the acid acts as an electron acceptor to the GO layer forming a negatively charged ion (NO_3^- and $H_SO_4^-$)[79] during the intercalation process. It has been reported that these strong inorganic Bronsted acids form stage 1 GO, with weaker acids[102,154] indicating that all spaces are occupied. The use of HNO_3 and H_2SO_4 as oxidising agents are by far the best characterized, since they are used as starting reagents in the production of cellular graphite[154].

Scanning electron microscope (SEM) was employed to examine the structure of the various oxidised and exfoliated graphite. The graphite oxides were mounted using a conductive carbon tape on the SEM stage and analysed under low vacuum at 0.5 torr with an electron beam power set at 20 kV. The SEM micrographs of these various types of graphite oxides and expanded graphite oxides are displayed in Figures 4.2 and 4.3. In general, the various types of graphite oxide exhibited a typical layered structure. The distance between each graphite layer was estimated using IPLab Spectrum Scientific Image Processing 3.1a (Power Macintosh Signal Analytics 1989-1996). Several measurements were obtained for each type of graphite oxide, with the errors provided taken from the standard deviation of the mean. The GO1 structure as shown in Figure 4.2a consisted of parallel graphite layers stacked in a periodic fashion with a distance of 2.38±0.16 μm. A difference in structure is observed in Figure 4.2c and 4.2e, prepared from a stronger oxidiser, $KClO_3$.

The GO2 (Figure 4.2c) shows slightly collapsed graphite layers with a distance of 7.17±0.21 μm. GO3 prepared from Method 2, shows flakiness of surface and the distance between the graphite layers is difficult to measure, as shown in Figure 4.2e. The GO4 and GO5 structures in Figure 4.3a and 4.3c, were oxidised in the presence of CH_3COOH-$KMnO_4$ and $C_{10}H_{21}OH$ has a distance of 4.86±0.12 μm and 6.77±0.15 μm, respectively.

Exfoliation of graphite oxide at high temperature caused graphite oxide to expand, which is a sudden increase in the dimension perpendicular to the graphite layers of the intercalated graphite oxide. This occurred due to the volatilisation and/or decomposition of intercalates from the edges of the graphite layers having enough pressure to separate the graphite layers causing irreversible expansion of graphite oxide. After exfoliation, an interconnected network structure is formed, often described as a worm-like, accordion bellow and/or honeycomb structure with low density, known as expanded graphite oxide. Kang et al[155] described the structure of expanded graphite oxide by a zig-zag model, where the distance between the pore decreased with increasing exfoliation temperature and expansion volume. Expanded graphite oxide has been reported to exhibit enhanced thermal, mechanical, and electrical properties in comparison with graphite oxide due to its network structure[4]. SEM micrographs of expanded graphite oxide shows that the structure of expanded graphite oxide consists of collapsed and deformed parallel graphite layers, resulting in multi-pores of different sizes ranging from micrometer to nanometer dimension[130]. Additionally, pore shape is approximately ellipsoidal[138,155]. Graphite oxide formed from different oxidising treatments, showed similar results in forming the various types of expanded graphite oxide, however the expansion volume and rates were different. Aronson et al[156] have shown that the mechanism of formation of graphite oxide and expanded graphite oxide could be as thin as a single graphite layer when it is in the form of Stage 1[156].

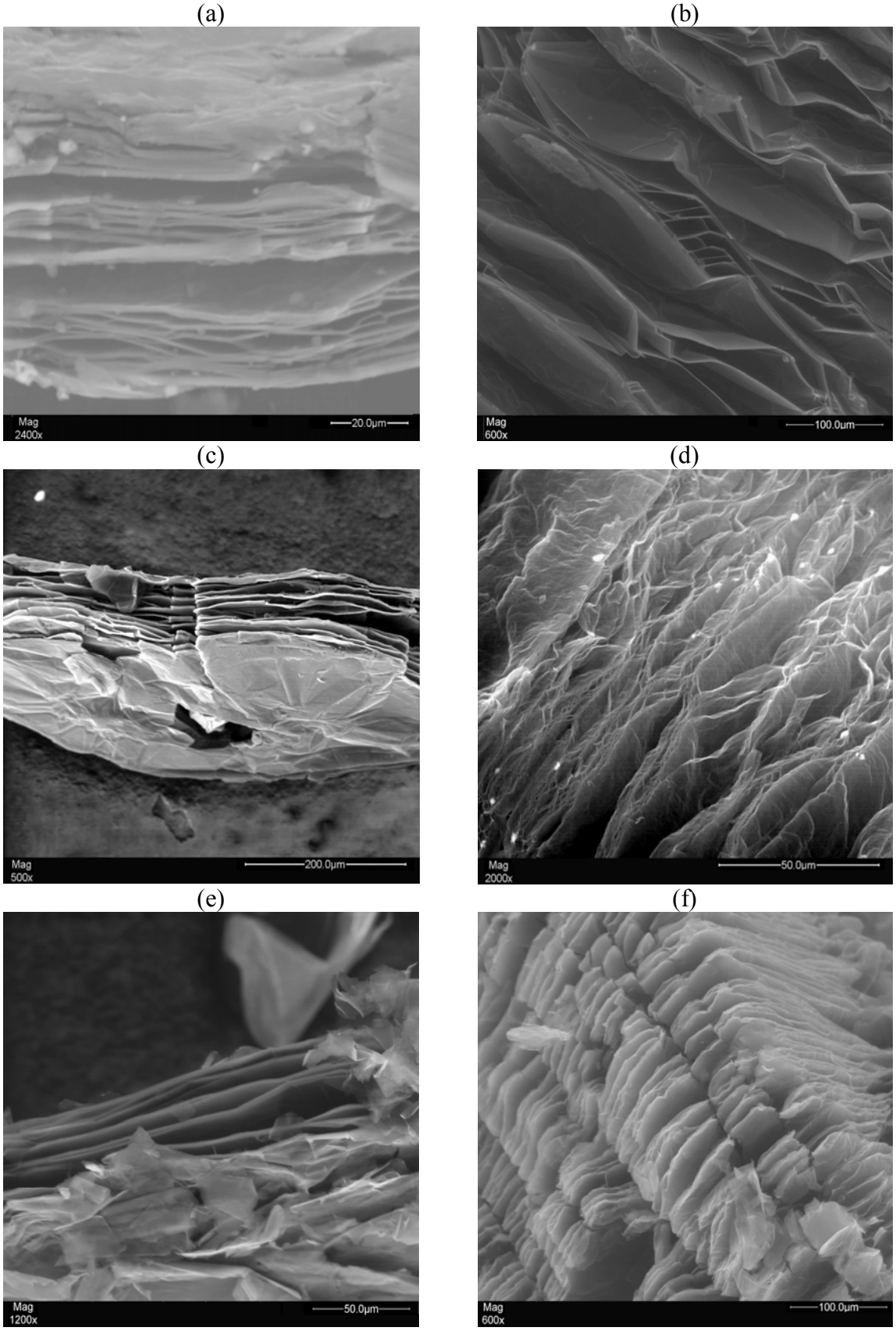

Figure 4.2 SEM micrographs of the structure of various types of graphite oxides and expanded graphite oxides (a) GO1 (b) EGO (c) GO2 (d) EGO2 (e) GO3 (f) EGO3

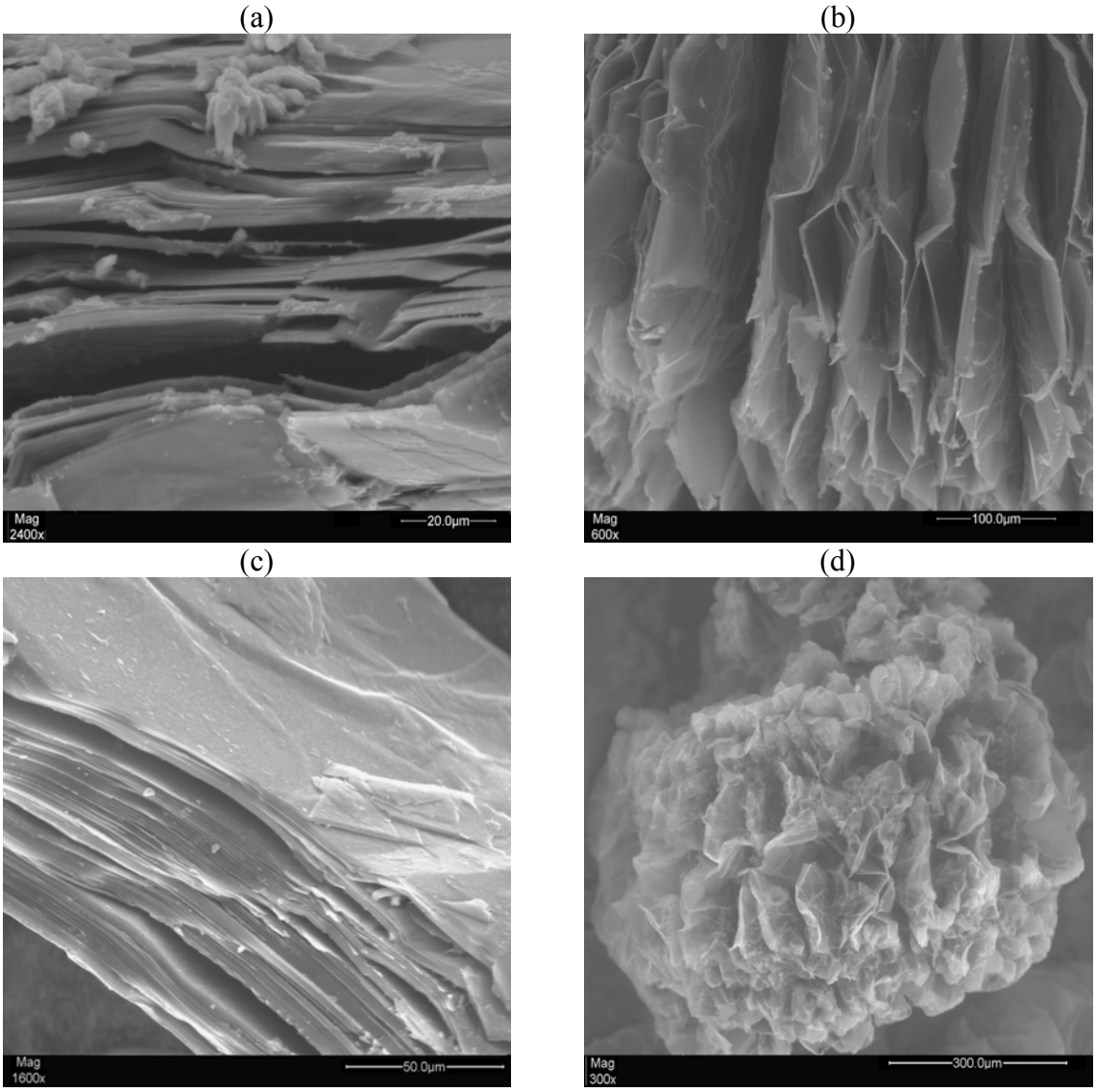

Figure 4.3 SEM micrographs of the structure of various types of graphite oxides and expanded graphite oxides (a) GO4 (b) EGO4 (c) GO5 (d) EGO5

4.3.2 BET surface area property of graphite oxide and expanded graphite oxide

The nitrogen (N_2) adsorption-desorption isotherms of the various types of GO and EGO were performed according to the experimental parameters described in Chapter 3. The isotherms of all GO and EGO can be considered as typical type two isotherms[118]. According to the Brunauer classification, materials with this type of isotherm are typical of materials with large pores[115]. The BET specific surface area, A_s, pore volume and average pore diameter derived from the isotherms were obtained and these are listed in Table 4.2. GO1 has an A_s of 0.87 $m^2.g^{-1}$. The oxidised graphite showed larger A_s in comparison with GO1, with the exception of GO4, which had an A_s of 0.79 $m^2.g^{-1}$.

During the oxidative treatment of graphite, unsaturated carbon bonds in the graphite layers held by weak forces were oxidised. This allowed intercalation of atoms or molecules in the spaces of the graphite layers, and caused the interlayer spacing to increase. As a result, the oxidation process caused development of porosity, mainly micro-pores in these oxidised graphites[157]. This was not the case for GO4, where the low A_s could be attributed to the CH_3COOH, a weak acid, which may not have intercalated in the graphite layers even in the presence of the oxidiser $KMnO_4$. According to Sorokina et al[103] intercalation of graphite with HNO_3-CH_3COOH was unsuccessful due to acid dissociation decreasing the threshold for intercalation. Consequently, even $KMnO_4$ does not intercalate in the graphite layers. Several studies have reported that the oxidiser, in particular $KMnO_4$, has a similar effect to that of electric current during anodic polarization of graphite in H_2SO_4[102]. In the case of GO2 and GO3, it is interesting to note that although both were formed using the Staudenmaier method, the A_s of GO3 is four times larger than GO2. The difference in the amount of $KClO_3$ used played a role in oxidative treatment of graphite thereby affecting the A_s. For GO2 the A_s was slightly larger than GO5 by approximately 0.14 $m^2.g^{-1}$, the diminutive difference was however negligible. The pore volume of oxidised graphite was lower than that of GO1, with the exception of GO3. It is evident that oxidative treatment of graphite affected the average pore diameter. Commonly, the average pore diameter of oxidised graphite was lower than GO1. The lowest average pore diameter was observed for GO2, which was 5.42 nm. From these measurements and the estimated distance obtained from SEM micrographs, these graphite oxides contain pores in the micrometer and nanometer dimensions.

Table 4.2 Surface area properties of various types of graphite oxides

	Graphite Oxide				
	GO1	GO2	GO3	GO4	GO5
BET surface area ($m^2.g^{-1}$)	0.87	0.92	3.25	0.79	1.07
Pore volume (10^{-2} $cc.g^{-1}$)	0.25	0.13	0.62	0.14	0.15
Average pore diameter (nm)	11.58	5.42	7.69	7.29	5.79

From Table 4.3, exfoliating oxidised graphite, at 800 °C produces expanded graphite oxide with larger A_s. The A_s of EGO2 after exfoliation increased to 19.04 $m^2.g^{-1}$, which was 21 times larger than that of the original A_s of GO2.

We assumed that exfoliating oxidised graphite that has a large A_s would produce an expanded graphite oxide with an even larger A_s. This however was not observed. For instance, EGO3 after exfoliation, produced a A_s that was only twice as large as that of the GO3. Therefore, no correlation between the A_s of graphite oxide and expanded graphite oxide was found. The pore volume as well as the average pore diameter is listed in Table 4.3. It is noted that EGO2 has the highest pore volume and lowest average pore diameter compared with the other studied graphite oxides.

Table 4.3 Surface area properties of various types of expanded graphite oxides

	Expanded Graphite Oxide				
	EGO1	EGO2	EGO3	EGO4	EGO5
BET surface area ($m^2.g^{-1}$)	3.89	19.04	6.38	6.08	11.26
Pore volume (10^{-2} cc.g^{-1})	0.75	3.41	1.73	1.23	2.04
Average pore diameter (nm)	7.74	7.16	10.82	8.08	7.26

The surface area properties of the various types of graphite oxide are affected by the oxidative treatment. The BET surface area analysis of the various types of graphite oxide and its expanded form showed that they are porous materials with an average pore diameter in the nanometer dimension.

4.3.3 Fourier Transform Infrared spectroscopy

The aim of using FTIR was to determine the change in surface chemistry after oxidative treatment of graphite and after the exfoliation process. FTIR was used according to the description in Chapter 3. Infrared spectra of oxidised graphite are shown in Figure 4.4a. The graphite prior to oxidation showed no significant features. Small absorption bands present between 568 cm^{-1} and 595 cm^{-1}, were probably due to potassium bromide (KBr).

The spectrum of various types of graphite oxides exhibited hydroxyl and carbonyl groups, as well as carboxyl groups situated mainly at the edges of the graphite layers[158,159]. A broad absorption band between 3000 and 3500 cm^{-1} was observed in most graphite oxides, two maxima at 3430 cm^{-1} and a small shoulder at around 3100 cm^{-1}, however the latter absorption band was absent in the GO3 spectrum. Hontoria-Lucas et al[157] reported that these bands are due to the presence of free and associated hydroxyl groups due to adsorbed and inhibited water and to structural hydroxyl groups on oxidised graphite. These results agree with those reported in the literature[160]. A weak absorption band at 2926 cm^{-1} was observed in GO1 that corresponds to the presence of the stretching vibration of aliphatic C-H bond.

However, this bond was absent in the other graphite oxide spectra, instead two sharp absorption bands at 2853 and 2925 cm^{-1} were observed that correspond to the presence of C-OH bonds.

The presence of C-OH bonds indicates that further oxidation leads to the formation of additional carboxyl and hydroxyl bonds. The spectrum of GO3 shows an absorption band at approximately 2425 cm^{-1}, which could be due to hydrogen bonded carboxylic acid. A sharp but weak absorption band located at 1570 and 1690 cm^{-1} was observed in all the graphite oxide spectra. GO1 have an absorption band at 1685 cm^{-1}, which had been assigned as C=O stretching vibration of carbonyl and carboxyl bonds, however this band is absent in the other graphite oxides. Consequently, at lower wavelength, 1640 cm^{-1}, the stretching vibrations of alkenes (C=C) and aromatic (C=C) bonds were observed.

The spectra of GO3, GO4, and GO5 show stretching vibrations of alkenes at 1639, 1640, and 1633 cm^{-1}. For GO2, only the stretching vibrations of alkenes at 1586 cm^{-1} were observed. Furthermore, GO3 showed the presence of aromatic bonds at 1639 cm^{-1}. According to literature[67,157,161] , it has been proposed that hydrated and dehydrated structures can co-exist. Therefore, the presence of O-H and C-O bonds is expected. Several reports have shown that that these bonds were observed in the more oxidised graphite[157]. These bonds were present in GO2, GO3, and even GO4. At 1385 cm^{-1}, a strong and sharp bending vibration was observed that has been assigned to vibrations of O-H. The three sharp bands between the region 1110 and 1225 cm^{-1} have been assigned to C-O bonds. These bands were present in GO4, however the C-O-H bond has a lower intensity, and its C-O bond was broader. Peckett et al[159] reported the presence of aliphatic C-H bonds in electrochemically-oxidised graphite. In our findings, the aromatic C-H bonds were present in some of the graphite oxide spectrum: GO1 and GO5.

The FTIR spectra of expanded graphite oxide, after exfoliation of graphite oxide at high temperatures are measured and shown in Figure 4.4b. Many studies have reported that exfoliation of graphite oxide leads to the formation of even more acidic groups, carboxylic acids and hydroxyl bonds[130], which caused the surface of the graphite to be polarized. All expanded graphite oxide exhibited similar absorption bands between 3300 and 3420 cm^{-1}, and 1000 and 1295 cm^{-1}. These absorption bands correspond to a strong O-H stretching vibration and the latter is due to C-O bonds, respectively. The absorption bands located at 1610 and 1640 cm^{-1} were observed in most of the expanded graphite oxides except for EGO1. These absorption bands have been assigned to the stretching vibration of aromatics.

Additionally, sharp aromatic C-H absorption bands were observed in the region between 700 and 900 cm^{-1}, however these were not present in the EGO3. Although the presence of C=C (alkenes, aromatic) and C-H (aromatic) groups were observed in the spectra of all graphite oxides and their expanded form.

The FTIR spectra of various types of graphite oxides and expanded graphite oxides confirm the formation of carbonyl, hydroxyl, and carboxyl groups. This evidence indicates that during oxidative treatment, inorganic acids oxidised unsaturated carbon bonds, leading to the presence of carbonyl, hydroxyl, and carboxylic acid functional groups on the graphite oxide surface. The expanded graphite oxide showed a polarized surface that could be attributed to the exfoliation process and/or already oxidised functional groups exposed.

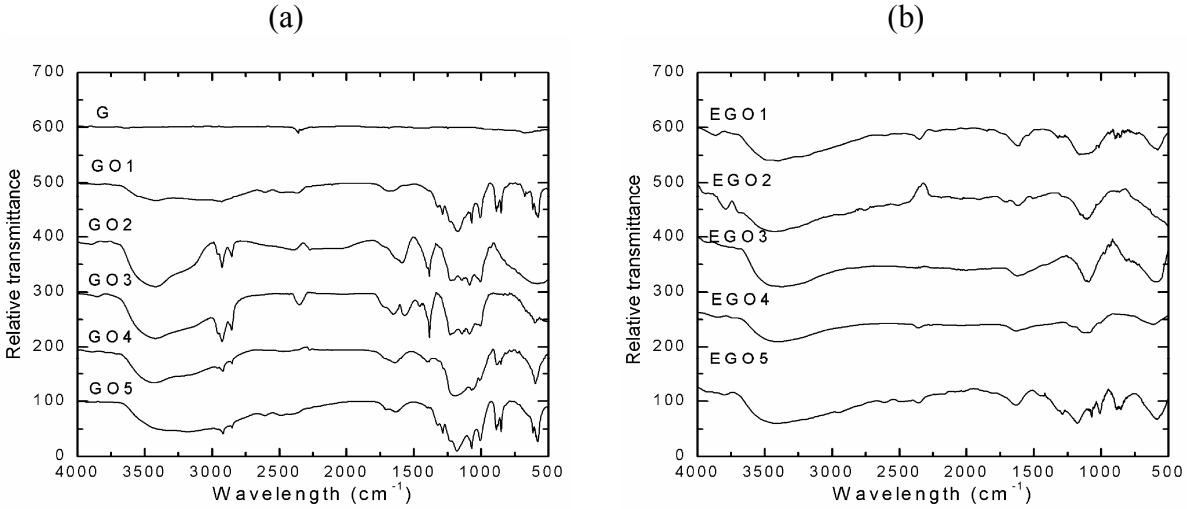

Figure 4.4 FTIR spectra of (a) graphite and various types of graphite oxides and (b) expanded graphite oxides

4.3.4 Crystalline structure of graphite oxide and expanded graphite oxide

Wide-angle X-ray diffraction (WAXD) was used to determine the influence of intercalation of Brønsted acids and other reagents on the order of the graphite layers by changes in the shape of the interlayer or *d* spacing reflections. The change in the *d* spacing of graphite layers was calculated by applying the Bragg equation. The WAXD measurements were obtained according to the experimental parameters given in Chapter 3.

The diffractograms of the various types of graphite oxides and expanded graphite oxides are exhibited in Figures 4.5, 4.6 and Table 4.4 lists the diffraction (001) and (002) planes *d* spacing calculated using the Bragg equation. The diffraction (001) and (002) planes corresponds to graphite oxide and graphite peaks[162,163].

The diffractogram of GO1 shows three peaks in 2θ=20 to 30°. The sharp diffraction peak at 2θ=26° indicates a high degree of order of GO1, thereby the graphite layers maintains their order and multi-layer structure. This peak corresponds to the (002) peak and has a *d* spacing of 0.335 nm. The *d* spacing observed in GO1 is consistent with that reported in the literature[132,159,164]. The GO2 oxidised using $KClO_3$ showed a change in its diffractogram. The peaks between the 2θ=20 and 30° was deresolved to a single broad peak at 2θ=26° with a *d* spacing of 0.347 nm, after oxidative treatment. The high *d* spacing can be explained by the formation of a stage 1 bi-intercalation compound of H_2SO_4 and HNO_3, whereby H_2SO_4 was substituted by HNO_3 in every other graphite layer. This finding agrees with that of obtained by Nakajima et al[67]. The GO2 diffractogram, a small and broad peak at approximately 2θ=12° was observed that corresponds to the (001) peak and has a *d* spacing of 0.755 nm. The formation of the (001) peak was due to the addition of $KClO_3$. It has been found that GO formed via stage 1 when prepared by the Staudenmaier method[67]. GO3 exhibited a similar diffractogram to that of GO2, with the exception of a marginal shift in the 2θ of the (001) and (002) peaks. The shift in the lower 2θ indicates that intercalation of the acids and reagents occurred in the graphite layers. This caused the *d* spacings of the (001) and (002) peaks to increase to 0.348 nm and 0.794 nm, respectively. The increase in *d* spacing is due to the bi-intercalation of H_2SO_4 and HNO_3 in the graphite layers. It is noted that a small peak at 2θ=29° with a *d* spacing of 0.310 nm was observed. The presence of this small peak suggests that some unsaturated carbons were unoxidised due to the small amount of $KClO_3$ and/or some $KClO_3$ that may not have been completely washed off with water[67].

The diffractograms of GO4 and GO5 resemble that of GO1, whereby the same numbers of peaks were observed in the 2θ=20 to 30° that corresponds to the (002) peak. As shown in Table 4.4, the (001) peak was not detected and no change in the *d* spacing of the (002) peak is observed for both GO4 and GO5. Therefore it was assumed that intercalation of acids and reagents may not have occurred in the graphite layers. Chen et al[105] reported the use of CH_3COOH as an intercalating agent.

They showed that graphite oxide acetic acid (GOA) types six stages and that the distance of two successive intercalated layers is 2.490 nm. The results obtained did not reflect the same findings.

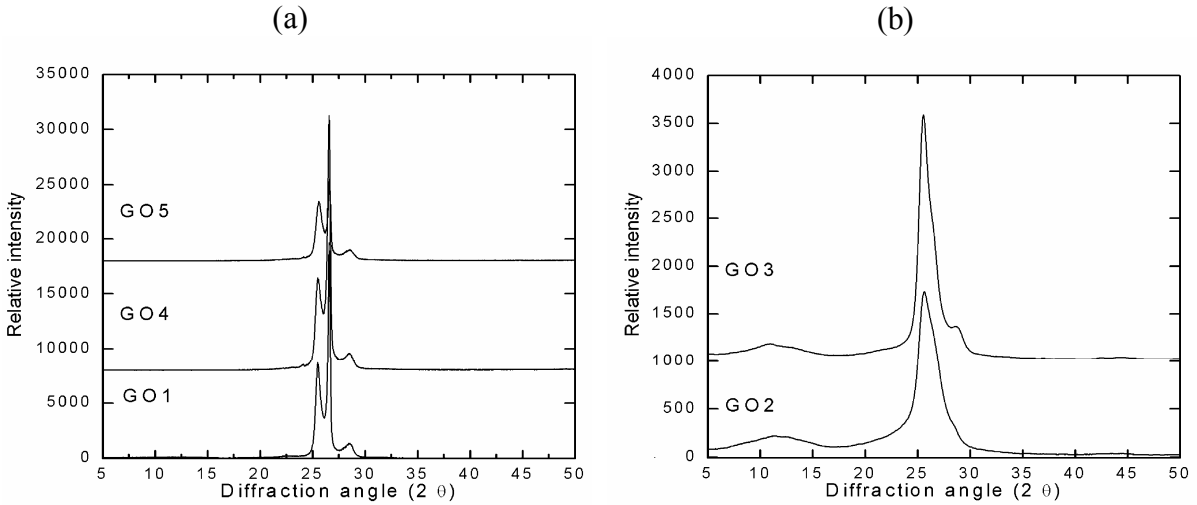

Figure 4.5 Diffractogram of various types of graphite oxides (a) GO1, GO4 and GO5 and (b) GO2 and GO3

The diffractograms of the various types of expanded graphite oxides are presented in Figure 4.6a and b. EGO1 exhibits a sharp (002) peak at approximately 2θ=26° with a *d* spacing of 0.344 nm, however a small and broad the (001) peak at 2θ=13° was observed. The presence of the (001) peak suggests that a maximum degree of expansion of GO1 may not have occurred. This was not the case for EGO2 and EGO3. The absence of the (001) peak and the increase in the *d* spacing of the (002) peak suggests a maximum degree of expansion. EGO4 exhibited a similar diffractogram to that of EGO2 and EGO3, however no change occurred in the *d* spacing of the (002) peak. Interestingly, the diffractogram of EGO5 after exfoliation resembled that of GO5, with no changes observed in the *d* spacing of the graphite layers. From the results, it is evident that *d* spacing of the various types of graphite oxides and expanded graphite oxides prepared depended on the methods of synthesis, moisture, and other factors[67].

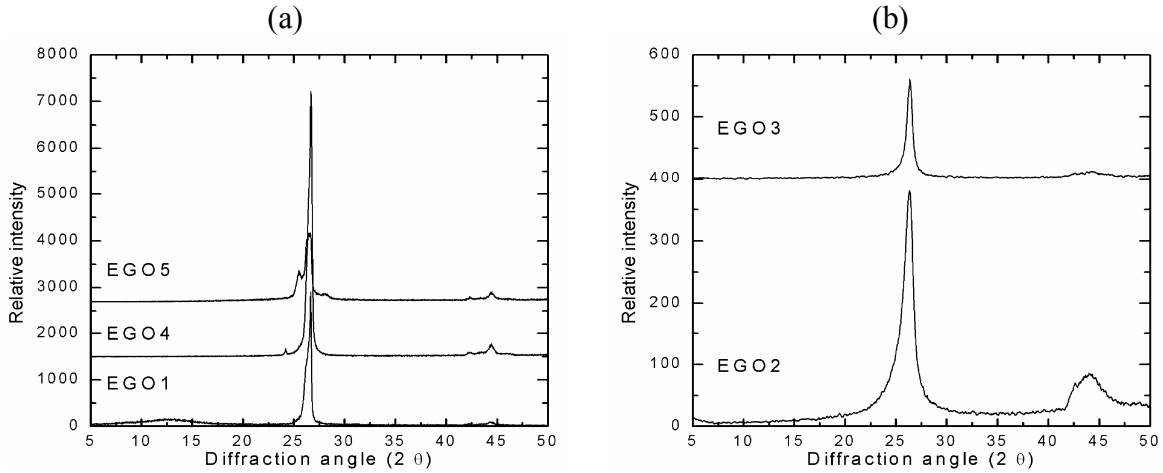

Figure 4.6 Diffractogram of various types of graphite oxides after exfoliation (a) EGO1, EGO4 and EGO5 and (b) EGO2 and EGO3

Table 4.4 WAXD measurements for various types of graphite oxides and expanded graphite oxides

Graphite Oxide	*d* spacing (nm)		$L_{(hkl)}$ (nm)	Expanded Graphite Oxide	*d* spacing (nm)		$L_{(hkl)}$ (nm)
	(001) peak	(002) peak	$L_{(002)}$		(001) peak	(002) peak	$L_{(002)}$
GO1	0.754	0.335	29.725	EGO1	0.697	0.334	19.318
GO2	0.755	0.347	3.653	EGO2	-	0.339	6.554
GO3	0.794	0.348	9.680	EGO3	-	0.337	12.080
GO4	-	0.335	24.151	EGO4	-	0.335	16.797
GO5	-	0.335	22.729	EGO5	-	0.335	10.736

-no diffraction peak was observed

In order to make a comparison with the crystalline structures of the various types of graphite oxides and its expanded form, the crystalline thickness has been obtained by applying the Scherrer equation. Since the (002) peak is of interest, the crystalline parameter $L_{(002)}$ was taken for detailed analysis using the Scherrer equation, which was defined in Chapter 3. Prior to using the Scherrer equation, the (002) peak for all graphite oxides and expanded graphite oxides were subjected to curve fitting. Lorentz curve fitting was performed using Origin data analysis and technical graphics software (Version 6; Microcal Software Inc). The Lorentz curve fitting was used as it resembles that of the shape of the diffractogram curves.

Figure 4.7, shows an example of Lorentz fitted curves for the diffractogram of GO1, the dash line represents the curves fitted for $L_{(002)}$. Figure 4.7, shows an example of Lorentz fitted curves for the diffractogram of GO1, the dash line represents the curves fitted for $L_{(002)}$.

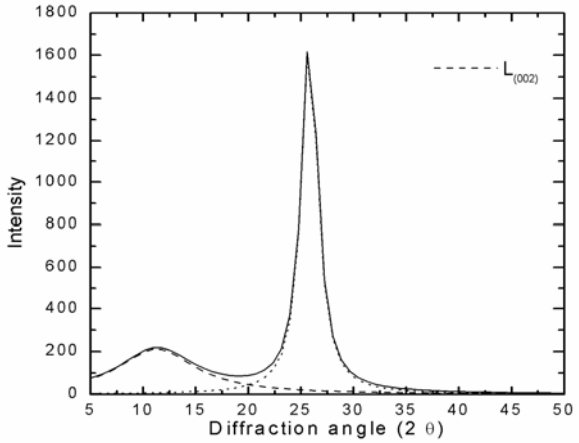

Figure 4.7 Lorentz fitted curves of diffractogram of GO2

GO1 had the highest $L_{(002)}$ (29.725 nm). In general, oxidative treatment decreased $L_{(002)}$. The oxidised graphites using the Staudenmaier method, GO2 and GO3 showed the lowest $L_{(002)}$.. The GO4 and GO5 showed a $L_{(002)}$ of 24.152 and 22.729 nm, respectively. Therefore, it seems that oxidation disrupted the crystallites[157]. It is evident from Table 4.4 that the transformation of some of the graphite oxide into expanded graphite oxide caused variation in $L_{(002)}$. $L_{(002)}$ of exfoliated oxidised graphite was determined in the same manner, prior to the exfoliation process. For GO1 after exfoliation, $L_{(002)}$ decreased to 19.318 nm. The decrease in $L_{(002)}$ was observed for EGO4 and EGO5. Conversely, this was not exhibited for EGO2 and EGO3. $L_{(002)}$ of EGO2 increased to 6.554 nm, twice the size of GO2. For EGO3, its $L_{(002)}$ increased by approximately 2.400 nm. The results obtained for $L_{(002)}$ confirm the BET surface area findings that graphite oxide and expanded graphite oxide are of nanoscale dimensions. $L_{(002)}$ of oxidised and exfoliated graphite has been reported by Hontorio-Lucas et al[165] and Chen et al[118] using the Scherrer equation. They reported that $L_{(002)}$ of graphite oxide and its expanded counterpart was approximately 15 nm.

4.3.5 Thermal decomposition of graphite oxide

Thermal decomposition behaviour of various types of graphite oxide in N_2 and air atmospheres is presented in weight loss (TGA) and derivative weight loss curves (DTG) curves in Figures 4.8 and 4.9, respectively.

The maximum rate of weight loss and its corresponding temperatures determined from the maximum peaks of DTG curves are listed in Table 4.5 and 4.6. The main maximum peaks observed from DTG curve, were assigned as decomposition stages for graphite oxide. SEM micrographs presented previously within this chapter, show that expanded graphite oxide was formed when graphite oxide was exfoliated at high temperatures. Exfoliation caused graphite oxide to expand instantaneously forming a structure similar to that of an accordion bellows. According to Chung et al[108], the mechanism of exfoliation, involves the volatilisation of intercalates. Duquesne et al[93] reported that the expansion of graphite oxide through the evolution of gases does not lead to deformation of the crystalline structure. However, the crystalline structure of graphite oxide after exfoliation deforms above 450 °C. This is because during expansion of graphite oxide there is competition between desorption and exfoliation processes. Desorption is related to the slow evaporation or volatilisation of intercalate that is trapped within the edges of the graphite layers. This process does not lead to the deformation of the crystalline structure of graphite oxide. However, it is the exfoliation process, corresponding to the rapid boiling of intercalates that leads to a loss of the graphite oxide crystallinity. It has been proposed that a redox process between graphite oxide and sulfuric acid (H_2SO_4) occurs, in addition to the volatilisation of intercalates. During the redox process water (H_2O) loss occurs in the graphite layers, while carbon dioxide (CO_2) and sulfur dioxide (SO_2) are evolved, as indicated by equation 4.1[124]. These gases escape through the edges of the graphite layers, causing the graphite layers to separate leading to their irreversible expansion. This redox process therefore leads to the transformation of graphite oxide to expanded graphite oxide.

$$C(s) + H_2SO_4(l) \rightarrow CO_2(g) + 2H_2O(g) + 2SO_2(g) \qquad \text{Equation 4.1}$$

As indicated in the redox process, H_2SO_4 is reduced to SO_2. Duquesne et al[93] reported, utilizing elemental analysis that only part of the H_2SO_4 participates in the expansion of graphite oxide. Exfoliation of graphite layers in graphite oxide occurs randomly.

The decomposition of graphite oxide in both nitrogen and air atmosphere occurs via the redox process above (Equation 4.1) as well as the volatilisation of intercalates. However, the decomposition stages of graphite oxide vary depending on the oxidative treatment utilised such as the type of intercalates and/or conditions.

4.3.6 Thermal decomposition of graphite oxide in nitrogen

The decomposition of GO1 exhibited smooth weight loss curve, showing a small weight loss followed by one main weight loss as indicated in Figure 4.8a. The DTG curve shows a small weight loss below 200 °C that is attributed to the loss of H_2O as well as volatilisation of low molecular weight components. One main weight loss was observed at 277 °C indicating that decomposition of GO1 occurs in one stage. The small weight loss below 200 °C occurs at a rate approximately 0.55 $\%.min^{-1}$ as indicated in Table 4.5.

The decomposition of GO2 occurred in two main stages and is indicated by the two peaks observed in DTG curve. The weight losses occurring at 211 and 420 °C have a rate of 1.35 and 1.58 $\%.min^{-1}$, respectively. GO2 undergo the redox process shown in Equation 4.1 during heating. Further weight loss is attributed to the volatilisation of HNO_3 that has a boiling temperature of 122 °C and decomposition of $KClO_3$ at 400 °C. A possible reaction occurring during the heating of GO2 is $KClO_3$ decomposition to produce potassium chloride (KCl) and oxygen (O_2) indicated by equation below (Equation 4.2)[166]

$$2KClO_3(s) \rightarrow 2KCl(s) + 3O_2(g) \qquad \text{Equation 4.2}$$

We propose that O_2 evolved reacts with the surface of graphite oxide to form CO_2. It has been reported that decomposition of graphite oxide is known not to be accompanied by liberation of O_2 and that carbon monoxide (CO) and CO_2 are the usual decomposition products. According to Hoffman, the absence of O_2 evolution is due to any highly reactive oxygen released from the graphite oxide structure reacting with the surface to form CO and CO_2[167].

The TGA curve of GO4 exhibits decomposition in several stages. This is evident from the peaks in its DTG curve. The weight loss of GO4 occurred in three stages at temperatures 189, 276, and 388 °C. The evolution of carbon and sulfur dioxide (Equation 4.1), water loss and volatilisation of HNO_3 occurred from the graphite layers. Weight loss below 188 °C can be attributed to volatilisation of CH_3COOH, since it has a boiling temperature of 118 °C, and in addition, $KMnO_4$ may decompose spontaneously above 150 °C. We proposed possible reactions that may occur during the heating of GO4.

$$2KMnO_4 + H_2SO_4 \rightarrow Mn_2O_7 + K_2SO_4 + H_2O \qquad \text{Equation 4.3}$$

$$Mn_2O_7 \rightarrow 2MnO_2 + O_3 \qquad \text{Equation 4.4}$$

The reaction between $KMnO_4$ and H_2SO_4 produces shown in Equation 4.3[167], manganese heptoxide (Mn_2O_7), potassium sulfate (K_2SO_4) and water (H_2O). Equation 4.4[167] indicates that heating Mn_2O_7 produces ozone. This caused more water loss from the graphite layers and possibly ozone (O_3) was evolved. The presence of the O_3 increases CO_2 evolution. Further weight loss of GO4 can be attributed to the decomposition of CH_3COOH, which can be a source of CO and CO_2 evolution. The TGA curves of these previously mentioned GO, showed a weight loss of approximately 20% at 700 °C. According to Xie et al[168], this is typical of graphite oxide after exfoliation at high temperatures. Mathur et al[169] studied the exfoliation mechanism of graphite oxide and they found that maximum weight loss corresponded to a maximum degree of expansion of graphite oxide. During heating, intercalate gradually diffused inside the graphite layers, however if saturation of graphite layers was reached, intercalate gradually escaped from the edges of the graphite layers and eventually further weight loss as exfoliation occurred. Consequently, this was not observed from GO1, GO2, and GO4, instead these graphite oxides exhibited a low degree of expansion after exfoliation.

GO3 was oxidised using Method 2, weight loss occurred in a similar manner to that of GO2, but at a slower rate and lower temperatures as indicated in Table 4.5. GO3 exhibited small weight loss below 300 °C and in addition; maximum weight loss at 359 and 402 °C with a rate of 2.22 and 1.28 $\%.min^{-1}$, respectively is observed. The TGA curve for GO3 exhibited a maximum weight loss of approximately 27% at 700 °C, which is 5% higher than GO2. The difference in maximum weight loss of GO3 to GO2 is ascribed to the volatilisation of $KClO_3$ in the graphite layers.

From the TGA curve of GO5, it is assumed that volatilisation of intercalates and evolution of gases was slower. This is supported by the maximum weight loss observed at 700 °C. GO5 had a maximum weight loss of approximately 45% indicating that the degree of expansion of GO5 is higher compared with other GO studied. Its DTG curve exhibited weight loss at 197 and 249 °C, and a maximum rate of weight loss was 3.69 and 5.28 $\%.min^{-1}$, respectively. The weight loss is attributed to the volatilisation of HNO_3 as well as $C_{10}H_{21}OH$ from the graphite layers, since $C_{10}H_{21}OH$ has a boiling temperature of 233 °C. Furthermore, the DTG curve shows that as the temperature increased, further weight loss occurred at 267 and 278 °C at a rate of 12.77 and 43.20 $\%.min^{-1}$, respectively.

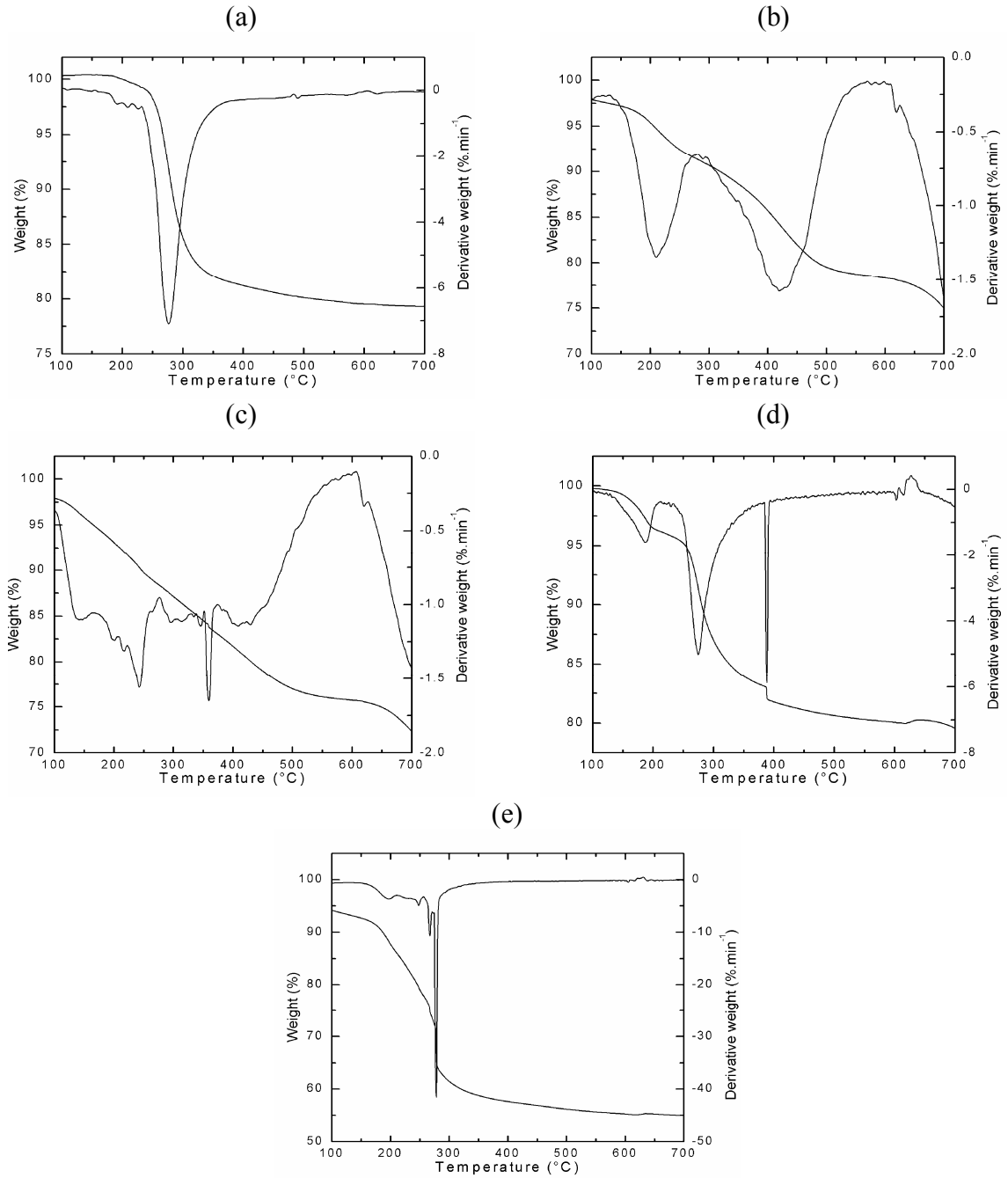

Figure 4.8 Thermal decomposition of various types of graphite oxides (a) GO1 (b) GO2 (c) GO3 (d) GO4 (e) (GO5) in N_2

Table 4.5 Degradation temperature and maximum rate weight loss of various types of graphite oxides decomposition stages in N_2 from their DTG curve

Graphite Oxide	Decomposition stages							
	1		2		3		4	
	(°C)	(%.min^{-1}) *	(°C)	(%.min^{-1}) *	(°C)	(%.min^{-1}) *	(°C)	(%.min^{-1}) *
GO1	200	0.55	277	7.10				
GO2	211	1.35	420	1.58				
GO3	143	1.09	245	1.59	359	2.22	402	1.28
GO4	189	1.54	276	5.02	388	6.07	-	-
GO5	197	3.69	249	5.28	267	12.77	278	43.20

rate of weight loss

4.3.7 Thermal oxidation decomposition of graphite oxide in air

The decomposition of GO in air occurs via a redox reaction between graphite oxide and H_2SO_4 as indicated in Equation 4.1, as well as the volatilisation of intercalates as previously discussed. The oxidation decomposition of GO1 and GO2 is similar to that of in a N_2 atmosphere, as evident by the TGA curves (Figure 4.9a and b). The DTG curve of GO1 indicates one main weight loss.

The decomposition of GO2 was comparable with that of obtained in N_2, however its maximum weight loss and temperature were different. The DTG curve of GO2 shows that decomposition occurred in two stages at 220 and 369 °C with a rate of 2.45 and 2.29 %.min^{-1}, respectively. The first stage, at 220 °C corresponds to evolution of gases (Equation 4.1), as well as the volatilisation of HNO_3. Further weight loss is observed with increased temperature due to evolution of gases from the graphite layers. As shown in Table 4.6, maximum rate of weight loss at these temperatures was higher than that of GO2 in N_2. We propose that the presence of oxygen in air and oxygen produced from the decomposition of potassium chlorate caused more carbon dioxide to be evolved.

In the case of GO4, the DTG curve showed three stages of decomposition at 161, 271, and 278 °C. The weight loss below 271 °C is attributed to the loss of water and volatilisation of HNO_3, and CH_3COOH. It is noted that although the number of decomposition stages of GO4 in both atmospheres were the same, the temperature of the last stage in air was lower compared with N_2. It is possible that Equations 4.4 and 4.5 occurred and the redox process between GO4 and H_2SO_4 dominated the decomposition of GO4 in air.

Table 4.6 Temperature and maximum rate weight loss of various types of graphite oxides decomposition stages in air from their DTG curve

Graphite Oxide	Decomposition stages									
	1		2		3		4		5	
	(°C)	(%.min^{-1}) *	(°C)	(%.min^{-1}) *	(°C)	(%.min^{-1}) *	(°C)	(%.min^{-1}) *	(°C)	(%.min^{-1}) *
GO1	279	7.10								
GO2	220	2.45	368	2.29						
GO3	214	2.92	253	23.66	360	5.46				
GO4	161	0.69	271	5.19	278	6.72				
GO5	197	3.47	240	4.27	247	4.74	277	6.47	291	14.02

rate of weight loss

The degree of expansion of GO4 was observed to be the same as in N_2. GO4 showed a weight loss of approximately 20% at 700 °C, which is indicative of low degree of expansion. The same trend is observed for GO1. It seems that its atmosphere does not affect the degree of expansion for both GO4 and GO1.

In the case of GO3, decomposition in air occurred in several stages similar to that of obtained in N_2 as indicated by the maximum weight loss peaks in the DTG curves (Figure 4.8c and 4.9c). The temperature at which maximum weight loss occurred is negligible. Incidentally, a higher rate of weight loss is observed at 265 °C. It is assumed that this is the threshold temperature for expansion of GO3. The maximum degree of expansion for GO3 in air is 15% higher compared with that of in N_2. Table 4.6, shows the rate of weight loss was higher for GO3 than GO2, although both were prepared according to the Staudenmaier method. The amount of $KClO_3$ used affects the rate of weight loss therefore, and it has been suggested that GO3 oxidised using low amount of $KClO_3$, has a higher $KClO_3$ concentration in its graphite layers due to intercalation. This is supported by the higher *d* spacing obtained from the WAXD measurement presented earlier in this chapter.

Figure 4.9e shows that GO5 decomposition occurred in several stages as indicated by the pronounced weight loss in air. As listed in Table 4.6, GO5 weight loss in air occurs at a slightly higher temperature compared with that of obtained in N_2. However, the rate of weight loss is lower. The TGA curves of GO5 in both atmospheres indicate that there is only a 5% difference in weight loss at 700 °C.

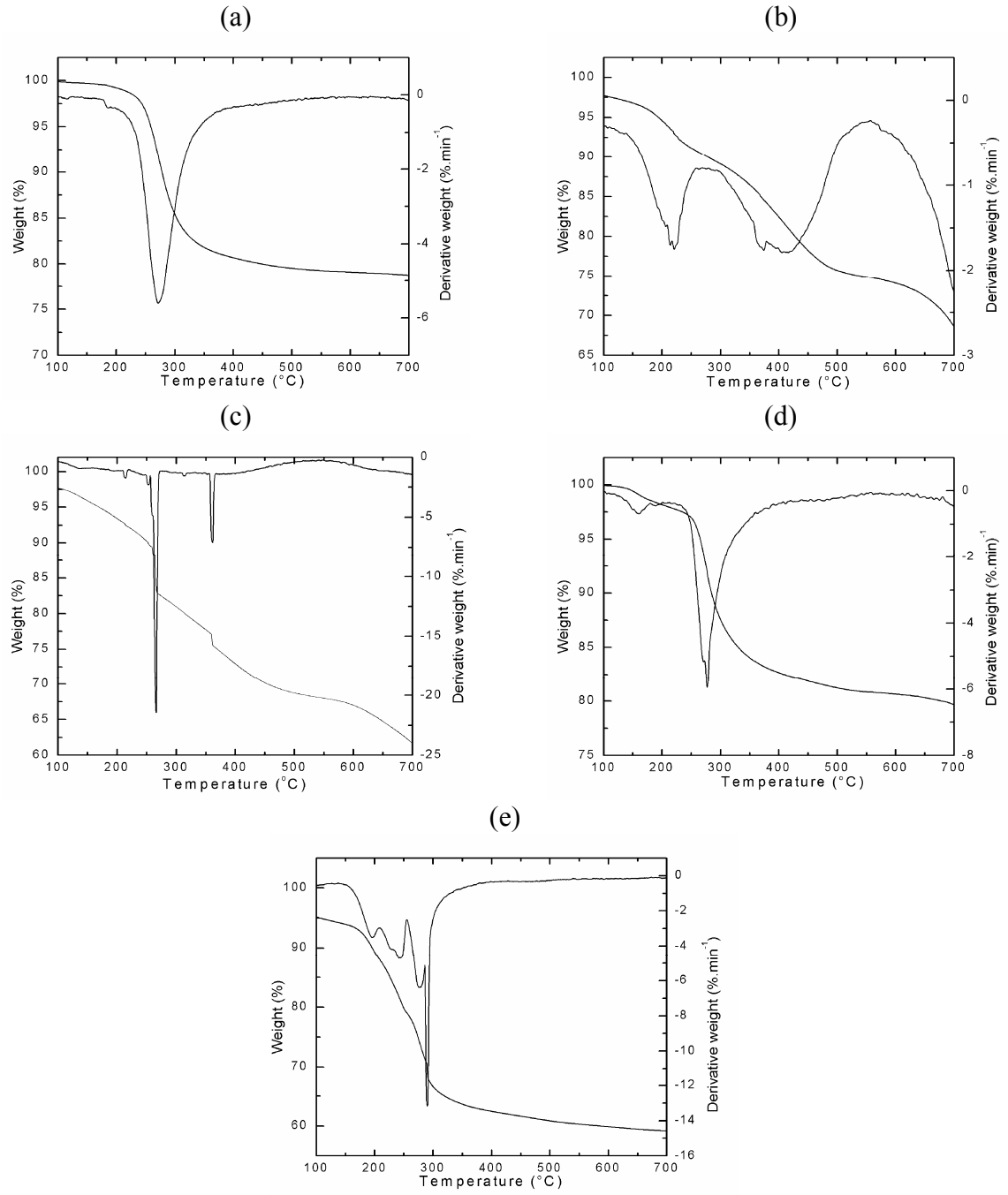

Figure 4.9 Thermal oxidation of various types of graphite oxides (a) GO1 (b) GO2 (c) GO3 (d) GO4 (e) (GO5) in air

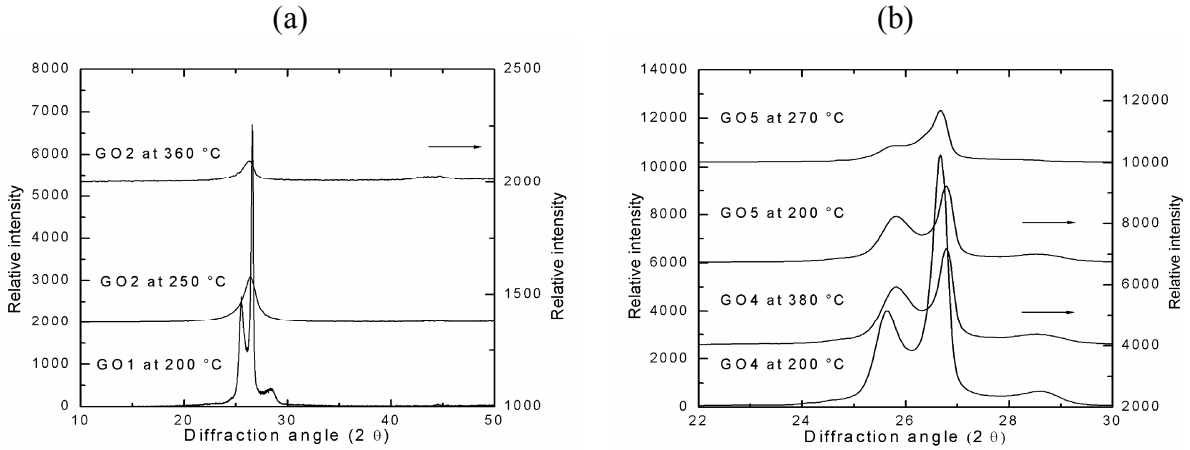

Figure 4.10 Diffractograms of (a) GO1, GO2 (b) GO4, GO5 at various temperatures

Some of the graphite oxides were exfoliated at various temperatures and they were analysed using WAXD. The effect of exfoliation at various temperatures on the crystalline structure of graphite oxide is shown in Figure 4.10. The temperatures of the main weight losses in the DTG curve under air were used as reference. The diffractogram of GO1 heated at 200 °C in Figure 4.19a showed three peaks in the range 2θ=24 to 30° similar to GO1 in Figure 4.5a. The (002) peak at 2θ=26° corresponds to *d* spacing 0.335 nm, which is the same as that observed for pristine graphite[132]. The absence of the (001) peak in the lower 2θ is due to exfoliation of graphite layers. This means that the small weight loss occurring below 200 °C does not alter the order of the graphite layers. After heating at 200 °C, GO2 (Method 1) shows a broad (002) peak at 2θ=26°, its *d* spacing is the same as that of GO1. The (001) peak observed at 2θ=12°, before heating, is absent. Heating GO2 at 360 °C resulted in a change in crystalline structure. The diffractogram of GO2 exhibits two peaks at 2θ=26 and 44°. A slight increase in *d* spacing of the (002) peak (0.338 nm) is observed. The presence of the (002) peak suggests that volatilisation of HNO_3 and decomposition of $KClO_3$ alter the crystalline structure of GO2. This is further supported by the absence of the (001) peak in the diffractogram. The diffractograms of GO4 and GO5, after heating at 250 °C shown in Figure 4.10b did not change, in fact; it is similar to Figure 4.5a. This indicates that the graphite layers remained ordered. For GO4 heated 380 °C, the (002) peak shifted slightly, 2θ=26° and in addition, became deresolved into one peak. In the case of GO5, the (002) peak shifted to higher 2θ. The results show that volatilisation and/or decomposition of intercalates from the graphite layers of these graphite oxide above 200 °C changed the ordering of the graphite layers.

4.3.8 Thermal expansion of graphite oxide

The thermal expansion, TE, of graphite oxides was measured to determine the effect of oxidation treatment on the degree of expansion at various temperatures. TE was measured by DMA parallel plate test mode according to the experimental parameters described in Chapter 3. The TE was obtained by measuring the TE over the temperature range 100 to 300 °C, and the results are listed in Table 4.7. The GO4 intercalated with H_2SO_4 CH_3COOH; $KMnO_4$ showed the highest TE at temperatures between 100 and 250 °C. Therefore, since CH_3COOH has two oxygens it becomes a source for CO_2 evolution. In addition, the reaction between $KMnO_4$ and H_2SO_4 as shown in Equation 4.3 and 4.4 can occur with further CO_2 evolved. It is interesting to note that at temperatures above 250 °C TE of GO4 becomes constant. This indicates that a maximum degree of TE is reached. From TGA results, it was previously mentioned that saturation of the graphite layers caused intercalates to diffuse from the graphite layers, resulting in low weight loss and therefore, low degree of expansion. As seen in Table 4.7 the TE of GO5 increased with temperature. In general the TE of GO2 was higher compared with GO3, however at temperature above 250 °C TE of GO3 was the highest. The high TE of GO3 is ascribed to the amount of $KClO_3$ used in the oxidative treatment. During heating volatilisation and/or decomposition of $KClO_3$ creates enough pressure to separate the graphite layers and cause the irreversible expansion of graphite oxide. Hence, greater amount of $KClO_3$ becomes a source for carbon dioxide evolution.

Table 4.7 Thermal expansion of various types of graphite oxides at various temperature ranges

Graphite Oxide	Temperature range (10^{-4} °C^{-1})			
	100-170	200-220	240-250	250-255
GO1	7.08	74.64	6338.40	1010.05
GO2	0.24	7.83	111.27	167.55
GO3	-	9.43	49.46	5008
GO4	16.87	207.15	615.65	601.65
GO5	14.08	77.49	382.28	1110.05

-thermal expansion at this temperature range cannot be measured

4.4 Conclusion

Graphite was intercalated with strong Brønsted inorganic acids, primarily HNO_3-H_2SO_4 and H_2SO_4 with various agents such as $KClO_3$, CH_3COOH-$KMnO_4$ and $C_{10}H_{21}OH$. A series of graphite oxides were obtained by using various intercalating agents. The crystalline structure, BET surface area, and thermal properties of oxidised graphite were investigated. In addition, the characterization of exfoliated oxidised graphite was reported.

The structures of various forms of graphite oxide observed using SEM, exhibited graphite layers stacked along the c-axis in a staggered array. An increase in the interlayer spacing in the graphite layers was observed, indicating that separation occurred during intercalation of acids and reagents. The graphite oxide was exfoliated at high temperatures to form expanded graphite oxide. The exfoliation process caused oxidised graphite to expand and form an interconnected network "worm-like" structure, composed of graphite layers with thickness in the nanometer and micrometer dimensions. The surface area measurements obtained from BET surface analysis revealed surface properties are affected by the oxidative treatment and exfoliation process. The surface area of most graphite oxide increased while the surface area of expanded graphite oxide was larger compared with graphite oxide. The average pore diameter of both graphite oxide and expanded graphite oxide were in the nanometer dimension. There was no correlation between the surface areas of graphite oxide and expanded graphite oxide.

FTIR analysis confirmed the presence of hydroxyl, carbonyl, and carboxylic acids on the surface of graphite oxides and expanded graphite oxides. Furthermore, these results verify the statement reported in the literature that inorganic acids result in oxidation of unsaturated carbon bonds in the graphite.

The WAXD measurements of graphite oxides and expanded graphite oxides depended on the acids and reagents intercalated in the graphite layers. Some changes in the diffractograms of graphite oxide and expanded graphite oxide and the *d* spacing of graphite layers were observed. This indicates that intercalation occurred between the graphite layers. In addition, the graphite oxidised using CH_3COOH-$KMnO_4$ and $C_{10}H_{21}OH$ were less efficient in oxidising the graphite in comparison with $KClO_3$ reagent.

The crystallite thickness of various graphite oxides and expanded graphite oxides calculated from the Scherrer equation was in the nanoscale dimensions, below 30 nm. The low crystallite thickness obtained was due to the oxidative treatment of graphite disrupting crystallites.

The thermal decomposition of graphite oxide in N_2 and air varied depending on intercalate utilised and conditions. However, the decomposition of graphite oxide occurs, regardless of atmosphere, by the same mechanism though at different rates with temperature change. At temperatures below 250 °C H_2O and other reagents such CH_3COOH-$KMnO_4$, $C_{10}H_{21}OH$, and HNO_3 were volatilised from the graphite layers and released as gases. Further weight loss was observed for some of the oxidised graphite as temperature increased and these were attributed to volatilisation and/or decomposition of acids and reagents leading to the irreversible expansion of graphite oxide. In addition, some of the reagents utilised in the oxidative treatment could possibly have been a source for evolution of CO_2. The weight loss of graphite oxide during thermal decomposition seemed to be affected by its surface properties. The WAXD measurements of some of the graphite oxide heated at various temperatures showed a change in their crystalline structure at temperatures above 200 °C. The results obtained from this analysis confirm that volatilisation and/or decomposition of intercalate caused changes to the order of the graphite layers.

The thermal expansion of graphite oxide showed an increase with temperature. The type of oxidising agents and reagent used in combination with the Brønsted acids play a role in the thermal expansion of graphite oxide. This was evident with the graphite oxide intercalated with $KClO_3$ and in addition, the amount of $KClO_3$ utilised affected thermal expansion. Graphite oxidised using a greater amount of $KClO_3$ had a higher thermal expansion compared with the other graphite oxides in the temperature range studied. This is due to volatilisation and/or decomposition of $KClO_3$ builds enough pressure to separate the graphite layers causing irreversible expansion of graphite oxide.

Chapter 5 Poly(ethylene-co-methyl-acrylate-co-acrylic-acid) layered graphite oxide composites via solution blending

5.1 Introduction

The effects on the crystal structure, thermal stability, thermo-mechanical and dielectric properties of poly(ethylene-co-methyl acrylate-co-acrylic acid) (EMAA) were investigated in the presence of graphite. Prior to dispersion, graphite was oxidised using the Staudenmaier method. Carbonyl, hydroxyl and carboxyl functionalites can be found on the surface of oxidised graphite, all of which can facilitate the chemical and physical interactions between the graphite and the EMAA matrix in the formation of EMAA layered graphite oxide composites when utilising a solution blending technique. The properties of EMAA in the presence of various types of graphite oxide and its expanded form will be investigated.

5.2 Experimental

5.2.1 Oxidation of graphite

The graphite flakes obtained from Graftech Inc., were pre-oxidised and are denoted as GO. These graphite flakes were oxidised using the Staudenmaier method[67], which has been described in Chapter 4. Briefly, the graphite was oxidised using Brønsted acids, nitric (HNO_3) and sulfuric (H_2SO_4) acid. Graphite was added to the pre-cooled (5 °C) mixture of concentrated HNO_3 (69%) (25 mL), (98%) (50 mL), $KClO_3$ (1:2) and continuously stirred. The acid-oxidised graphite was then filtered for recovery. The oxidised graphite filtrate was washed with methanol, until the measured pH was greater than 5. The graphite oxide was dried for recovery, and is denoted as SGO.

5.2.2 Preparation of EMAA layered composite

EMAA layered composites were prepared by solution blending, which involved dissolving the EMAA pellets in hot chloroform, to which GO and SGO were added in weight fractions of 0.01, 0.02, and 0.05. Expanded GO and SGO were obtained as described in Chapter 3 and are denoted as EGO and SEGO, respectively. EGO and SEGO were dispersed into the polymer solution with an Ultra-Turrax (IKA Works Asia Sdn Bhd) disperser. The shearing

mechanism of the disperser has also been described in Chapter 3. The hot EMAA graphite oxide solutions were then poured slowly into stirred cold ethanol to precipitate the composites. The graphite oxide filled EMAA precipitates were filtered using a Buchner funnel with suction and dried in a pre-heated vacuum oven at 50 °C for 24 h.

EMAA layered composites were made into film specimens by taking approximately 1 to 2 g and hot-pressing between two PTFE sheets and heated aluminum disks. The press (Thomas Optical and Scientific Co. Pty Ltd) with an Activon (Graseby-Specac) temperature controller was pre-heated to 150±1 °C prior to pressing. An aluminum template (3x2x1 mm) was used to form the film specimen into the desired shape. Pure and filled EMMA was firstly melted for 2 min without pressure, after which the pressure was raised to 13 kPa and held for 2 min, and then further increased to 20 kPa for an additional 3 min.

Table 5.1 lists the nomenclature for the EMAA layered composites used in this study. The prefixes of GO, SGO, EGO and SEGO refer to the type of graphite oxide filler dispersed in the EMAA matrix. The concentration levels of the graphite filler are supplied as suffixes, such that EMAA-GO1 refers to EMMA filled with 1 %wt of GO.

Table 5.1 Abbreviations of EMAA layered composites in various types of graphite oxides and expanded graphite oxides in varying concentration

	GO (%wt)	EGO (%wt)		SGO (%wt)	SEGO (%wt)
EMAA	0	0	EMAA	0	0
EMAA-GO1	1		EMAA-SGO1	1	
EMAA-GO2	2		EMAA-SGO2	2	
EMAA-GO5	5		EMAA-SGO5	5	
EMAA-EGO1		1	EMAA-SEGO1		1
EMAA-EGO2		2	EMAA-SEGO2		2
EMAA-EGO5		5	EMAA-SEGO5		5

5.3 Results and Discussion

5.3.1 Structural characteristic of graphite oxide and expanded graphite oxide

Oxidative treatment of graphite using the Staudenmaier method forms a material known as graphite-intercalated compound (GIC) or graphite oxide (GO). Graphite oxide is comprised of graphite layers and intercalated layers in a staggered array. The structure of the various types of graphite oxide was obtained according to the SEM experimental parameters described in Chapter 3. The SEM micrographs of GO, SGO and its expanded form, EGO and SEGO are presented in Figures 5.1a to d. The structure of the various types of graphite oxides have been previously described in Chapter 4. The SEM micrographs of GO and SGO indicate a typical layered graphite structure in which the graphite layers are arranged in a regular and periodic order. The structure of SGO shows separated graphite layers indicating intercalation of acids and reagents occurred in the graphite layers. The separation of the graphite layers for each type of graphite oxide was estimated by image analysis techniques, utilising the IPLab Spectrum Scientific Image Processing 3.1a (Power Macintosh Signal Analytics 1989-1996) application. Several measurements were obtained for each type of graphite oxide, with the errors provided taken from the standard deviation of the mean. The graphite layers of GO were found to be separated by a distance of 1.25±0.14 μm, whereas the separation of the graphite layers of the SGO was found to be 2.23±0.13 μm.

The differences in the structure of GO and SGO after exfoliation at 800 °C are clearly seen in Figure 5.1, where the ordered structures of GO and SGO are lost. As indicated in Chapter 4, exfoliation corresponds to the boiling or decomposition of intercalates as well as the evolution of gases due to redox processes occurring between graphite oxide and H_2SO_4. These effects cause the graphite layers to collapse and deform randomly and produced an interconnected network, resembling a worm-like or honeycomb structure. The worm-like structure consists of multi-pores of almost an ellipsoidal shape created due to the expansion of the graphite layers. The multi-pores vary in size, possibly ranging from micro to nanometer dimensions[78].

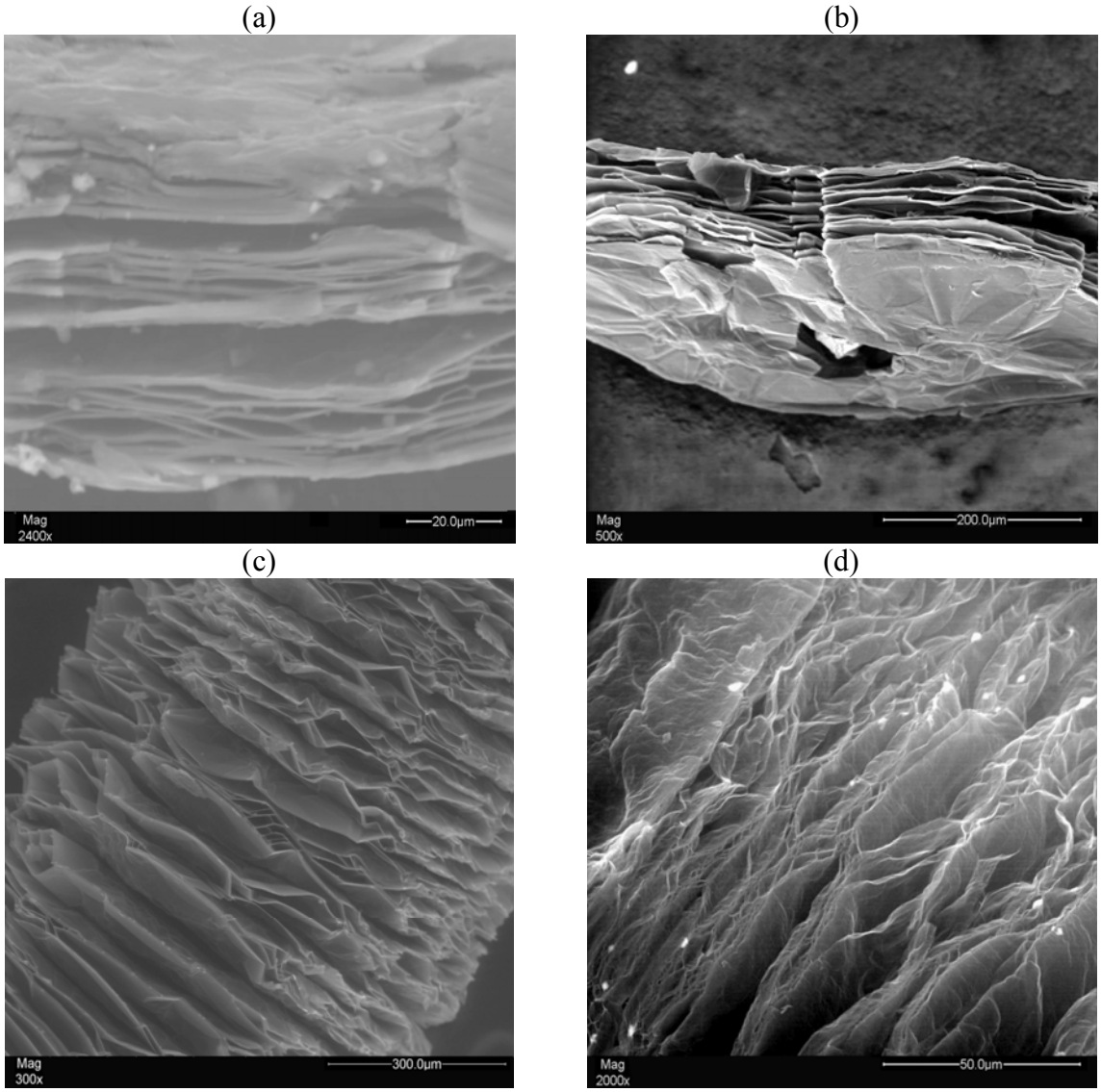

Figure 5.1 SEM micrographs of the various types of graphite oxides (a) GO (b) SGO (c) EGO (d) SEGO

The separation of the graphite layers in EGO and SEGO was estimated in the same manner as for GO and SGO. The estimated separation of the graphite layers of EGO and SEGO, were observed to be higher than its precursor. The graphite layers of EGO had a distance of 2.73±0.35 µm, whilst the distance of the graphite layers in SEGO was 4.75±1.23 µm. The estimated distance of the graphite layers correlates well with that provided by the BET surface area measurements of the graphite oxide materials. The BET surface area measurements were obtained according to the experimental conditions described in Chapter 3. The intercalation of Brønsted acids and $KClO_3$ in the graphite layers produced SGO with large surface area that

was higher than that of GO, as indicated in Table 5.2. Exfoliation of the graphite oxides formed expanded graphite oxide with an even larger surface area, with SEGO demonstrating a larger surface area than EGO. The increase in the distance of the graphite layers and surface area measurements is consistent with that of other oxidised graphite reported[118,157].

Table 5.2 BET surface area properties of graphite oxides and expanded graphite oxides

	Type of Graphite Oxide			
	GO	SGO	EGO	SEGO
BET surface area ($m^2.g^{-1}$)	0.87	0.92	3.89	19.04

The internal structure of graphite particles in the EMAA matrix was obtained using Transmission electron microscope (TEM) according to the experimental parameters described in Chapter 3. Figure 5.2 shows the TEM micrographs of EGO in the EMAA matrix, taken from different sites on the same ultra-thin film. Consequently, the low contrast between the graphite particles and EMAA is due to both are carbon based materials. The black spheres and the white domains are referred to as the exfoliated graphite particles and the EMAA matrix, respectively. From the TEM micrographs graphite particles with reduced size were observed which was produced from the high shearing provided by the Ultra-Turrax disperser during dispersion. Graphite particles were reduced in size, which resulted in their uniform dispersion in the EMAA matrix. Hence, the shape of the EGO in the EMAA matrix remains a platelet structure.

(a) (b)

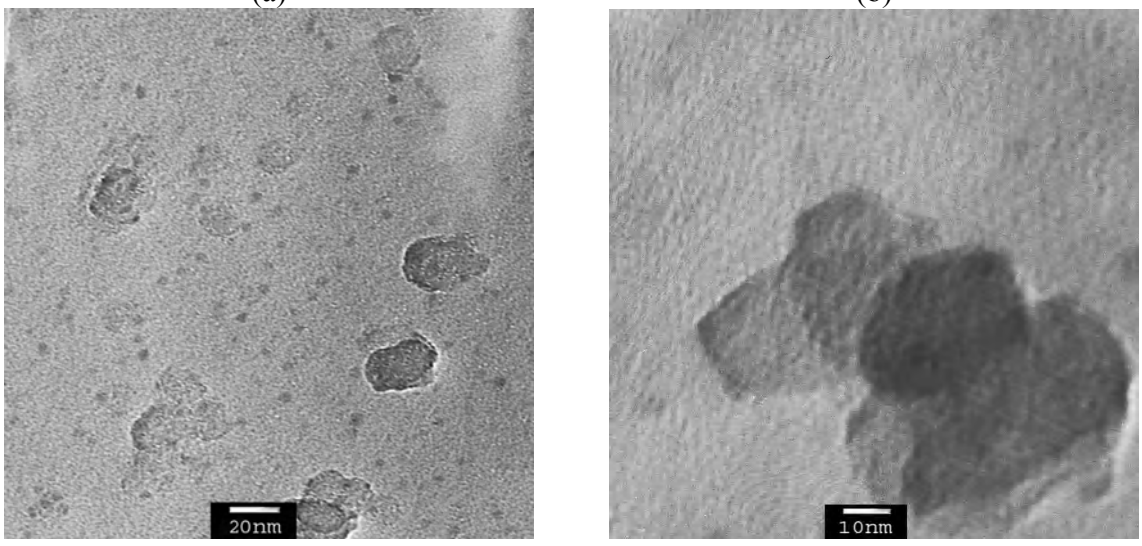

Figure 5.2 TEM micrographs of EMAA-EGO at 5 %wt of EGO

5.3.2 Interlayer spacing and crystalline thickness of graphite oxide and expanded graphite oxide filler in EMAA

Wide-angle X-ray diffraction (WAXD) was employed to characterise the graphite oxide materials and EMMA layered composites. WAXD provided a precise measurement of graphite layers, interlayer (*d* spacing), and crystalline structure. The change in the *d* spacing of graphite layers was calculated by using the Bragg equation as described in Chapter 3. The calculated *d* spacing of graphite oxides used in this study is tabulated in Tables 5.3 and 5.4.

The diffractograms of GO, SGO, EGO and SEGO are displayed in Figure 5.3. GO diffractogram consists of a set of sharp peaks between 2θ=26 to 28° that indicate a high degree of order for this type of graphite oxide. These peaks correspond to the diffraction of the (002) plane, which is the graphite plane[170]. The (002) peak has a *d* spacing of 0.335 nm between two graphite layers. This *d* spacing is the same as observed for pristine crystalline graphite[171], indicating that the graphite layers of GO are ordered and multi-layered. In addition to the (002) peak, a small and broad peak at approximately 2θ=11° was observed. This peak corresponds to the diffraction of the (001) plane, which is the graphite oxide plane. The (001) peak relates to a *d* spacing of 0.754 nm, which is the repeat thickness of aggregate of graphite layers[172].

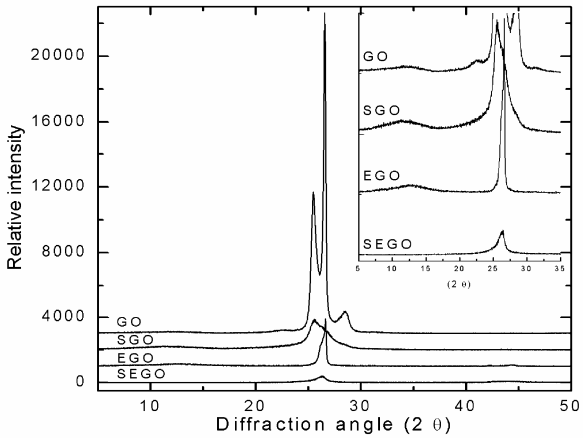

Figure 5.3 Diffractograms of the various types of graphite oxides: GO, SGO, EGO and SEGO. Inset exhibits the diffraction (001) peak, between the diffraction angles 0 to 15°

The (002) peaks observed in the diffractogram of GO after oxidative treatment deresolved to a single peak, however no change was observed for the (001) peak as shown in the SGO diffractogram. The single (002) peak corresponds to a *d* spacing of 0.347 nm. The high *d*

spacing of the (002) peak is indicative that intercalation of the Brønsted acids and $KClO_3$ occurred in the graphite layers. According to Hontoria-Lucas et al[157], oxidation of graphite produces a transformation of its crystalline structure into a new, laminar, but more open structure than that of graphite oxide. It is the resultant structure that facilitates physical as well as chemical intercalation of molecules with the graphite oxide.

In general, both expanded graphite oxides, EGO and SEGO, exhibited a single (002) peak between 2θ=26 and 27°, corresponding *d* spacings of 0.335 and 0.339 nm, respectively. The (001) peak observed in the diffractogram of EGO corresponded to a *d* spacing of 0.697 nm. The presence of this peak suggests that the stacking of the hexagonal graphite layers were mostly still intact. However, this was not the case for SEGO, where the (001) peak was no longer visible in its diffractogram, as shown by the inset in Figure 5.3. The absence of this peak indicates that graphite layers after exfoliation at high temperatures were expanded. It was concluded that the degree of expansion of SEGO was higher than that of EGO.

Table 5.3 Interlayer, *d* spacings of the (001) and (002) peak in the diffractograms of GO, SGO, EGO and SEGO

Type of Graphite Oxide	*d* spacing (nm)	
	(001) peak	(002) peak
GO	0.754	0.335
SGO	0.755	0.347
EGO	0.697	0.335
SEGO	-	0.339

-no diffraction of the (001) peak is observed

The diffractograms of the EMAA layered composites are presented in Figures 5.4a to d. The diffractogram of pure EMAA consists of a broad peak, corresponding to the diffraction of (110) and (200) planes. These peaks are overlapped by an amorphous halo[173] due to the crystal structure of polyethylene segments, found at 2θ=22°. The (110), (200) and (002) peaks at approximately 2θ=22 and 26° are apparent in all diffractograms of filled EMAA. The presence of the (002) peak suggests that some graphite layers were unexfoliated in the EMAA matrix. However, no diffraction peak in the low 2θ region was observed as shown in Figure 5.4d. It is assumed that those graphite layers may have been dispersed in the EMAA matrix and they did not maintain their parallel registry, but were dispersed in an exfoliated or disordered manner in the EMAA matrix. The results obtained were similar to those reported by Uhl et al[2] with PA-6 graphite nanocomposites.

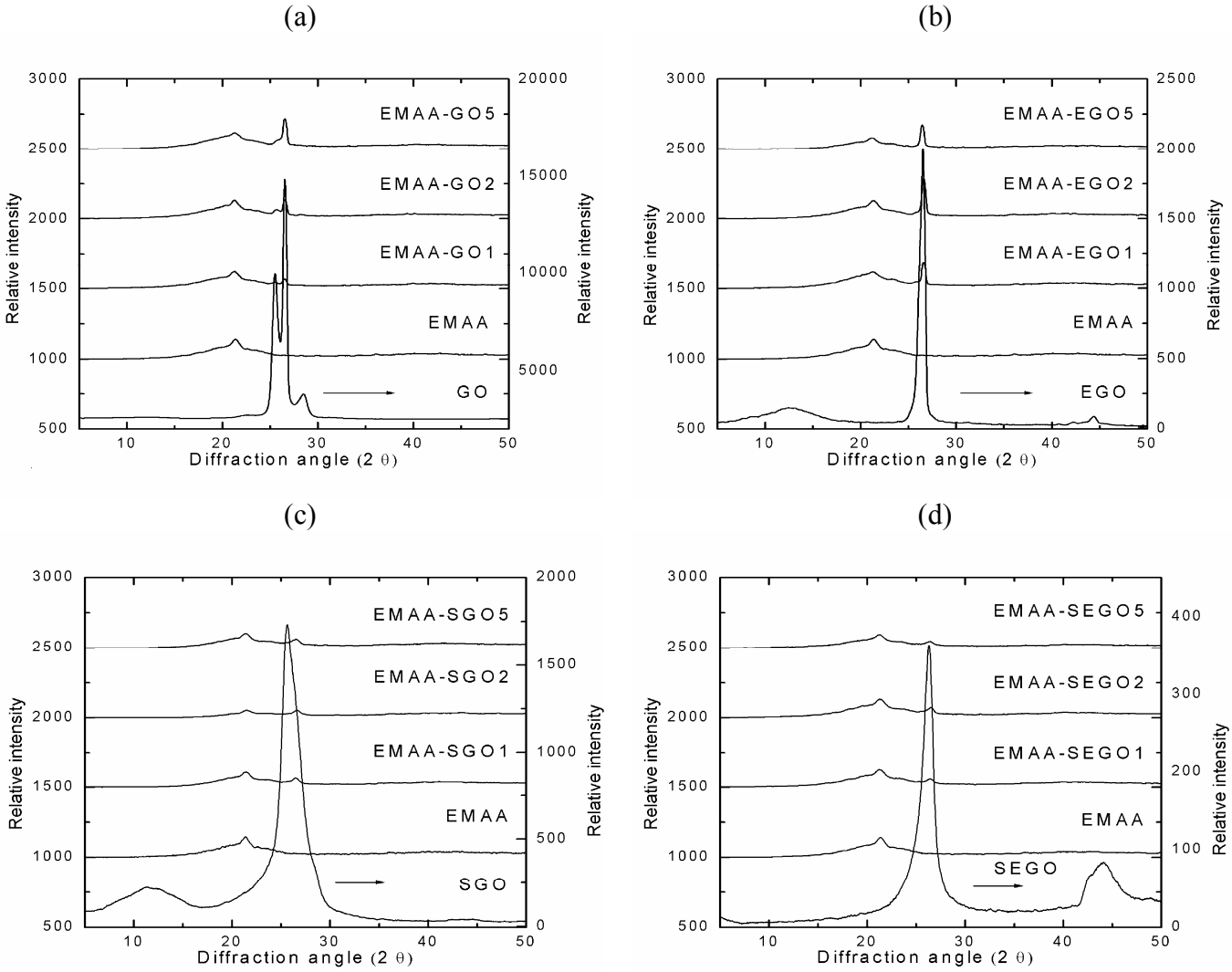

Figure 5.4 Diffractograms of filled EMAA (a) EMAA-GO (b) EMAA-EGO (c) EMAA-SGO and (d) EMAA-SEGO

The results reported in Table 5.4 indicate no change in the *d* spacing, in particular of the (002) peak. This suggests that no EMMA intercalation occurred in the graphite layers of all the studied graphite oxides. The graphite particles in the filled EMAA were mostly in order and multi-layered. In addition, no detectable effect on the crystal structure of EMAA matrix was observed. From the WAXD measurements, it is suggested that addition of EMAA was unable to promote exfoliation of graphite layers. The WAXD measurements are in agreement with those of Chen et al[130]. From their studies, preparation of polystyrene (PS) graphite composites via intercalation showed that the WAXD measurements of expanded graphite in the composites did not increase the *d* spacing of the graphite layers.

PS did not intercalate the spaces of the graphite layers, instead it intercalated between the interlamellar spaces of the graphite layers. Nevertheless, the intercalation of acids did cause the *d* spacing of the graphite layers to expand, however upon mixing with EMAA, no further effect on the *d* spacing of the graphite layers was observed[9,130,161,170].

Table 5.4 WAXD measurements of the diffraction (100) and (002) peaks in the diffractogram of filled EMAA

	d spacing (nm)			*d* spacing (nm)	
	(100) peak	(002) peak		(100) peak	(002) peak
EMAA	0.415				
EMAA-GO1	0.419	0.336	EMAA-SGO1	0.415	0.337
EMAA-GO2	0.417	0.335	EMAA-SGO2	0.413	0.335
EMAA-GO5	0.417	0.335	EMAA-SGO5	0.415	0.337
EMAA-EGO1	0.417	0.335	EMAA-SEGO1	0.417	0.337
EMAA-EGO2	0.416	0.335	EMAA-SEGO2	0.416	0.337
EMAA-EGO5	0.419	0.336	EMAA-SEGO5	0.419	0.337

The crystalline thickness, $L_{(002)}$ of graphite oxide fillers in the presence and absence of EMAA matrix was estimated by using the Scherrer equation, which was defined in Chapter 3. Prior to any measurements, the diffractograms of filled EMAA were subjected to curve fitting. The (002) peak, which has the strongest intensity, was taken for detailed analysis using Lorentz curve fitting. The Lorentz curve fitting was chosen as it closely represented the shape of the diffractogram curves. Figure 5.5, shows an example of Lorentzian curve fitting for EMAA-GO5, which was performed using the Origin 6, Microcal Software Inc, Version 6, with the dashed lines representing the curve fitting of $L_{(002)}$.

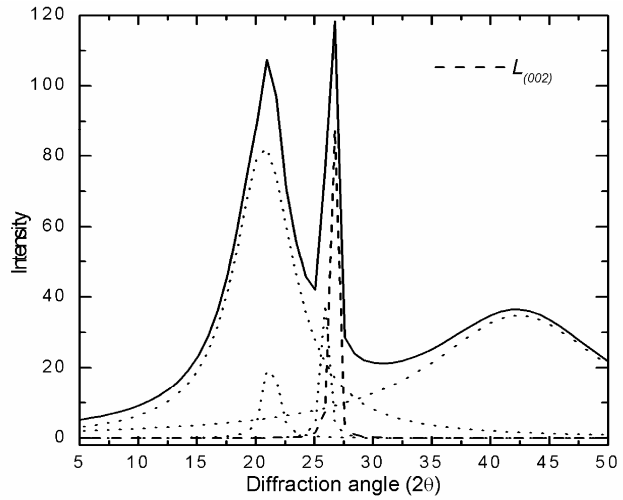

Figure 5.5 EMMA-GO5 after Lorentz fitted curve

$L_{(002)}$ of graphite oxide materials was obtained in a similar manner to that of filled EMAA. $L_{(002)}$ of GO was estimated to be 9.52 nm. Consequently, exfoliation of GO increased the $L_{(002)}$ to 10.27 nm. $L_{(002)}$ of SGO (9.50 nm) and SEGO (9.50 nm) decreased. In the case of filled EMAA, $L_{(002)}$ of the various types of graphite oxide generally decreased to 9.30 nm. The reason for the decrease in $L_{(002)}$ is unclear. Nevertheless, the various types of graphite oxides in the EMAA matrix are in the nanoscale size dimensions. The results obtained show that solution blending of graphite oxide, regardless of type, in the EMAA matrix using an Ultra Turrax disperser was unable to affect the order of its crystalline structure and exfoliate it uniformly in the EMAA matrix[174].

5.3.3 Crystallisation, melting behaviour and crystallinity of filled EMAA

The crystallisation and melting behaviour of pure and filled EMAA was studied using DSC. Pure and filled EMAA were cooled and heated from 20 to 200 °C under N_2 flow at a rate of 10 °C.min^{-1}, as described in Chapter 3. The primary objective of the DSC analysis was to determine the differences in nucleation behaviour and degree of crystallinity, χ_c, between EMAA and the various types of graphite oxides.

Figures 5.6a to d shows the crystallisation curves of prepared EMAA layered composites. The melting curves of EMAA layered composites are shown in Appendix 2. Crystallisation temperature, T_c, of EMAA in the presence of graphite particles increased in general, indicating that graphite particles behaved as a heterogenous nucleating agent for EMAA crystals[174]. The results reported in Table 5.5, show that the T_c, of EMAA-GO decreased at GO concentrations above 1 %wt. The opposite trend in T_c was observed for EMAA-EGO. The T_c, of EMAA in the presence of oxidised graphite, SGO and SEGO, were higher than those of EMAA filled with GO and EGO. This is due to the oxidative treatment of graphite producing materials with larger surface area as revealed from BET surface area analysis. From the FTIR analysis reported in Chapter 4, oxidised graphite contained more polar functional groups, such as carbonyl, hydroxyl, and carboxyl groups on the graphite oxide surfaces. These polar functional groups on the surface of the various types of graphite oxide enhance surface polarity, and compatibility with the polar terpolymer. The T_m obtained from the melting curves of all filled EMAA was lower than that of pure EMAA. It is suggested that the lamellar EMAA crystals may be somewhat thinner in the filled EMAA than the pure EMAA.

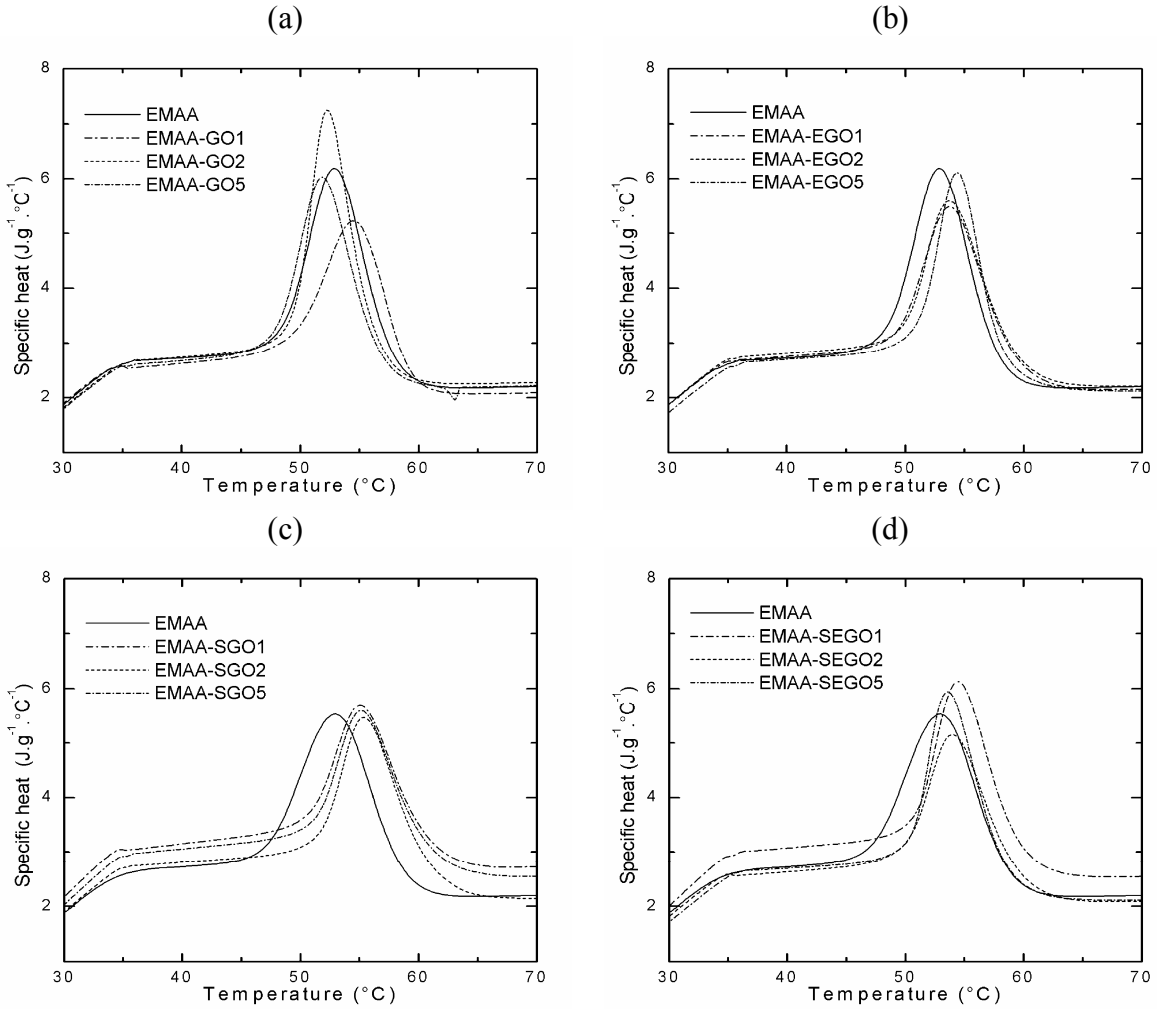

Figure 5.6 Crystallisation curves of filled EMAA (a) EMAA-GO (b) EMAA-EGO (c) EMAA-SGO (d) EMAA-SEGO

The χ_c of filled EMAA was calculated according to Equation 3.11 (Chapter 3) on the basis that pure PE crystals have an enthalpy of ΔH_f=293 J.kg^{-1} [143]. χ_c of EMAA decreased upon addition of graphite oxide (Table 5.5) in all cases. This indicates that graphite particles behaved as nucleating sites for EMAA crystal formation. The presence of graphite particles reduced the crystalline domains formed by EMAA causing the overall χ_c to be reduced. Zheng et al[30], studied χ_c of expanded graphite reinforced HDPE. They reported that the decrease in χ_c with increasing expanded graphite filler in HDPE could be attributed to a decrease in mobility of HDPE chains due to the formation of crystallites, and as a result, the domains of the crystalline phase were reduced in size. In addition, Zheng et al suggested that imperfection of crystals in the presence of inhomogeneities contributed to a decrease in the χ_c of HDPE[30].

The addition of graphite particles did not affect the crystalline structure of EMAA, confirming the findings obtained from the WAXD analysis of filled EMAA.

Table 5.5 Crystallisation, melting temperatures and crystallinity of filled EMAA

	T_c (°C)	T_m (°C)	χ_c		T_c (°C)	T_m (°C)	χ_c
EMAA	53	74	0.85				
EMAA-GO1	55	73	0.71	EMAA-SGO1	55	73	0.77
EMAA-GO2	52	74	0.84	EMAA-SGO2	55	73	0.81
EMAA-GO5	52	73	0.75	EMAA-SGO5	55	72	0.79
EMAA-EGO1	54	74	0.79	EMAA-SEGO1	5.5	72	0.83
EMAA-EGO2	54	73	0.79	EMAA-SEGO2	54	72	0.69
EMAA-EGO5	55	71	0.79	EMAA-SEGO5	54	73	0.79

5.3.4 Thermal stability of filled EMAA

The thermal degradation behaviour of pure and filled EMAA was studied using TGA. Pure and filled EMAA was heated from 30 to 800 °C under N_2 flow at a heating rate of 20 °C.min^{-1}. The weight loss curves (TGA curves) and derivative weight loss curves (DTG curves) of EMAA with varying types of graphite oxide and concentration levels are shown in Figures 5.7a and d, and 5.8a and d.

The degradation of all EMAA layered composites occurred in one step between 300 and 600 °C, and is attributed to random chain scission during heating. The TGA curves of EMAA filled with GO and EGO exhibit a sharp weight loss curve, and hence a fast rate of degradation. This trend was not observed for EMAA containing either SGO or SEGO.

The degradation process of EMAA matrix in the presence of this oxidised graphite was slower, as indicated by the reduced steepness of the relevant TGA curves, or alternatively, the enhanced broadness of the DTG peaks. The onset of degradation temperature, $T_{d\ onset}$, and maximum rate of degradation temperature, T_d, determined from the maxima of the DTG curves are listed in Table 5.6. The incorporation of graphite oxide into the EMAA matrix resulted in a shift in the TGA and DTG curves towards higher temperatures, indicating enhanced thermal stability. The $T_{d\ onset}$ of EMAA in the presence of graphite oxides were higher compared with pure EMAA. The T_d for filled EMAA was approximately 9 to 19 °C higher than that of the pure EMAA. The high $T_{d\ onset}$ and T_d of filled EMAA indicated enhance thermal stability. Consequently, the T_d of EMAA filled with oxidised graphite, SGO and SEGO, was approximately 10 °C higher than that measured when EMAA was filled with

GO and EGO. It appears that the process of oxidising graphite prior to dispersion delayed the degradation of EMAA, shifting it to higher temperatures. It can be suggested that oxidised graphite provided a better physical barrier between heat and EMAA matrix compared with GO and EGO[174].

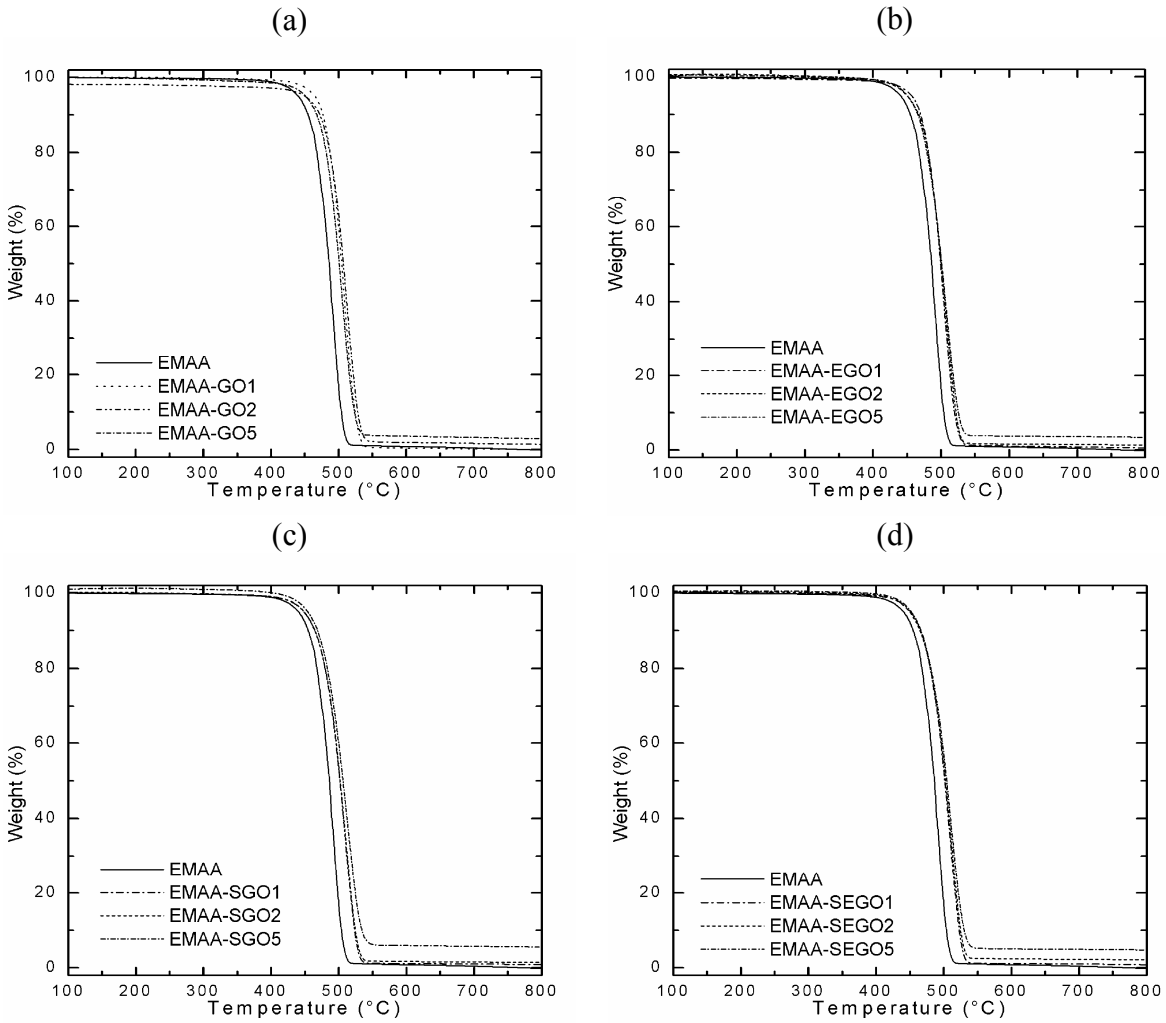

Figure 5.7 Weight loss curves of filled EMAA (a) EMAA-GO (b) EMAA-EGO (c) EMAA-SGO (d) EMAA-SEGO

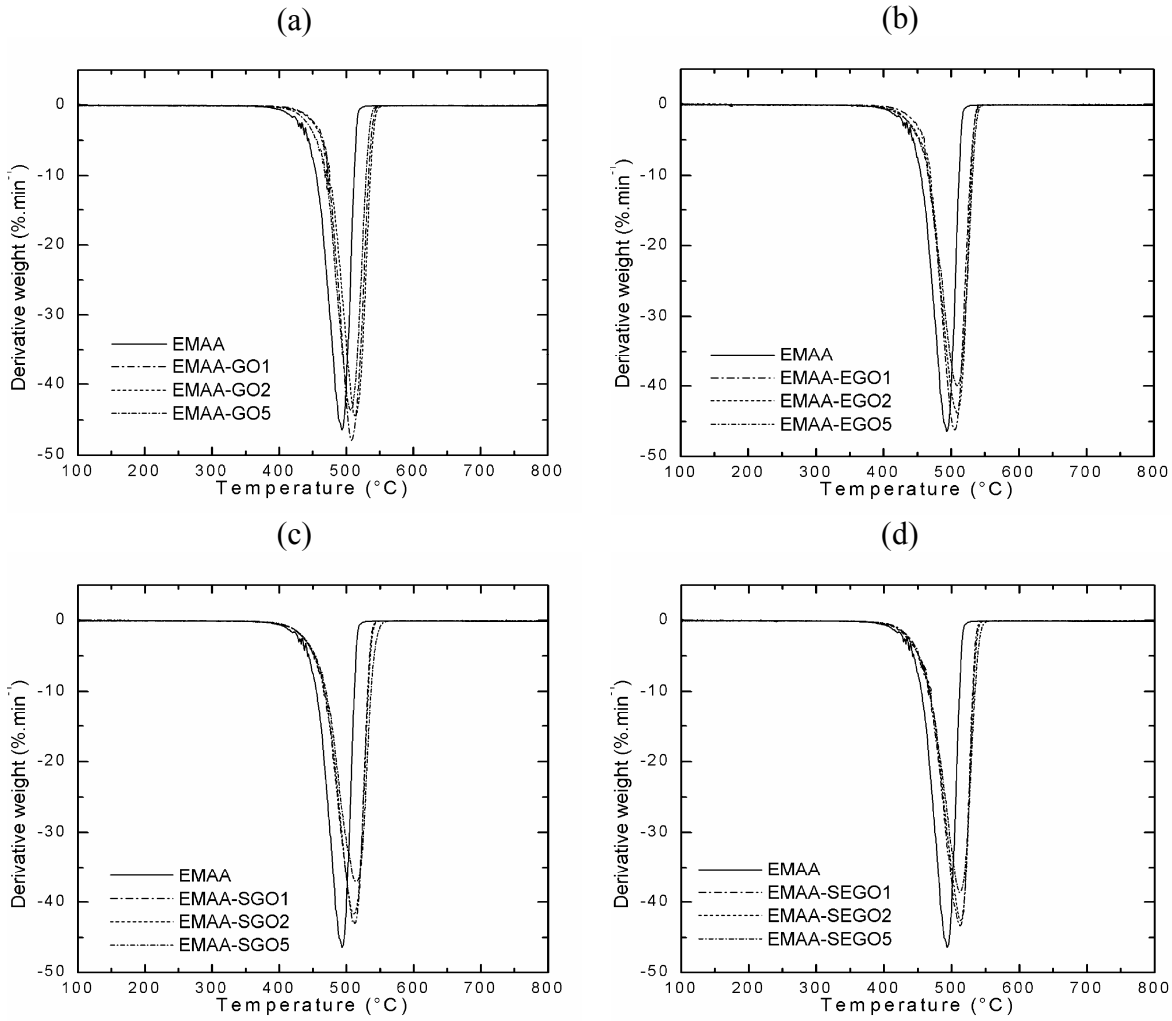

Figure 5.8 Derivative weight loss curves of filled EMAA (a) EMAA-GO (b) EMAA-EGO (c) EMAA-SGO (d) EMAA-SEGO

The results obtained were in contrast to those reported by Uhl et al[2]. They prepared a series of PA-6-graphite nanocomposites using a variety of graphite, including pristine graphite, expandable graphite (treated with sulfuric acid) and expanded graphite by melt blending. They reported enhanced thermal stability for PA-6 at 1 %wt of expandable graphite. However, higher concentration levels of expandable graphite appeared to facilitate the $T_{d\ onset}$, shifting to lower temperatures. The T_d of this PA-6 showed no difference at concentrations above 1 %wt of expandable graphite. In addition, degradation shifted to lower temperatures. Uhl et al suggested that low thermal stability could be attributed to the release of acid decomposition products at lower temperatures[2].

Table 5.6 Onset degradation and maximum rate of degradation temperatures of filled EMAA

	$T_{d\ onset}$ (°C)	T_d (°C)		$T_{d\ onset}$ (°C)	T_d (°C)
EMAA	466	497			
EMAA-GO1	469	508	EMAA-SGO1	467	513
EMAA-GO2	473	514	EMAA-SGO2	467	511
EMAA-GO5	470	507	EMAA-SGO5	469	516
EMAA-EGO1	467	505	EMAA-SEGO1	473	514
EMAA-EGO2	466	508	EMAA-SEGO2	468	514
EMAA-EGO5	468	509	EMAA-SEGO5	466	512

The enhancement of thermal stability of the EMAA matrix in the presence of graphite oxides may be attributed to the tortuous path that graphite particles create in the filled EMAA, delaying diffusion of the volatile decomposition products in the EMAA matrix, which is not a process that occurs in the pure EMAA.

In addition, incorporating oxidised graphite, SGO and SEGO into EMAA matrix produced EMAA layered composites with higher thermal stability compared with that of EMAA filled with GO and EGO and was solely attributed to oxidative treatment of graphite. The higher thermal stability could be attributed to the volatilisation and/or decomposition of intercalates at higher temperatures, such as HNO_3, but in particular $KClO_3$, which has a boiling temperature of 122 °C and degradation temperature of 400 °C.

The difference between the thermal stability of EMAA filled with SGO and SEGO was negligible. The same trend was observed for EMAA filled with GO and EGO. There is little difference in the thermal stability of EMAA in the presence of GO and EGO. In addition, as shown in Figure 5.7, pure EMAA degraded completely at 800 °C, while filled EMAA shows higher char content or reduced weight loss at 800 °C as filler concentration increases. The char content of EMAA filled with 5 %wt of EGO was 4%. However, the char content of EMAA filled with GO at the same concentration level was marginally higher. The difference between the char content of EMAA filled with GO and EGO was negligible. In the case of these results show that further oxidative treatment of graphite (SGO and SEGO) prior to dispersion in EMAA matrix enhances the thermal stability of EMAA layered composites. This attribute is beneficial when applied to fire retardant application.

5.3.5 Mechanical property of EMAA layered composite

5.3.5.1 Tensile property

Figure 5.9 demonstrates a typical example of stress-strain curves of EMAA-SGO composite obtained according to the experimental parameters given in Chapter 3.

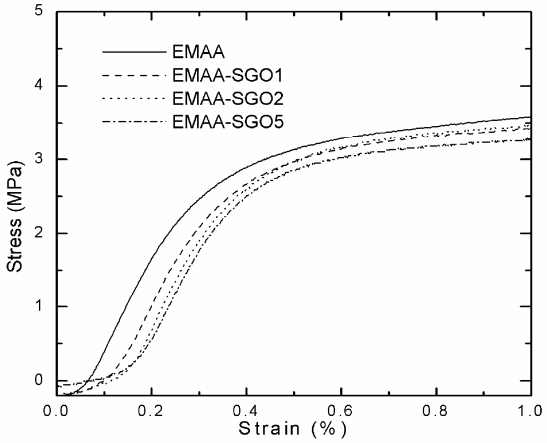

Figure 5.9 Stress-strain curve of filled EMAA-SGO

From the stress-strain relationships of all the EMAA layered composite materials, the shear modulus, G and yield stress were calculated, and are given in Table 5.7. The errors indicated on the σ/ε curve of G and yield stress were calculated from the 95% confidence interval from five replicates. G is commonly used as a measure of the stiffness of the specimen and is typically calculated from the slope of the initial linear portion of the σ/ε curve. However, close inspection of the stress-strain curves obtained from all of the filled EMAA indicated that no linear region existed, as is typical in elastomeric materials. Therefore, the shear modulus reported was calculated from stress required to reach a fixed strain of 2% for each material. In general, the modulus of EMAA was found to decrease upon addition of graphite oxide fillers.

The yield stress of EMAA containing GO and SEGO was found to be lower than that of pure EMAA. However, this was not the case for EMAA filled with EGO and SGO. The results, reported in Table 5.8, are influenced by the combination of changes in graphite composition, type, treatment together with nucleation of EMAA crystallisation and the interactions of these variables. Interpretation of the results for G and yield stress is complex and was found to require statistical analysis.

Table 5.7 Shear moduli and yield stress of filled EMAA

	G (MPa)	Yield stress (MPa)		G (MPa)	Yield stress (MPa)
EMAA	9.27±1.28	2.23±0.04			
EMAA-GO1	6.57±1.06	2.32±0.13	EMAA-SGO1	6.89±4.70	2.50±0.15
EMAA-GO2	4.23±1.66	1.76±0.06	EMAA-SGO2	3.87±1.37	2.48±0.13
EMAA-GO5	1.93±1.24	1.83±0.33	EMAA-SGO5	4.68±2.66	2.58±0.15
EMAA-EGO1	3.64±0.74	2.35±0.22	EMAA-SEGO1	3.34±1.87	2.34±0.07
EMAA-EGO2	4.63±0.71	2.45±0.07	EMAA-SEGO2	3.53±1.62	2.14±0.40
EMAA-EGO5	5.90±0.06	2.44±0.14	EMAA-SEGO5	7.32±1.57	2.18±0.03

A statistical analysis was performed on G and yield stress values obtained for the filled EMAA. The objective of this statistical analysis was to determine the effects of assigned variables for the various types of graphite oxide that may contribute to the mechanical properties of EMAA layered composites. The variables considered were concentration levels, oxidative treatment and structure or type of graphite oxide filler. The relationship or interaction as well as the independent effects of these variables on the EMAA layered composites were investigated. The effects of these variables were determined by applying analysis of variance (ANOVA), in particular the Balance ANOVA using the statistical software, Minitab. The probability, p-value, from the analysis of variance of G and yield stress is shown in Table 5.8. The analyses of G and yield stress quantify the individual effects of concentration, oxidative treatment, structure, or type of filler and the interaction between these variables were assessed. The common a-level of 0.05 was chosen for the test.

In the analysis of G, the individual effects of concentration, oxidative treatment, structure, or type of filler and the interaction between these variables were assessed. The p-value, for the interaction variables for both concentration-structure and concentration-treatment of filler was 0.000, and 0.001, respectively. Since the p-value calculated from both interaction variables is less than the chosen a-level of 0.05, the effect on G is significant. This means a significant variation in G of filled EMAA is associated with the variation in both the concentration-structure and concentration-treatment of filler. The effects of concentration-structure are similar to concentration-oxidative treatment-structure of filler. The interaction between variables oxidative treatment-structure of filler as well as the interaction between the three variables is greater than 0.05, indicating that these variables does not play an important role in the outcome of the G of EMAA. It is noted that the interaction between oxidative treatment-structure of filler is lower compared with the interaction between the three variables.

Therefore, the former interactions are more significant than the latter. Interestingly, the effects of the independent variables indicate that concentration level of graphite oxide in the EMAA matrix is more significant than oxidative treatment and structure of filler.

The individual effects as well as the interaction between these variables were also evaluated for the yield stress of filled EMAA. Table 5.8 shows the p-value for concentration-structure, oxidative treatment-structure of filler and interaction between the three variables were lower than 0.05. The effects of these interaction variables play a significant role in the final outcome of EMAA yield stress. However, the interaction between the oxidative treatment-structure of filler and the interactions between the three variables are more significant compared with that of concentration-structure of filler. The p-value for the interaction between concentration-oxidative treatment of filler is greater than 0.05. Thus, the interaction between these two variables is not significant. The individual effects of the variables are significant as indicated by their low p-value. The individual variables concentration level and oxidative treatment of filler have a p-value of 0.000 and is significant compared with the individual variable structure of filler. The individual variables affect the yield stress of EMAA matrix in the presence of graphite oxide.

From these results it indicates that the G of EMAA matrix is affected by concentration level of graphite oxide independently and the interaction between concentration-structure of filler of graphite oxide. In addition, the yield stress of EMAA matrix is affected by independent and the interactions between the variables.

Table 5.8 Analysis of variance of G and yield stress of filled EMAA

Variables	G	Yield stress
	p-value	p-value
concentration	0.007	0.000
oxidative treatment of filler	0.097	0.000
structure of filler	0.901	0.015
concentration-oxidative treatment of filler	0.001	0.045
concentration-structure of filler	0.000	0.003
oxidative treatment-structure of filler	0.102	0.000
concentration-oxidative treatment-structure of filler	0.835	0.000

5.3.5.2 Thermo-mechanical property

The dynamic mechanical and thermal behaviour of the pure and filled EMAA were determined according to the experimental parameters described for DMA in extension mode in Chapter 3. The storage modulus, E′, was used to assess the elastic (stiffness) behaviour of the materials tested, with the resultant values as a function of temperature presented in Figures 5.10a to d. For the purpose of clarity an inset was added, which displays the E′ from 10 to 35 °C.

At –35 °C, E′ of filled EMAA decreased upon addition of graphite oxide. This indicated the layered composites decreased in stiffness at this temperature with increasing graphite oxide concentration. The lowest E′ of EMAA was observed at 5 %wt of SEGO. As the temperature increased to 25 °C, some of the filled EMAA showed an increase in E′ as represented in the inset. The E′ of filled EMAA above 1 %wt of GO were approximately 3 to 19 MPa. EMAA filled with 2 and 5 %wt of EGO possessed a lower E′ than that of pure EMAA. In the case of EMAA filled with oxidised graphite, E′ was found to be lower at 1 %wt of SGO and 5 %wt of SEGO as listed in Table 5.9. The E' of EMAA in the presence of graphite oxide was similar to those of tensile properties, in that no correlation could be made between the type of graphite oxide filler and/or concentration level in the EMAA and E′. As with results obtained from tensile testing DMA results are complex. The independent variables as well as the interactions between these variables from analysis of variance of tensile properties may have played role in the E' of EMAA layered composites.

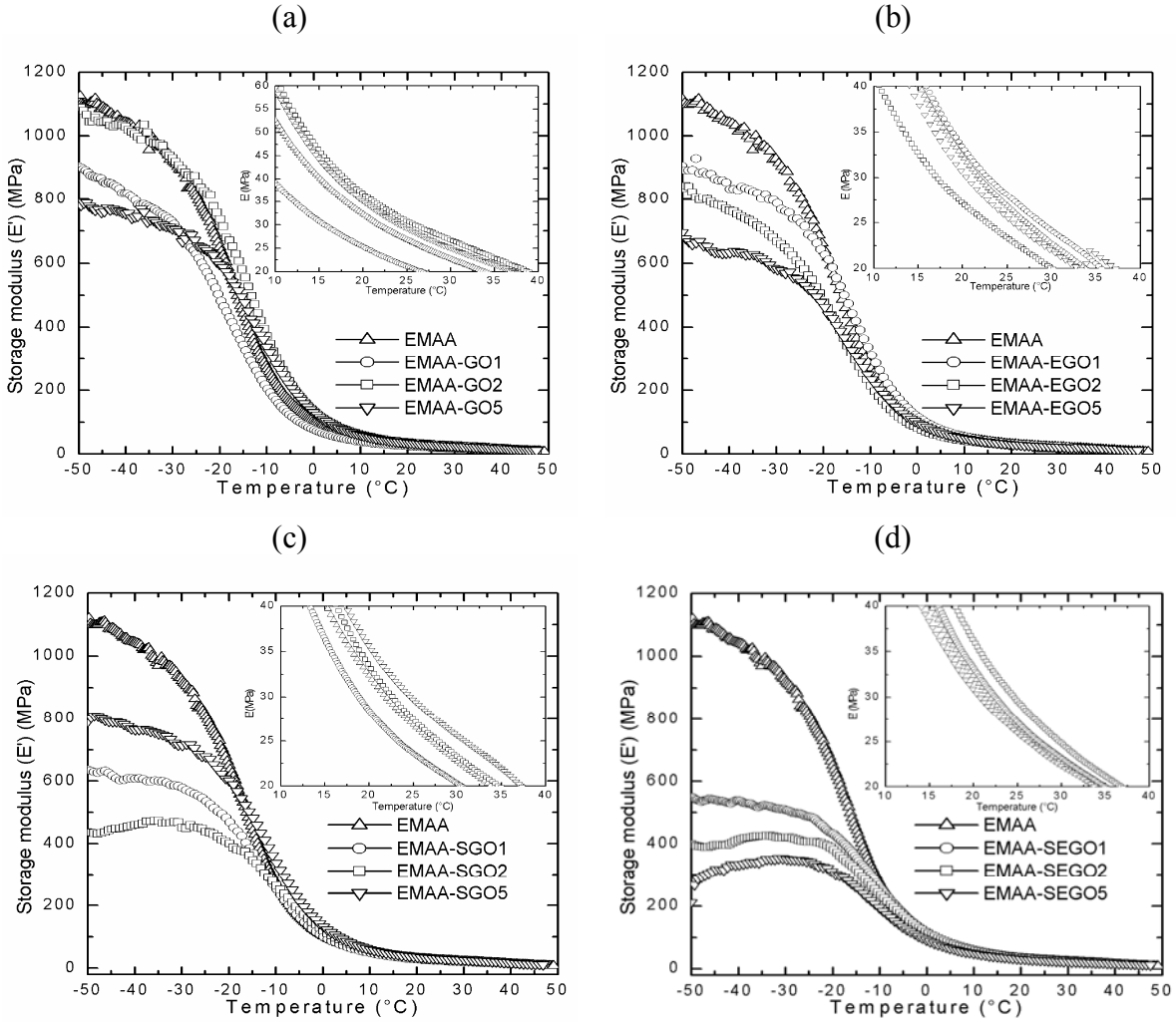

Figure 5.10 Storage moduli curve (a) EMAA-GO (b) EMAA-EGO (c) EMAA-SGO (d) EMAA-SEGO. Inset of E′ curves at temperatures between 10 to 40 °C

Table 5.9 Storage moduli and glass transition temperatures of filled EMAA

E′ (MPa)	Temperature (°C)				E′ (MPa)	Temperature (°C)			
	-35	10	25	T_g		-35	10	25	T_g
EMAA	948.0	52.6	26.8	-7.6					
EMAA-GO1	776.3	39.2	21.1	-6.2	EMAA-SGO1	600.1	48.7	23.6	-1.7
EMAA-GO2	987.8	61.7	45.4	-1.5	EMAA-SGO2	484.5	58.1	27.5	-0.1
EMAA-GO5	734.6	59.4	29.3	-0.9	EMAA-SGO5	751.4	60.7	29.7	-1.9
EMAA-EGO1	388.2	55.5	28.1	-6.3	EMAA-SEGO1	523.8	55.9	27.2	-5.1
EMAA-EGO2	729.8	41.4	23.4	-6.9	EMAA-SEGO2	425.4	60.5	27.1	-1.6
EMAA-EGO5	631.1	49.8	25.6	-6.3	EMAA-SEGO5	345.2	49.2	25.9	-3.7

The glass transition temperature, T_g, is the reversible change in an amorphous polymer between a viscous or rubbery condition to or from a hard or relatively brittle condition. T_g can be determined from the peak of either loss modulus, E″ (Appendix 3), or loss tangent, Tan(δ) curves[146,147]. In this study, T_g was obtained from the peak of the Tan(δ) curve (Figures 5.11a and d). In all cases, the T_g of filled EMAA was found to be higher when compared with pure EMAA, as listed in Table 5.9. The increase in T_g is ascribed to the decreased mobility of the polymer molecules. This was due to the interaction between the polar groups of EMAA and the graphite oxides. This observation is consistent with the behaviour of other filled polymeric systems[11]. Consequently, EMAA filled with SGO and SEGO had higher T_g compared with that of EMAA filled with GO and EGO. This is due to the presence of more oxidised graphite surface as a result of oxidative treatment.

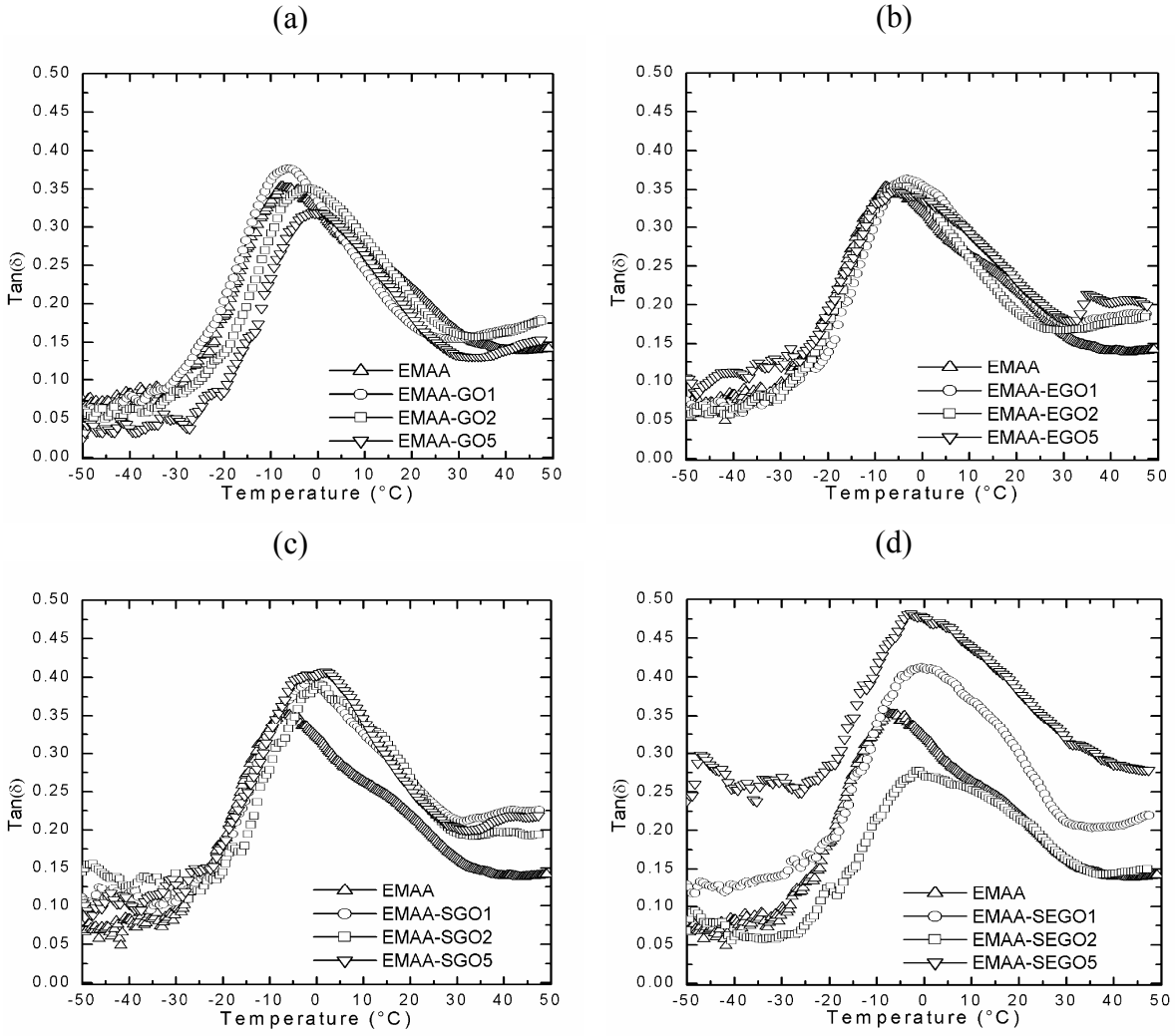

Figure 5.11 Tan(δ) curves of filled EMAA (a) EMAA-GO (b) EMAA-EGO (c) EMAA-SGO (d) EMAA-SEGO

5.3.6 Dielectric property

Like most polymers, EMAA is not electrically conductive, and has an electrical conductivity of about 10^{-16} $S.cm^{-1}$ at room temperature, consistent with the magnitude of an insulator[11]. Several studies have shown that addition of graphite can increase the electrical conductivity of polymers[78]. In addition, many researchers have shown that EGO is a better conducting material than GO due to its interconnected network structure, which forms the conducting network[122,175]. The permittivity and loss factor of filled EMAA were measured to characterise molecular relaxations. The definitions of these properties have been described in Chapter 3. The permittivity, ε', is the energy stored in a material and the dielectric loss factor, ε", is the conductivity of the material[11,148]. The dielectric properties EMAA composites at room temperature are listed in Table 5.10.

Table 5.10 Dielectric properties of filled EMAA at 25 °C

	log Permitivity ε'	log Loss factor ε"		log Permitivity ε'	log Loss factor ε"
EMAA	0.22	nd	EMAA	0.22	nd
EMAA-GO1	0.61	.88	EMAA-SGO1	0.33	nd
EMAA-GO2	0.88	0.96	EMAA-SGO2	1.33	1.28
EMAA-GO5	0.14	1.08	EMAA-SGO5	0.16	nd
EMAA-EGO1	0.14	nd	EMAA-SEGO1	0.39	nd
EMAA-EGO2	0.20	nd	EMAA-SEGO2	0.16	nd
EMAA-EGO5	0.20	nd	EMAA-SEGO5	1.32	1.24

nd; not detected

The dielectric properties of pure EMAA were measured for comparison. In general, ε' of filled EMAA was observed to decrease upon addition of graphite oxide filler. Interestingly, ε' of EMAA was at its highest when filled with 2 %wt of SGO and 5 %wt of SEGO, 1.33 and 1.32, respectively. It is proposed that at this concentration the energy stored was high due to polar surfaces present as a result of oxidative treatment. ε" of pure EMAA was, as expected, undetectable. The ε" of EMAA-GO increased upon addition of GO, however this was not observed for EMMA-EGO. In the case of EMAA in the presence of oxidised and exfoliated graphite, ε" was only detected for EMAA filled with 2 %wt of SGO and 5 %wt of SEGO. It is assumed that these graphite oxides are highly dispersed in the EMAA matrix. As seen in Table 5.10 some ε" of EMAA layered composites were not detected suggesting that graphite

particles did not form a conducting network as a result of random dispersion in the EMAA matrix.

The dielectric property or electrical conductivity of EMAA in the presence of graphite oxide fillers in general did not improve. The electrical conductivity depends very much on the geometry of the conducting filler, and it has been reported that filler particles with a higher aspect ratio, such as sheet-like or fibre-like objects, have an advantage in forming a conducting network in a polymer matrix compared with fillers of a round or elliptical shape, which have a lower aspect ratio[9,10]. Several studies have shown that intensive processing[176] significantly affects both dielectric properties and the structure of polymer graphite nanocomposites[4,177]. In this case, the high shear environment provided by the dispersive action of the Ultra-Turrax disperser reduced the graphite particle size and resulted in their uniform dispersion in the EMAA matrix, as shown by transmission electron microscopy (Figure 5.2). Consequently, high shearing disrupted the connections between the graphite layers causing them to separate, thus too low to provide a conducting path network for electrons[174].

5.4 Conclusion

Various types of graphite oxide were dispersed in EMAA, in different concentrations by solution blending. The effects of the various types of graphite oxides on the crystalline structure, thermal and thermo-mechanical properties of EMAA layered composites were investigated. The structure, surface area, and interlayer spacing (*d* spacing) of graphite oxide before dispersion were investigated.

The WAXD measurements of the oxidised graphite, formed using the Staudenmaier method, showed a significant change in its interlayer spacing, indicating that intercalation of HNO_3-H_2SO_4 and $KClO_3$ occurred in the graphite layers. Oxidation of graphite changed the crystalline structure as well as increasing the surface area, as shown by WAXD and BET analyses.

The WAXD analysis of EMAA layered composites revealed that there was no change in *d* spacing in the graphite layers regardless of type of graphite oxide filler in the EMAA matrix. This indicated that the graphite layers were ordered and multi-layered and that the dispersion technique used was unable to affect the order or exfoliate the graphite layers in the EMAA matrix uniformly. In addition, the dispersion technique used was unable to affect the order or

exfoliate the graphite layers in the EMAA matrix. The crystalline thickness of the various types of graphite oxide, calculated using the Scherrer equation, decreased in the EMAA matrix. The crystalline thickness of the various types of graphite oxide in the EMAA matrix was in the nanoscale dimension.

The crystallisation behaviour and degree of crystallinity of filled EMAA from DSC analysis showed that the various types of graphite oxide acted as a heterogenous nucleating agent. The graphite particles act as nucleating sites thereby decreased EMAA chain mobility and, as a result, induced the crystallisation of EMAA within the layered composites. In addition, the EMAA crystallinity decreased upon addition of all graphite oxides. Additionally, oxidative treatment of graphite flakes showed that it was an efficient nucleating agent. This was due to its large surface area and surface polarity, present as a result of the oxidative treatment it was exposed to, which increased its compatibility with EMAA matrix.

The thermal stability of EMAA, determined from TGA, was enhanced in the presence of the various types of graphite oxide. The graphite particles were found to act as a physical barrier between heat and EMAA matrix, thereby delaying its degradation. The oxidative treatment of graphite flakes further enhanced the thermal stability of EMAA due to intercalate trapped between the graphite layers being volatilised and/or decomposed at higher temperatures.

The tensile properties, including shear modulus and yield stress, of EMAA were found to decrease upon addition of graphite oxide filler. The analysis of variance showed that the shear modulus is affected by the complex interaction of variables, between concentration level and structure of graphite oxide. The interaction between concentration, oxidative treatment and structure of graphite oxide greatly affected the yield stress of EMAA layered composites. The complex interaction between these variables plays an important role in the resulting shear properties of EMAA. The elastic modulus of EMAA layered composites determined from DMA measurement decreased upon addition of graphite oxide filler. The results showed no correlation between the type of graphite oxide or concentration level in the EMAA and the resultant elastic modulus. The reduction in elastic modulus is due to the weak interfacial adhesion between the various types of graphite oxide due to high shearing provided by the Ultra-Turrax disperser. The elastic modulus of EMAA layered composites was similar to its shear modulus obtained from tensile testing. Therefore, the assigned variables may play a role in the elastic modulus of EMAA layered composites. The glass transition of most EMAA materials studied was found to have been increased in the presence of graphite oxide fillers

due to reduction in chain mobility of the EMAA molecules as a result of interaction between EMAA and graphite oxide.

The dielectric properties of EMAA in the presence of graphite did not improve due to the absence of a conducting network in the EMAA matrix, even in the presence of up to 5 %wt of graphite oxide, in both expanded and unexpanded forms. This is attributed to the high shearing provided by the Ultra-Turrax disperser disrupted the conducting path network.

Chapter 6 Poly(propylene-graft-maleic anhydride) layered expanded graphite oxide composites via solution blending

6.1 Introduction

The thermal and thermo-mechanical properties of polypropylene (PP) in the presence of layered expanded graphite oxide (EGO) were investigated. However, since PP does not include any polar groups in its backbone, uniform dispersion of the EGO in PP matrix is not likely. Therefore, maleic anhydride (MA) was grafted to the PP matrix to act as a compatibiliser with the EGO. The grafting of MA onto PP is expected to increase the polarity of the PP matrix and hence result in enhanced adhesion to the EGO. The hydrogen bonding between the polar functional groups on the surface of EGO and MA grafted to PP matrix is considered to be a key attribute in the formation of poly(propylene-graft-maleic anhydride) layered expanded graphite oxide composites (PPMA-EGO). Two types of PPMA-EGO composites were prepared via solution blending using different mixing methods - distributive (low shear) and dispersive (high shear) mixing. The effects of the preparative mixing methods in the formulation of PPMA-EGO on the properties of the PPMA matrix were investigated.

6.2 Experimental

6.2.1 Preparation of grafted poly(propylene-graft-maleic anhydride)

A reactive extrusion procedure was adopted for the functionalisation of PP. An *Axon* BX-12 extruder, equipped with a 12.5 mm Gateway screw, was utilized for the procedure. Firstly, 2.5 g of MA was dissolved in approximately 50 to 70 mL of acetone. The dissolved MA was then added to and stirred in a large beaker containing 250 g of PP to ensure even coating of MA onto the PP pellet surfaces. The acetone was then evaporated by gentle heating over a steam cone, leaving a thin coating on the polymer bead surface. The remaining solvent was removed by placing the coated PP beads onto a large Petri dish and into a vacuum oven for 3 h at 30 °C. Additionally, 2.5 g of benzoyl peroxide was tumble mixed with the coated PP prior to reactive extrusion. The extruder was configured for a screw speed of 70 rpm, with the heating zones set at temperatures of 150, 200, 200 °C for feed, metering, compression respectively, and 160 °C for the die zone. The coated pellets were gravity-fed into the hopper, with molten strands immersed in ice-cooled deionised water prior to pelletizing. The PPMA

was subsequently purified by Soxhlet extraction for 24 h with acetone to remove any residual MA or low volatility impurities. The PPMA was finally dried under vacuum (10^{-1} torr) at 30 °C for 24 h.

6.2.2 Preparation of PPMA-EGO composite

Two types of PPMA-EGO, utilising two different mixing methods, were prepared by solution blending. EGO was prepared by exfoliating graphite flakes at 800 °C for 30 s, which was added to a hot-chloroform PPMA solution. EGO was added to the solution to provide weight fractions of 0.01, 0.02 and 0.05, relative to the PPMA.

The PPMA-EGO mixtures were then subjected to either highly distributive (low sheared) or highly dispersive (high sheared) mixing. These mixing methods were applied by a continuous stirring method, utilizing a magnetic stirrer (PPMA-stEGO), or with an Ultra-Turrax (IKA Works Asia Sdn Bhd) disperser (PPMA-shEGO), operating at a speed of 12000 rpm, respectively. The shearing mechanism of the disperser has been described in Chapter 3. The hot mixtures of PPMA-EGO were then poured slowly into stirred cold ethanol. The PPMA-EGO precipitates were filtered on a Buchner funnel and dried under vacuum at 50 °C for 24 h.

PPMA-EGO films were prepared by hot-pressing a small amount, approximately 0.5 to 1 g, of PPMA-EGO between two PTFE sheets and heated aluminium platens. An aluminium template (3x2x1 mm) was used to form the films to the desired shape. The press (Thomas Optical and Scientific Co. Pty Ltd) with Activon (Grasby-Specac) temperature controller was preheated to 170±1 °C prior to pressing. No pressure was applied initially for 2 min to allow the PPMA-EGO to melt. The pressure was then raised slowly to 13 kPa and held for 2 min, and pressure was further increased to 20 kPa for an additional 3 min.

Table 6.1 demonstrates the nomenclature for the PPMA-EGO materials made in this study. The prefixes of 'st' and 'sh' refer to the distributive and dispersive mixing methods, respectively. The concentration levels of EGO are supplied as suffixes, such that PPMA-stEGO1 refers to PPMA filled with 1 %wt of EGO prepared by the described distributive mixing method.

Table 6.1 Abbreviations of filled PPMA-EGO composites

Distributive mixing (EGO %wt)		Dispersive mixing (EGO %wt)	
PPMA	0	PPMA	0
PPMA-stEGO1	1	PPMA-shEGO1	1
PPMA-stEGO2	2	PPMA-shEGO2	2
PPMA-stEGO5	5	PPMA-shEGO5	5

6.3 Results and Discussion

6.3.1 Structural characteristic of sheared expanded graphite oxide

As previously described in Chapter 5 exfoliating GO at high temperatures increased the dimension perpendicular to the graphite layers of the GO. The graphite layers collapsed and deform randomly forming an interconnected network structure. Prior to dispersion of EGO in PPMA (Figure 6.1a), SEM was obtained. Figure 6.1b and c shows the effect of shearing on the structure of EGO. The graphite processed in a low shear environment (stEGO), was found to have intact accordion-like structure. However, EGO subjected to high shearing (shEGO) demonstrated disruption to the interconnected network of the accordion bellow.

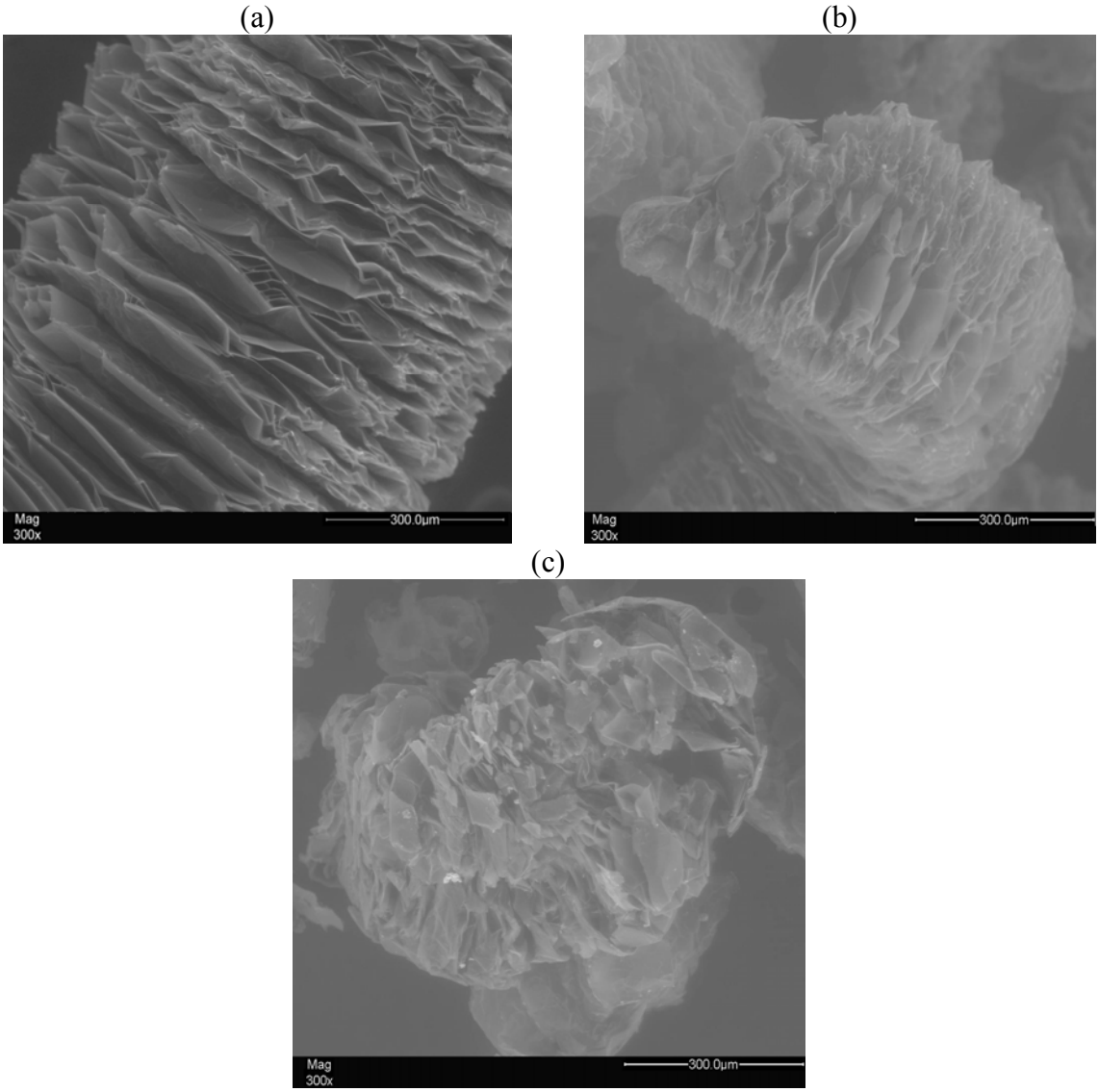

Figure 6.1 SEM micrographs of EGO (a) EGO and after shearing (b) stEGO (c) shEGO

Figures 6.2a and b represent the SEM micrographs of PPMA-stEGO and Figures 6.2c and d represent the micrographs of PPMA-shEGO. It was found that fracturing of PPMA-EGO resulted in debonding at the interface between the PP and the surface of the graphite particles. This resulted in more graphite particles being revealed in the SEM technique than might be expected based on the bulk composition. The SEM micrographs clearly demonstrate the difference in the dispersion techniques of the graphite particles. Figures 6.2a and b of low sheared PPMA-stEGO represent a distributive mixing, meaning the graphite particles were circulated within the PPMA matrix. Figures 6.2c and d shows a dispersive mixing (high

sheared) of graphite particles within the PPMA-shEGO. Dispersive mixing was the process whereby the graphite particles were sheared with a high shearing action provided by the Ultra-Turrax disperser to reduce particle size and cause random scattering within the PPMA matrix.

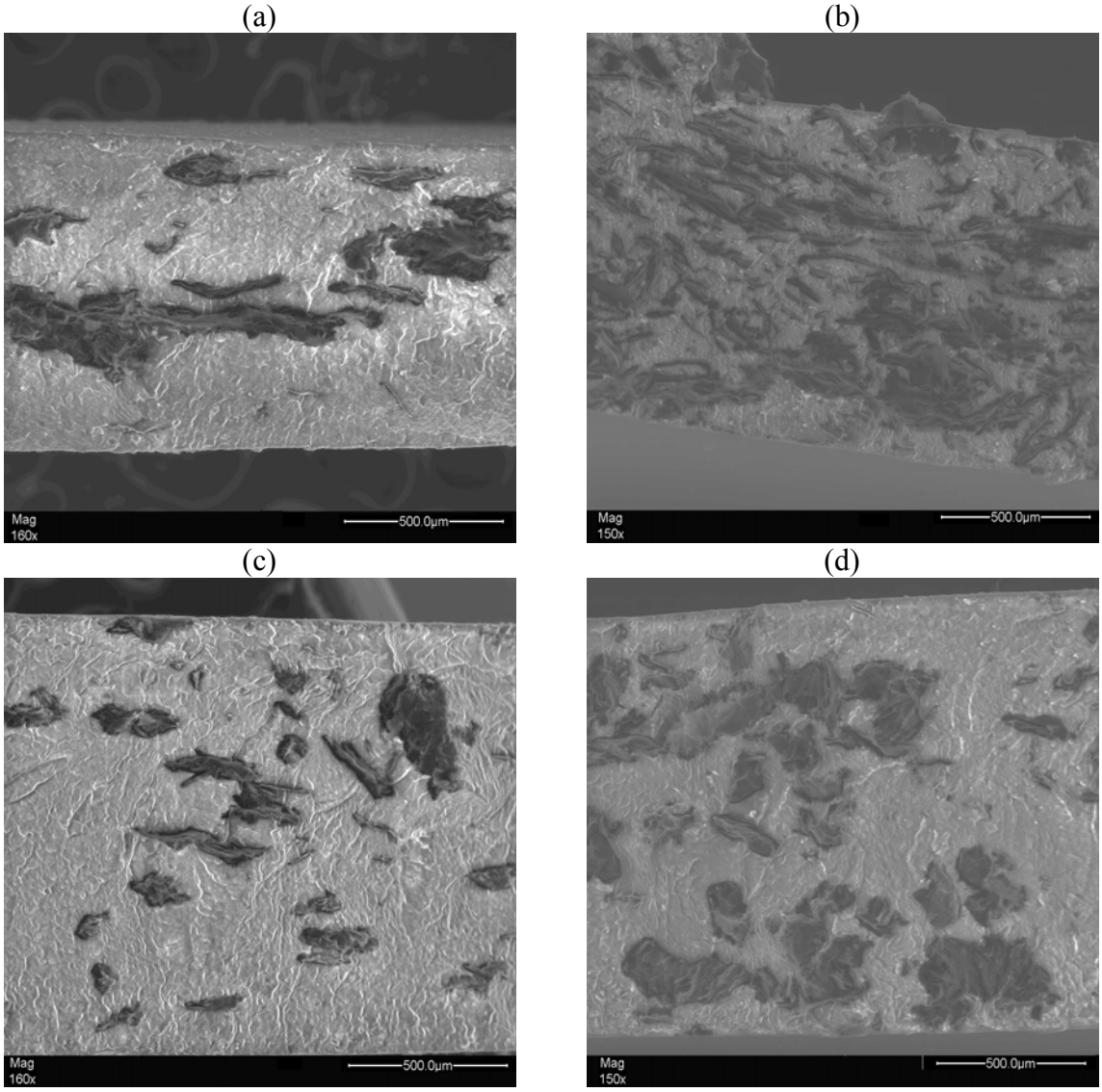

Figure 6.2 SEM micrographs of PPMA-EGO (a) PPMA-stEGO2 (b) PPMA-stEGO5 (c) PPMA-shEGO2 and (d) PPMA-shEGO5

It can be seen by comparison of Figure 6.3 and Figure 6.1c that the internal structure of shEGO in PPMA was different to that of the original shEGO. The interconnected network of shEGO in PPMA-shEGO is not observed, but rather an ordered and multilayered structure similar to that of GO in Figure 6.1a is observed. In addition, evidence of PPMA intercalation in the graphite layers is absent.

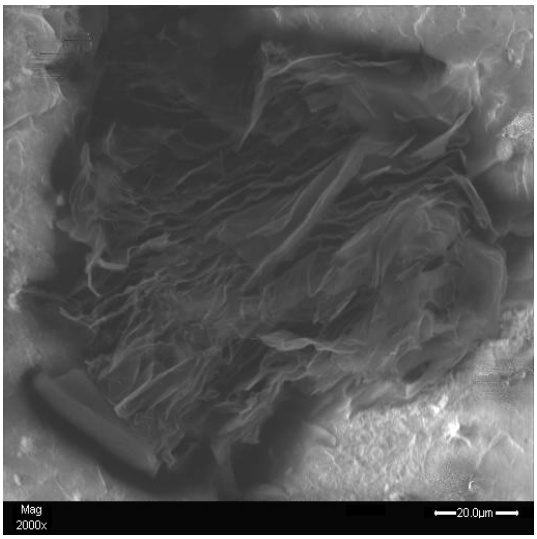

Figure 6.3 SEM micrographs of PPMA-shEGO5

6.3.2 BET surface area property of sheared expanded graphite oxide

The surface area properties of GO, stEGO and shEGO were obtained to determine the effect of the preparative mixing method on the surface area properties of EGO. The BET surface area, A_s and average pore diameter measurements were measured according to the experimental parameters described in Chapter 3. Briefly, prior to surface area measurements, all EGO were degassed under vacuum. Degassed EGO was then immersed in N_2 in preparation for surface area measurements. The surface area measurements obtained are listed in Table 6.2. The adsorption-desorption isotherms of N_2 in both EGO materials exhibit typical type of II isotherms[115,178]. The A_s of GO was found to be 0.87 $m^2.g^{-1}$ and with an average pore diameter of 11.57 nm. The surface area properties of stEGO and shEGO were higher compared with GO. The A_s of stEGO and shEGO were found to be more than five times higher than the A_s of GO, with A_s of 3.89 and 4.79 $m^2.g^{-1}$, respectively. These results suggest that the intensity of shearing affects the surface area properties of EGO, as measured by BET surface analyser. The high shearing action provided by the Ultra Turrax disperser resulted in more graphite particles with a larger A_s. and increase average pore diameter in comparison with shEGO. Hence, the average pore diameter of GO and both types of EGO were in the nanometer dimension.

Table 6.2 Surface area properties of GO, and sheared expanded graphite oxide: stEGO and shEGO

	GO	stEGO	shEGO
BET surface area A_s (m^2g^{-1})	0.87	3.89	4.79
Average pore diameter (nm)	11.57	7.73	10.79

6.3.3 Interlayer spacing and crystalline thickness of sheared expanded graphite oxide filler in PPMA

WAXD was used to determine the change in interlayer, *d* spacing of EGO in PPMA matrix according to the experimental conditions provided in Chapter 3. The diffractogram of GO, as previously discussed from Chapter 5, consists of peaks corresponding to the diffraction of the (001) and (002) planes at 2θ=11° and 26° (*d* spacing 0.701 and 0.335 nm). The diffraction (001) and (002) peaks correspond to graphite oxide and graphite. In the case of stEGO and shEGO (Figure 6.4) the (002) peaks are observed in the same range when GO was exfoliated to form EGO. The shifting of the (002) peaks to lower 2θ indicates separation of graphite layers. A marginal difference in the 2θ of stEGO and shEGO was observed (2θ=27° stEGO and 26° shEGO), which indicates that the interlayer separation was maintained after shearing. In addition, the presence of the (001) peak is no longer detected in either diffractogram, indicating that graphite layers may have been exfoliated.

(a)

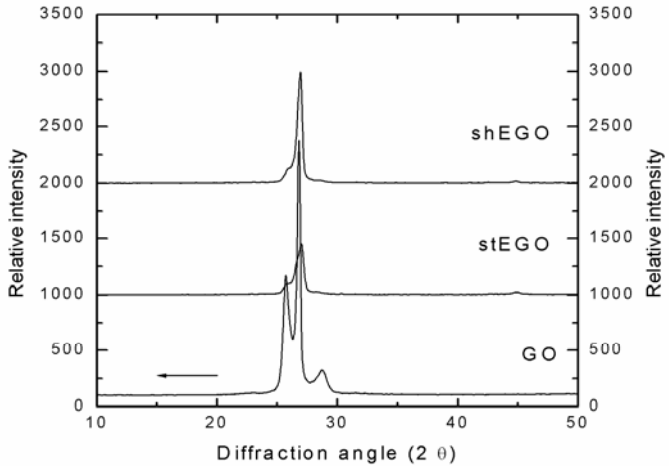

Figure 6.4 Diffractogram of GO and EGO after shearing: stEGO and shEGO

The diffractogram of pure PPMA exhibited three prominent peaks corresponding to diffraction planes; (110), (040) and (130) at 2θ=14, 17 and 19°. This diffraction planes represents the monoclinic (α) crystalline phase of PPMA[7,22,179]. Additionally, a small β peak at 2θ=16° is visible as a shoulder of (040) peak as shown in Figures 6.5a and b[34,179].

In Figures 6.5a and b, the diffractograms, of PPMA-EGO showed (α) crystalline phase within the 2θ range of 14 to 20° and the (002) peak at about 2θ=26°. This indicates that the stable (α) crystalline phase will form predominantly in the materials regardless of crystallisation temperature[179]. With the exception of PPMA-shEGO1, the β peak is no longer visible for most of the PPMA-EGO. The presence of the β peak in PPMA-shEGO1 is a result of PPMA-EGO film preparation involving melting and rapid cooling causing rapid crystallisation. Grady et al and Kotek et al[34] previously reported the formation of β crystalline phase, whereby β crystals form via crystallisation in the presence of special nucleation agents such as graphite. Their findings showed that graphite behaved as a nucleating agent promoting the nucleation of the β crystalline phase of PP[34]. The (α) crystalline phase is the most thermodynamically stable, however the β crystalline phase is less thermodynamically stable and has a higher growth rate[34], which explains the findings observed for PPMA-stEGO1.

The (110) and (040) peaks of PPMA in the diffractograms of PPMA-EGO show a marginal shift in 2θ. The diffractograms of PPMA-stEGO demonstrated a shift to higher 2θ of the (110) and (040) peaks, however this was not observed in the diffractograms of PPMA-shEGO, where the (110) and (040) peaks were found to have moved to lower 2θ. Cheng et al[180] reported that the shift in (110) and (040) peaks to higher 2θ indicated tighter packing in the crystal unit cell in directions perpendicular to the chain direction. The relative intensities of the (110) and (040) peaks changed in the diffractogram of PPMA-EGO. It is interesting to note that the relative intensity of (040) increased upon addition of EGO. The variation of the relative intensity of (040) peak with respect to (110) peak was determined from WAXD and plotted as a function of concentration. This relationship is plotted in Figure 6.6. The (040)/(110) ratio was considerably more intense for PPMA-EGO than for pure PPMA. The peak ratio related to PPMA-stEGO was found to be enhanced in comparison with that related to PPMA-shEGO. These findings are in agreement with those reported by Zipper et al[181]. These authors found that the enhanced (040)/(110) ratio in the presence of graphite was a result of the strong preferential orientation parallel to the surface of PPMA-EGO.

Furthermore, the high relative intensity of (040)/(110) ratio suggests high crystallinity. It was therefore concluded that in this study there was a higher concentration of graphite particles serving as nucleating sites within the PPMA-EGO relative to pure PPMA. The nucleating effect of EGO in the crystallisation and melting behaviour of PPMA-EGO was further investigated using differential scanning calorimetry.

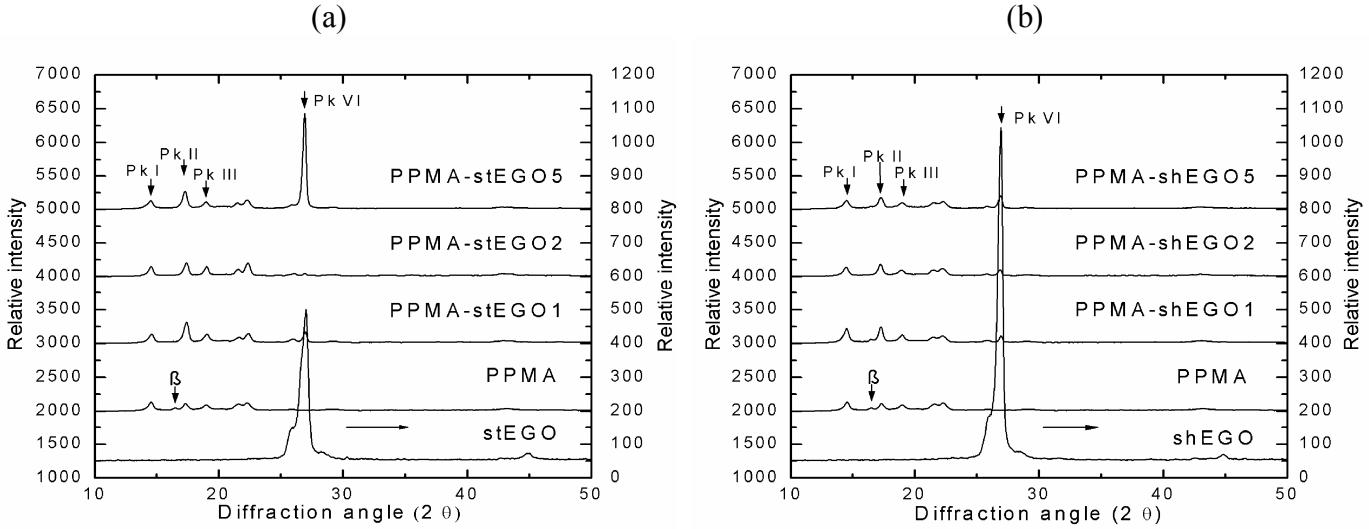

Figure 6.5 Diffractograms of (a) PPMA-stEGO (b) PPMA-shEGO

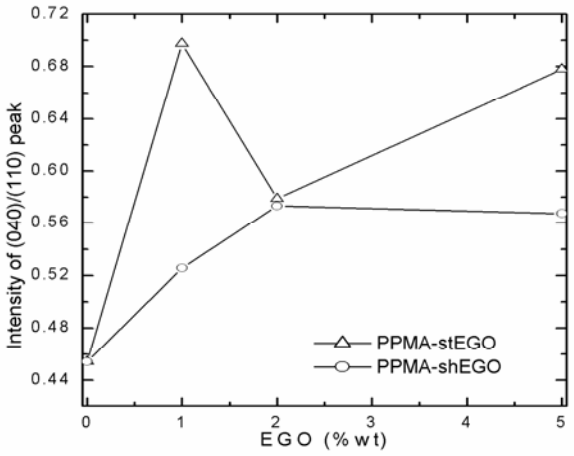

Figure 6.6 (a) Relative intensity ratio of (040)/(110) peaks in the diffractogram of PPMA-EGO as a function of EGO concentration

The (002) peaks within the diffractograms of PPMA-EGO indicate that some of the graphite layers may not have been exfoliated within the PPMA matrix. The *d* spacing calculated from the (002) peaks, using the Bragg equation (Equation 3.9), is listed in Table 6.3. It was found that *d* spacing of graphite layers in PPMA-EGO changed to a small, but measurable degree. This indicates that graphite layers in the PPMA-EGO were still ordered and multilayered and thus the preparative mixing methods used were unable to exfoliate the graphite layers in the PPMA matrix[132].

Table 6.3 Interlayer, *d* spacing and crystalline thickness of the (002) peak of stEGO and shEGO in the diffractogram of PPMA-EGO

	d spacing of (002) peak (nm)	$L_{(002)}$ (nm)		*d* spacing of (002) peak (nm)	$L_{(002)}$ (nm)
stEGO	0.329	11.356	shEGO	0.331	18.384
PPMA-stEGO1	0.330	29.702	PPMA-shEGO1	0.330	25.744
PPMA-stEGO2	0.331	32.174	PPMA-shEGO2	0.331	38.608
PPMA-stEGO5	0.331	22.710	PPMA-shEGO5	0.331	29.704

The crystalline thickness of both types of EGO was calculated using the Scherrer equation. The Scherrer equation estimates the crystalline thickness perpendicular to the reflection plane of $L_{(hkl)}$. The $L_{(hkl)}$ was estimated from FWHM of the (002) peak of EGO in the presence and absence of PPMA matrix. The diffractograms of EGO and PPMA-EGO were subjected to Lorentz curve fitting and hence full details of $L_{(002)}$ analysis was described in Chapter 3. $L_{(002)}$ estimated from the Scherrer equation are listed in Table 6.3. The results reported in Table 6.3 indicate that both types of EGO were found to be in the nanometer dimension, however $L_{(002)}$ of stEGO was lower in comparison with shEGO. For PPMA-EGO, $L_{(002)}$ of stEGO and shEGO in PPMA matrix, increased and both types of EGO were in the nanometer dimension in the PPMA matrix.

6.3.4 Crystallisation, melting behaviour and crystallinity of PPMA-EGO

The thermal behaviour, such as T_c and T_m of PPMA in the presence of stEGO and shEGO were determined with DSC. Specimens of PPMA-EGO were cooled and melted from 20 to 200 °C at a rate of 10 °C.min^{-1}.

Figure 6.7 contains DSC thermograms of all PPMA-EGO materials, and demonstrates in all cases the presence of a characteristic peak of monoclinic (α) crystalline phase PPMA[182], confirming the WAXD findings. According to Jin et al[183], PP crystallises with the diffraction (004) plane parallel and diffraction (110) plane perpendicular to the interface. The crystallisation with the diffraction (004) plane lying flat is consistent with nucleation at the interface. Lotz et al[184] reported that the diffraction (110) plane, which has the lowest density of the methyl functional group, is likely to be involved in epitaxial interactions.

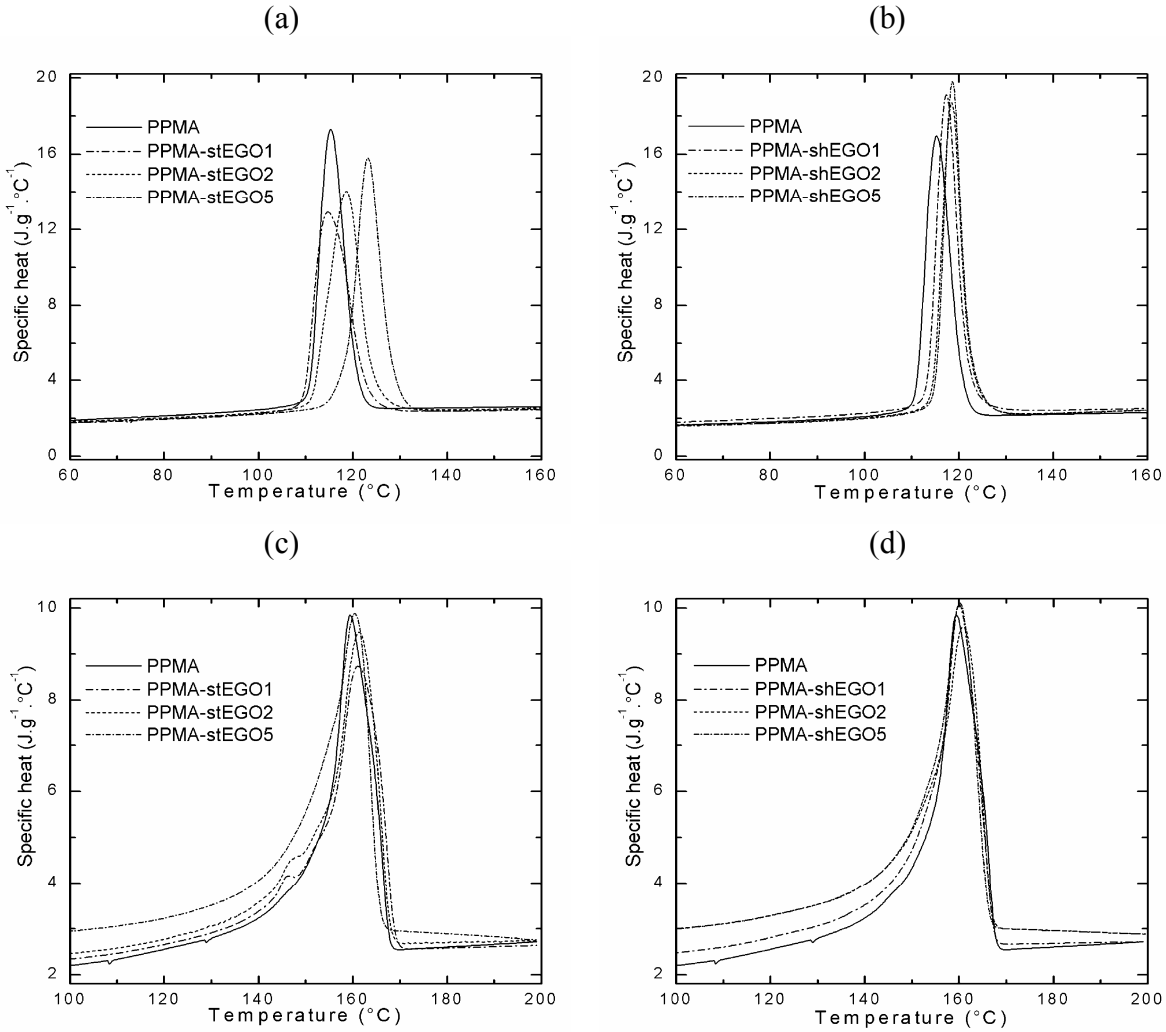

Figure 6.7 Crystallisation curves of (a) PPMA-stEGO (b) PPMA-shEGO and melting curves of (c) PPMA-stEGO (d) PPMA-shEGO

T_c and T_m measured from the peak maximum of the DSC thermograms, for all PPMA-EGO materials are shown in Figure 6.7 and listed in Table 6.4. The pure PPMA has a T_c of 115 °C and a T_m of 159 °C. In the presence of stEGO the T_c of PPMA shifts to higher temperature as stEGO concentration increases.

A similar trend in T_c was observed for PPMA-shEGO. The results reported in Table 6.7 show that the T_c of PPMA-stEGO was marginally higher compared with PPMA-shEGO. For example PPMA filled with 5 %wt of stEGO was 123 °C, while PPMA filled with 5 %wt of EGO was 121 °C. The T_m of PPMA-EGO was marginally higher than pure PPMA. The differences of the temperature changes between the layered composites in particular the T_m was not significant. The results obtained suggest that EGO behaved as a heterogeneous nucleating agent for the PPMA. Introduction of EGO provided more nucleating sites as a result of its large surface area. Increases in both T_c and T_m have been reported for layered composites such as PVDF-clay[60], PP-clay[182] and PA-6-graphite[10].

Table 6.4 Crystallisation, melting temperatures and crystallinity of PPMA-EGO

	T_c (°C)	T_m (°C)	χ_c		T_c (°C)	T_m (°C)	χ_c
PPMA	115	159	0.47				
PPMA-stEGO1	117	160	0.48	PPMA-shEGO1	117	160	0.49
PPMA-stEGO2	119	161	0.49	PPMA-shEGO2	119	160	0.48
PPMA-stEGO5	123	160	0.52	PPMA-shEGO5	121	160	0.47

The change in PPMA χ_c, was calculated based on a value of ΔH_f=209 $J.g^{-1}$, which is the enthalpy of fusion of pure PP crystals[142]. A marginal increase in χ_c, of PPMA was observed in the presence of stEGO. The χ_c of PPMA in PPMA-stEGO increased from 0.47 to 0.52 at 5 %wt of stEGO. In contrast, the χ_c of PPMA decreased at shEGO concentration above 1 %wt. The decrease in χ_c may have been a result of the greater dispersion of graphite particles within the PPMA-shEGO, such that when the concentration was high, there was concomitantly more surface area to adsorb PPMA. The graphite particles behaved as a heterogeneous nucleating agent but at the same time, the graphite particles hinder chain mobility, leading to reduction in the rate of crystallite growth and, as a result the domains of the crystalline phase as well as the crystal size of PPMA is reduced.

Interestingly, PPMA filled with 1 %wt of shEGO had a high χ_c (0.49), which can be attributed to the presence of the β crystalline phase. This confirms the WAXD findings obtained for PPMA-shEGO1. This is possibly due to β crystalline phase being less thermodynamically stable, however it has a higher growth rate.

6.3.5 Thermal stability of PPMA-EGO

The thermal stability of PPMA-EGO under N_2 (thermal degradation, pyrolysis) was investigated. TGA was undertaken, from 30 to 800 °C at the rate of 20 °C.min^{-1}. The weight loss curves (TGA), and the derivative weight loss curves, (DTG), for PPMA-EGO are presented in Figure 6.8. The thermal degradation parameters such as $T_{d\ onset}$ and T_d of PPMA-EGO calculated from the DTG curves for thermal degradation are listed in Table 6.5.

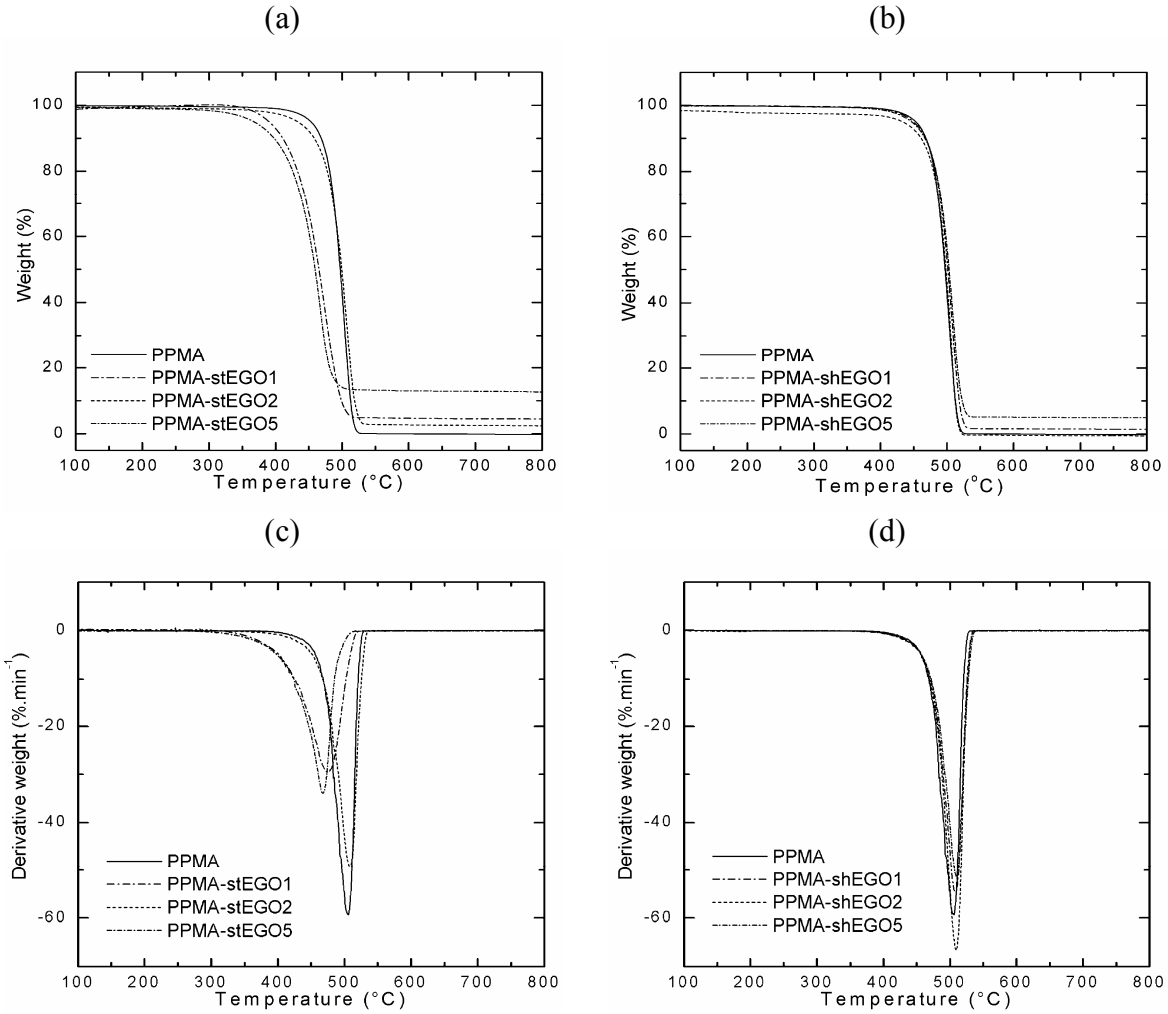

Figure 6.8 Weight loss curves of (a) PPMA-stEGO (b) PPMA-shEGO and derivative weight loss curves (c) PPMA-shEGO (d) PPMA-shEGO

The TGA curve of pure PPMA indicates that degradation occurs in a single stage, at temperatures between 400 to 550 °C. This process is attributed to scissioning of the main chain[185], with predominately the evolution of hydrocarbon species resulting in the observed weight loss. At temperatures beyond 550 °C, no residue remained. The TGA curves of all

PPMA-EGO materials studied showed that degradation occurred in a similar manner to that of as pure PPMA. However, the initial degradation began at earlier temperatures as low as 416 °C. This can be ascribed to the loss of water from the graphite layers, as well as degradation of low-molecular weight products in the graphite layers such as acids.

The low $T_{d\ onset}$ of PPMA-stEGO indicates poor thermal stability compared with pure PPMA. The decrease in T_d of PPMA-stEGO was typically in the range of 1 to 31 °C. $T_{d\ onset}$ of PPMA-shEGO decreased upon addition of shEGO similar to PPMA-stEGO, indicating poor thermal stability. However, this was not supported by the T_d of PPMA-shEGO. Incorporating shEGO, into PPMA produced materials with higher T_d as listed in Table 6.5. These results show that PPMA-shEGO has higher thermal stability relative to PPMA-stEGO and pure PPMA.

Table 6.5 Onset degradation and maximum rate of degradation temperatures and char content of PPMA-EGO in varying EGO concentration

	Temperature (°C)				Temperature (°C)		
	$T_{d\ onset}$	T_d	Char (%)		$T_{d\ onset}$	T_d	Char (%)
PPMA	482	505	0				
PPMA-stEGO1	430	475	5	PPMA-shEGO1	477	506	2
PPMA-stEGO2	476	506	2	PPMA-shEGO2	476	509	0
PPMA-stEGO5	418	468	13	PPMA-shEGO5	481	510	5

The thermal stability of PPMA-EGO is possibly related to the tortuous diffusion path of degradation products, which is strongly related to the distribution of graphite particles in the PPMA matrix and hence dependent on the preparative mixing method. In addition, some of the PPMA-EGO formed a stable char at 800 °C (Table 6.5). For example, the char content of PPMA-stEGO1 was found to be 8%. The char layer containing EGO is believed to offer protection to the underlying PPMA from the degradation processes by acting as a physical barrier that limits the heat and mass transfer between the gas and condensed phase, thereby delaying degradation of PPMA[186]. The increase in char content has been reported by Xie et al[168] and they showed that this data provide positive evidence that EGO can promote the formation of carbonaceous materials in the condensed phase.

The difference between the thermal stability of PPMA-stEGO and PPMA-shEGO was related to the surface area of EGO. PPMA-shEGO has higher thermal stability compared with PPMA-stEGO due to high shearing action provided by the Ultra-Turrax. High shearing

caused graphite particles to reduce particle size and randomly scattered within the PPPMA matrix.

6.3.6 Thermo-mechanical property of PPMA-EGO

The dynamic mechanical behaviour of PPMA-EGO was determined according to the experimental parameters described for DMA in three-point bend mode in Chapter 3. The storage moduli, E′, used to compare the elastic behaviour of the tested materials, are presented in Figure 6.9. It is apparent that in the presence of EGO, the E′ of all PPMA-EGO increased relative to that of pure PPMA, throughout the entire temperature range studied. The E′ of PPMA-EGO at several temperatures is listed in Table 6.6. The maximum E′ of PPMA-EGO at room temperature was observed at 5 %wt of EGO. E′ of PPMA filled with 5 %wt of stEGO was 11.4 GPa. The results reported in Table 6.6 show that EGO at small concentrations was found to have a reinforcing effect, consistent with other layered composites at ambient temperature[11,187]. The enhanced E′ of PPMA-EGO can be attributed to the high strength and interfacial adhesion between the graphite layers and the PPMA matrix. These characteristics should provide good load transfer from the PPMA matrix to the graphite layers[180]

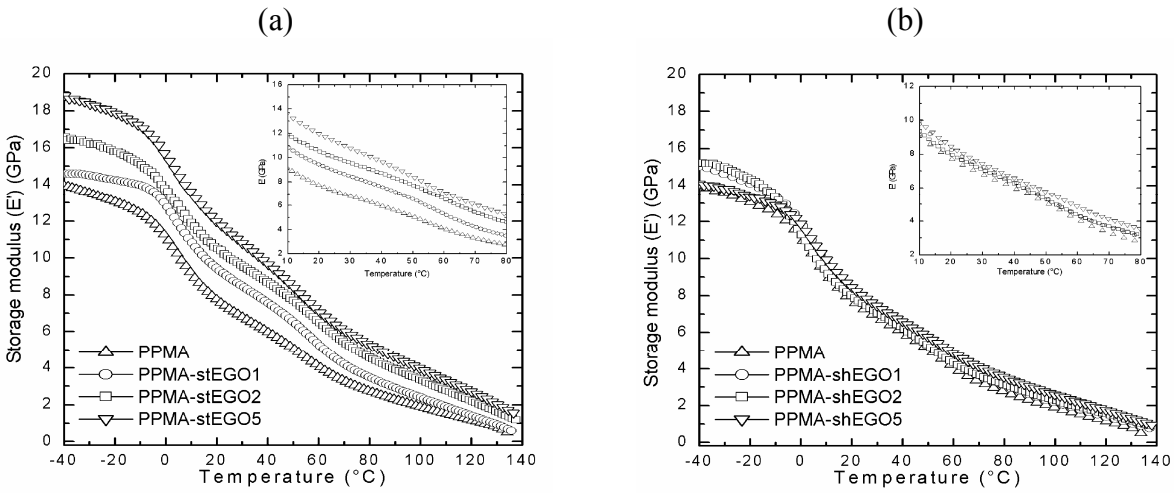

Figure 6.9 Storage moduli curves of (a) PPMA-stEGO (b) PPMA-shEGO as a function of temperature

While the E′ of filled PPMA increased with subsequent additions of both types of EGO, it was found that the reinforcing effect of stEGO was more prominent than that of shEGO.

The lower E′ of PPMA-shEGO is attributed to there being a greater concentration of graphite particles (as result of high shearing) than MA groups. This over abundance of shEGO results in some filler particles being unable to bond to MA groups due to a lack of bonding sites.

Table 6.6 Storage moduli and glass transition temperatures of PPMA-EGO

E′ (GPa)	Temperature (°C)					E′ (GPa)	Temperature (°C)				
	-35	10	25	75	T_g		-35	10	25	75	T_g
PPMA	13.7	9.2	7.2	2.9	3.4	PPMA	13.8	9.2	7.2	2.9	3.4
PPMA-stEGO1	14.6	10.9	8.9	3.8	3.5	PPMA-shEGO1	14.9	9.8	7.7	3.3	3.8
PPMA-stEGO2	16.4	11.9	10.0	4.9	3.7	PPMA-shEGO2	15.2	9.3	7.5	3.4	-1.9
PPMA-stEGO5	18.6	13.5	11.4	5.6	4.2	PPMA-shEGO5	13.9	9.9	7.9	3.8	4.1

The E″ and Tan(δ), can be used to determine the glass transition temperature, T_g, as it is related to viscoelastic behaviour[146,147]. The T_g is often measured from either the maxima of E″ or Tan(δ) curves as shown in Figure 6.10. The T_g was measured from the E″ curve, with Tan(δ) curves used to provide clarity of changes in behaviour. As shown in Table 6.6, the T_g of pure PPMA was found to be 3.4 °C. In all cases, the T_g of the PPMA-stEGO, composites was found to be higher in comparison with pure PPMA. This trend was observed for most of the PPMA-shEGO materials, especially higher EGO concentrations. The shift in T_g to higher temperatures was ascribed to a decrease in mobility of the polymer backbone, due primarily to the strong interactions, such as hydrogen bonding between the polar groups of PPMA. This observation is consistent with the behaviour of other filled polymeric systems that include a compatibiliser[11]. The Tan(δ) curves were found to exhibit similar behaviour to that observed in E″ curves, as discussed above. The results demonstrate a dependence of T_g of PPMA-EGO on EGO concentration.

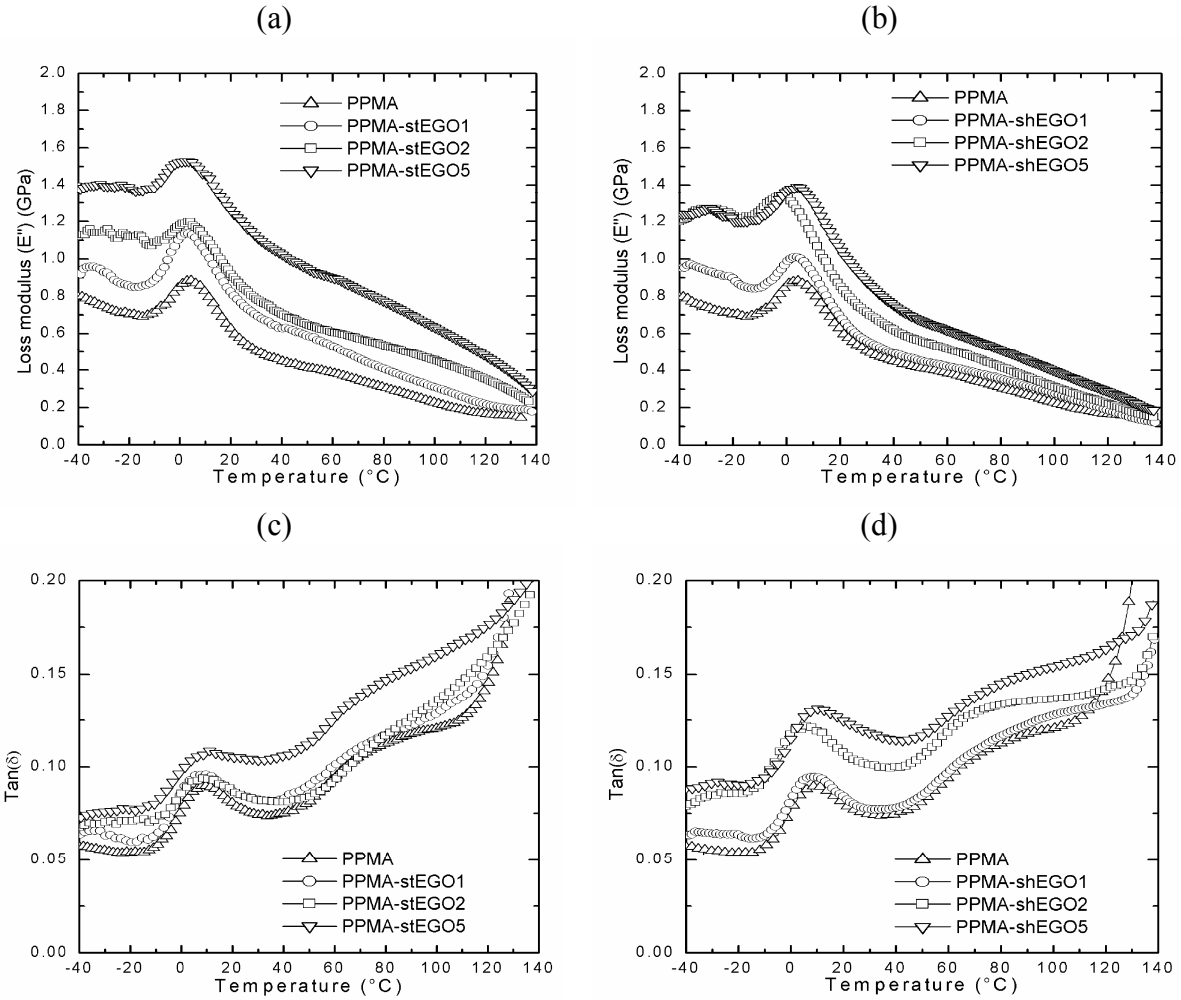

Figure 6.10 Loss moduli curves of (a) PPMA-stEGO (b) PPMA-shEGO and Tan(δ) curves of (c) PPMA-stEGO (d) PPMA-shEGO as a function of temperature

6.3.7 Dielectric property of PPMA-EGO

The conductivity of PPMA is approximately 10^{-17} S.cm^{-1} at room temperature, which is typical of that of an insulator. Recently, it was reported that remarkably low volume fractions of EGO, incorporated by in-situ polymerisation, was required to traverse the percolation threshold, to result in the transition from insulating to semiconducting behaviour in PA-6-EG[10] and PS-EG[134]. This is due to the interconnected network structure of EGO that forms the conducting network[168].

The permittivity, ε', and loss factor, ε", which characterise molecular relaxations, were defined in Chapter 3. The dielectric properties of PPMA-EGO are listed in Table 6.7. The ε'

of PPMA-stEGO was generally found to be higher than that of pure PPMA (0.11). In the case of PPMA-shEGO, ε' decreased upon addition of EGO, with the exception of PPMA-shEGO2, where ε' increased to 1. The ε" of most of the PPMA-stEGO increased with additional EGO at ambient temperature, however only PPMA-shEGO2 ε" was detected. The incorporation of EGO was found to not improve the dielectric properties of PPMA. From the results reported in Table 6.7, the mixing method of EGO greatly influences the resulting dielectric properties of composites, as does the structure of the layered filler. The interconnected network structure of EGO may be expected to result in it behaving as a conducting filler. The interconnected network of EGO was lost when it was incorporated into the PPMA matrix, due to the shearing effect of the mixing methods used. The somewhat non-uniform mixing of the graphite particles within the PPMA matrix, as shown in Figure 6.2a to d, are believed to have prevented the formation of a conducting network.

Table 6.7 Dielectric properties of PPMA-EGO at 25 °C

	log Permittivity ε'	log Loss factor ε"		log Permittivity ε'	log Loss factor ε"
PPMA	0.11	nd	PPMA	0.11	nd
PPMA-stEGO1	-0.16	0.44	PPMA-shEGO1	0.09	nd
PPMA-stEGO2	0.19	0.06	PPMA-shEGO2	1.00	6.24
PPMA-stEGO5	0.45	0.43	PPMA-shEGO5	0.09	nd

nd; not detected

6.4 Conclusion

Two types of PPMA-EGO were prepared by solution blending. Two different mixing methods were used to prepare PPMA-EGO - distributive mixing (low shear) and dispersive mixing (high shear). The effect of preparation method of the PPMA-EGO composites on the properties of the PPMA matrix was investigated.

The preparative mixing method was found to significantly affect the surface area and layered structure of the included expanded graphite oxide. Prior to its dispersion within the PPMA matrix, the structure and surface area of EGO was investigated. An interconnected network was observed, composed of graphite layers with thickness varying from the micrometer to nanometer dimension. The BET surface analysis showed that both types of EGO had a large surface area and an average pore diameter in the nanometer dimension. However, highly

sheared EGO had enhanced surface area compared with EGO exposed to low shear conditions. The crystalline thickness of both types of EGO calculated utilising the Scherrer equation, was found to be in the nanometer dimension in each case. It was found that the EGO crystalline thickness in PPMA-EGO was affected by the graphite particle surface area provided by the preparative mixing method. PPMA-shEGO exposed to a high shearing dispersive environment demonstrated an increase in crystalline thickness compared with layered composites prepared under low shear.

The WAXD revealed PPMA-EGO (α) peaks. The interlayer spacing (*d* spacing) of graphite layers was found not to change when it was incorporated into the PPMA matrix. This indicates that the graphite layers were both ordered and multilayered within the PPMA matrix, a conclusion, which was confirmed by the SEM micrographs. In addition, the crystalline thickness of both types of EGO was found to be in the nanometer dimension when present in the PPMA matrix.

The crystallisation temperature and degree of crystallinity, obtained from DSC analysis, of PPMA-EGO indicated that EGO behaved as a heterogenous nucleating agent for PPMA crystal formation. Elevated crystallisation temperatures and crystallinity were found in PPMA-stEGO in comparison with PPMA-shEGO. Both crystallisation temperature and crystallinity were found to be affected by the surface area of EGO.

The thermal stability of PPMA, as measured by TGA, was found to be affected by the surface area of included EGO. High sheared PPMA-shEGO showed decreased onset of degradation temperature, however higher degradation temperatures. This indicates that PPMA-shEGO had higher thermal stability relative to PPMA-stEGO and pure PPMA matrix. Low sheared PPMA-stEGO showed poorer thermal stability. The higher thermal stability was due to the graphite particles within the PPMA-EGO behaved as a physical barrier between the heat and PPMA matrix thereby delaying PPMA matrix degradation.

The thermo-mechanical properties obtained from DMA measurements indicated that EGO had a reinforcing effect on the elasticity of the PPMA matrix. This is believed to be due to hydrogen bonding between PPMA and EGO, and influenced by the measured change in surface area properties. It was found that the method of incorporation of EGO into PPMA significantly affected the measured stiffness of the composites, with distributive mixing producing higher stiffness materials in comparison with those produced by dispersive mixing. The glass transition temperature of PPMA was found to be generally higher in the presence of

EGO, due to decreased mobility of polymer molecules resulting from the hydrogen bonding between PPMA and EGO.

The dielectric properties of PPMA-EGO did not improve relative to pure PPMA. The non-uniform distribution and therefore absence of a continuous network of graphite prevented the formation of a conducting material.

Chapter 7 Poly(propylene-graft-maleic anhydride) layered expanded graphite oxide composites via melt blending

7.1 Introduction

The crystalline structure, thermal, mechanical, and electrical properties of poly(propylene-g-maleic anhydride) (PPMA) in the presence of varying concentrations of expanded graphite oxide (EGO) were investigated. Carbonyl, carboxyl and hydroxyl functionalites found on the EGO surface can facilitate the chemical and physical interactions between EGO and the PPMA matrix in the formation of PPMA layered expanded graphite oxide composites (PPMA-EGO) when utilising a melt blending technique. The properties of PPMA in the presence of EGO were investigated.

7.2 Experimental

7.2.1 Preparation of PPMA-EGO composite

The PPMA-EGO composites reported in this study were prepared by melt blending. The PPMA pellets were melted in a heated kneading mixer, Haake Rheomix 600 (Haake Rheocord 90), with the experimental parameters provided in Chapter 3. The rotor speed was set to 60 rpm and all heating zones were set to 200 °C. EGO was prepared as described in Chapter 3. Briefly, 10 g of GO was heated in a pre-heated muffle furnace at 800 °C for 30 s. EGO was added in weight fractions of 0.01, 0.02, 0.03, 0.05, and 0.07, to the molten PPMA. The mixture was mixed for 20 min after the addition of the graphite. When the processing was complete, the PPMA-EGO was removed from the kneader and cooled to room temperature.

The PPMA-EGO composites were made into films by hot-pressing. A small amount, approximately 1 to 2 g, of PPMA-EGO was placed between two PTFE sheets and heated between aluminium platens. A PTFE template (3x2x0.5 mm) was used to form the films to the desired shape. The press (Thomas Optical and Scientific Co Pty Ltd) with Activon (Grasby-Specac) temperature controller was preheated to 180±1 °C prior to pressing. No pressure was applied initially for 2 min to allow the PPMA-EGO to pre-melt. The pressure was then raised slowly to 13 kPa and held for 2 min, with the pressure subsequently increased to 20 kPa for an additional 3 min.

Table 7.1 lists the nomenclature for the PPMA-EGO composites prepared. The concentration levels of EGO are supplied as suffixes, such that PPMA-EGO1 refers to PPMA filled with 1 %wt of EGO.

Table 7.1 Abbreviations of filled PPMA-EGO composites

	(EGO %wt)
PPMA	0
PPMA-EGO1	1
PPMA-EGO2	2
PPMA-EGO3	3
PPMA-EGO5	5
PPMA-EGO7	7

7.3 Results and Discussion

7.3.1 Structural characteristic of expanded graphite oxide

Exfoliation of GO at 700 °C results in the decomposition of low-molecular weight components trapped in the graphite layers as well as the evolution of carbon dioxide (CO_2) and sulfur dioxide (SO_2) leading to the irreversible expansion of GO, thus producing expanded graphite oxide (EGO). As previously described in Chapter 4, exfoliation is where the graphite layers separate and expand producing an interconnected network structure often described as either worm-like, accordion bellow and/or a honeycomb structure.

The BET surface analysis, discussed earlier in Chapter 5, demonstrated that the exfoliation of GO to EGO produced a material with a large surface area, A_s. The A_s of GO was found to be 0.87 $m^2.g^{-1}$, however after exfoliation, the A_s of EGO increased to 3.89 $m^2.g^{-1}$. The transformation of the crystalline structure of GO to EGO using SEM is shown in Figure 7.1.

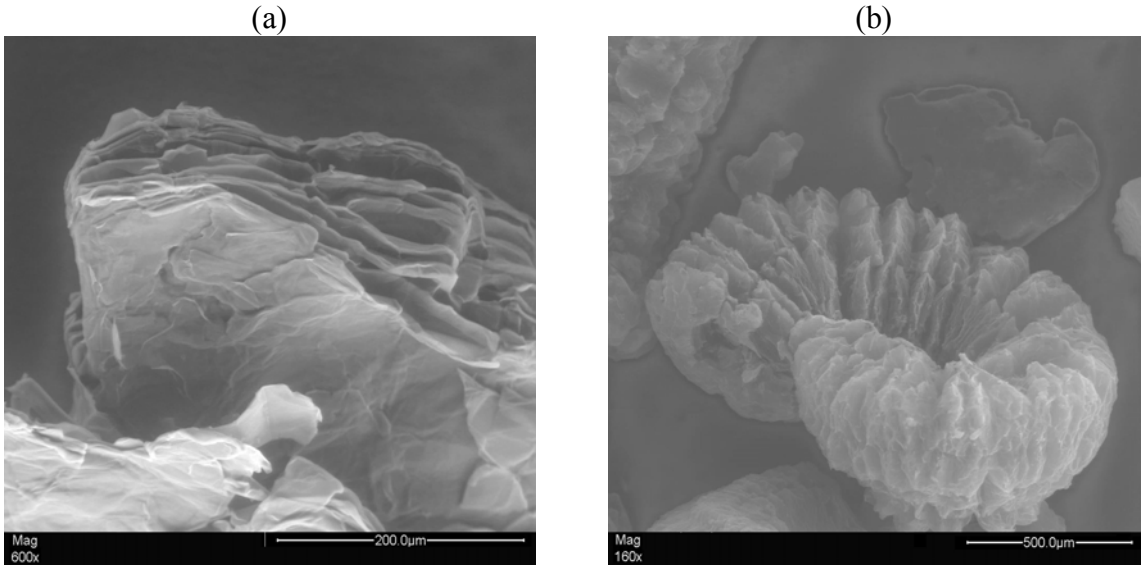

Figure 7.1 SEM micrographs of (a) GO (b) EGO after exfoliation of GO at 700 °C

Figures 7.2a to f show the SEM micrographs of fracture surfaces of PPMA-EGO composites containing 3, 5 and 7 %wt of EGO. The internal structure of EGO in PPMA-EGO is shown in Figures 7.2b, d and f. It can be seen by comparison that the internal structure of EGO in the PPMA-EGO composites were different to that of the EGO shown in Figure 7.1b. The graphite layers within PPMA-EGO composites were severely collapsed and the apparent interlayer spacing diminished. This means that the interconnected network of EGO was destroyed under mechanical mixing due to the absence of PPMA in the graphite layers.

Shen et al[175] prepared PPMA expanded graphite nanocomposites by melt blending. They reported that the absence of PPMA in the graphite layers was due to the highly entangled nature of the PPMA chains, such that within a highly viscous melt the graphite layers cannot intercalate under shear stress provided by the mixer or compression; at most they can infiltrate only the larger pores of expanded graphite. The graphite particles in the PPMA-EGO are shown in Figures 7.2a, c and e exist in the form of relatively isolated “islands” because of the absence of PPMA intercalation and the breakable nature of EGO[175].

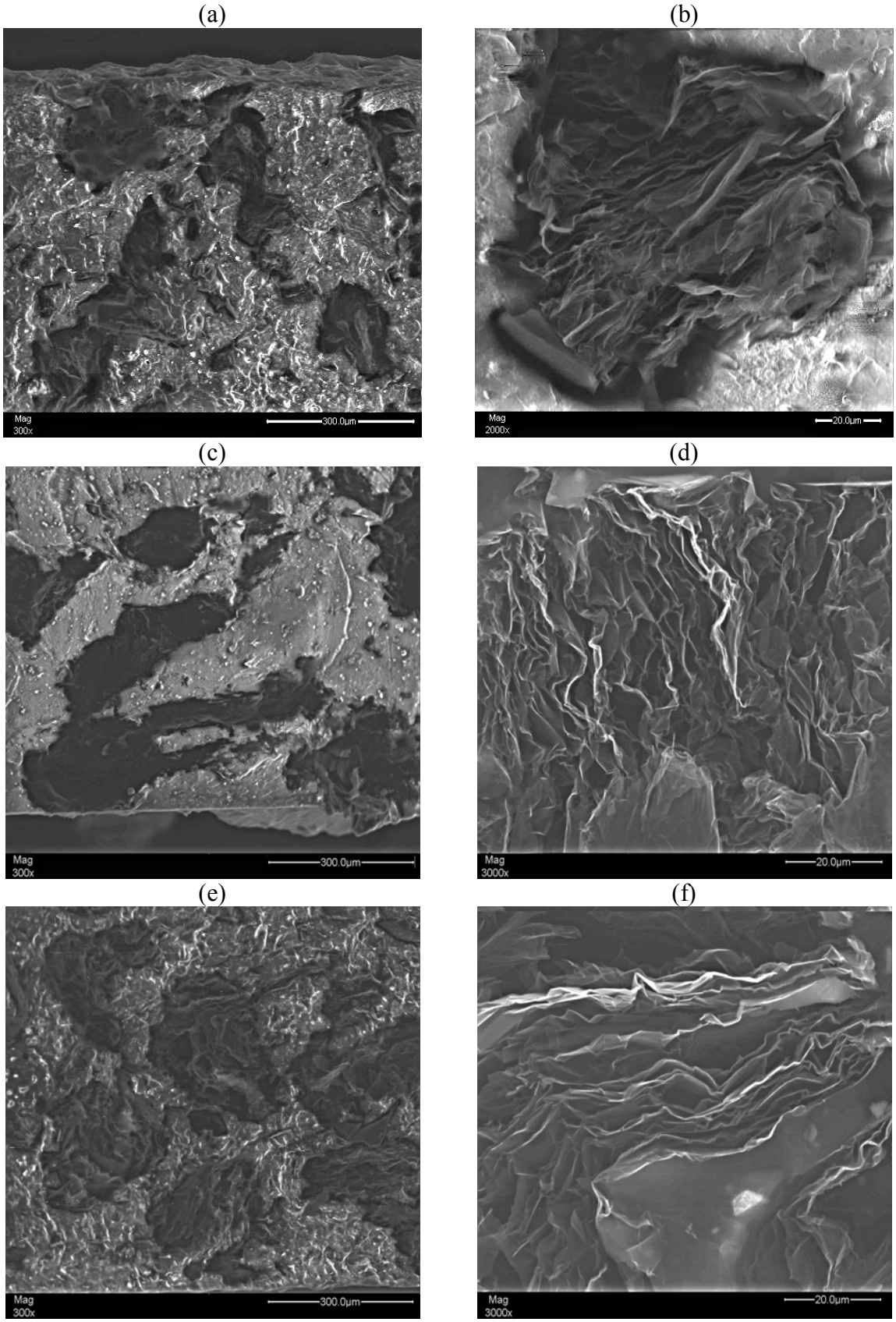

Figure 7.2 SEM micrographs of fractured surface of PPMA-EGO (a), (b) PPMA-EGO3 and (c), (d) PPMA-EGO5 and (e), (f) PPMA-EGO7; (b), (d) and (f) internal structure of EGO in corresponding EGO concentration

7.3.2 Interlayer spacing and crystalline thickness of expanded graphite oxide filler in PPMA

WAXD was used to determine the crystalline structure of PPMA-EGO, and its individual components, in the diffraction angle between 2 and 50°, at room temperature, as described in Chapter 3. The 2θ was converted to interlayer spacing, *d* spacing using the Bragg equation, as described in Chapter 3. The transformation of GO to EGO after exfoliation resulted in the appearance of a strong and broad peak, which corresponds to diffraction (002) plane, which is the graphite plane. The (002) peak at approximately 2θ=26° has a *d* spacing of 0.333 nm.

Figure 7.3 shows the diffractograms of PPMA filled in increasing order of EGO concentration. The diffractogram of pure PPMA demonstrates four peaks between 2θ=14° to 21°, which is indicative of the monoclinic (α) crystalline phase of isotactic PP[34]. The peaks corresponding to (α) crystalline phase are diffraction (110), (040), (130), and (120) planes, (α) peaks are found at approximately 2θ=14, 16, 18 and 21°, respectively. These results are consistent with other studies[34,179].

The PPMA-EGO diffractograms were found to posses the same number of (α) peaks within the same 2θ range as pure PPMA diffractogram, but also include the (002) peak related to EGO. The diffractograms of PPMA-EGO indicate that the PPMA exists mainly in the (α) crystalline phase. The *d* spacing relating to the (040) and the (002) peaks, and other WAXD measurements of PPMA-EGO, are listed in Table 7.2. A marginal shift of the PPMA (040) peak to higher 2θ was observed in all cases upon addition of EGO.

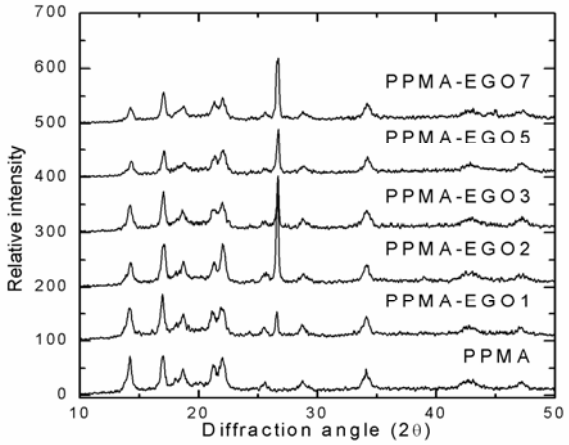

Figure 7.3 Diffractograms of pure and filled PPMA in varying EGO concentration

The change in *d* spacing revealed by the shift of the EGO the (002) peak due to the presence of PPMA is negligible, indicating the lack of significant intercalation in the graphite layers by the PPMA matrix (Table 7.2). The results reported in Table 7.2 demonstrate that the average *d* spacing corresponding to the (002) peak of the PPMA-EGO diffractogram was 0.335 nm, which is the same as that of observed for pure crystalline graphite[171]. This further indicates that the graphite layers remained ordered and multilayered within the PPMA matrix, and that intercalation was prevented, in agreement with the SEM micrographs provided in Figure 7.2.

Table 7.2 WAXD measurements of the diffraction (040) and (002) peaks of the diffractogram of filled PPMA-EGO

PPMA-EGO (EGO %wt)	(040) peak		(002) peak		
	2θ (°)	*d* spacing (nm)	2θ (°)	*d* spacing (nm)	$L_{(002)}$ (nm)
0	16	0.522	27*	0.333*	19.32*
1	16	0.521	26	0.335	38.64
2	17	0.519	27	0.334	38.66
3	17	0.520	27	0.334	55.19
5	17	0.518	27	0.336	32.19
7	17	0.519	27	0.334	27.60

diffraction (002) peak of EGO

crystalline thickness $L_{(002)}$ of EGO

The crystalline thickness, $L_{(002)}$ of EGO in PPMA-EGO was estimated from the FWHM of the (002) peak using the Scherrer equation, which has been described in Chapter 3. The calculated $L_{(002)}$ of EGO is listed in Table 7.2. The results reported in Table 7.2 demonstrate that EGO, prior to dispersion in PPMA, had a $L_{(002)}$ of 19.32 nm, while $L_{(002)}$ of EGO within PPMA-EGO increased. $L_{(002)}$ of EGO in PPMA-EGO was highest at 3 %wt. However, at 5 and 7 %wt of EGO, $L_{(002)}$ in PPMA-EGO was approximately 20 to 30 nm lower than PPMA filled with 3 %wt of EGO. These results suggest that $L_{(002)}$ of EGO in PPMA-EGO is in the nanometer dimension.

7.3.3 Crystallisation and melting behaviour of PPMA-EGO

The crystallisation behaviour of PPMA-EGO was studied by DSC in the temperature range of 20 to 200 °C at a heating rate of 10 °C.min^{-1} under N_2 purge. The detailed experimental conditions are provided in Chapter 3. The characteristic peak due to melting and crystallisation of the monoclinic (α) crystalline phase of PP, within PPMA-EGO composites, is visible in the crystallisation and melting curves shown in Figure 7.4.

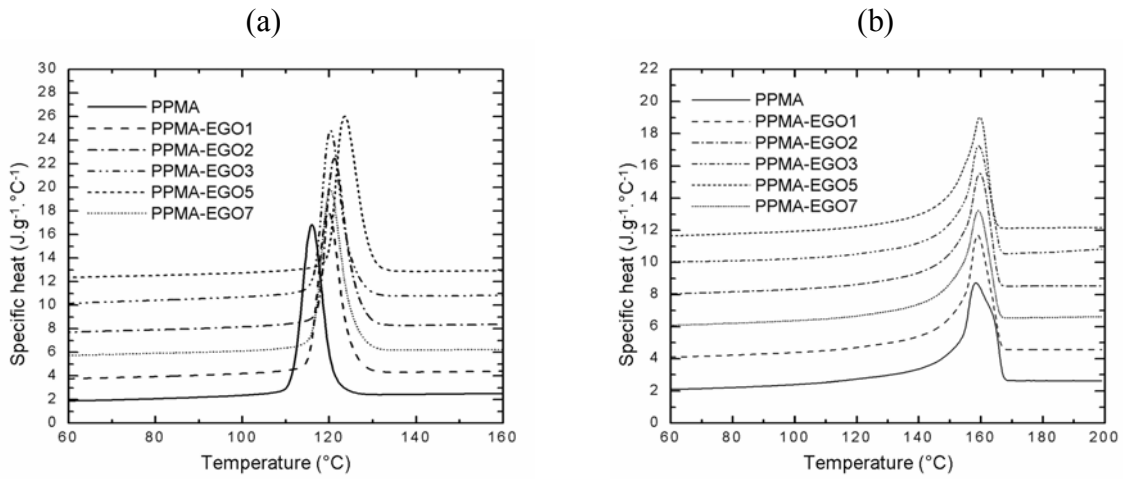

Figure 7.4 (a) Crystallisation and (b) melting curves of pure and filled PPMA with varying EGO concentrations

The measured T_c, and T_m and their $T_{c\ onset}$ and $T_{m\ onset}$, ΔH_f and χ_c determined from the exothermic and endothermic peaks are listed in Table 7.3. The $T_{c\ onset}$ and T_c of PPMA increased in the presence of EGO. $T_{c\ onset}$ for PPMA increased from 121 °C (pure PPMA) to 125 °C at 1 %wt of EGO. T_c of PPMA increased from 116 °C (pure PPMA) to 119 °C for 1 %wt of EGO. These results indicate that graphite particles act as heterogenous nucleation sites for PPMA crystallisation. The graphite particles induced crystallisation at higher temperature, which is attributed to the large surface area to volume ratio of EGO. This produced more nucleating sites for the PPMA crystallisation.

The enthalpy of fusion was determined by integration of the melting endotherm in the temperature range 120 to 175 °C and χ_c, calculated based on a value of ΔH_f=209 $J.g^{-1}$ [142] for pure PP crystals are listed in Table 7.3. The χ_c of PPMA-EGO decreased as EGO concentration increases, with the exception of PPMA containing 1 %wt of EGO. This is attributed to the physical presence of EGO, with high concentration constraining the mobility of PPMA chains. The reduced mobility in PPMA domains caused the decrease in χ_c. These results coincide with Weng et al findings[188]. They reported that although graphite particles behaved as a heterogenous nucleating agent for PA-6, the graphite particles hindered the transport of molecular chains, leading to a reduction in the rate of crystallite growth[188].

Table 7.3 Crystallisation and melting temperatures, enthalpy and crystallinity of pure and filled PPMA

	Temperature (°C)				ΔH_f (J.g^{-1})	χ_c
	$T_{c\ onset}$	T_c	$T_{m\ onset}$	T_m		
PPMA	121	116	152	158	96.0	0.45
PPMA-EGO1	125	119	153	158	96.9	0.46
PPMA-EGO2	126	120	152	159	94.7	0.45
PPMA-EGO3	126	121	153	160	94.8	0.45
PPMA-EGO5	125	120	153	159	86.0	0.41
PPMA-EGO7	129	125	152	160	91.3	0.44

A change in $T_{m\ onset}$ and T_m of PPMA-EGO was observed, however negligible. The EGO incorporated into PPMA behaved as heterogenous nucleating agent that resulted in both an increase in T_c and decrease χ_c.

7.3.4 Thermal stability of PPMA-EGO

The thermal stability of PPMA-EGO was investigated using TGA in the temperature range of 30 to 700 °C. The detailed experimental conditions were described in Chapter 3. The weight loss curves (TGA curves) and derivative weight loss curves (DTG curves) area provided in Figure 7.5. The initial (onset) degradation, $T_{d\ onset}$ and maximum degradation rate temperatures, T_d, of PPMA-EGO are listed in Table 7.4. The fraction of non-volatiles that remain at 700 °C, was denoted as char.

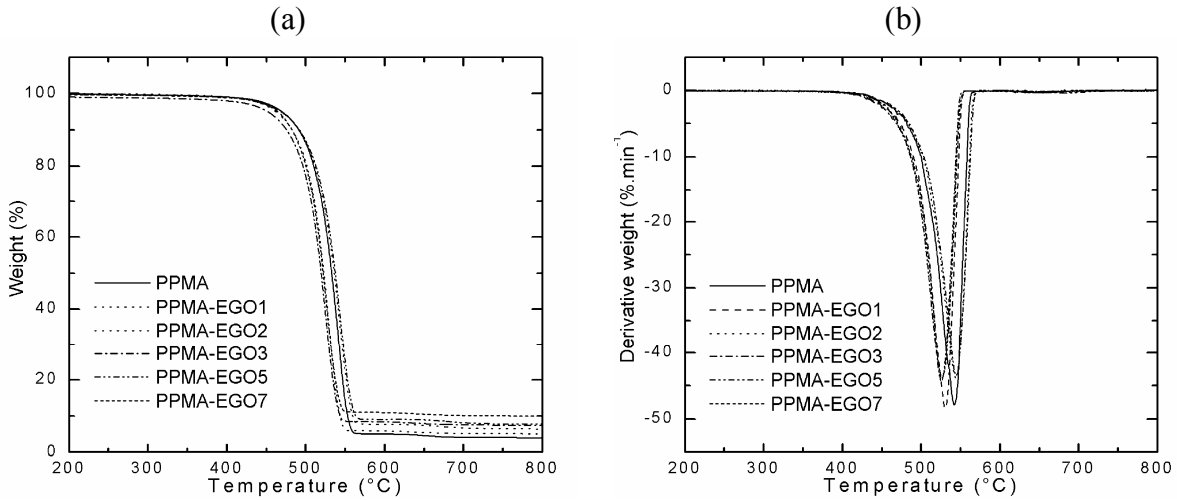

Figure 7.5 (a) Weight loss curves (b) derivative weight loss curves of PPMA-EGO

The thermal stability of PPMA-EGO with varying EGO concentrations is shown in Figure 7.5a and b. For the pure PPMA, there is only one sharp degradation stage occurring between 400 and 600 °C, with a T_d of 464 °C. This degradation stage is attributed to chain scission of PPMA. The TGA curves of all PPMA-EGO degraded in a similar manner to that of pure PPMA, in that degradation also occurred in a single stage. $T_{d\ onset}$ of most of the PPMA-EGO was found to be higher than PPMA, with the exception of 2 and 3 %wt of EGO. The T_d of all PPMA-EGO composites increased with EGO concentration by up to 5 °C, indicating delayed degradation of PPMA. Some of the PPMA-EGO composites formed a stable char residue at 700 °C.

Table 7.4 Onset degradation and maximum rate of degradation temperatures and char content of PPMA-EGO

	$T_{d\ onset}$ (°C)	T_d (°C)	Char (%)
PPMA	464	498	3
PPMA-EGO1	468	499	5
PPMA-EGO2	461	499	7
PPMA-EGO3	462	500	8
PPMA-EGO5	466	503	8
PPMA-EGO7	474	504	10

From the results obtained, it is apparent that the presence of EGO resulted in improvement in thermal stability. This is believed to be related to the tortuous path in the PPMA-EGO that hinders diffusion of the volatile decomposition of products in the PPMA-EGO compared with pure PPMA. In addition, some char was observed to form, which acted as barrier protecting the underlying PPMA matrix from the incident heat, thereby raising the observed degradation temperatures in nitrogen atmosphere[132,133,186].

It is noted that the char residues formed by some of these PPMA-EGO composites at 700 °C are larger than the EGO concentration of corresponding PPMA-EGO. The increase in char residues was observed in Chapter 5 and thus was considered as positive evidence that graphite oxide can promote the formation of carbonaceous materials in the condensed phase[168]. Gopakumar and Page[34] studied the thermal stability of PP filled with graphite under N_2 by using TGA. They found that PP filled with graphite was more thermally stable in comparison with pure PP. The improvement in thermal stability in the presence of graphite in N_2 atmosphere has been reported for other polymer composites [2,93,131,189,190].

7.3.5 Thermo-mechanical property of PPMA-EGO

The viscoelastic behaviour of PPMA-EGO under dynamic stress and elevated temperature were obtained in three-point bend mode using DMA. The thermal and mechanical properties were acquired according to the experimental conditions described in Chapter 3. The temperature dependence of E′ over the range of -30 to 120 °C is displayed in Figures 7.6a and while Figure 7.6b show an expanded view between 20 to 80 °C. The E′ of PPMA in the presence of EGO was found to increase throughout the studied entire temperature range. The maximum E′ of PPMA-EGO was observed at 3 %wt of EGO. The increased E′ indicates that EGO has a reinforcing effect on the elastic behaviour of the PPMA matrix, presumably due to strong interfacial adhesion, resulting from hydrogen bonding between the attached polar groups present in the PPMA matrix and surface of EGO[132]. The low E′ obtained for 5 and 7 %wt of EGO can be attributed to there being a higher concentration of graphite particles than MA groups. This results in some graphite particles being unable to bond to MA groups due to a lack in bonding sites. The increase in E′ of polymer matrices in the presence of graphite particles has been previously been reported for epoxy-based thermosets[132], PI[191] and PPMA[11].

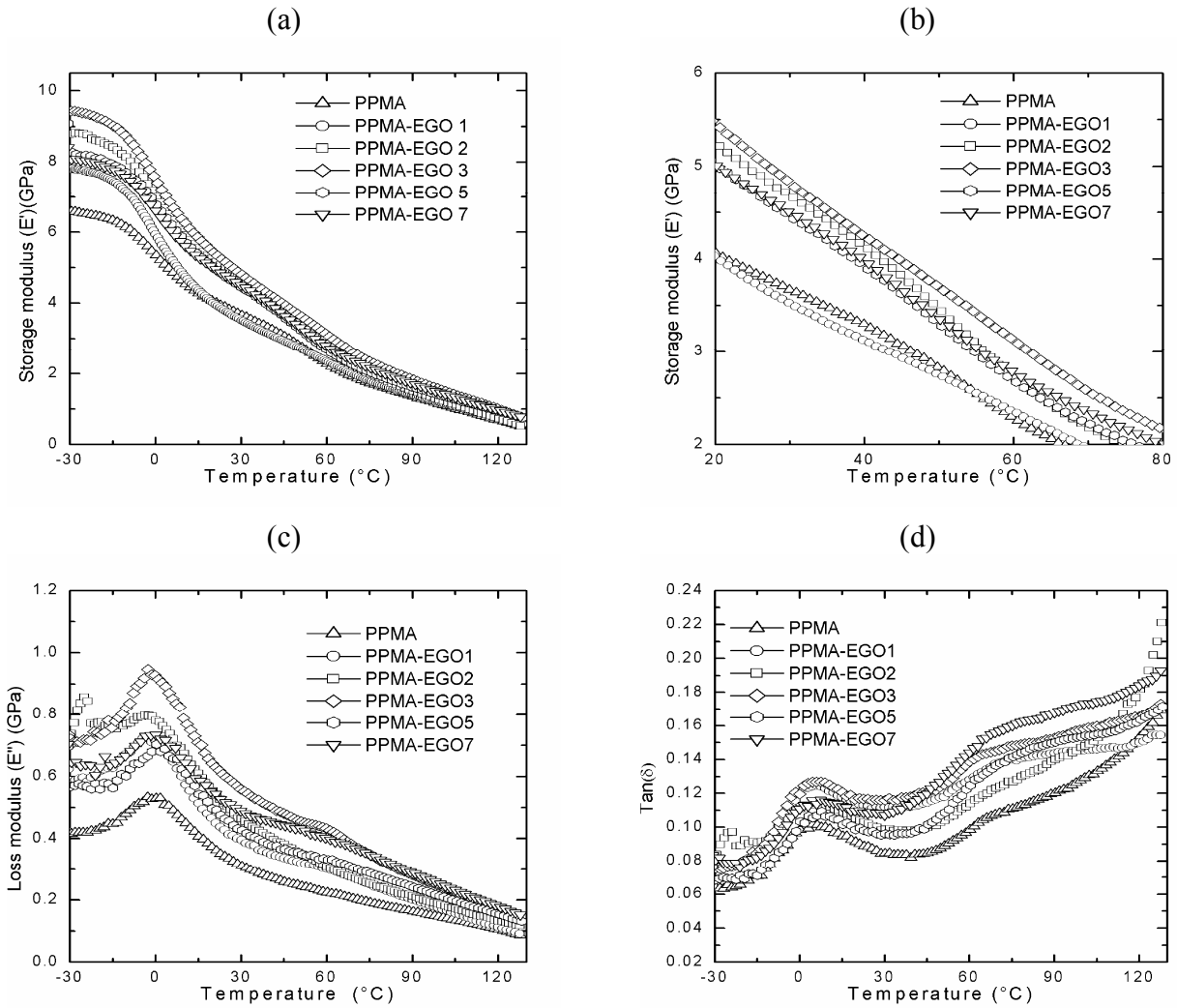

Figure 7.6 Dynamic mechanical curves of PPMA-EGO (a) storage moduli (b) E′ (expanded view) between 20 to 80 °C (c) loss moduli and (d) Tan(δ) as a function of temperature

Either of the peak maxima of the E″ and Tan(δ) curves (Figure 7.6) may be taken as the temperature of the glass transition, T_g,. The maxima of Tan(δ) were used to obtain the T_g of the PPMA-EGO composites. Figure 7.6d shows the variation of the Tan(δ) as a function of temperature. The T_g of the PPMA-EGO was found to be higher than pure PPMA. At 1 %wt of EGO, the T_g of PPMA increased from 5.6 °C (pure PPMA) to 8.5 °C (Table 7.5). The increase in T_g is attributed to the graphite particles reducing the mobility of the chain segment of the macromolecular matrix, due to hydrogen bonding. From the FTIR analysis determined earlier in Chapter 4, exfoliation of GO exposed carbonyl, hydroxyl, and carboxyl functional groups on the graphite surface thereby aiding both physical and chemical interactions between

the PPMA and EGO[132]. The presence of these functional groups on the graphite surface is believed to increase its compatibility with the PPMA matrix. The increase in E′ and T_g for polymer reinforced with graphite particles has been reported for epoxy[132] and PI[191].

Table 7.5 Storage moduli and glass transition temperatures of pure PPMA and PPMA-EGO

E′ (GPa)	Temperature (°C)							
	-25	10	25	50	75	100	125	T_g
PPMA	6.5	4.6	3.9	2.8	1.7	1.1	0.6	5.6
PPMA-EGO1	7.9	4.8	3.8	2.8	1.8	1.2	0.7	8.5
PPMA-EGO2	8.8	5.9	4.9	3.5	1.9	1.4	0.6	5.9
PPMA-EGO3	9.4	6.3	5.1	3.7	2.4	1.5	0.9	6.3
PPMA-EGO5	8.2	5.8	4.8	3.3	2.0	1.4	0.8	7.9
PPMA-EGO7	8.1	5.7	4.7	3.4	2.2	1. 5	0.6	7.2

7.3.6 Electrical conductivity

The electrical conductivity, σ_c of PPMA-EGO at room temperature was determined according to the experimental conditions described in Chapter 3. PPMA, like most polymers, is electrically non-conductive and has a σ_c of 10^{-15} S.cm^{-1} in the dry state at room temperature[11]. The electrical conductivity of composites containing conducting fillers dispersed in insulating matrices has been studied previously[192-195]. Several studies have shown that addition of exfoliated graphite oxide can improve the conductivity of an insulating polymer matrix. This is reportedly due to the interconnected network structure, consisting of numerous nanolayers adhering to one another, possessing both sheet-like and fibre-like particles that form the conducting network[10,127,128]. When the EGO concentration within the PPMA-EGO composites was raised above 2 %wt, it was possible to detect and measure the conductivity, σ_c, and this was found to be $1.80\text{x}10^{-12}$ and $1.55\text{x}10^{-12}$ S.cm^{-1}, for 3 and 5 wt% EGO, respectively. Upon addition of 7 %wt of EGO, the σ_c of PPMA was found to further increase by nine orders of magnitude, such that the σ_c of PPMA at 7 %wt of EGO was measured to be $1.25\text{x}10^{-3}$ S.cm^{-1}. The interconnected network of EGO in the PPMA-EGO was broken, as shown in Figure 7.2, due to the mechanical mixing process employed. Therefore, it is only at high EGO concentration that the graphite particles come into contact and form a conducting network. These findings are similar to those reported by Xiao et al[134] and Shen et al[175].

The electrical properties of polypropylene expanded graphite via melt blending were reported by Shen et al[175]. From their studies, they reported that the formation of the conducting network composed of small and compacted graphite particles must occur in a narrow range of expanded graphite concentration.

7.4 Conclusion

PPMA-EGO composites, containing a range of EGO concentrations, were prepared by melt blending. The WAXD measurements of PPMA-EGO exhibited (α) crystalline phase with high relative intensity, indicating a crystalline structure. The diffractograms of PPMA-EGO revealed no change in the *d* spacing of the graphite layers. This indicated that the graphite layers remained ordered and multilayered and that the processing conditions were unable to affect the order in the structure of EGO in PPMA matrix.

The crystallisation behaviour of PPMA-EGO indicated that the graphite particles behaved as a heterogeneous nucleating agent. The graphite particles induce the crystallisation of PPMA at higher temperatures by serving as nucleation sites for PPMA crystals. However, the crystallisation growth was reduced at EGO concentrations above 1 %wt, which corroborated the observation obtained from the WAXD measurements of PPMA-EGO in which the relative intensity of the (004) peak decreased above 1 %wt of EGO.

The thermal stability of PPMA-EGO increased with the incorporation of EGO under thermal degradation condition. EGO was found to provide a heat barrier for the PPMA thereby increasing the observed degradation temperatures of the PPMA-EGO composites.

The storage modulus of PPMA-EGO determined from DMA measurements indicated that EGO has a reinforcing effect on the elastic behaviour of PPMA matrix, due primarily to hydrogen bonding between PPMA and EGO. The glass transition of PPMA increased in the presence of EGO due to a decrease in mobility of PPMA chains, due to the same interaction between the PPMA and EGO.

The electrical conductivity of PPMA-EGO was measured at EGO concentration above 2 %wt. The electrical conductivity of PPMA-EGO reached 1.25×10^{-3} $S.cm^{-1}$ at 7 %wt of EGO. The EGO concentration was found to be the most critical factor in the enhancement of the electrical conductivity of PPMA-EGO.

Chapter 8 Conclusions

Polymer layered composites were prepared in the presence of layered graphite oxide and expanded graphite oxide such as EMAA layered composites and PPMA-EGO composites. These polymer layered graphite oxide composites were prepared using two methods:

- Solution blending
- Melt blending

A series of oxidised and exfoliated graphite flakes were prepared using Brønsted acids (HNO_3 and H_2SO_4) in combination with oxidising agents and reagents such as:

- Method 1 Staudenmaier method - HNO_3-H_2SO_4 and $KClO_3$
- Method 2 Modified Staudenmaier method - HNO_3-H_2SO_4 and $KClO_3$ (greater amount used compared with Method 1)
- Method 3 HNO_3-H_2SO_4 and CH_3COOH-$KMnO_4$
- Method 4 HNO_3-H_2SO_4 and $C_{10}H_{21}OH$.

The graphite oxide structure determined from scanning electron microscopy showed graphite layers in a periodic pattern. An increase in interlayer spacing in the graphite layers for some of the oxidised graphite was observed. This indicates that intercalation of acids and reagents occurred. A difference in structure is observed for some of the oxidised graphite. Graphite oxidised using Staudenmaier method ($KClO_3$) showed a different structure to other oxidised graphite. Graphite oxidised using the same amount as stated in the Staudenmaier method showed slightly collapsed graphite layers. In contrast the graphite oxidised using a modified version of Staudenmaier method (larger amount of $KClO_3$) showed flakiness of surface. The separation of the graphite layers after oxidative treatment was estimated using IPLab Spectrum Scientific Image Processing. Hence, graphite oxidised using the Staudenmaier method (Method 1) had the highest separation of graphite layers.

Exfoliation of graphite oxide at high temperature formed an expanded graphite oxide: an interconnected network structure similar to that of an accordion bellows composed of graphite layers with thickness varying from micrometer to nanometer dimension. However, the expansion volume and rate of expansion of graphite oxides were different.

The surface area measurements from BET analysis indicate that some graphite surface area

increased after oxidative treatment. Graphite oxide prepared from the modified Staudenmaier method had the highest surface area. It seems that a large amount of $KClO_3$ increased the surface area of graphite oxide. BET surface area analysis of expanded graphite oxide indicated a larger surface area compared with graphite oxide. There was no correlation between the surface areas of graphite oxide and expanded graphite oxide. The average pore diameter of graphite oxide and expanded graphite oxide were in the nanometer dimension.

The presence of hydroxyl, carbonyl and carboxyl functional groups on the surface of all graphite oxides and expanded graphite oxides were confirmed using FTIR analysis.

The interlayer spacing of graphite layers for some of the graphite oxide obtained from WAXD measurements increased indicating that intercalation of acids and reagents occurred in the graphite layers. Oxidising agents and reagents CH_3COOH-$KMnO_4$ and $C_{10}H_{21}OH$ were less efficient in intercalating the graphite layers in comparison with $KClO_3$. The interlayer spacing of some of the oxidised graphite changed after exfoliation, particularly graphite oxidised using $KClO_3$. The crystalline thickness of graphite oxide and expanded graphite oxide calculated from the Scherrer equation was in the nanometer dimension (<30 nm). The low crystalline thickness is due to the oxidative treatment of graphite disrupts the graphite crystallites. Hence, exfoliation of oxidised graphite further disrupts the graphite crystallites.

The thermal decomposition of graphite oxides studied using TGA in both nitrogen and air atmospheres varied depending on the oxidising agent and reagents utilised. However, the decomposition of graphite oxides was consistent with a redox process, regardless of type of intercalates, at different rates with temperature changes. Carbon dioxide, water and sulfur dioxide were evolved leading to irreversible expansion of graphite oxide. WAXD measurements of some of the graphite oxide heated at various temperatures confirmed that volatilisation and/or decomposition of intercalate occurred due to the changed order of the graphite layers. Hence, surface area properties of graphite oxide play a role in the thermal decomposition of graphite oxide.

The thermal expansion of graphite oxide estimated using a DMA technique (parallel plate mode) increased with temperature and depended on the type of oxidising agents and reagents used in combination with Brønsted acids. High thermal expansion was obtained from HNO_3-H_2SO_4; $KClO_3$ (Method 3). The amount of $KClO_3$ used affected the thermal expansion of graphite oxide, a larger amount of $KClO_3$ resulted in higher thermal expansion at higher temperature. This is due to more $KClO_3$ intercalated in the graphite layers as indicated by an

increase in the interlayer spacing and when heated $KClO_3$ volatilised and/or decomposed from the graphite layers, during which enough pressure developed and separated the graphite layers causing expansion of graphite oxide. Hence, the $KClO_3$ becomes a source for carbon dioxide evolution.

Four poly(ethylene-co-methyl acrylate-co-acrylic acid) (EMAA) layered composites were prepared with varying concentration via solution blending using an Ultra Turrax disperser (high sheared). Graphite was oxidised using Staudenmaier method (HNO_3-H_2SO_4; $KClO_3$).

- EMAA layered graphite oxide composites (EMAA-GO)
- EMAA layered graphite oxide composites (EMAA-EGO)
- EMAA layered graphite oxide composites (EMAA-SGO) – oxidised graphite using Staudenmaier method
- EMAA layered expanded graphite oxide composites (EMAA-SEGO) – exfoliated oxidised graphite

The WAXD measurements of all filled EMAA showed that there was no change in interlayer spacing of the graphite layers. This indicated that EMAA intercalation did not occur and therefore the graphite layers in the EMAA layered composites were ordered and multi-layered. In addition, the dispersion technique (Ultra-Turrax) used was unable to affect the crystalline structure (order or exfoliate) of graphite layers in the EMAA layered composites. The crystalline thickness of the various types of graphite oxide filler in the EMAA matrix was in the nanoscale dimension, however the crystalline thickness of these graphite oxide fillers decreased in the EMAA matrix. TEM showed that the graphite particles in the EMAA are in nanometer dimension (10 nm). Some graphite particles in the EMAA matrix were reduced in size due to the high shearing provided by the Ultra-Turrax disperser during dispersion. This resulted in a uniform dispersion of graphite particles in the EMAA matrix.

The crystallisation temperature and crystallinity from DSC measurements indicate that graphite oxide and its expanded form acted as heterogeneous nucleating agents to induce crystallisation of EMAA. The crystallinity of EMAA decreased upon addition of graphite oxide due to decreased mobility of EMAA segments.

EMAA crystallisation temperatures were higher in the presence of oxidised and exfoliated graphite because of its large surface area and surface polarity as a result of oxidative treatment.

The thermal stability of EMAA layered composites studied using TGA was enhanced. The graphite particles act as a barrier between heat and EMAA thereby delaying degradation. EMAA filled with SGO and SEGO had higher thermal stability compared with GO and EGO due to sulfuric acid trapped in the graphite layers being volatilised and/or decomposed at higher temperature.

The tensile properties such as shear modulus and yield stress of EMAA decreased in the presence of graphite oxide and its expanded form. No trend was observed in the shear modulus and yield stress and interpretations of the tensile properties was complex and therefore statistical analysis was employed. Variables were assigned such as concentration levels, oxidative treatment of filler, and structure of filler. The interaction as well as the independent effects of these variables was considered. Analysis of variance (ANOVA) showed that tensile properties, particularly the shear modulus were affected by concentration level of graphite oxide and the interaction between concentration level-structure of graphite oxide filler. While the yield stress of EMAA matrix is affected by independent as well as the interactions between the variables.

The elastic modulus of most of the EMAA layered composites from DMA measurement decreased in the presence of graphite oxide filler. The results showed no correlation between the type of graphite oxide or concentration level in EMAA and elastic modulus. The elastic modulus obtained was similar to the results obtained for shear modulus. Therefore, the assigned variables (independent or interaction) for tensile properties play a role in the elastic modulus of EMAA layered composites. The glass transition temperature of most EMAA layered composites was higher in the presence of graphite oxide fillers. This is due to the reduction in chain mobility of the EMAA as a result of the interaction between the polar groups attached onto the EMAA and the surface of graphite oxide.

The dielectric properties of EMAA layered composites did not improve relative to pure EMAA. This is due to the high shearing provided by the Ultra-Turrax disperser reducing the particle size of the graphite flakes and thereby disrupting the connections between the graphite layers, which were confirmed by transmission electron microscopy.

As a result the contacts between the graphite layers were too low to form a conducting network for the movement of electrons in the EMAA matrix.

Two types of poly(propylene-graft-maleic anhydride) layered expanded graphite oxide composites (PPMA-EGO) were prepared by solution blending using two different mixing methods:

- PPMA-stEGO – magnetic stirrer: distributive mixing (low sheared)
- PPMA-shEGO – Ultra-Turrax disperser: dispersive mixing (high sheared)

The surface area properties and crystalline thickness of both types of EGO prior to dispersion in PPMA matrix were determined from BET surface area and WAXD measurements. These measurements showed that both types of EGO had higher surface area properties and crystalline thickness than graphite oxide. The crystalline thickness of both types of EGO was found to be in the nanometer dimension. The surface area properties and crystalline thickness were affected by the preparative mixing method employed. Dispersive mixing of shEGO had a higher surface area and crystalline thickness compared with distributive mixed stEGO.

The WAXD revealed PPMA-EGO consisted of (α) crystalline phase. The interlayer spacing of graphite layers was found not to change when it was incorporated into the PPMA matrix. This indicated that the graphite layers were both ordered and multilayered in the PPMA matrix. In addition, the crystalline thickness of both types of EGO was found to be in the nanometer dimension when present in the PPMA matrix. In addition, the preparative mixing method using a stirrer and the Ultra-Turrax disperser were both unable to affect the crystalline structure of graphite layers in the PPMA matrix.

The crystallisation temperature and degree of crystallinity obtained from DSC analysis of PPMA-EGO indicated that EGO acted as a nucleating agent for PPMA crystals in PPMA-EGO. However, the nucleating effect of EGO was found to be affected by the surface area of EGO. Low sheared stEGO in PPMA-stEGO resulted in nucleation and increased high crystallisation and crystallinity in comparison with that of high sheared EGO in PPMA-shEGO.

The thermal stability of PPMA-EGO, as measured by TGA, was affected by the surface area of EGO. High sheared PPMA-shEGO has better thermal stability; in contrast PPMA-stEGO showed poor thermal stability under nitrogen. This is due to high shearing provided by the Ultra-Turrax disperser reducing graphite particle size and producing more graphite particles, as a result more graphite particles within the PPMA-EGO behaved as a physical barrier between heat and PPMA matrix thereby increasing decomposition temperature.

The storage modulus of PPMA-EGO obtained from DMA measurements indicated that EGO had a reinforcing effect on the elastic behaviour of the PPMA matrix even at low EGO concentration. This was due to the strong hydrogen bonding between PPMA and EGO. In addition, the elastic behaviour of PPMA-EGO was affected by surface area due to the type of mixing method employed. Distributive mixing produced higher storage modulus in comparison with those produced by dispersive mixing. The low storage modulus obtained from dispersive mixing was attributed to there being a greater concentration of graphite particles as a result of high shearing provided by the Ultra-Turrax disperser than maleic anhydride groups on PPMA. Therefore some shEGO may have been unable to bond to maleic anhydride groups, which was attributed to lack of bonding sites. The glass transition temperature of all PPMA-EGO was higher compared with pure PPMA matrix. This is due to the hydrogen bonding between the polar groups between PPMA and EGO.

The dielectric properties of PPMA were improved upon addition of EGO relative to pure PPMA. This is because of the non-uniform distribution of graphite particles in the PPMA matrix and therefore absence of a continuous conducting network of graphite.

PPMA-EGO at various EGO concentrations (1 to 7 %wt) was prepared by melt blending. Scanning electron microscopy of EGO in PPMA-EGO revealed the interconnected network structure of EGO was lost due to shearing provided by the mechanical mixing because of the absence of PPMA in the graphite layers. The WAXD measurements; *d* spacing of PPMA-EGO showed the same results as that of other polymer layered composites studied in that no change occurred in the *d* spacing of the graphite layers. In addition the mechanical mixing utilised was unable to affect the order of the graphite layers in the PPMA matrix. Therefore the graphite layers in the PPMA remained ordered and multilayered. The crystalline thickness of EGO in PPMA increased. The crystalline thickness of EGO was observed at 3 %wt in PPMA.

The thermal properties of PPMA in the presence of EGO obtained from DSC measurements and TGA indicated that EGO behaved as a nucleating agent and a barrier between heat and PPMA. From the DSC measurements the crystallisation temperature of PPMA in the presence of EGO increased. The graphite particles induce the crystallisation of PPMA at higher temperatures by serving as nucleation sites for PPMA crystals. The thermal stability of PPMA obtained from TGA was higher with the incorporation of EGO in nitrogen atmosphere. EGO acted as a barrier between heat thereby delaying decomposition of PPMA matrix.

The storage modulus and glass transition temperature of PPMA in the presence of EGO indicated that EGO had a reinforcing effect on the elastic behaviour of PPMA matrix. The enhanced elastic behaviour was due to the strong polar interaction between PPMA matrix and EGO polar groups. The maximum storage modulus of PPMA was observed at 3 %wt of EGO. At higher EGO (5 and 7 %wt) concentration the storage modulus of PPMA was lower relative to PPMA 3 %wt of EGO. This is due to higher concentration of graphite particles than maleic anhydride groups. Therefore, some graphite particles were unable to bond to maleic anhydride groups due to lack of bonding sites.

The electrical conductivity of PPMA-EGO was only measurable for EGO concentrations above 3 %wt. The graphite particles during dispersion were probably reduced in size and/or graphite layers were disrupted (broken) due to the melt mixing of the Haake Rheocord mixer. Therefore it was only at higher EGO concentration the graphite particles could form a conducting network. PPMA-EGO electrical conductivity was observed at 7 %wt of EGO (1.25×10^{-3} $S.cm^{-1}$). The EGO concentration played a role in the improvement of electrical conductivity of the PPMA-EGO.

Three types of polymer layered graphite oxide composites were prepared using polyolefins (EMAA and PPMA) with functionality groups that enhanced interfacial adhesion, with various forms of layered graphite oxides. The analyses of these properties using various techniques indicate that preparative mixing method employed played an important role in the polymer layered composite properties. Solution blending using dispersive mixing provided by the high shearing action of the Ultra-Turrax disperser that disrupted the connections between the graphite layers played role in the properties of polymer layered graphite oxide composites. Melt blending via mechanical mixing, like the solution blending using dispersive mixing had a similar effect on the connections between the graphite layers. However, the mechanical

mixing was less intensive when compared with dispersive mixing. As a result, the change in properties of these polymer layered graphite oxide composites such as thermal and mechanical properties were pronounced compared with composites prepared from solution blending via dispersive mixing. Therefore a strong interfacial adhesion between the polymer matrix that can withstand high shearing or mechanical mixing utilised to mix polymer matrix and various forms of graphite oxide was important. Another factor that needs to be appreciated is that of layered graphite oxide is a difficult material to work with in comparison with layered silicates. The limited improvement in properties of these polymer layered graphite oxide composites can be explained by layered graphite oxide properties such as chemical inertness and small *d* spacing. Layered graphite oxides chemical inertness makes it incompatible with polymer matrices. To overcome this layered graphite oxide requires strong acidic oxidative reagents to weaken the bonding between the graphite layers and generate oxidised functional groups. Layered graphite oxide small *d* spacing makes it difficult for polymer to intercalate. Nevertheless, the presence of graphite particles affects the thermal, mechanical and electrical properties of the polymer matrix. The graphite particles in the polymer matrix behaved as a heterogenous nucleating agent and a thermal barrier between heat and the polymer matrix. Graphite behaved as a reinforcer for polymer matrix thereby improving elastic behaviour.

8.1 Future research

Graphite is a conducting filler for polymers, however in our investigation conductivity was affected by type of blending method and techniques employed to disperse layered graphite oxide in the polymer matrix. In our findings, electrical conductivity of the polymer composite was only measured at 3, 5 and 7 %wt of expanded graphite oxide via melt blending. A series of polymer layered composites filled with either layered graphite oxides or expanded graphite oxides (1 to 10 %wt) could be prepared, to determine the concentration effect of either layered graphite oxides or expanded graphite oxides on the polymer matrix.

Other ways to prepare polymer layered composites filled with either layered graphite oxide or expanded graphite oxide would be to prepare a masterbatch; a concentrated mixture of fillers in the polymer matrix, and then disperse the mixture into more polymer matrix using an extruder. The initial masterbatch may be prepared using an extruder. The polymer layered composites can finally be extruded as a tape that could be used for measurement of properties or pressed thinner using a heat press.

Various functionalised polymer matrix (thermoplastics) could be used to prepare polymer layered graphite oxide or expanded graphite oxide composites such as polyacrylates, polyimide, polyamide and polyamide-imide. The high polarity of these polymer matrices would enhance their interfacial adhesion with layered graphite oxide and as a result improve their thermal and mechanical properties.

It was difficult to obtain visual imaging using transmission electron microscopy (TEM) because there was not enough contrast between the polymer matrix and filler, therefore atomic force microscopy (AFM) could be employed to determine whether the polymer layered composites have an intercalated or exfoliated structure. The visual image from AFM would compliment the WAXD and SEM obtained.

Creep recovery is a DMA test that determines polymer relaxations and fundamentals of polymer behaviour in the long term. It involves applying a constant load for a certain period of time then removing the load from a sample. The distortion and the recovery of a sample are determined by analysing both creep and recovery. Creep recovery test is useful for studying polymer layered graphite oxide composites mechanical properties to determine creep resistance. In addition, this test can be repeated multiple times at various temperatures and therefore can mimic real life conditions.

References

1. Zanetti, M., Lomakin, S. and Camino, G., Polymer layered silicate nanocomposites, *Macromolecular Materials and Engineering*, **279**, 1, (2000).

2. Uhl, F.M., Yao, Q., Nakajima, H., et al., Expandable graphite/polyamide-6 nanocomposites, *Polymer Degradation and Stability*, **89**, 70, (2005).

3. Fu, X. and Qutubuddin, S., Polymer-clay nanocomposites:exfoliation of organophilic montmorillonite nanolyers in polystyrene, *Polymer*, **42**, 807, (2001).

4. Chen, G.H., Wu, D.J., Weng, W.G., et al., Dispersion of graphite nanosheets in a polymer matrix and the conducting property of the nanocomposites, *Polymer Engineering and Science*, **41**, 2148, (2001).

5. Gangopadhyay, R. and De, A., Conducting Polymer Nanocomposites: A Brief Overview, *Chemistry of Materials*, **12**, 608, (2000).

6. Jana, S. C. and Jain, S., Dispersion of nanofillers in high performance polymers using reactive solvents as processing aids, *Polymer*, **42**, 6897, (2001).

7. Saujanya, C. and Radhakrishnan, S., Structure development and crystallization behaviour of PP/nanoperticulate composite, *Polymer*, **42**, 6723, (2001).

8. Favier, V., Canova, G., Shrivastava, S., et al., Mechanical percolation in cellulose whiskers nanocomposites, *Polymer Engineering Science*, **37**, 1732, 1997).

9. Chen, G.H., Wu, D.J., Weng, W.G., et al., Preparation of polymer/graphite conducting nanocomposite by intercalation polymerization, *Journal of Applied Polymer Science*, **82**, 2506, (2001).

10. Pan, Y.X., Yu, Z.Z., Yu, C., et al., A new process of fabricating electrically conducting nylon 6/graphite nanocomposites via intercalation polymerization, *Journal of Polymer Science: Part B Polymer Physics*, **38**, 1626, (2000).

11. Zheng, W. and Wong, S.C., Electrical conductivity and dielectric properties of PMMA/expanded graphite composites, *Composites Science and Technology*, **63**, 225, (2003).

12. Krishnamoorti, R. and Vaia, R.A., *Polymer nanocomposites: synthesis, characterisation, and modelling*, American Society, Washington, D.C., 2001.

13. Usuki, A., Kojima, M., Kawasumi, M., et al., Synthesis of nylon 6 clay hybrid, *Journal of Materials Resources*, **8**, 1179, (1993b).

14. Usuki, A., Koiwai, A., Kojima, Y., et al., Interaction of nylon 6-clay surface and mechanical properties of nylon 6-clay hybrid, *Journal of Applied Polymer Science*, **55**, 119, (1995).

15. Okada, A. and Usuki, A., The chemistry of polymer-clay hybrids, *Materials Science Engineering C*, **3**, 109, (1995).

16. Giannelis, E. P., Krishnamoorti, R. and Manias, E., *Polymer-silicate nanocomposites: model systems for confined polymers and polymer brushes*; Ed.^Eds.; Springer-Verlag, Berlin Heidelberg, 1999,

17. LeBaron, P.C., Wang, Z. and Pinnavaia, T.J., Polymer-layered silicate nanocomposites: an overview, *Applied Clay Science*, **15**, 11, (1999).

18. Uhl, F.M. and Wilkie, C.A., Polystyrene/graphite nanocomposites: effect on thermal stability, *Polymer Degradation and Stability*, **76**, 111, (2002).

19. Giannelis, E.P., Polymer layered silicate nanocomposites, *Advanced Materials*, **8**, 29, (1996).

20. Korakianiti, A., Papefthimiou, V., Daflou, T., et al., Characterisation of polypropylenen(PP) nanocomposites for industrial applications,*Macromolecules Symposium*, **205**, 71, (2004).

21. Ishida, H., Campbell, S. and Blackwell, J., General approach to nanocomposite preparation, *Chemistry of Materials*, **12**, 1260, (2000).

22. Ellis, T.S. and D'Angelo, J.S., Thermal and mechanical properties of a polypropylene nanocomposite, *Journal of Applied Polymer Science*, **91**, 1639, (2003).

23. Pinnavaia, T. J.and Beall, G. W., *Polymer-clay nanocomposites*, John Wiley & Sons, Ltd, New York, 2000.

24. Giannelis, E. P., Polymer-layered silicates nanocomposites: synthesis, properties and applications, *Applied Organometallic Chemistry*, **12**, 675, (1998).

25. Zhang, Q., Fu, Q., Jiang, L., et al., Preparation and properties of polypropylene/montmorillonite layered nanocomposites, *Polymer International*, **49**, 1561, (2000).

26. Vaia, R.A. and Giannelis, E.P., Lattice model of polymer melt intercalation organically-modified layered silicates, *Macromolecules*, **30**, 7990, (1997).

27. Xiao, M., Sun, L., Liu, J., et al., Synthesis and properties of polystyrene/graphite nanocomposites, *Polymer*, **43**, 2245, (2002).

28. Uhl, F.M., Lamelas, F.J. and Wilkie, C.A., Flame retardancy of graphite nanocomposites, *Abstract Paper. - American Chemical Society*, **220th**, MSE, (2000).

29. Zheng, W., Wong, S.C. and Sue, H.J., Transport behaviour of PMMA/expanded graphite nanocomposites, *Polymer*, **73**, 6767, (2002).

30. Zheng, W., Lu, X. and Wong, S.C., Electrical and mechanical properties of expanded graphite-reinforced high-density polyethylene, *Journal of Applied Polymer Science*, **91**, 2781, (2004).

31. Shen, Z., Simon, G. P. and Cheng, Y.B., Comparison of solution intercalation and melt intercalation of polymer-clay nanocomposites, *Polymer*, **43**, 4251,(2002).

32. Berglund, L., Nano-sized fillers - advantages and disadvantages, *Fillers & Additives for Plastics 2000, Collected Papers of the International Conference, 4th, Copenhagen, Denmark, Oct. 25-26, 2000*, 3.1, (2000).

33. Liu, X. and Wu, Q., Polyamide 66/clay nanocomposites via melt intercalation, *Macromolecular Materials and Engineering*, **287**, 180, (2002).

34. Gopakumar, T.G. and Page, D.J.Y.S., Polypropylene/graphite nanocomposites by thermo-kinetic mixing, *Polymer Engineering and Science*, **44**, 1162, (2004).

35. Li, X., Kang, T., Cho, W.J., et al., Preparation and characterization of poly(butyleneterephthalate)/organoclay nanocomposites, *Macromolecular Rapid Communications*, **22**, 1306, (2001).

36. Vaia, R.A., Ishii, H. and Giannelis, E.P., Synthesis and properties of two-dimensional nanostructures by direct intercalation of polymer melts in layered silicates, *Chemistry of Materials*, **5**, 1694, (1993).

37. Vaia, R.A., Krawiec, W., Scanlon, L.G., et al., Kinetics of polymer melt intercalation, *Macromolecules*,**28**,8080,(1995).

38. Yano, K., Usuki, A., Okada, A., et al., Synthesis a properties of polyimide clay hybrid, *Journal of Polymer Science Part A: Polymer Chemistry*, **31**, 2493, (1993).

39. Messersmith, P.B. and Giannelis, E.P., Synthesis and characterization of layered silicate- epoxy nanocomposites, *Chemistry of Materials*, **6**, 1719, (1994).

40. Lan, T. and Pinnavaia, T.J., Clay reinforced epoxy nanocomposites, *Chemistry of Materials*, **6**, 2216, (1994).

41. Pantoustier, N., Alexandre, M., Degree, P., et al., Poly(.epsilon.-caprolactone) layered silicate nanocomposites: effect of clay surface modifiers on the melt intercalation process, *e-Polymers [online computer file]*, (2001).

42. Messersmith, P.B. and Giannelis, E.P., Synthesis and barrier properties of poly(E-caprolactone) layered silicate nanocomposite, *Journal of Polymer Science Part A: Polymer Chemistry*, **33**, 1047, (1995).

43. Messersmith, P.B. and Giannelis, E.P., Synthesis and barrier properties of poly(E-caprolactone)-layered silicate nanocomposites, *Journal of Polymer Science: Part A: Polymer Chemistry*, **33**, 1047, (1995).

44. Messersmith, P.B. and Giannelis, E.P., Polymer-layered silicate nanocomposites: in situ interclative polymerization of e-caprolactone in layered silicates, *Chemistry of Materials*, **5**, 1064, (1993).

45. Zhu, J. and Wilkie, C.A., Thermal and fire studies on polystyrene-clay nanocomposites, *Polymer International*, **49**, 1158, (2000).

46. Chen, G., Qi, Z. and Shen, D., Shear-induced ordered structure in polystyrene/clay nanocomposite, *Journal of Materials Resource*, **15**, 351, (2000).

47. Liu, L., Qi, Z. and Zhu, X., Studies on Nylon 6/Clay Nanocomposites by melt intercalation process, *Journal of Applied Polymer Science*, **71**, 1133, (1999).

48. Fornes, T.D., Hunter, D.H. and Paul, D.R., Nylon-6 nanocomposites from alkylammonium-modified clay: the role of alkyl tails on exfoliation, *Macromolecules*, **37**, 1793, (2004).

49. Delozier, D.M., Orwoll, R.A., Cahoon, J.F., et al., Preparation and characterisation of polyimide organoclay nanocomposites, *Polymer*, **43**, 813, (2002).

50. Ranade, A., D'Souza, N. A. and Gnade, B., Exfoliated and intercalated polyamide-imide nanocomposites with montmorillonite, *Polymer*, **43**, 3759, (2002).

51. Yano, K., Usuki, A., Okada, A., et al., Synthesis and properties of polyimide-clay hybrid, *Journal of Polymer Science: Part A: Polymer Chemistry*, **31**, 2493, (1993).

52. Agag, T., Koga, T. and Takeichi, T., Studies on thermal and mechanical properties of polyimide-clay nanocomposites, *Polymer*, **42**, 3399, (2001).

53. Massam, J. and Pinnavaia, T.J., Clay nanolayer reinforcement of a glassy epoxy polymer, *Materials Resource Society Symposium Proceedings*, **520**, 223, (1998).

54. Hyun, Y.H., Lim, S.T., Choi, H.J., et al., Rheology of Poly(ethylene oxide)/Organoclay Nanocomposites, *Macromolecules*, **34**, 8084, (2001).

55. Xu, W., Ge, M. and He, P., Non-isothermal crystallization kinetics of polypropylene/montmorillonite nanocomposites, *Journal of Polymer Science, Part B: Polymer Physics*, **40**, 408, (2002).

56. Kawasumi, M., Hasegawa, N., Kato, M., et al., Preparation and mechanical properties of polypropylene clay hybrids, *Macromolecules*, **30**, 6333, (1997).

57. Usuki, A., Kato, M., Okada, A., et al., Synthesis of polypropylene clay hybrid, *Journal of Applied Polymer Science*, **63**, 137, (1997).

58. Vaia, R.A., Jandt, K.D., Kramer, E.J., et al., Microstructural evolution of melt intercalated polymer organically modified layered silicates nanocomposites, *Chemistry of Materials.*, **8**, 2628, (1996).

59. Burnside, S.D. and Giannelis, E.P., Synthesis and properties of new(dimethylsiloxane) nanocomposites, *Chemistry of Materials*, **7**, 1597, (1995).

60. Priya, L. and Jog, J. P., Poly(vinylidene fluoride)/clay nanocomposites prepared by melt intercalation: crystallization and dynamic mechanical behaviour studies, *Journal of Polymer Science, Part B: Polymer Physics*, **40**, 1682, (2002).

61. Di, Y., Iannace, S., Maio, E.D., et al., Nanocomposites by melt intercalation base on polycaprolactone and organoclay, *Journal of Polymer Science: Part B: Polymer Physics*, **41**, 670, (2003).

62. Porter, D., Metcalfe, E. and Thomas, M. J. K., Nanocomposite fire retardants-a review, *Fire and Materials*, **24**, 45, (2000).

63. Gilman, J.W., Flammability and thermal stability studies of polymer layered-silicate (clay) nanocomposites, *Applied Clay Science*, **15**, 31, (1999).

64. Fukushima, H. and Drzal, L. T., A carbon nanotube alternative: graphite nanoplatelets as reinforcements for polymers, *ANTEC*, 2230, (2003).

65. Chung, D.D.L., Review graphite, *Journal of Materials Science*, **37**, 1475, (2002).

66. Pierson, H. O., *Handbook of Carbon, Graphite, Diamond, and Fullerenes*, Noyes Publications, Park Ridge, New Jersey, 1993.

67. Nakajima, T. and Matsuo, Y., Formation process and structure of graphite oxide, *Carbon*, **32**, 469, (1994).

68. Sato, Y., Shiraishi, S., Watano, H., et al., Pyrolytically prepared carbon from fluorine-GIC, *Carbon*, **41**, 1149, (1941).

69. Nakajima, T., Koh, M., Gupta, V., et al., Electrochemical behaviour of graphite highly fluorinated by high oxidation state complex fluorides and elemental fluorine, *Electrochimica Acta*, **45**, 1655, (2000).

70. Remy, H., *Introduction and main groups of the periodic table*; Kleinberg, J., Ed.^Eds.; Elsevier Publishing Company, Amsterdam, 1956, p 418.

71. Ebert, L.B., Brauman, J.I. and Huggins, R.A., Carbon monofluoride. Evidence for a structure containing an infinite array of boats, *Journal of American Chemical Society*, **96**, 7841, (1974).

72. Panich, A.M., Nuclear Magnetic Resonance Study of Fluorine-Graphite Intercalation Compounds and Graphite Fluorides. Review article, *Synthetic Metals*, **100**, 169, (1999).

73. Ubbelohde, A.R., *Graphite and its crystal compounds*, Oxford, London, 1960.

74. Sato, Y., Hagiwara, R. and Ito, Y., Thermal decomposition of 1st stage fluorine-grapite intercalation compounds, *Journal of Fluorine Chemistry*, **110**, 31, (2001).

75. McDonnell, F.R.M.P. and Ubbelohde, A.R., Physical properties associated with "aromatic" electrons. III. Pseudometallic properties of potassium-graphite and graphite-bromine., *Journal of Chemical Society*, 191, (1951).

76. Remy, H., *Sub-groups on the periodic table and general topics*; Kleinberg, J., Ed.^Eds.; Elsevier Pub. Co., London, 1956, p758.

77. He, H., Klinowski, J., Forster, M., et al., A new structural model for graphite oxide, *Chemical Physics Letters*, **287**, 53, (1998).

78. Chen, G., Weng, W., Wu, D., et al., PMMA/graphite nanosheets composite and its conducting properties, *European Polymer Journal*, **39**, 2329, (2003).

79. Shioyama, H., The interaction of two chemical species in the interlayer spacing of graphite, *Synthetic Metals*, **114**, 1, (2000).

80. Sasa, T., Takahashi, Y. and Mukaibo, T., Crystal structure of graphite bromine lamellar compounds, *Carbon*, **9**, 407, (1971).

81. Ruiz, F.A. and Bankole, A.O., Mineral reinforcement of linear-low density polyethylene film, bags, and liners, *Annual Technology Conference - Society Plastic Engineering*, **50th**, 1670, (1992).

82. Sharma, P.K. and Hickey, G.S., Kinetics of the formation of intercalation compounds in crystalline graphite, *Special Publication - Royal Society of Chemistry*, **173**, 76, (1996).

83. Udod, I.A., Sodium-graphite intercalation compound of the first stage: two-dimensional structure and stability, *Synthetic Metals*, **88**, 127, (1997).

84. Funabiki, A., Inaba, M., Abe, T., et al., Stage transformation of lithium graphite-graphite intercalation compounds caused by electrochemical lithium intercalation, *Journal Electrochemical Society*, **146**, 2443, (1999).

85. Beguin, F. and Setton, R., New ternary lamellar compounds of graphite, *Carbon*, **13**, 293, (1975).

86. Nalimova, V.A., Zakharov, A.P., Avdeev, V.V., et al., Synthesis of new ternary alkali metal GICs at high pressures, *Synthetic Metals*, **48**, 247, (1992).

87. Pruvost, S., Herold, C., Herold, A., et al., Co-intercalation into graphite of lithium and sodium with an alkaline earth metal, *Carbon*, **42**, 1825, (2004).

88. Zerda, A. S. and Lesser, A.J., Intercalated clay nanocomposites: morphology, mechanics and fracture behaviour, *Materials Research Society Symposium Proceedings*,**661**,KK7.2/1, (2001).

89. Oh, W.C., Cho, S.J. and Ko, Y.S., The stability of potassium-graphite deintercalation compounds, *Carbon*, **34**, 29, (1999).

90. Wang, C., Kakwan, I., Appleby, J., et al., In situ investigation of electrochemical lithium intercalation into graphite powder, *Journal of Electroanalytical Chemistry*, **489**, 55, (2000).

91. Endo, M., Kim, C., Nishimura, K., et al., Recent development of carbon materials for Li ion batteries, *Carbon*, **38**, 183, (2000).

92. Thevenot, L., Willmann, P. and Billaud, D., X-ray diffraction analysis of the structure of the new lithium rich graphite intercalation compound $Li_2C_6O_{0.5}$, *Carbon*, **37** , 1373, (1999).

93. Duquesne, S., Bras, M. L., Bourbigot, S., et al., Expandable graphite: a fire retardant additive for polyurethane coatings, *Fire and Materials*, **27**, 103, (2003).

94. Scharff, P., Xu, Z.Y., Stumpp, E., et al., Reversibility of the intercalation of nitric acid into graphite, *Carbon*, **29**, 31, (1991).

95. Scharff, P., Stumpp, E., Barteczko, K., et al., Investigations on the kinetics of the anodic intercalation process of graphite in 65% nitric acid by using AC impedance measurements, *Berichte der Bunsen Gesellschaft Physical Chemistry*, **94**, 568, (1990).

96. Avdeev, V.V., Tverezovskaya, O.A., Sorokina, N.E., et al., Electrochemical study of the graphite-HNO_3 system, *Inorganic Materials (Translation of Neorganicheskie Materialy)*, **36** , 276, (1999).

97. Sorokina, N.E., Leshin, V.S. and Avdeev, V.V., Electrochemical intercalation in the graphite-H_2SO_4-R (R=CH_3COOH, H_3PO_4) system, *Journal of Physics and Chemistry of Solids*, **65**, 185, (2004).

98. Savoskin, M.V., Yaroshenko, A.P., Whyman, G.E., et al., Theoretical study of stability of raphite intercalation compounds with Bronsted acids, *Carbon*, **41**, 2757, (2003).

99. Alliata, D., Kötz, R., Haas, O., et al., In-situ AFM study of interlayer spacing during anion intercalation into HOPG in aqueous electrolyte, *Langmuir*, **15**, 8483,(1999).

100. Zheng, G., Wu, J., Wang, W.P., et al., Characterization of expanded graphite-polymer composites prepared by in situ polymerization, *Carbon*, **42**, 2839, (2004).

101. Weng, W.G., Chen, G.H., Wu, D.J., et al., Preparation and characterization of nanoparticles from graphite via electrochemically oxidizing method, *Synthetic Metals*, **139**, 221, (2003).

102. Avdeev, V.V., Sorokina, N.E., Nikol'skaya, I.V., et al., Synthesis of intercalation compounds in the system graphite-HNO_3-H_2SO_4, *Inorganic Materials (Translation of Neorganicheskie Materialy)*, **33**, 584, (1997).

103. Sorokina, N.E., Maksimova, N.V. and Avdeev, V.V., Intercalation of Graphite in the Ternary Systems C-HNO_3-R (R = H_2O, CH_3COOH, H_3PO_4 , H_2SO_4), *Inorganic Materials (Translation of Neorganicheskie Materialy)*, **38**, 564, (2002).

104. Kang, F., Zhang, T.Y. and Leng, Y., Electrochemical behaviour of graphite in electrolyte of sulfuric acid and acetic acid, *Carbon*, **35**, 1167, (1997).

105. Chen, X., Song, K. and Li, J., Preparation of lower-sulfur content and expandable graphite, *Carbon*, **34**, 1599, (1996).

106. Inagaki, M., Tashiro, A., Washino, Y.I., et al., Exfoliation process of graphite via intercalation compounds with sulfuric acid, *Journal of Physics and Chemistry of Solids*, **65**, 133, (2004).

107. Martin, W.H. and Brockelehurst, J.E., The thermal expansion behaviour of pyrolytic graphite-bromine residue compounds, *Carbon*, **1**, 133, (1964).

108. Chung, D.D.L., Review Exfoliation graphite, *Journal of Materials Science*, **22**, 4190, (1987).

109. Chung, D.D.L., Intercalate vaporisation during exfoliation of graphite intercalated with bromine, *Carbon*, **25**, 361, (1987).

110. Furdin, G., Exfoliation process and elaboration of new carbonaceous materials, *Fuel*, **77**, 479, (1998).

111. Anderson, S.H. and Chung, D.D.L., Exfoliation of intercalated graphite, *Carbon*, **22**, 253, (1984).

112. Olsen, L.C., Seeman, S.E. and Scott, H.W., Expanded pyrolytic graphite:structural and transport properties, *Carbon*, **8**, 85, (1970).

113. Chung, D.D.L. and Wong, S.C., Effect of exfoliation on the electrical resistivity of intercalated graphite, *Synthetic Metals*, **12**, 533, (1985).

114. Toyoda, M. and Inagaki, M., Heavy oil sorption using exfoliated graphite: New application of exfoliated graphite to protect heavy oil pollution, *Carbon*, **38**, 199, (2003).

115. Tryba, B., Morawski, A.W., Kalenczuk, R.J., et al., Exfoliated graphite for removing wasted oil and colors from water, *Environmental Technology for Oil Pollution, Proceedings of U.S. United Engineering Foundation Conference and 2nd International Conference Analysis and Utilization of Oily Wastes AUZO'99, Jurata, Poland, Aug. 29-Sept. 3, 1999*, **1**, 167, (1999).

116. Toyoda, M., Moriya, K., Aizawa, J., et al., Sorption of heavy oil by exfoliated graphite, *Environmental Technology for Oil Pollution, Proceedings of U.S. United Engineering Foundation Conference and 2nd International Conference Analysis and Utilization of Oily Wastes AUZO'99, Jurata, Poland, Aug. 29-Sept. 3, 1999*, **1**, 139, (1999).

117. Wenci, S. and Wen, W., Expanded graphite: a new kind of biomedical material, *Carbon*, **37**, 356, (1999).

118. Chen, G., Weng, W., Wu, D., et al., Preparation and characterization of graphite nanosheets from ultrasonic powdering technique, *Carbon*, **42**, 753, (2004).

119. Uhl, F.M. and Wilkie, C.A., Nylon/graphite nanocomposites, *Polymer Preprint. (American Chemical Society, Division Polymer Chemistry)*, **42**, 176, (2001).

120. Semko, I.S., Popov, R.E. and Chernysh, I.G., Electrical properties of composites based on polypropylene and thermally expanded graphite, *International Polymer Science and Technology*, **24**, 71, (1997).

121. Chen, X.M., Shen, J.W. and Huang, W.Y., Novel electrically conductive polypropylene/graphite nanocomposites, *Journal of Materials Science Letters*, **21**, 213, (2002).

122. Shen, J.W., Huang, W.Y., Zuo, S.W., et al., Polyethylene/grafted polyethylene/graphite nanocomposites: preparation, structure and electrical properties, *Journal of Applied Polymer Science*, **97**, (2005).

123. Busick, D.N., Spontak, R.J. and Balik, C.M., Effects of graphite content on the morphology and barrier properties of poly(vinylidene fluoride) composites, *Polymer*, **40**, 6023, (1999).

124. Duquesne, S., Bras, M.L., Bourbigot, S., et al., Thermal degradation of polyurethane and polyurethane/expandable graphite coatings, *Polymer Degradation and Stability*, **74**, 493, (2001).

125. Zhang, C., Yi, X.S., Yui, H., et al., Morphology and electrical properties of short carbon fiber-filled polymer blends: High-density polyethylene/poly(methyl methacrylate), *Journal of Applied Polymer Science*, **69**, 1813, (1998).

126. McLachlan, D.S., Measurement and analysis of a model dual-conductivity medium using a generalised effective-medium theory, *Journal Physics C: Solid State Physics*, **21**, 1521, (1988).

127. Weber, M. and Kamal, M.R., Estimation of the volume resistivity of electrically conductive composites, *Polymer Composites*, **18**, 711, (1988).

128. Lux, F., Review: Models proposed to explain electrical conductivity of mixtures made of conductive and insulating materials, *Journal of Materials Science*, **28**, 285, (1993).

129. Ou, Y., Zhu, J. and Feng, Y.P., Interfacial design of the nonpolar polyolefin ternary composites with high strength, high toughness and high modulus, *Journal of Applied Polymer Science*, **59**, 287, (1996).

130. Chen, G.H., Wu, D.J., Weng, W.G., et al., Preparation of polystyrene-graphite conducting nanocomposites via intercalation polymerization, *Polymer International*, **50**, 980, (2001).

131. Duquesne, S., Delobel, R., Le Bras, M., et al., A comparative study of the mechanism of action of ammonium polyphosphate and expandable graphite in polyurethane, *Polymer Degradation and Stability*, **77**, 333, (2002).

132. Yasmin, A. and Daniel, I.M., Mechanical and thermal properties of graphite platelet/epoxy composites, *Polymer*, **45**, 8211, (2004).

133. Modesti, M., Lorenzetti, A., Simioni, F., et al., Expandable graphite as an intumescent flame retardant in polyisocyanurate-polyurethane foams, *Polymer Degradation and Stability*, **77**, 195, (2002).

134. Xiao, P., Xiao, M. and Gong, K., Preparation of exfoliated graphite/polystyrene composite by polymerization-filling technique, *Polymer*, **42**, 4813, (2001).

135. Wischnitzer, S., *Introduction to electron microscopy*, New York : Pergamon Press, c1981, New York, 1989.

136. Goodhew, P.J. and Humphreys, F.J., *Electron microscopy and analysis*, Taylor and Francis Pub, London, 1997.

137. Belfry, S., Ultramicrotomy of Industrial Materials., www.unbca/fredericton/science/emunit/ancillary.html. Ed.^Eds.,New Brunswick, July 26 2005.

138. Gregg, S.J. and Sing, K.S., *Adsorption, Surface Area and Porosity*, Academic Press Inc, London, 1967.

139. Griffiths, P.R. and De Haseth, J.A., *Fourier transform infrared spectrometry*, Wiley, New York, 1986.

140. Ewing, G.W., *Analytical instrument handbook*, Marcel Dekker, Inc, New York, 1997.

141. Liang, G., Xu, J., Bao, S., et al., Polyethylene/maleic anhydride grafted polyethylene/organic-montmorillonite nanocomposites. I. preparation, microstructure, and mechanical properties, *Journal of Applied Polymer Science*, **91**, 3974, (2004).

142. Quirk, R.P. and Alsamarraie, A.A., *Physical Constants of Poly(propylene), : in Polymer Handbook*, John Wiley and Sons, New York, 1989.

143. Mahajan, S.J., Deopura, B.L. and Wang, Y., Structure and properties of drawn tapes of high-density polyethylene/ethylene copolymer blends. I., *Journal of Applied Polymer Science*, **60**, 1517, (1996).

144. Adisson, E., Ribeiro, M., Deffieux, A., et al., Evaluation of the heterogeniety in linear low-density polyethylene comonomer unit distribution by differential scanning calorimetry characterization of thermally treated sample, *Polymer*, **33**, 4337, (1992).

145. Menard, D., *Dynamic mechanical analysis; a practical introduction*, Boca Raton, CRC Press, 1999.

146. Wong, S., Shanks, R. and Hodzic, A., Interfacial improvements in poly(3-hydroxybutyrate)-flax fibre composites with hydrogen bonding additives, *Composites Science and Technology*, **64**, 1321, (2004).

147. Ehrenstrein, G.W., *Polymer materials, Structure, properties, applications*, Munich:Hansen Publishers, 2001.

148. Twombly, B. and Shepard, D.D., Simultaneous dynamic mechanical analysis and dielectric analysis of polymers (DMA-DEA), *Instrumentation Science & Technology*, **22**, 259, (1994).

149. *Eumetric system III Microdielectrometer User's guide*, Micromet Instrumentaion, Inc.

150. Frackowiak, E., Kaiser, W., Krohn, H., et al., Electrochemical redox capacity of thermally exfoliated graphite in sulfuric acid, *Molecular Crystal Liquid Crystal Science Technology, Section. A*, **244**, 221, (1994).

151. Greinke, R.A.,. Expandable graphite method,. Ed.^Eds.; UCAR Graph-Tech.Inc., United States of America, 1998, p1.

152. Puzyreva, E.V. and Komarova, T V., Influence of various factors on the process of producing expanded graphite, *Solid Fuel Chemistry*, **16**, 113, (1892).

153. Bonnissel, M., Luo, L. and Todeur, D., Compacted exfoliated natural graphite as heat conduction medium, *Carbon*, **39**, 2151, (2001).

154. Xiao, P., Sun, L., Xiao, M., et al., Preparation and properties of exfoliated graphite/polystyrene composite, *Materials Research Society Symposium Proceedings*, **661**, KK5.3/1, (2001).

155. Kang, F., Zheng, Y.P., Wang, H.N., et al., Effect of preparation conditions on the characteristics of exfoliated graphite, *Carbon*, **40**, 1575, (2002).

156. Aronson, S., Frishberg, C. and Frankl, G., Thermodynamic properties of the graphite-bisulfate lamellar compounds, *Carbon*, **9**, 715, (1971).

157. Hontoria-Lucas, C., Lopez-Peinado, A.J. and Lopez-Gonzalez, J.D., Study of oxygen-containing groups in a series of graphite oxides: physical and chemical characterization, *Carbon*, **33**, 1585, (1995).

158. Kovtyukhova, N.I., Ollivier, P.J., Martin, B.R., et al., Layer-by-layer assembly of ultrathin composite films from micron-sized graphite oxide sheets and polycations, *Chemistry of Materials*, **11**, 771, (1999).

159. Peckett, J., W., Trens, P., Gougeon, R. D., et al., Electrochemically oxidised graphite. Characterisation and some ion exchange properties, *Carbon*, **38**, 345, (2000).

160. Zawadzki, J., *In Chemistry and Physics of Carbon*, Marcel Dekker, New York, 1989.

161. Nakajima, T., Mabuchi, A. and Hagiwara, R., A new structure model of graphite oxide, *Carbon*, **26**, 357, (1988).

162. Uhl, F.M. and Wilkie, C.A., Preparation of nanocomposites from styrene and modified graphite oxides, *Polymer Degradation and Stability*, **84**, 215, (2004).

163. Matsuo, Y., Niwa, T. and Sugie, Y., Preparation and characterization of cationic surfactant intercalated graphite oxide, *Carbon*, **37**, 897, (1999).

164. Matsuo, Y., Tahara, K. and Sugie, Y., Structure and thermal properties of poly(ethylene oxide) intercalated graphite oxide, *Carbon*, **35**, 113, (1997).

165. Tsukruk, V.V., Sidorenko, A. and Yang, H., Polymer nanocomposite coating with non-linear elastic response, *Polymer*, **43**, 1695, (2002).

166. Potassium Chlorate MSDS sheet, http://hummelcroton.com/kclo3_m.html, July 26 2005.

167. Blythe, W., Potassium Permanganate MSDS sheet, http://wm-blythe.co.uk/WMBLYTHE/CSDS.nsf/0/45c4ca1796607ae28025672, July 26 2005.

168. Xie, R. and Qu, B., Expandable graphite systems for halogen-free flame retarding of polyoelfins. 1.Flammability characterisation and synergistic effect, *Journal of Applied Polymer Science*, **80**, 1181, (2000).

169. Mathur, R.B., Bahl, D.P. and Nagoal, K.C., Studies on the exfoliation mechanism of intercalated graphite flakes, *Carbon*, 499, (1986).

170. Inagaki, M. and Nakashima, M., Graphite exfoliated at room temperature and its structural annealing, *Carbon*, **32**, 1253, (1994).

171. Smith, W.F., *Principles of materials science and engineering*, McGraw-Hill, Inc, New York, 1996.

172. Kotov, N.A., Dekany, I. and Fendler, J.H., Ultrathin graphite oxide-polyelectrolyte composites prepared by self-assembly: transition between conductive and non-conductive states, *Advanced Materials*, **8**, 637, (1996).

173. Wang, K.H., Choi, M.H., Koo, C.M., et al., Morphology and physical properties of polyethylene/silicate nanocomposite prepared by melt intercalation, *Journal of Polymer Science, Part B: Polymer Physics*, **40**,1454, (2002).

174. Cerezo, F.T., Preston, C.M.L. and Shanks, R.A., Structural, mechanical and dielectric properties of poly(ethylene-co-methyl acrylate-co-acrylic acid) graphite oxide nanocomposites, *1st Advanced Materials Modern Science of Advanced Materials*, 1, (2004).

175. Shen, J.W., Chen, X.M. and Huang, W.Y., Structure and electrical properties of grafted polypropylene/graphite nanocomposites prepared by solution intercalation, *Journal of Applied Polymer Science*, **88**, 1864, (2003).

176. Xu, J., Hu, Y., Song, L., et al., Preparation and characterization of polyacrylamide-intercalated graphite oxide, *Materials Resource Bulletin*, **36**, 1833, (2001).

177. Xiao, P., Xiao, M., Liu, P., et al., Direct synthesis of a polyaniline-intercalated graphite oxide nanocomposite, *Carbon*,**38**,626,(2000).

178. Brunauer, S., Deming, L., Deming, W., et al., On a theory of the van der Waals adsorption of gases, *Journal of American Chemical Society*, **62**, 1723, (1940).

179. Kim, Y.C., Ahn, W. and Kim, C.Y., A study on multiple melting of isotactic polypropylene, *Polymer Engineering and Science*, **37**, 1003, (1997).

180. Cheng, S.Z.C., Janimak, J.J. and Rodriguez, J., *In polypropylene, structure and morphology*, Chapman and Hall, London, 1995.

181. Zipper, P., Chernev, B. and Schnetzinger, K., Site-resolved x-ray scattering studies, Investigations on plates from pp-graphite composites, *Macromolecules Symposium*, **181**, 411, (2002).

182. Zhu, W., Zhang, G. and Yu, J.D., Crystallization behaviour and mechanical properties of polypropylenen copolymer by in situ copolymerization with a nucleating agent and/or nano-calcium carbonate, *Journal of Applied Polymer Science*, **91**, 431, (2004).

183. Jin, Y., Rogunova, M., Hiltner, A., et al., Structure of polypropylene crystallized in confined nanolayers, *Journal of Applied Polymer Science: Part B: Polymer Physics*, **42**, 3380, (2004).

184. Lotz, B. and Wittman, J.C., The molecular origin of lamellar branching in the alpha (monoclinic) form of isotactic polypropylene, *Journal of Applied Polymer Science: Part B: Polymer Physics*, **24**, 1541, (1986).

185. Ding, R., Hu, Y., Gui, Z., et al., Preparation and characterisation of polystyrene/graphite oxide nanocomposite by emulsion polymerization, *Polymer Degradation and Stability*, **81**, 473, (2003).

186. Qu, B. and Xie, R., Intumescent char structures and flame-retardant mechanism of expandable graphite-based halogen-free flame -retardant linear low density polyethylene blends, *Polymer International*, **52**, 1415, (2003).

187. Alexandre, M. and Dubois, P., Polymer-layered silicate nanocomposites: preparation, properites and uses of a new class of materials, *Materials Science Engineering*, **28**, 1, (2000).

188. Weng, W., Chen, G., Wu, D., et al., Fabrication and characterization of Nylon 6-foliated graphite electrically conducting nanocomposites, *Journal of Polymer Science: Part B: Polymer Physics*, **42**, 2844, (2004).

189. Li, Z.and Qu, B., Flammibility characterization and synergistic effects of expandable graphite with magnesium hydroxide in halogen-free flame-retardant EVA blends, *Polymer Degradation and Stability*, **81**, 401, (2003).

190. Zhu, J., Uhl, F. M., Morgan, A. B., et al., Studies on the mechanism by which the formation of nanocomposite enhances thermal stability, *Chemistry of Materials*, **13**, 4649, (2001).

191. Cho, D., Lee, S., Yang, G., et al., Dynamic mechanical and thermal properties of phenylethynyl-terminated polyimide composites reinforces with expanded graphite nanoplatelets, *Macromolecule Materials Engineering*, **290**, 179, (2004).

192. Du, X.S., Xiao, M., Meng, Y.Z., et al., Facile synthesis of exfoliated and highly conductive poly(arylene disulfide)-graphite nanocomposites, *Polymers for Advanced Technologies*, **15**, 320, (2004).

193. Zou, J.F., Zyu, Z.Z., Pan, Y.X., et al., Conductive mechanism of polymer/graphite conducting composites with low percolation threshold, *Journal of Polymer Science: Part B Polymer Physics*, **40**, 954, (2002).

194. Ezquerra, T.A., Kulescza, M., Cruz, C.S., et al., Charge transport in polyethylene-graphite composite materials, *Advanced Materials*, **2**, 597, (1990).

195. Krupa, I. and Chodak, I., Physical properties of thermoplastic-graphite composites, *European Polymer Journal*, **37**, 2159, (2001).

Appendices

Appendix 1

Lorentz

Function

$$y = y_0 + \frac{2A}{\pi}\frac{w}{4(x - x_c)^2 + w^2}$$

Brief Description

Lorentzian peak function.

Sample Curve

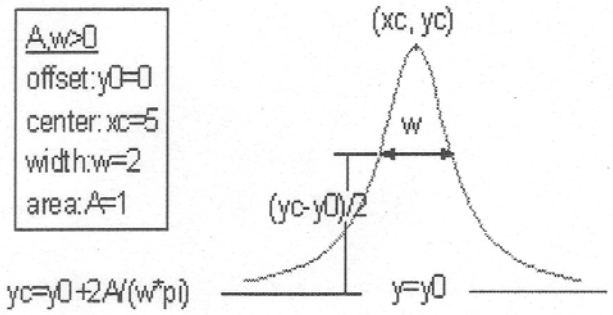

Parameters

Number: 4

Names: y0, xc, w, A

Meanings: y0 = offset, xc = center, w = width, A = area

Initial Values: y0 = 0.0 (vary), xc = 0.0 (vary), w = 1.0 (vary), A = 1.0 (vary)

Lower Bounds: w > 0.0

Upper Bounds: none

Script Access

lorentz(*x,y0,xc,w,A*)

Function File

FITFUNC\LORENTZ.FDF

Appendix 2

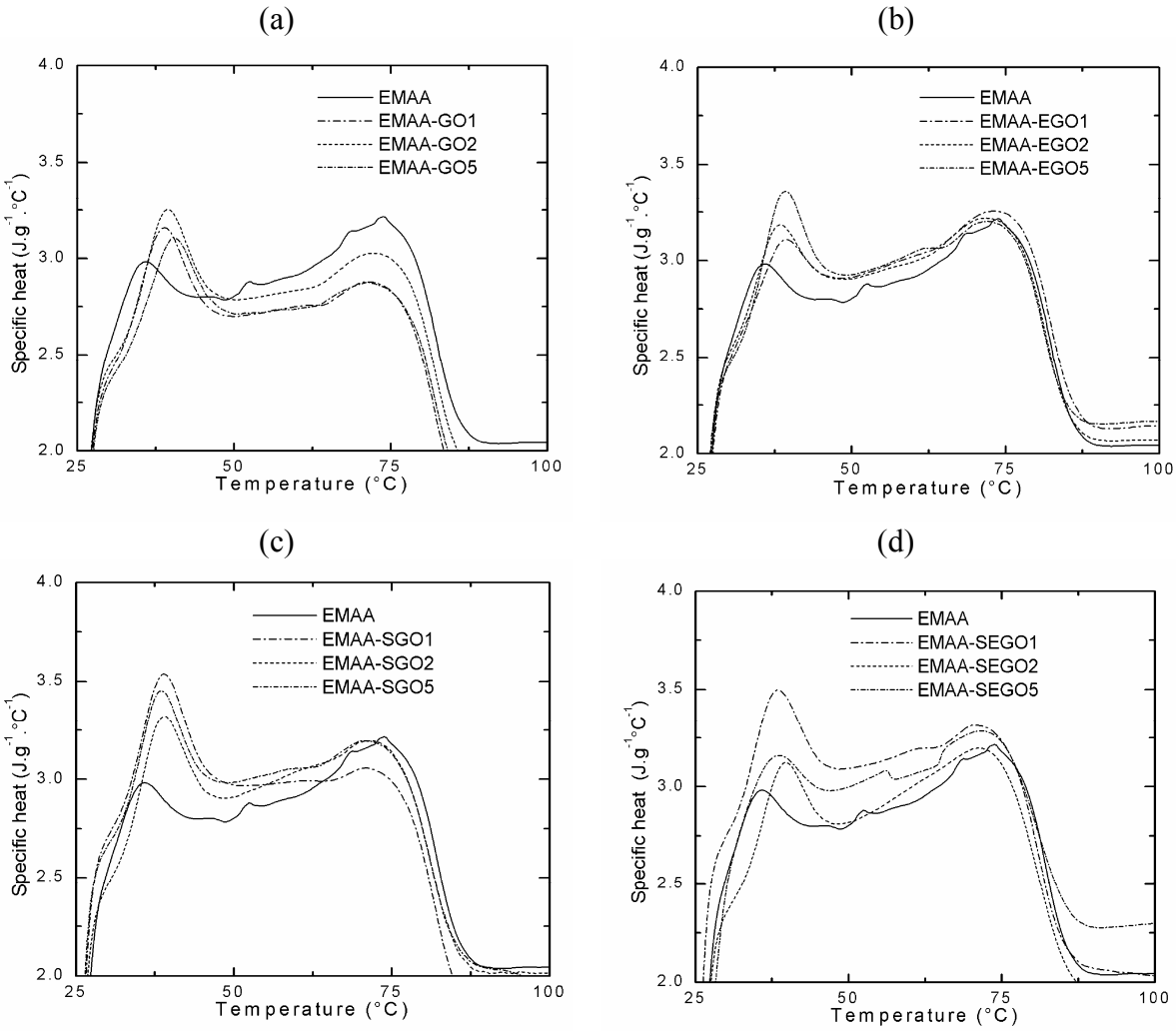

Melting curve of filled EMAA (a) EMAA-GO (b) EMAA-EGO (c) EMAA-SGO (d) EMAA-SEGO

Appendix 3

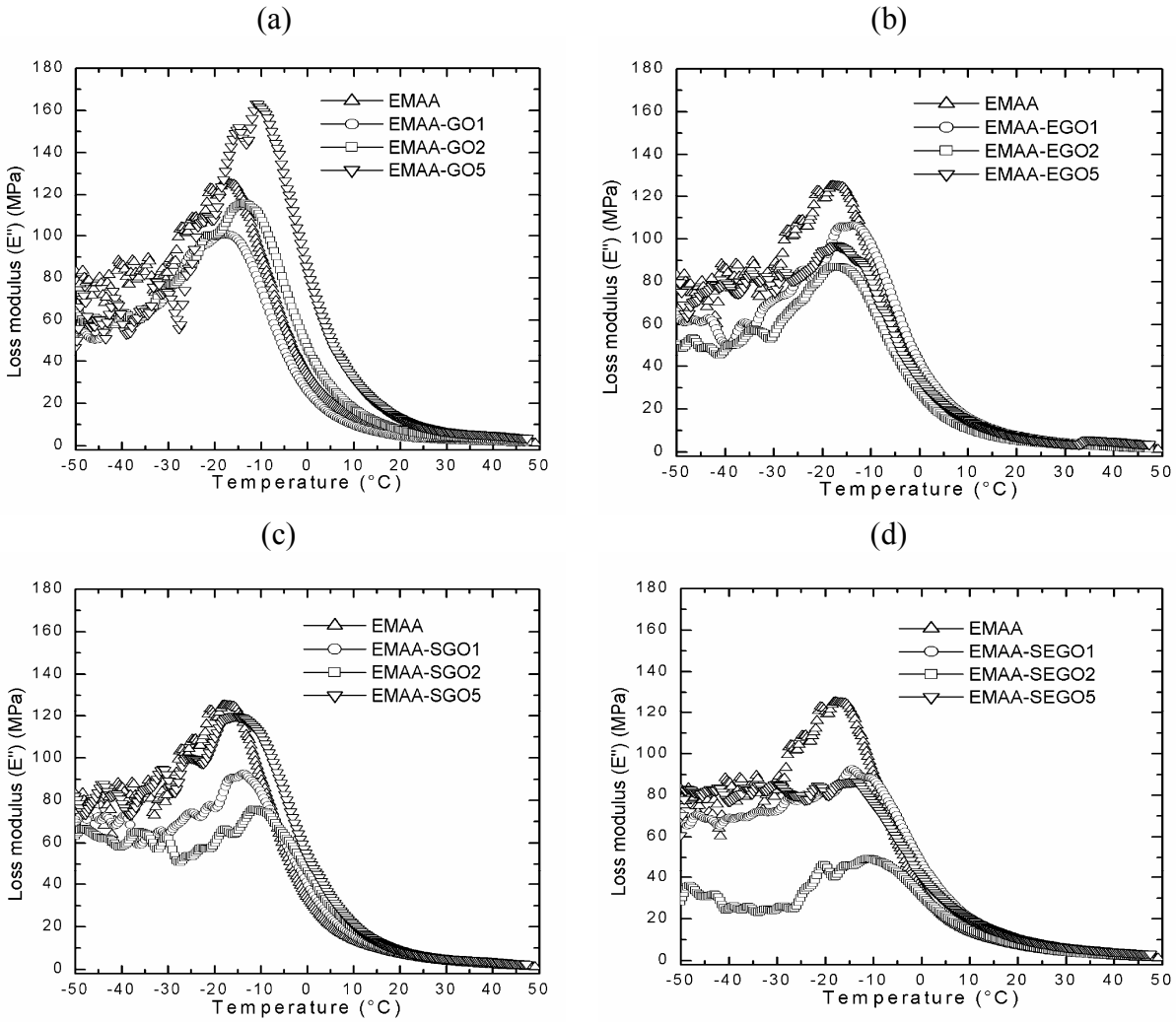

Loss moduli, E″ curves of filled EMAA (a) EMAA-GO (b) EMAA-EGO (c) EMAA-SGO (d) EMAA-SEGO